

**UNIVERSIDADE FEDERAL DE SÃO CARLOS  
CENTRO DE CIÊNCIAS EXATAS E DE TECNOLOGIA  
PROGRAMA DE PÓS-GRADUAÇÃO EM CIÊNCIA E  
ENGENHARIA DE MATERIAIS**

DEVELOPMENT OF BIO-INSPIRED ELECTROMECHANICAL DEVICES  
BASED ON PBMA-*b*-(PSS-*r*-PS) AMPHIPHILIC BLOCK COPOLYMER

Matheus Colovati Saccardo

São Carlos-SP  
2024



**UNIVERSIDADE FEDERAL DE SÃO CARLOS**  
**CENTRO DE CIÊNCIAS EXATAS E DE TECNOLOGIA**  
**PROGRAMA DE PÓS-GRADUAÇÃO EM CIÊNCIA E**  
**ENGENHARIA DE MATERIAIS**

**DEVELOPMENT OF BIO-INSPIRED ELECTROMECHANICAL DEVICES  
BASED ON PBMA-b-(PSS-r-PS) AMPHIPHILIC BLOCK COPOLYMER**

Matheus Colovati Saccardo

Doctoral thesis conducted under the cotutelle agreement presented to the Graduate Program in Materials Science and Engineering as a partial requirement to obtain the title of DOCTOR IN MATERIALS SCIENCE AND ENGINEERING conferred by the Federal University of Sao Carlos (UFSCar) and the title of DOCTOR IN MOLECULAR SCIENCE conferred by University of Padova (UNIPD)

Advisor (UFSCar): Dr. Carlos Henrique Scuracchio

Advisor (UNIPD): Dr. Edmondo Maria Benetti

Funding agency: FAPESP - Process: 2020/02696-6 and 2022/04348-0

São Carlos-SP

2024





To Edécio Antonio Saccardo, Suzana Colovati Saccardo, and  
Beatriz Colovati Saccardo.

**CANDIDATE'S VITAE**

Master of Science in Materials Science and Engineering by UFSCar (2020)

Bachelor in Materials Science and Engineering by UTFPR (2017)





## UNIVERSIDADE FEDERAL DE SÃO CARLOS

Centro de Ciências Exatas e de Tecnologia  
Programa de Pós-Graduação em Ciência e Engenharia de Materiais

---

### Folha de Aprovação

---

Defesa de Tese de Doutorado do candidato Matheus Colovati Saccardo, realizada em 08/04/2024.

#### Comissão Julgadora:

Prof. Dr. Carlos Henrique Scuracchio (UFSCar)

Prof. Dr. Leonardo Bresciani Canto (UFSCar)

Prof. Dr. Antonio José Felix de Carvalho (USP)

Profa. Dra. Francesca Lorandi (UNIPD)

Prof. Dr. Edmondo Maria Benetti (UNIPD)



## ACKNOWLEDGMENTS

With deep admiration and gratitude, I wish to acknowledge and honor all those who participated in the successful completion of this endeavor. Your contributions have been invaluable, and I thank you for your dedication and unwavering commitment.

I want to express my sincere gratitude to God, whose limitless grace and power make everything possible.

I am incredibly grateful to my advisors, Professor Carlos Henrique Scuracchio from UFSCar and Professor Edmondo Maria Benetti from UNIPD, for their unwavering support throughout my journey. Carlos, I express my deepest gratitude for your dedication, availability, and guidance. Your continuous encouragement towards research and collaboration has significantly contributed to the development of my work. Eddy, thank you for welcoming me into your research group for a year and trusting me. Your teachings, friendship, availability, and guidance were invaluable to me. The experience I gained during that time has profoundly impacted my personal and professional growth.

I sincerely thank Professor Leonardo Bresciani Canto, Professor Francesca Lorandi, and Professor Antonio José Felix de Carvalho for their precious contributions as committee members. Thank you for agreeing to be a part of this significant milestone in my life. I sincerely appreciate the time and effort each of you invested in evaluating my research work. Your expertise and commitment to excellence have helped me uphold a high research standard.

I am incredibly grateful to Professor Francesca Lorandi for her priceless teachings in the laboratories and during our relaxed gatherings at Bar dei Chimici. Additionally, I deeply appreciate her constant availability, unwavering belief in my abilities, and genuine friendship. Furthermore, I sincerely thank Professor Cristian Pezzato for imparting his knowledge about science, Italian

language, and culture. Special thanks for the great advice you've given me for my scientific and personal life.

I extend my deepest gratitude to Professor Laos Alexandre Hirano, my co-supervisor during my master's degree, who helped me during my PhD. Professor Hirano's expertise in electromechanical devices, electronics, and robotics was vital to my research. His guidance was fundamental in developing the electromechanical characterization system, a critical component for completing this work. Thank you, Professor Hirano, for your unwavering support and dedication to my academic and professional growth.

I also express my sincere gratitude to Dr. Apostolos Vagias for his invaluable contribution in conducting the GISAXS analyses at the Technical University of Munich. His profound expertise was fundamental in interpreting and analyzing the data, significantly enhancing our understanding of the copolymer's morphology. Thank you, Dr. Apostolos Vagias, for your availability and support during my analyses.

During my PhD I was blessed to meet fantastic people I am deeply grateful for. Thank you to my friends from the Smart Materials Research Team (SMaRT) research group, Prof. Ariel Gustavo Zuquello, Prof. Roger Gonçalves, Prof. Rafael Barbosa, Dr. Kaique Afonso Tozzi, Thiago Maffei, Victor Bhuler Salomão, Paulo Gall, and Paulo Victor de Araújo Fernandes for the scientific contributions, teachings and good times we spent together during work and get-togethers.

Special thanks to my friends from the Laboratory of Macromolecular and Organic Chemistry (MOC) research group Andrea Rossa, Alberto Fracasso, Carlos Pavon Regana, Gianluca Gazzola, Irene Filipucci, Vincenzo Guir, André Plath and Freud Lange, who welcomed me very well and made me feel at home. Thank you for teaching me about the Italian language and culture. Thank you, Andrea Rossa and Alberto Soppelsa, for the amazing trips to Alleghe and

the unforgettable time spent at Rodolfo's house. Those trips to the mountains, barbecues, and engaging conversations made the experiences special.

I also want to thank Alberto Fracasso for opening his home to me and treating me like family. Your warmth and hospitality made me feel welcome from the very beginning. Moreover, your ability to bring joy to the laboratory even when reactions didn't go as planned (quite often!) was commendable. Thank you for always brightening up the atmosphere and keeping the team motivated. I want to express my sincere gratitude to Carlos Pavon, Irene Filipucci, and Gianluca Gazzola for teaching me the intricacies of chemistry and always being available to help me. Your expertise, patience, and enthusiasm have been invaluable to my learning experience. Thank you for making a complex subject accessible and attractive and for your unwavering support throughout my studies.

I want to express my deepest gratitude to my cherished friends who enriched my life during working hours and beyond. Your company has enhanced my work and leisure experience, and I am grateful for the joyous moments we have shared. Thank you, Lucas Theodoro, Rudge Theodoro, Durval Venore, Alberto Soppelsa, Franklin Andrade, Martina Varotto, Giulia Tomei, Ewerton Teotônio, Andre Balogh, Beatriz Suquizaqui, Marcos Vinicius, Jessica Pereira, Marcos Nicolino, Daniel Morales, Vahab Seif, and Onur Dogan.

Special acknowledgment to The Federal University of São Carlos, Graduate Program in Materials Sciences Engineering (PPGCEM), and all professionals, professors, secretaries, technicians, and other collaborators essential to developing a program of excellence. The University of Padova (UNIPD), Department of Chemical Sciences, and to all professionals, professors, secretaries, technicians, and other collaborators essential to developing a program of excellence.

This study was financed in part by the Coordenação de Aperfeiçoamento de Pessoal de Nível Superior - Brasil (CAPES) - Finance Code 001.

I express my sincere gratitude to CAPES - Coordination for the Improvement of Higher Education Personnel for their generous financial support through the scholarship, process number 88887.501393/2020-00, enabling the completion of this work.

The São Paulo Research Foundation (FAPESP) for funding and supporting research through processes: 2020/02696-6 and 2022/04348-0.

Before I conclude, I want to express my deepest gratitude to several people who have played a significant role in my life. First, I would like to thank my parents, Edelcio and Suzana, who have provided abundant love and support throughout my life. They created a nurturing environment that enabled me to thrive in my educational and moral development. I am also grateful to my sister, Beatriz, for her affection and joy in my life. Her presence has been a source of happiness and comfort to me. Lastly, I want to express my appreciation to Ingrid Seme Amed de Moraes. Her affection, dedication, and advice have been invaluable to me. Even when I struggled to believe in myself, her unwavering support has been a constant source of strength. She has believed in me more than anyone else and has inspired me to dream big, feel better, grow, believe in myself, and always strive for my best.

Thank you all for being an integral part of my journey.



## ABSTRACT

Technological advances in the aerospace, biomedical, and robotics industries stimulate the need for innovative and sustainable devices, such as electromechanical devices (EMDs), which are bio-inspired materials capable of mimicking biological systems in appearance, functionality, and operation. For practical applications, EMDs must combine several properties, such as i) high ionic conductivity, ii) flexibility, iii) mechanical resistance, and iv) chemical, thermal, and structural stability. Such properties can be obtained by engineering amphiphilic copolymers, which can self-assemble into well-defined morphologies with nanometric domains. Thus, it is possible to effectively dissociate ionic conductivity from mechanical properties, adjusting the flexibility, Young's modulus, and ionic conductivity according to the size of the blocks and the number of functional groups. Therefore, in this project, reversible addition-fragmentation chain transfer (RAFT) polymerization was used to synthesize the diblock copolymer Poly(butyl methacrylate)-b-(sulfonated polyneopentyl styrene-r-polystyrene) (PBMA-b-(PNeoSS-r-PS)). Subsequent thermolysis of the PNeoSS segments removes the neopentyl group, resulting in a sulfonated polystyrene-r-polystyrene (PSS-r-PS) backbone, yielding an amphiphilic block copolymer with ionic conductivity, which was used to prepare an EMD. In general, it can be concluded that RAFT polymerization is a robust and versatile technique that allows control of the degree of polymerization, molecular weight, polydispersity, and chemical composition of the copolymer. The copolymer presented a molecular weight of  $65 \text{ kg}\cdot\text{mol}^{-1}$ , with a 50% ratio between flexible and rigid blocks, alongside an 8.8% degree of sulfonation, lamellar morphology, capable for enhancing flexibility and ionic conductivity. Finally, the device was tested and characterized electromechanically using an electromechanical characterization system, showing promise for application as a sensor.

**Keywords:** Electromechanical devices; Amphiphilic block copolymer; Electromechanical response; RAFT polymerization; Sensor



## RESUMO

### DESENVOLVIMENTO DE DISPOSITIVOS ELETROMECAÑICOS BIOINSPIRADOS BASEADOS EM COPOLÍMERO EM BLOCO ANFIFÍLICO DO TIPO PBMA-b-(PSS-r-PS)

Os avanços tecnológicos na indústria aeroespacial, biomédica e robótica estão estimulando a necessidade de dispositivos inovadores e sustentáveis, como os dispositivos eletromecânicos (EMDs), que são materiais bio-inspirados capazes de imitar sistemas biológicos em aparência, funcionalidade e operação. Para aplicações práticas os EMDs devem combinar diversas propriedades, como: i) alta condutividade iônica, ii) flexibilidade, iii) resistência mecânica e iv) estabilidade química, térmica e estrutural. Tais propriedades podem ser obtidas por meio da engenharia de copolímeros anfifílicos, uma vez que podem se auto montar em morfologias bem definidas com domínios nanométricos. Assim, é possível dissociar a condutividade iônica das propriedades mecânicas, ajustando a flexibilidade o módulo de Young e a mobilidade iônica conforme o tamanho dos blocos e quantidade de grupos funcionais. Portanto, neste projeto a polimerização por transferência reversível de cadeia por adição-fragmentação (RAFT) foi usada para sintetizar o copolímero dibloco Poli(metacrilato de butila)-b-(poli neopentil estireno sulfonado-r-poliestireno) (PBMA-b-(PNeoSS-r-PS)). Subsequente termólise dos segmentos PNeoSS remove o grupo neopentil, resultando em uma cadeia principal de poliestireno sulfonado-r-poliestireno (PSS-r-PS), originando um copolímero em bloco anfifílico com condutividade iônica, utilizado para preparar um EMD. De um modo geral, pode-se concluir que a polimerização RAFT é uma técnica robusta e versátil, que permitiu o controle do grau de polimerização, peso molecular, polidispersividade e composição química do copolímero. O copolímero sintetizado usado para preparar o EMD apresentou peso molecular de  $65 \text{ kg.mol}^{-1}$ , uma relação de 50% entre os blocos flexíveis e rígidos, com um grau de sulfonação de 8,8%, morfologia lamelar, e há potencial para otimizar sua flexibilidade e condutividade iônica. Por fim, o dispositivo foi testado e caracterizado eletromecanicamente, se mostrando promissor para aplicação como sensor.

**Palavras-chave:** Dispositivos eletromecânicos; Copolímero em bloco anfifílico; Resposta eletromecânica; Polimerização RAFT; Sensor.



## PUBLICATIONS

- Saccardo, M. C., Zuquello, A.G., Gonçalves, R., Tozzi, K. A., Barbosa, R., Hirano, L. A., Scuracchio, C. H. Electromechanical Evaluation of Ionomeric Polymer-Metal Composites Using Video Analysis. *Materials Research*. 2021, v. 24, n. Supl 2 <doi.org/10.1590/1980-5373-mr-2021-0317>.
- Barbosa, R., Gonçalves, R., Tozzi, K. A., Saccardo, M. C., Zuquello, A. G., Scuracchio, C. H. Improving the swelling, mechanical, and electrical properties in natural rubber latex/carbon nanotubes nanocomposites: Effect of the sonication method. *J. Appl. Polym. Sci.* 2022, e52325. <doi.org/10.1002/app.52325>.
- Tozzi, K. A., Gonçalves, R., Barbosa, R., Saccardo, M. C., Zuquello, A., Sgreccia, E., Narducci, R., Scuracchio, C. H., di Vona, M. L.. Improving electrochemical stability and electromechanical efficiency of IPMCs: tuning ionic liquid concentration. *J Appl Electrochem*, 2023. <doi.org/10.1007/s10800-022-01776-w>.
- Zuquello, A., Saccardo, M. C., Gonçalves, R., Tozzi, K. A., Barbosa, R., Hirano, L. A., Scuracchio, C. H. PI controller for IPMC actuators based on Nafion®/PT using machine vision for feedback response at different relative humidities. *Materials Research*, 2023. <doi.org/10.1590/1980-5373-MR-2021-0518 >.
- Barbosa, R., Gonçalves, R., Blanco, E. de O., Saccardo, M. C., Tozzi, K. A. Zuquello, A. G., Scuracchio, C. H. Multi-sensing properties of hybrid filled natural rubber nanocomposites using impedance spectroscopy. *Electrochimica Acta*, 2023. <doi.org/10.1016/j.electacta.2022.141341>.
- Barbosa, R., Gonçalves, R., Blanco, E. de O., Saccardo, M. C., Tozzi, K. A. Zuquello, A. G., Cruz, S. A., Scuracchio, C. H. Novel IP<sup>2</sup>C sensors with flexible

electrodes based on plasma-treated conductive elastomeric nanocomposites. *Smart Materials and Structures*, 2024. <doi.org/10.1088/1361-665X/ad1c50>.

- Gonçalves, R., Tozzi, K. A., Saccardo, M. C., Zuquello, A. G., Barbosa, R., Blanco, G. E. de O., Hirano, L. A., Scuracchio, C. H. Review on the use of impedance spectroscopy for IPMC-like devices: application, models, and a new approach to data treatment. *Materials Advances*, 2024 <doi.org/10.1039/D3MA00593C>.

- Saccardo, M. C., Barbosa, R., Zuquello, A. G., Blanco, G. E. de O., Tozzi, K. A., Gonçalves, R., Scuracchio, C. H. Beyond Static: Tracking the Dynamic Nature of Water Absorption and Young's Modulus in IPMC Devices. *Journal of Applied Polymer Science*. (Submitted).

- Blanco, G. E. de O., Valerio, L. R., Barbosa, R., Gonçalves, R., Saccardo, M. C., Zuquello, A. G., Tozzi, K. A., Scuracchio, C. H. Development of an alternative membrane for ionomeric polymer and metal composite actuators based on sulfonated peek: effect of different humidity, counterions and sulfonation degrees. *Sensors and Actuators A: Physical* (Submitted).

- Barbosa, R., Gonçalves, R., Blanco, E. de O., Saccardo, M. C., Paiva, R. da S., Mastelaro, V. R., Cruz, S. A., Scuracchio, C. H. Plasma Treatment of Nafion Membranes: A Trade-Off Between Surface Modification and Electrochemical Degradation. *Journal of Power Sources* (Submitted).

## SUMMARY

	Page
APPROVAL SHEET .....	i
ACKNOWLEDGMENTS.....	iii
ABSTRACT .....	vii
RESUMO .....	ix
PUBLICATIONS.....	xi
SUMMARY.....	xiii
LIST OF TABLES.....	xvii
LIST OF FIGURES.....	xix
LIST OF ACRONYMS.....	xxv
1 INTRODUCTION .....	1
1.1 Motivation .....	1
1.2 Objectives .....	5
1.3 State-of-the-art and unique contributions.....	6
2 LITERATURE REVIEW .....	7
2.1 Active polymers.....	7
2.2 Sensors and actuators based on iEAPs.....	10
2.3 Nafion morphology.....	12
2.4 Block Copolymers (BCPs) .....	16
2.4.1 Block copolymers synthesis.....	17
2.4.2 Reversible deactivation radical polymerization (RDRP).....	20
2.4.3 Reversible Addition-Fragmentation Chain Transfer (RAFT) .....	25
2.4.4 Phase separation in block copolymers.....	30
2.4.4.1 Order to disorder transition (ODT) .....	38
2.4.5 Phase separation in amphiphilic block copolymers.....	39
3 MATERIALS AND METHODS .....	47
3.1 Materials .....	47
3.1.1 PBMA-b-(PSS-r-PS) synthesis.....	47
3.1.2 Preparation of electromechanical device .....	47
3.1.3 Electromechanical System.....	48
3.2 Experimental.....	49

3.2.1	Synthesis of neopentyl styrene sulfonate (NeoSS) monomer .....	49
3.2.1.1	Synthesis of 4-vinylbenzenesulfonyl chloride .....	49
3.2.1.2	Synthesis of Neopentyl p-Styrene Sulfonate .....	49
3.2.2	Synthesis of PBMA-CPADB macroinitiator.....	50
3.2.3	Synthesis of PBMA-b-(PNeoSS-r-PS) block copolymer .....	51
3.2.4	Preparation of PBMA-b-(PSS-r-PS) amphiphilic block copolymer.....	51
3.2.5	Preparation of PBMA-b-(PSS-r-PS) membrane .....	51
3.2.6	Bio-inspired electromechanical device preparation .....	52
3.2.7	Electromechanical system development .....	54
3.3	Characterizations .....	56
3.3.1	Gel permeation chromatography (GPC).....	56
3.3.2	Nuclear Magnetic Resonance (NMR).....	57
3.3.3	Fourier transform infrared spectroscopy (FTIR) .....	57
3.3.4	Thermogravimetric Analysis (TGA) .....	57
3.3.5	Differential Scanning Calorimetry (DSC).....	58
3.3.6	Atomic force microscopy (AFM) .....	58
3.3.7	X-ray reflectivity (XRR).....	59
3.3.8	Grazing-incident small-angle scattering (GISAXS).....	59
3.3.9	Rheology .....	60
3.3.10	Scanning electron microscopy (SEM) .....	60
3.3.11	Water uptake (WU).....	61
3.3.12	Ion exchange capacity (IEC) .....	61
3.3.13	Ionic conductivity .....	62
3.3.14	Electromechanical Performance.....	62
4	RESULTS AND DISCUSSIONS.....	65
4.1	Synthesis of PBMA-CPADB macroinitiator.....	65
4.1.1	PBMA-CPADB RAFT proposed mechanism .....	69
4.2	Synthesis of PBMA-b-(PNeoSS-r-PS) block copolymer .....	71
4.2.1	PBMA-b-(PNeoSS-r-PS) RAFT proposed mechanism.....	77
4.3	Preparation of PBMA-b-(PSS-r-PS) amphiphilic block copolymer.....	79
4.4	Morphological Characterization .....	86
4.4.1	Atomic force microscopy (AFM) .....	86



4.4.2	X-ray reflectivity and Grazing-incident small-angle X-ray scattering .....	90
4.4.3	Order-to-disorder transition .....	97
4.5	Ionomer Characterization.....	99
4.5.1	Ion exchange capacity and water uptake.....	99
4.5.2	Electrochemical Characterization.....	101
4.5.3	Platinum electrodes morphology.....	105
4.6	Electromechanical Response .....	108
5	CONCLUSIONS.....	113
6	SUGGESTIONS FOR FUTURE WORKS .....	115
7	REFERENCES .....	117
	ANNEX A .....	155
	ANNEX B .....	157
	ANNEX C .....	161



**LIST OF TABLES**

	Page
Table 1: Classification of Electroactive Polymers.....	9
Table 2: Benefits and limitations of NMP, ATRP, and RAFT.....	25
Table 3: Correlation between the main chain transfer agents and monomers.	30
Table 4: Reactions involved in the deposition process.....	52
Table 5: PBMA-CPADB macroinitiator synthesis conditions. ....	68
Table 6: PBMA-b-(PneoSS-r-PS) copolymer synthesis conditions. ....	74
Table 7: PBMA-b-(PNeoSS-r-PS) and PBMA-b-(PSS-r-PS) block copolymers library. ....	76
Table 8: Summary of extracted data from the XRR fit for PBMA-b-(PNeoSS-r-PS) block copolymer. ....	92
Table 9: Summary of extracted data from the GISAXS simulations using the BornAgain software for PBMA-b-(PNeoSS-r-PS) block copolymer. ....	93
Table 10: Summary of extracted data from the XRR fit for PBMA-b-(PSS-r-PS). ....	95
Table 11: Summary of extracted data from the GISAXS simulations using the BornAgain software for PBMA-b-(PSS-r-PS) block copolymer.....	95
Table 12: IEC, WU, and ionic conductivity for PBMA-b-(PSS-r-PS) and Nafion. ....	100
Table 13: Impedance parameters obtained from data fitting. ....	103



## LIST OF FIGURES

	Page
Figure 1: Bio-inspired materials and devices presenting some applications. ....	1
Figure 2: Bio-inspired electromechanical devices applications. ....	2
Figure 3: Unwanted products from the sulfonation of polystyrene.....	4
Figure 4: Active polymer applications.....	7
Figure 5: Timeline of active polymers landmarks and development.....	8
Figure 6: Actuation mechanism of electromechanical devices based on a) electronic and b) ionic electroactive polymers.....	10
Figure 7: a) IPMC, b) Nafion's chemical structure, c) IPMC bending movement, and d) Nafion's morphology, showing the ionomeric channels (light blue). ....	11
Figure 8: Most important morphological models for ionomers. a) Ionic cluster network, b) core-shell, c) local order, d) sandwich-like, e) rod-like, f) water channel, and g) unified morphological.....	13
Figure 9: Block copolymer applications, including drug delivery, sutures, biosensors, solar cells, electromechanical devices, and sustainable materials.	17
Figure 10: Commercial synthesis of styrene-butadiene-styrene (SBS) block copolymers by living anionic polymerization. ....	19
Figure 11: Simplified schematic representation of radical polymerization, living anionic polymerization, and reversible deactivation radical polymerization.....	21
Figure 12: Simplified radical polymerization mechanisms by reversible deactivation. a) stable radical-mediated polymerization, b) atom transfer radical polymerization, and c) degenerative-transfer radical polymerization.....	23
Figure 13: Schematic representation of controlled topologies, compositions, and functionalities of polymers and copolymers prepared by RAFT. ....	27
Figure 14: Proposed mechanisms for RAFT polymerization. ....	28
Figure 15: Chemical structure of the main RAFT agents. ....	28
Figure 16: Phase diagram of symmetric conformational diblock copolymer [205]. .....	36
Figure 17: Order and disorder states in a symmetric diblock copolymer.....	39
Figure 18: a) Illustration of a spherical micelle self-assembling in solution and b) adsorption at a surface.....	40

Figure 19: a) Amphiphilic structures self-assembly leads to a range of different structures: a) Spherical micelle, b) lamellar phase, c) inverted micelle, d) cylindrical micelle, and e) vesicle.....	40
Figure 20: Schematics of block, star, and graft amphiphilic block copolymers.	42
Figure 21: Different block copolymer self-assembly as a function of packing parameter p-range.....	43
Figure 22: Examples of polymers with varied nature of hydrophilic and hydrophobic blocks.....	45
Figure 23: Synthesis of neopentyl styrene sulfonate, b) NMR spectroscopy of 4-vinylbenzenesulfonyl chloride, and c) NMR spectroscopy of neopentyl styrene sulfonate.....	50
Figure 24: Step-by-step of the electroless plating process, featuring samples captured both before and after platinum reduction, resulting in the formation of metallic electrodes.....	53
Figure 25: a) IPMC control system (top view) and b) humidity control system..	54
Figure 26: IPMC power source scheme. ....	56
Figure 27: a) Chemical structure of the polymerization components, b) $^1\text{H}$ NMR spectrum of the polymerization solution at 0h in $\text{CDCl}_3$ , and c) $^1\text{H}$ NMR spectra of the polymerization aliquots obtained at various intervals in $\text{CDCl}_3$ . ....	65
Figure 28: a) RAFT polymerization of the macroinitiator, highlighting relevant protons, b) GPC traces for PBMA-CPADB with different DP, c) NMR spectra of BMA ( $c_1$ ) and PBMA ( $c_2$ ) in $\text{CDCl}_3$ , d) Kinetic plot and conversion over time, e) GPC traces in DMF at 60 °C, and f) $M_n$ and $\bar{D}$ as a function of conversion.....	66
Figure 29: PBMA-CPADB macroinitiator RAFT mechanisms: (i) Initiation and propagation, (ii) pre-equilibrium, (iii) reinitiation, (iv) main equilibrium, and (v) termination.....	70
Figure 30: a) Synthesis of PBMA-b-(PNeoSS-r-PS) by RAFT polymerization, b) NMR spectroscopy of the copolymer in $\text{CDCl}_3$ , and c) GPC analysis of macroinitiator and copolymer in DMF at 60 °C. ....	71
Figure 31: a) Macroinitiator, Sty, and NeoSS chemical structure, b) NMR spectrum of the polymerization solution at 0h, and c) NMR spectra of the polymerization aliquots obtained at various intervals.....	72

Figure 32: a) PBMA-b-(PNeoSS-r-PS) RAFT polymerization reaction, b) GPC traces in DMF at 60 °C, c) NeoSS kinetic plot and conversion over time, d) Sty kinetic plot and conversion over time, e) PBMA-b-(PNeoSS-r-PS) $M_n$ and $\bar{D}$ as a function of conversion. ....	73
Figure 33: PBMA-b-(PNeoSS-r-PS) GPC traces in DMF at 60 °C. a) Entries 1-4, b) Entries 5-8, and c) Entries 9-12. ....	75
Figure 34: Copolymer RAFT mechanisms: (i) Initiation and propagation, (ii) pre-equilibrium, (iii) reinitiation, (iv) main equilibrium, and (v) termination. ....	79
Figure 35: TGA thermograms for a) PBMA and b) PBMA-b-(PNeoSS-r-PS). DSC curves for c) PBMA and d) PBMA-b-(PNeoSS-r-PS). ....	80
Figure 36: a) FTIR and b) GPC analysis of the copolymer before (black) and after (red) thermolysis, c <sub>1</sub> ) PBMA, c <sub>2</sub> ) PBMA-b-(PNeoSS-r-PS), and c <sub>3</sub> ) PBMA-b-(PSS-r-PS) spectra in CDCl <sub>3</sub> . ....	82
Figure 37: a) FTIR spectra for PBMA-b-(PNeoSS-r-PS) before (black) and after (colorful) thermolysis for Entries 1-12, b) image (a) amplified for Entries 1-6, and c) image (a) amplified for Entries 7-12. ....	84
Figure 38: GPC analysis of the copolymers before (black) and after (colorful) thermolysis in DMF at 60 °C. ....	84
Figure 39: a) NMR spectra in CDCl <sub>3</sub> and (CD <sub>3</sub> ) <sub>2</sub> SO for PBMA-b-(PSS-r-PS) in DMF. The yellow circles indicate the peaks that arise due to the interactions between -OH and CDCl <sub>3</sub> . ....	85
Figure 40: AFM images for Entry 01, presenting the topography in 2D and 3D, phase 2D and 3D, and profile. ....	86
Figure 41: AFM images for Entry 05, presenting the topography in 2D and 3D, phase 2D and 3D, and profile. ....	87
Figure 42: AFM images for Entry 09, presenting the topography in 2D and 3D, phase 2D and 3D, and profile. ....	88
Figure 43: AFM images for Entry 09 after thermolysis, presenting the topography in 2D and 3D, phase 2D and 3D, and profile. ....	89
Figure 44: a) XRR data, $R(q_z)$ vs. $q_z$ . Experimental data (black circles) and fit (red line), b) Fast Fourier Transform (FFT) analysis, c) Scattering length density (SLD) profile vs. distance away from the Si substrate ( $z$ ), d) Experimental (left)	

and simulated (right) panels for GISAXS patterns. The intensity scale bar spans the range from 0.5 to $5 \times 10^5$ , and e) Sketch of modelled architecture using BornAgain software. ....	91
Figure 45: a) XRR data, $R(q_z)$ vs. $q_z$ . Experimental data (black circles) and fit (red line), b) Fast Fourier Transform (FFT) analysis, c) Scattering length density (SLD) profile vs. distance away from the Si substrate (z), d) Experimental (left) and simulated (right) panels for GISAXS patterns. The intensity scale bar spans the range from 0.5 to $5 \times 10^5$ , and e) Sketch of modelled architecture using BornAgain software. ....	94
Figure 46: Assumed domain-edge structure for PBMA-b-(PNeoSS-r-PS). Dashed lines represent PNeoSS-PS-PS-PNeoSS or PBMA-PBMA separations. ....	96
Figure 47: a) Log $G'$ versus log $G''$ for the PBMA-b-(PSS-r-PS) sample at various temperatures, b) low frequency region emphasizing the slope = 2 for 200 °C, showing $T_{odt}$ . ....	98
Figure 48: Nyquist plot for a) RH = 60 and 90% and b) RH = 30%, c) Modified Randles circuit, d) Bode plot of the impedance magnitude ( $ Z $ ) e) Bode phase, and f) ionic conductivity as a function of RH. ....	102
Figure 49: a) SEM micrographs of the platinum electrode surface and b) lateral cryofracture showing platinum layer thickness ....	106
Figure 50: IPMC electromechanical response when subjected to different displacement profiles. a) Damping vibration spectrum, b) movement with constant linear speed, c) movement with non-linear speed, d) Sinusoidal movement. RH was controlled at 90%. ....	109
Figure 51: IPMC voltage amplitude when subjected to 0.1, 0.2, 0.4, and 2.0 Hz frequency stimuli. ....	111
Figure A52: The acrylic chamber project, designed using FreeCAD, presents an isometric view of the assembled box alongside detailed front views of its individual components. ....	155
Figure A53: a) The acrylic chamber, assembled post laser-cutting of its individual components, showcases a seamless union achieved through the	



application of chloroform. b) Integrated within are electronic components configured to control the stepper motor and data acquisition. ....	155
Figure A54: Basic structure of a stepper motor and position control. A stepper motor rotates with a fixed step angle. The rotation angle and speed of the stepping motor can be controlled accurately using pulse signals from the controller. The length of rotation of the stepping motor is proportional to the number of pulse signal (pulse number) given to the driver.....	156
Figure B55: Relative humidity reading in real time, which can be observed both directly from the Arduino program and on the LabView front panel, as shown in Appendix C.....	160
Figure C56: Front panel of the developed control system. ....	161
Figure C57: Pattern recognition software (part 1). ....	162
Figure C58: Pattern recognition software (part 2). ....	163



**LIST OF ACRONYMS**

- AIBN**: 2,2'-Azobis(2-methylpropionitrile)  
**AFM**: Atomic Force Microscopy  
**A<sup>m</sup>**: Activator  
**A<sup>m+1</sup>X**: Stable specie  
**ATRP**: Atom Transfer Radical Polymerization  
**BMA**: Butyl Methacrylate  
**BCP**: Block Copolymer  
**CDCl<sub>3</sub>**: Deuterated Chloroform  
**(CD<sub>3</sub>)<sub>2</sub>SO**: Deuterated Dimethyl Sulfoxide  
**CLRP**: Controlled/Living Free Radical Polymerization  
**CPADB**: 4-Cyano-4-(phenylcarbonothioylthio)pentanoic acid  
**CSIRO**: Commonwealth Scientific and Industrial Research Organization  
**CTA**: Chain Transfer Agent  
**DFT**: Density Functional Theory  
**DMF**: Dimethylformamide  
**DP**: Degree of Polymerization  
**DPD**: Dissipative Particle Dynamics  
**DSC**: Differential Scanning Calorimetry  
**EAP**: Electroactive Polymer  
**eEAP**: Electronic Electroactive Polymer  
**EIS**: Electrochemical Impedance Spectroscopy  
**EMD**: Electromechanical Devices  
**f<sub>A</sub>**: Volume fraction of phase A  
**f<sub>B</sub>**: Volume fraction of phase B  
**FTIR**: Fourier-Transform Infrared Spectroscopy  
**G'**: Storage Modulus  
**G''**: Loss Modulus  
**GISAS**: Grazing-Incidence Small-Angle Scattering  
**GISANS**: Grazing-Incidence Small-Angle Neutron Scattering  
**GISAXS**: Grazing-Incidence Small-Angle X-ray Scattering  
**GPC**: Gel Permeation Chromatography

**I\***: Dissociated initiator

**iEAP**: Ionic Electroactive Polymer

**IEC**: Ion Exchange Capacity

**IL**: Ionic Liquid

**INIFERTER**: Initiator, Transfer Agent, and Terminator

**IPMC**: Ionomeric Polymer-Metal Composites

**IUPAC**: International Union of Pure and Applied Chemistry

**k<sub>act</sub>**: Activation rate constant

**K<sub>c</sub>**: Combination rate constant

**k<sub>d</sub>**: Dissociation rate constant

**k<sub>deact</sub>**: Deactivation rate constant

**k<sup>n</sup><sub>ex</sub>**: Degenerative chain transfer rate constant

**k<sup>m</sup><sub>ex</sub>**: Degenerative chain transfer rate constant

**LabView**: Laboratory Virtual Instrument Engineering Workbench

**LPA**: Living Anionic Polymerization

**LM7812**: Positive voltage regulator

**LM7912**: Negative voltage regulator

**MADIX**: Macromolecular Design by the Interchange of Xanthate

**MeOH**: Methanol

**M<sub>n</sub>**: Number average molecular weight

**M<sup>th</sup>**: Theoretically estimated molecular weight

**M<sub>w</sub>**: weight average molecular weight

**N**: Entropy to the Gibbs free energy (chain size)

**SEM**: Scanning Electron Microscopy

**SD**: Sulfonation Degree

**STM**: Scanning Tunnelling Microscope

**NaSS**: Sodium 4-vinylbenzenesulfonate

**NeoSS**: Neopentyl p-Styrene Sulfonate

**NI-9218**: Data acquisition module

**NI-9263**: Voltage output module

**NMP**: Nitroxide Mediated Polymerization

**NMR**: Nuclear Magnetic Resonance

**ODT:** Order to Disorder Transition  
**OPA551:** Operational amplifier  
**OSP:** Open-Source Physics  
**P<sub>1</sub>\*:** Propagating polymeric radical  
**PB:** Polybutadiene  
**PBMA:** Poly(butyl methacrylate)  
**PBMA-b-(PNeoSS-r-PS):** Poly(butyl methacrylate)-b-Poly(polyneopentyl styrene sulfonate-r-polystyrene)  
**PBMA-b-(PNeoSS-r-PS):** Poly(butyl methacrylate)-b-Poly(styrene sulfonate-r-polystyrene)  
**PBO:** Polybutylene Oxide  
**PCL:** Polycaprolactone  
**PEG:** Poly(ethylene Glycol)  
**PEO:** Polyethylene Oxide  
**PLA:** Polylactic Acid  
**P<sub>m</sub>-X:** Dormant polymer chains  
**P<sub>m</sub>\*:** Active propagating species  
**P<sub>m+1</sub>\*:** Long propagating radicals  
**PNIPAM:** poly(N-isopropyl acrylamide)  
**P<sub>n</sub>-X:** Dormant polymer chains  
**P<sub>n</sub>\*:** Active propagating species  
**P<sub>n</sub>S(Z)C=S:** Polymeric thiocarbonyl compound  
**PPO:** polypropylene oxide  
**PS:** Polystyrene  
**PSO:** Polystyrene Oxide  
**PTFE:** Polytetrafluoroethylene  
**PVA:** Polyvinyl Alcohol  
**PVCL:** Polyvinyl Caprolactam  
**PVP:** Polyvinyl Pyrrolidone  
**Q<sub>dev</sub>:** Capacitance of the device  
**Q<sub>phase</sub>:** Capacitance of the PSS-PS phase  
**q/r:** Metric for the shape of the polymer molecule

**R:** Gast Constant

**R\*:** Radical

**RAFT:** Reversible addition–fragmentation chain-transfer

**Rchar:** Charge Resistance of the device

**Rdev:** Resistance of the device

**RDRP:** Reversible-Deactivation Radical Polymerization

**RphaseQphase:** Resistive-Capacitive element of the PSS-PS phase

**RSC(Z)=S:** Thiocarbonyl Compound

**SAXS:** Small-angle X-ray scattering

**SBS:** Styrene-b-Butadiene-b-Styrene triblock copolymer

**SEM:** Scanning Electron Microscopy

**SLD:** Scattering Length Densitie

**S<sup>R</sup>:** Residual contribution of the entropy

**SSD:** Sample-to-Detector Distance

**SSL:** Strong Segregation Limit

**Sty:** Styrene

**TEMPO:** (2,2,6,6-Tetramethylpiperidin-1-yl)oxyl

**TFE:** Tetrafluoroethylene

**Tg:** Glass Transition Temperature

**TGA:** Thermogravimetric Analysis

**THF:** Tetrahydrofuran

**T<sub>ODT</sub>:** Order to Disorder Transition Temperature

**TPE:** Thermoplastic Elastomers

**TTS:** Time Temperature Superposition

**RH:** Relative Humidity

**RSC(Z)=S:** Thiocarbonyl compound

**X:** Control agents

**XRR:** X-Ray Reflectivity

**X\*:** Stable free radicals

**Đ:** Polydispersity index (M<sub>w</sub>/M<sub>n</sub>)

**α<sub>i</sub>:** X-ray incident angle

**α<sub>c</sub>:** X-ray critical angle

$\omega$ : Angular Frequency

$\Delta G^C$ : Change in Gibbs energy

$\Delta_{\text{mix}}S$ : Entropy of mixing

$\Delta S^C$ : Combinatorial contribution of the entropy of mixing

$\Phi_A^*$ : Proportion of sites occupied by the solvent

$\Phi_B^*$ : Proportion of sites occupied by the polymer

$W$ : Warburg element

$WSL$ : Weak Segregation Limit

$WU$ : Water uptake capacity

$\chi_{AB}$ : Flory-Huggins Interaction Parameter

$\chi_{ABN}$ : Enthalpic-entropic balance

$|Z|$ : Impedance magnitude





## 1 INTRODUCTION

### 1.1 Motivation

Technological advances in the aerospace industry, biomedicine, and robotics drive the need for innovative, more efficient, and sustainable materials. Therefore, researchers increasingly seek nature-inspired technological solutions, focusing on developing bio-inspired devices [1]. This field aims to imitate biological behaviors regarding appearance, functionality, and operation by developing artificial intelligence, artificial vision, and artificial muscles [2]. Biomimicry provides efficient, simple, low-cost solutions with little environmental impact for developing these devices [3]. Thus, using advanced materials becomes essential since their inherent characteristics make them similar to organic systems, as illustrated in Figure 1 [3].

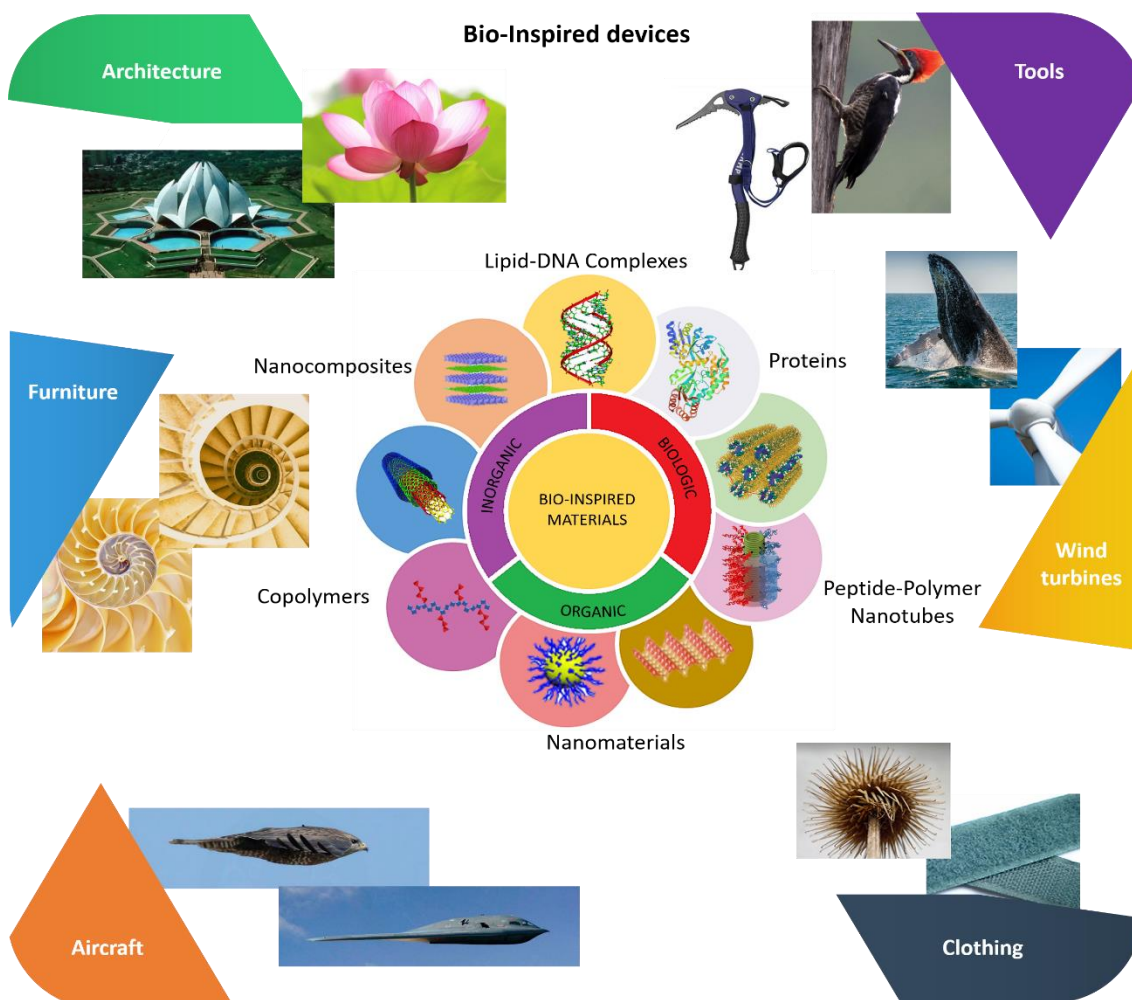


Figure 1: Bio-inspired materials and devices presenting some applications.

An essential class of advanced and bio-inspired materials is represented by electromechanical devices, such as Ionomeric Polymer-Metal Composites (IPMCs), which are devices capable of mimicking biological systems in terms of appearance, functionality, and operation [4]. They are sandwich-type composites formed by an ionic conductive polymeric membrane between metallic electrodes and can bend in response to electrical stimulus and vice-versa [5]. Its main advantages over other types of actuators are low density, miniaturization capability, biocompatibility, and low driven voltage (<5V) [6]. For this reason, they are promising materials for a wide range of technological applications in strategic areas, such as actuators [7, 8], sensors [9–11], artificial muscles [12, 13], robotics [14–16], aerospace industry [17], oil exploration [18], energy harvesting [19], and biomedicine [19, 20], as illustrated in Figure 2.

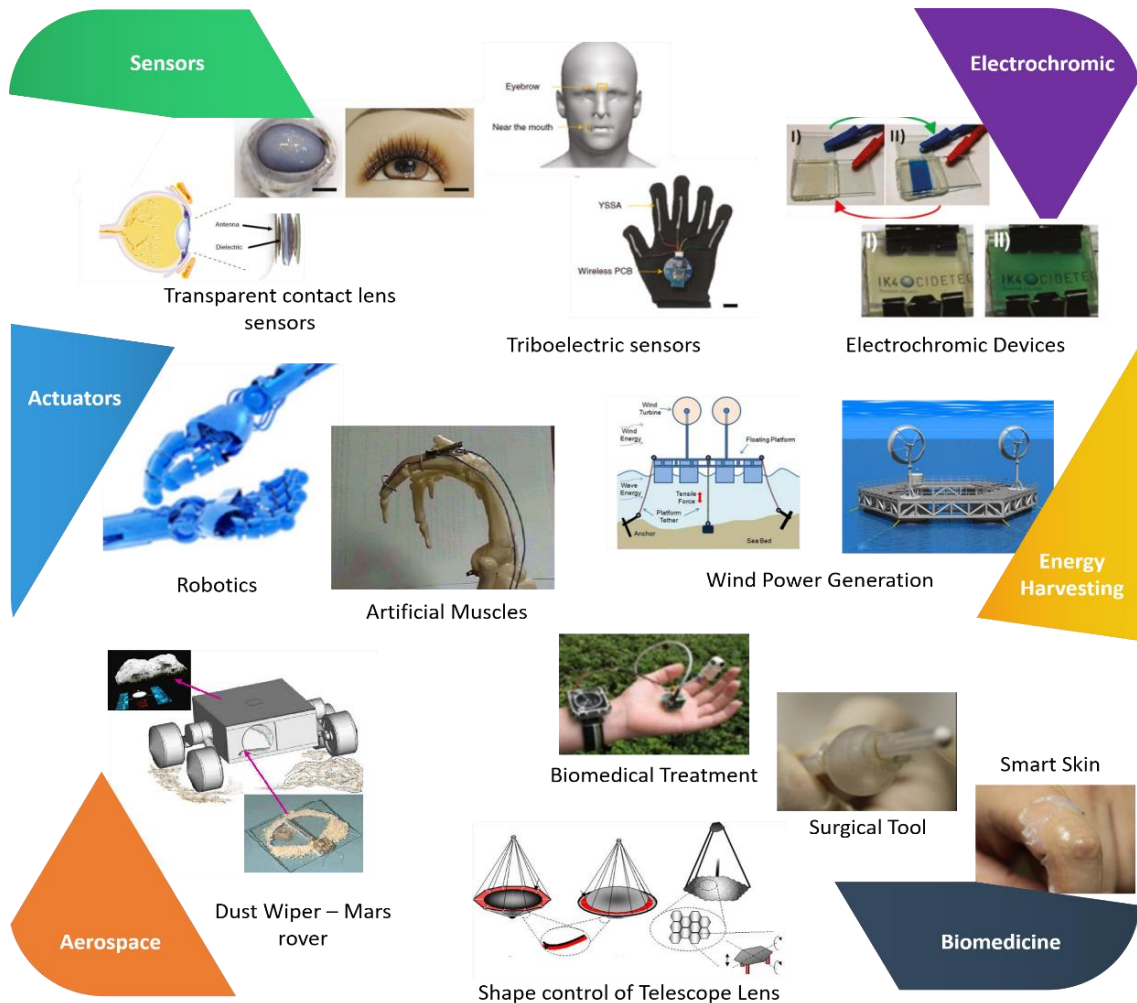


Figure 2: Bio-inspired electromechanical devices applications.

Perfluorinated commercial membranes like Nafion, Flamion, and Aciplex are widespread in the fabrication of IPMC devices due to their high ionic conductivity and excellent chemical, thermal, and structural stability [22], [23]. However, it is worth mentioning that these membranes were initially designed for fuel cell applications, and their properties were subsequently adapted for use in IPMCs [24]. One significant drawback is their random and complex morphology, which undergoes variations based on the membrane's hydration level [25]. Consequently, devices made with these membranes often exhibit non-linearities and time-dependent behaviors. Thus, complex and adaptative models are required to describe ion migration and control IPMCs [26]–[28]. However, there is room for improvement in the design and development of membranes specifically tailored for IPMC devices by focusing on developing membranes with a more stable and controllable morphology [29].

In fact, for practical applications, electromechanical devices must possess i) well-defined morphology, ii) high ionic conductivity, iii) flexibility, iv) mechanical resistance, and v) chemical, thermal, and structural stability [30]. These requirements can be fulfilled by engineering the structure of amphiphilic block copolymers that serve as electroactive membranes in the devices. These copolymers can self-assemble into well-defined morphologies with nanosized domains [31]. Besides, when a rigid, conductive phase is dispersed in a low glass transition temperature ( $T_g$ ) domain, good mechanical properties and elevated ionic conductivity are simultaneously attained [32], [33]. Hence, it is possible to effectively decouple the conductivity from mechanical properties, adjusting the flexibility and Young's modulus of the material by tuning the block's size.

These amphiphilic block copolymers are usually prepared by sulfonating the polystyrene-based block copolymers using sulfonating agents [34]. However, this procedure presents many drawbacks (Figure 3), such as difficulty in controlling degree of sulfonation, formation of undesired by-products, chains scission and sulfoxide crosslink [35], oxidation [36], incomplete sulfonation [37], and extensive post-treatment steps (washing, neutralization, or purification, to remove residual sulfonating agents and by-products), scale-up challenges, and

the disposal of reaction by-products or unreacted sulfonating agents may require careful management to prevent environmental harm [38]. To overcome this, direct polymerization of sulfonated monomers in aqueous media using controlled radical polymerization has been demonstrated [39]. Nevertheless, it is not easy to prepare non-polar/polar block copolymers by this route because of the insolubility of hydrophobic monomers in aqueous media [40][41].

On the other hand, researchers have addressed the synthesis challenge of ionic-neutral block copolymers by strategically introducing protecting groups into the hydrophilic monomer [42]–[44]. This innovative approach entails transforming the hydrophilic units into hydrophobic monomers, thereby expanding the versatility and functionality of the resultant copolymer. Through this method, copolymers could be initially synthesized conventionally in organic solvents using techniques such as nitroxide-mediated polymerization (NMP) [45][46], atom transfer radical polymerization (ATRP) [47][48], and reversible addition–fragmentation chain-transfer (RAFT) polymerization [49][50] followed by a conversion into amphiphiles through chemical or heat treatments at low temperatures.

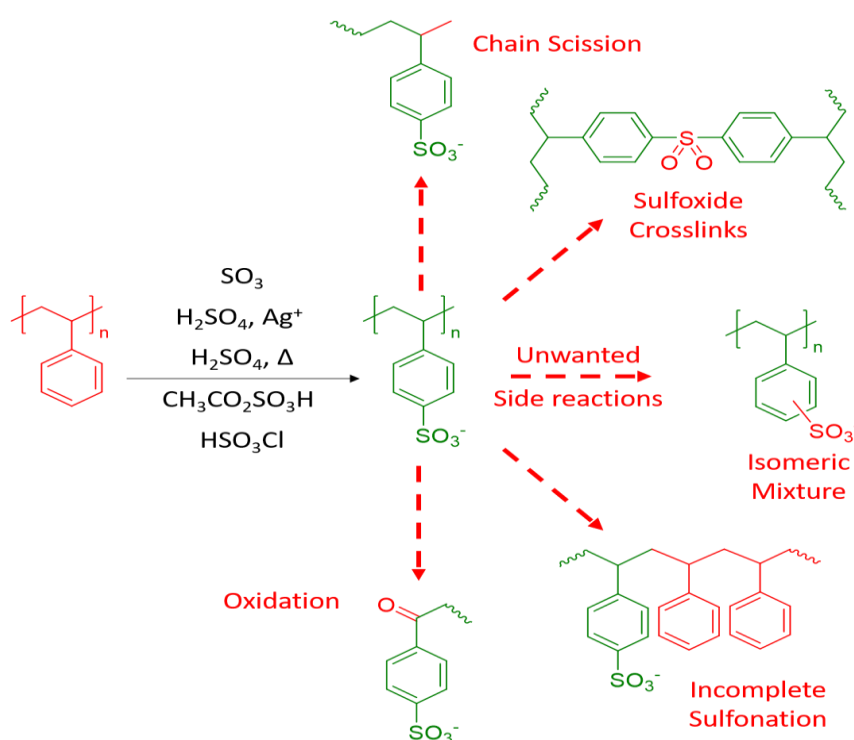


Figure 3: Unwanted products from the sulfonation of polystyrene.

Among these techniques, RAFT stands out as one of the most versatile techniques. It offers unprecedented flexibility as it can be employed in various systems and reaction conditions, enabling the synthesis of polymers and copolymers with well-defined architecture and narrow molar weight distribution [51]–[53]. Therefore, in this work, RAFT polymerization was used to synthesize Poly(butyl methacrylate)-*b*-(poly(neopentyl *p*-styrene sulfonate)-*r*-polystyrene) (PBMA-*b*-(PNeoSS-*r*-PS)) block copolymer with well-defined morphology. Subsequent thermolysis of PNeoSS segments removes the neopentyl group, resulting in a polystyrene sulfonate-*r*-polystyrene (PSS-PS) backbone with the desired ionic conductivity. Finally, this copolymer was used to prepare optimized electromechanical devices, presenting high ionic conductivity, flexibility, and mechanical resistance suitable for sensor application.

## 1.2 Objectives

This project aims to develop an amphiphilic block copolymer specifically synthesized to be applied as a bio-inspired electromechanical device. And as specific objectives:

- i) Synthesize PBMA-*b*-(PNeoSS-*r*-PS) block copolymer with lamellar morphology, varying the molecular weight of the blocks and degree of sulfonation;
- ii) Prepare an amphiphilic block copolymer PBMA-*b*-(PSS-*r*-PS) through deprotection of the sulfonic acid group using thermolysis of the NeoSS segments;
- iii) Prepare an electromechanical device (Ionomeric Polymer-Metal Composite) that presents flexibility, mechanical resistance, and elevated ionic conductivity using the electroless plating process;
- iv) Prepare an electromechanical system capable of characterizing the device at different relative humidity;
- v) Investigate its electromechanical response, correlate it with its morphology, sulfonation degree, and determine the best application (sensor or actuator).

### **1.3 State-of-the-art and unique contributions**

The synthesis of new materials drives technological development, fostering innovation, improving existing technologies, and creating entirely new applications. Continually exploring novel materials plays a pivotal role in addressing societal challenges, advancing scientific knowledge, and shaping the future of technology. In this case, synthesizing a new amphiphilic copolymer is crucial for creating versatile electromechanical devices with tailored properties, making them valuable in a wide range of state-of-the-art technologies, especially in medicine, nanotechnology, and materials science.

Besides, despite extensive research on charged polymers (polyelectrolytes and ionomers), a thorough understanding of these systems is far from complete. The situation of charged neutral block copolymer melts is even worse. Thus, in this project, the morphological investigation and analysis of the copolymer is fundamental to deepening our understanding and unlocking their full potential and applications.

Also described in this thesis is the development of a low-cost system for the control and characterization of electromechanical devices in different relative humidity. Combining electromechanical and electrochemical data, some behaviors could be better understood and related to some characteristics of this device, enabling the identification of the most suitable applications.

## 2 LITERATURE REVIEW

### 2.1 Active polymers

In general, polymers have low density, low cost, malleability, easy processing and fabrication, ability to be molded into complex shapes, and their properties can be adjusted according to demand [54]. Besides these properties, active polymers can respond to external stimuli such as pH, temperature, humidity, and electricity with mechanical deformation, color, and size variation [55]. Such characteristics make active polymers promising in developing technologies and bio-inspired devices with reduced size and weight and more profitable, sustainable, and efficient, as illustrated in Figure 4 [56].

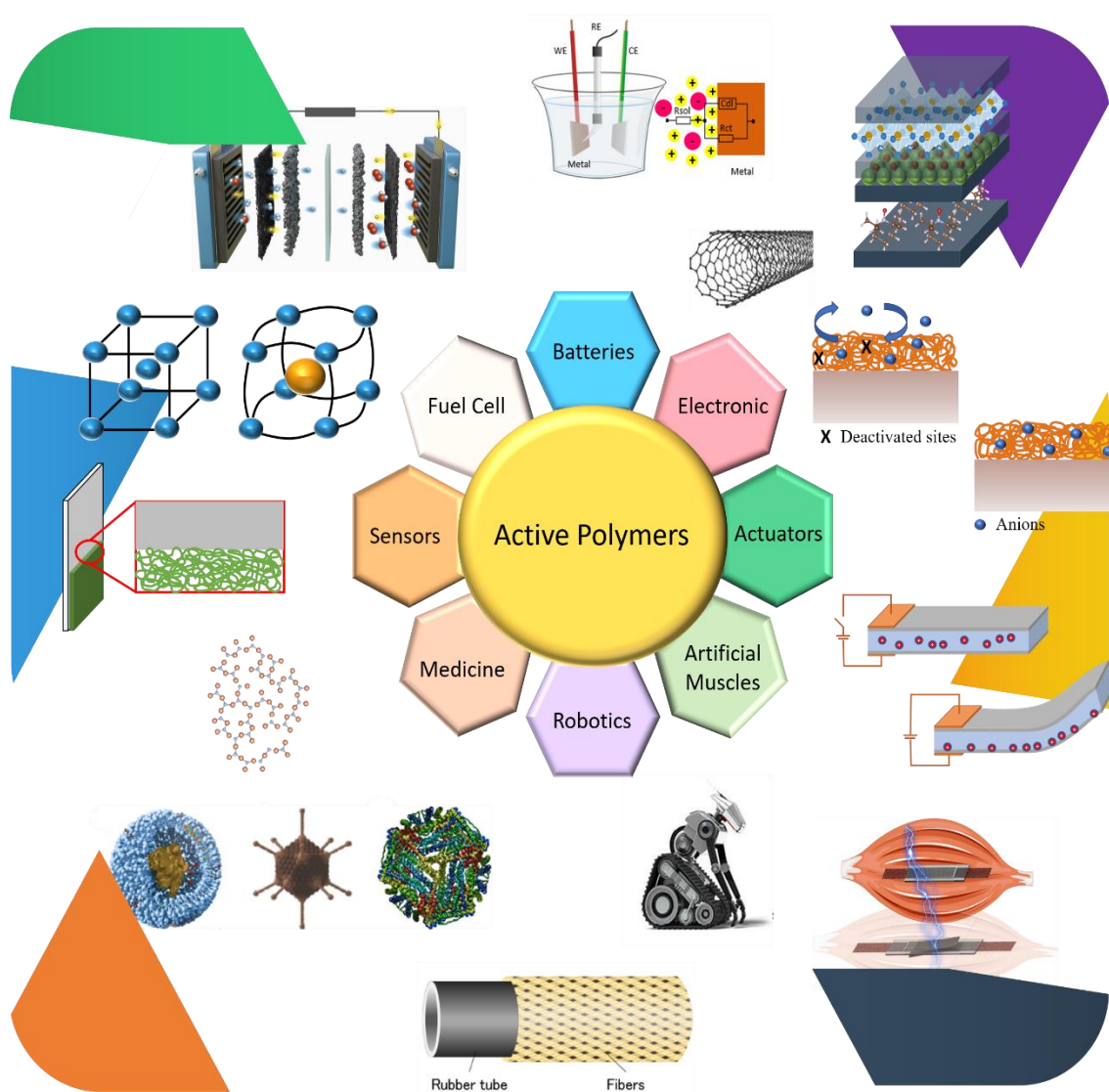


Figure 4: Active polymer applications.



Active polymers capable of responding to electrical stimuli are known as electroactive polymers (EAPs). Figure 5 illustrates the critical milestones in discovering and developing active polymers. The field of EAPs can be traced back to 1880 when Wilhelm Roentgen experimented to investigate the impact of an electric current on the mechanical properties of an elastic band [57]. This work laid the groundwork for the field, as later, in 1899, Sacerdote [58] built upon Roentgen's findings and proposed a theory about the deformation response to an applied electric field. Following this historic milestone, Eguchi discovered the first piezoelectric polymer in 1925. In 1969, Kawai's discovery that polyvinylidene fluoride (PVDF) exhibits a robust piezoelectric effect sparked interest in developing other conductive polymer systems with similar capabilities [59].

After discoveries made by Kawai, Bar-Cohen and his team embarked on research to examine other polymeric systems. These efforts led to the emergence of a series of materials with similar responses [60]. Since the early 1990s, many electroactive polymer actuators have been developed with exceptional deformation capabilities, revolutionizing their potential for high-technology applications. The first commercial device that used an EAP was an artificial muscle developed by Eamex Corporation, Japan, in 2002 [61]. Unlike electroactive ceramics (EAC), EAPs can generate deformations that are two orders of magnitude greater. Additionally, they have advantages over shape memory metal alloys (SMAs) in terms of response speed, low density, and resilience [60]. However, EAPs still face limitations such as low actuation force and reduced displacement amplitude [62].

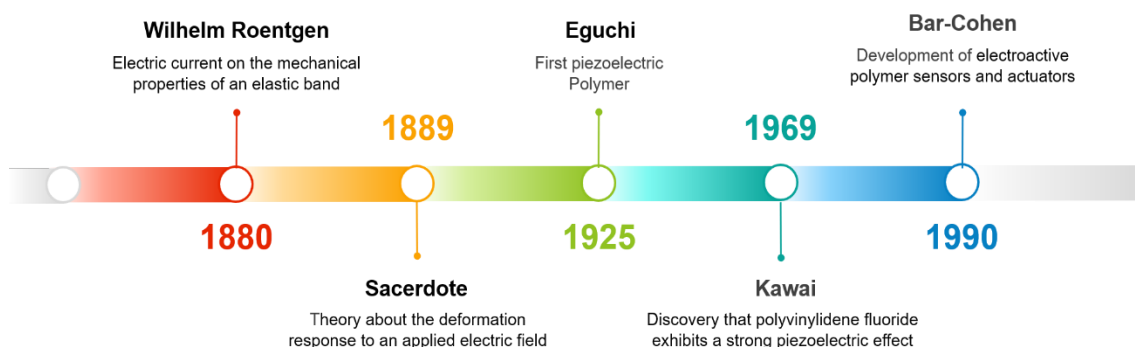


Figure 5: Timeline of active polymers landmarks and development.



Table 1: Classification of Electroactive Polymers.

EAP Type	Actuator Type	Actuation Mechanism	Activation Voltage	Response Time	Example
Electronic	Ferroelectric Polymers	Piezoelectricity	0.1 kV	Fast	Poly(vinylidene fluoride) (PVDF)
	Dielectric Polymers	Electrostatic Field Force	0.4 kV	Fast	Si Elastomer, Polyurethane
Ionic	Conductive Polymer, IPMC	Electromechanical	1.0-5.0 V	Slow	Polypyrrole, Nafion, Flemion
	Ionic Polymer Gels	Ion diffusion via polymer gel	1.0 V	Slow	Polyvinyl Alcohol

These multifunctional devices can be used for actuation, sensing, energy generation, and the development of IPMCs. As presented in Table 1, they can be classified, in terms of their operation mechanism, into two categories [59]: i) electronic EAPs (eEAPs), which are driven by electric fields or coulombic forces, and ii) ionic EAPs (iEAPs), which change shape and size by mobility or diffusion of ions [63]. This ionic motion causes a pressure gradient across the membrane, leading to a spatially nonuniform mass accumulation, which causes the device to bend [59][64]. A schematic representation of the operating mechanism of an eEAP and iEAP is shown in Figure 6.

An iEAP can be activated at 1 to 5 volts, inducing a bending displacement or change in shape. Therefore, versatile devices based on iEAPs could be developed for many technological applications. For example, NASA's Jet Propulsion Laboratory (JPL) designed a wiper for the camera lens of the MUSES-CN rover that used an IPMC [65]. Likewise, European Space Agency (ESA) researchers created a spherical wind-propelled tumbleweed rover to jump over obstacles. The conceptual design selected a Si-based EAP [poly(dimethylsiloxane)] for the artificial muscle that would allow the spherical rover to jump over obstacles [66].

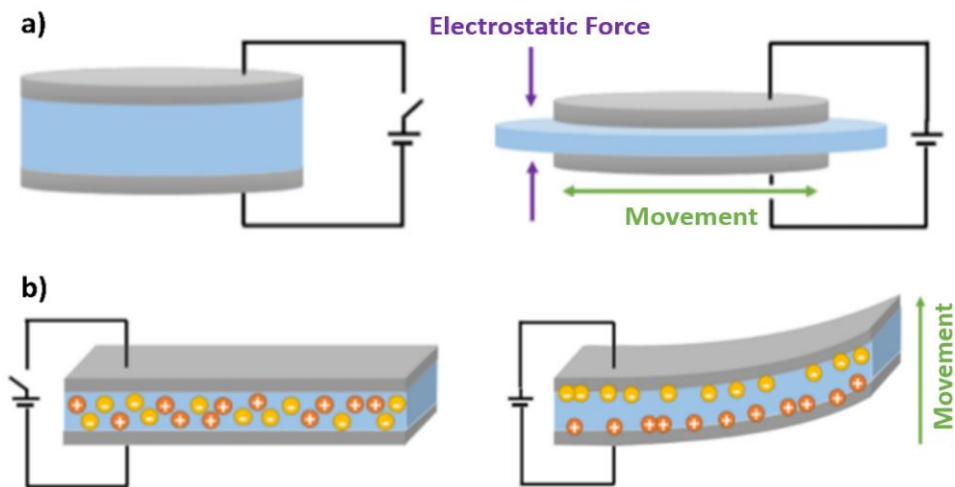


Figure 6: Actuation mechanism of electromechanical devices based on a) electronic and b) ionic electroactive polymers.

Other examples of applications are artificial muscles [67], amperometric sensors of motion [68] and humidity [69], energy harvesting [70], and supercapacitors [71]. Examples of iEAPs include gels [72], conductive polymers [73], carbon nanotubes [74], and IPMCs [75]. Disadvantages include high humidity maintenance requirements, difficulties sustaining constant displacement with direct bias, and relatively slow deformation due to charge and molecule migration in the polymeric phase [76].

## 2.2 Sensors and actuators based on iEAPs

IPMCs (Figure 7a) are the most studied materials for sensors and actuator applications because of their versatility, low weight, and significant deformation capability (>40%) with low activation energy (<5V) [75]. The study with IPMCs began in 1939 by preparing these composites using colloidal platinum precipitation on polymeric substrates [77]. However, the metallic layer experienced delamination, rendering its use impractical. Introducing sputtering deposition techniques opened up new possibilities for developing these composites. However, even with these advancements, the produced samples still exhibited delamination of the metal surface [78].

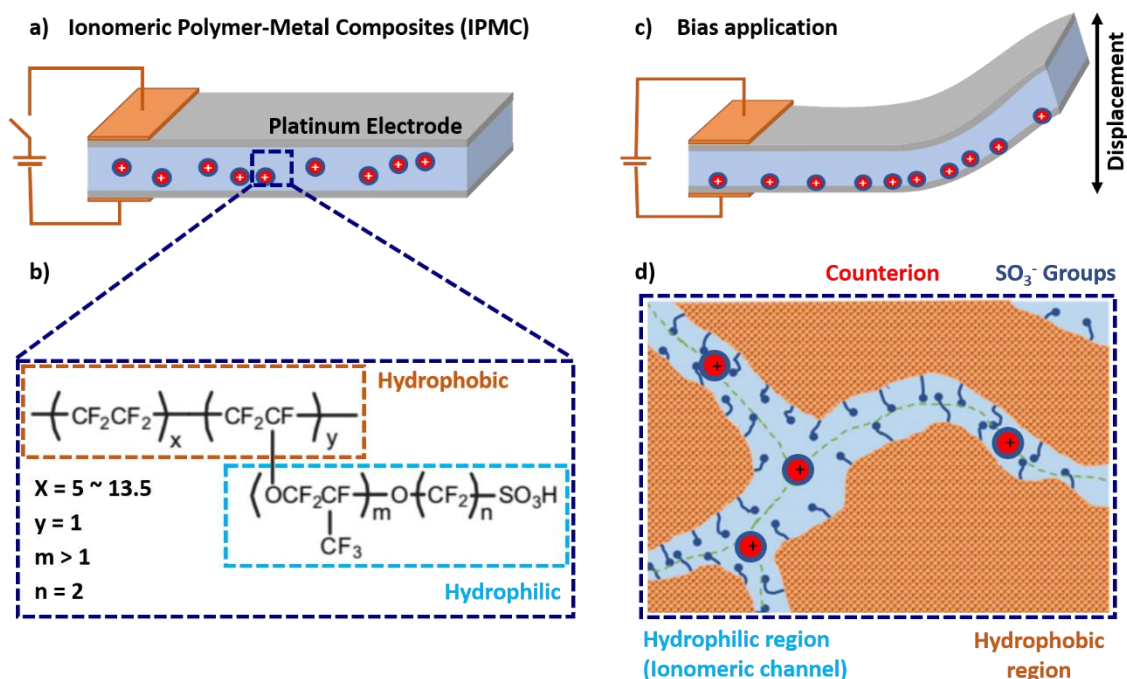


Figure 7: a) IPMC, b) Nafion's chemical structure, c) IPMC bending movement, and d) Nafion's morphology, showing the ionomeric channels (light blue).

It was not until 1960 that researchers at Dow Chemical demonstrated that the permeability characteristic of ionomeric resins could facilitate the selective reduction of metallic salts on the surface of polymeric membranes. This was achieved using chemical reducers like sodium borohydride ( $\text{NaBH}_4$ ) or hydrazine ( $\text{N}_2\text{H}_4$ ) [79]. Subsequently, in the 1980s, several Japanese groups further refined and optimized this method, paving the way for developing more sophisticated and durable composites [77].

The concept of IPMCs as multifunctional smart devices with actuation, energy harvesting, and sensing capabilities was initially introduced by Shahinpoor, Bar-Cohen, and their collaborators in 1997-1998. NASA JPL supported this research. However, the original idea of ionic polymers and gel polymer actuators can be traced back to the early 1990s [6]. In fact, Japanese researchers Adolf et al. [80] and Oguro, Takenaka, and Kawami [81] were granted the first two patents on IPMC in 1993. Subsequently, patents were issued for actuation and sensing applications, leading to numerous developments and research in this field [6].

Nafion<sup>®</sup> is the most used electroactive polymer to prepare IPMCs. This polymer is formed by a backbone similar to poly(tetrafluoroethylene), PTFE, with sulfonated groups grafted laterally to the main chain, as shown in Figure 7b. It is an ionomer, where the counterion can be monovalent or bivalent cations and ionic liquids [82]. Due to chemical incompatibility with the continuous phase (PTFE), the sulfonated groups agglomerate in an inverted micelle structure, in which the ionic part of the polymer remains confined [83]. Mobile counterions guarantee the system's neutrality within these micelles. A sufficient amount of sulfonated groups ensures the coalescence of these micelles in channels that extend three-dimensionally [84], Figure 7d.

The ionomeric phase is highly hydrophilic, absorbing water molecules that become complex with the cation [85]. So, the IPMC device operation mechanism consists of the migration of hydrated ions in response to an electric field generated between the electrodes after applying a bias [86]. This ionic movement causes a pressure gradient, leading to an anisotropic mass accumulation that generates the device's bending, as shown in Figure 7c. This electromechanical response depends on the electrical stimulus intensity [59], counterion type [87], and the membrane's hydration level, which depends on environmental conditions such as humidity and temperature [88].

### **2.3 Nafion morphology**

The perfluorinated ionomers Nafion, Flemion, and Aciplex were developed by DuPont, Asahi Glass Company (AGC), and Asahi Kasei, respectively [82]. They are generated through the copolymerization of a perfluorinated vinyl ether comonomer with tetrafluoroethylene (TFE), resulting in a chemical structure consisting of a PTFE-like main chain with sulfonated groups laterally grafted onto it. Since the introduction of these ionomers, numerous structural models have been proposed for Nafion [89-101] to establish the connection between its distinct properties and morphology. Figure 8 showcases the most important models that have been created.

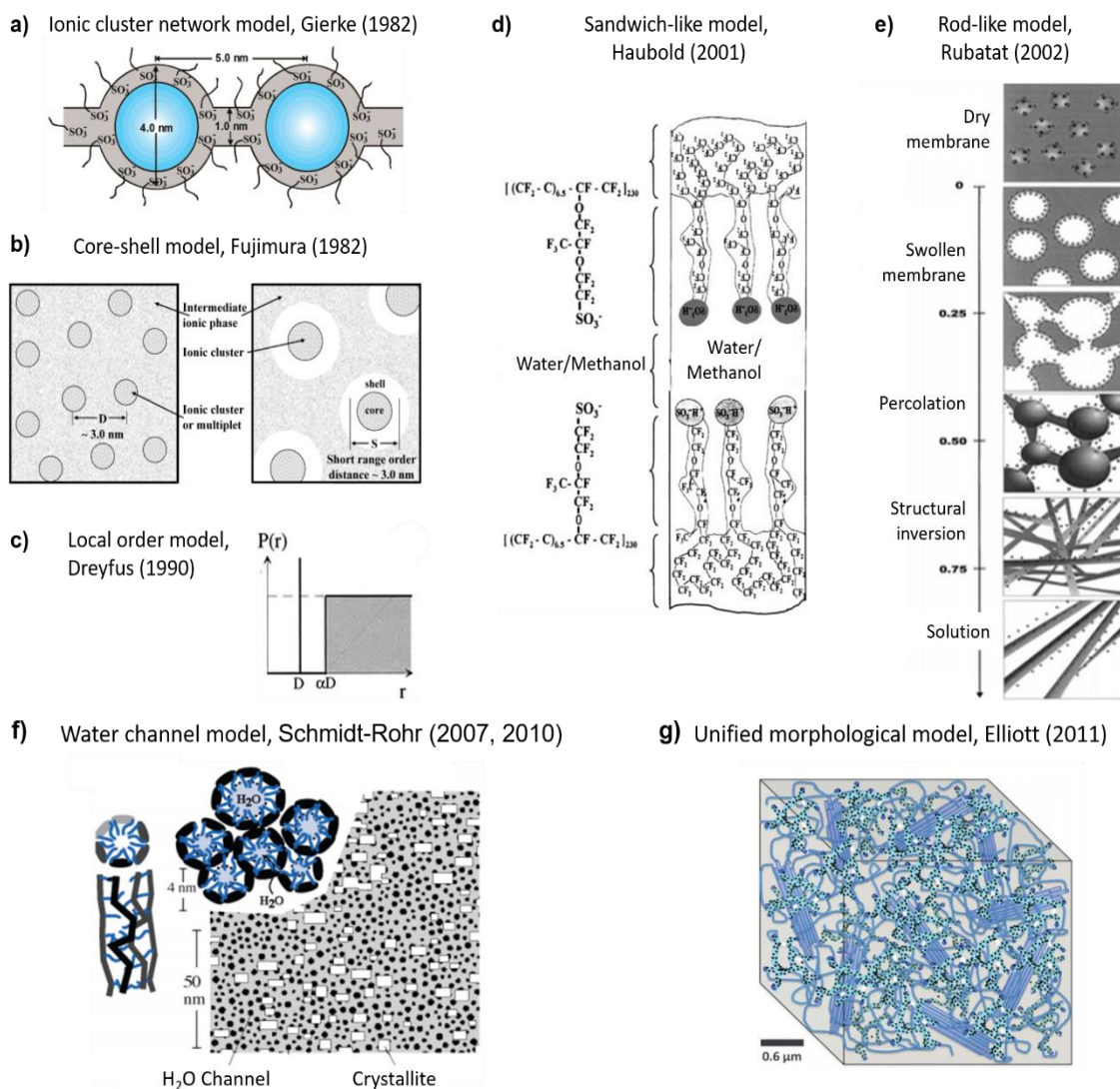


Figure 8: Most important morphological models for ionomers. a) Ionic cluster network, b) core-shell, c) local order, d) sandwich-like, e) rod-like, f) water channel, and g) unified morphological.

The ionic cluster network model developed by Gierke et al. [89]–[91] in the 1980s remains a significant contribution to the morphological studies of polymeric membranes. This model has served as the underlying conceptual framework for understanding the properties of these membranes, including the transport of ions and water as well as ionic permeability. In this model, the clusters (40 Å), with sulfonated ends organized as inverted micelles, are believed to act as ion exchange sites, while the cylindrical pores or channels (10 Å) provide a pathway for ionic transport.

Several other morphological models have been proposed and are also noteworthy. They include the modified core-shell model proposed by Fujimura et al. [92], the local order model proposed by Dreyfus et al. [93], the lamellar model proposed by Litt [94], the sandwich model proposed by Haubold et al. [95], and the rod-like model proposed by Rubatat et al. [96]. These models all share the understanding that ionic groups form clusters within the polymer matrix, creating a network that allows for significant swelling by polar solvents and efficient transport of ions through these nanometer-scale domains. However, they differ significantly regarding these ionic clusters' geometry and spatial distribution.

The study conducted by Elliott et al. [97] made significant progress in interpreting SAXS data using the maximum entropy method. This method demonstrated a consistent morphological pattern, which reconciled these materials' microscopic and macroscopic swelling behavior. The results showed that as water absorption increased, there was a corresponding increase in the average separation between clusters and a decrease in the number of clusters. This finding concluded that the most probable scattering model for Nafion is one of an ion cluster morphology with a hierarchical scale of structures.

These discoveries led Gebel [98] to propose a conceptual explanation for this polymeric membrane's swelling and dissolution behavior. In this qualitative model, the membrane under investigation, which has a higher concentration of sulfonated groups than a commercial membrane, is assumed to be dry and contain isolated spherical ionic clusters. Upon exposure to water, these clusters swell and eventually percolate, resulting in an inversion of the structural arrangement (forming inverted micelles). This process continues until the membrane completely dissolves in the solution, forming rod-shaped structures that separate to produce a colloidal dispersion of isolated rods.

In two subsequent papers, Schmidt-Rohr and Chen [99], [100] introduced a novel method for calculating the SAXS curve by numerically transforming a given scattering density distribution through Fourier transformation. Their model proposes the existence of long, parallel hydrophilic channels filled with water that form cylindrical inverted micelles (ionomeric channels) in Nafion,

particularly in its 20% hydrated form. This model can accurately reproduce all the SAXS characteristics observed in Nafion, providing a detailed explanation for the material's exceptional transport properties.

In 2011, Elliot et al. [101] introduced a groundbreaking model incorporating structural information on SAXS patterns. This model employed a maximum entropy approach with mesoscale morphology simulations using Dissipative Particle Dynamics (DPD). The DPD parameters were derived from atomistic calculations and the Density Functional Theory (DFT). The integration of these two methods revealed that the nanoscale ionic clustering in Nafion is closely associated with the larger-scale organization of the  $\text{CF}_2$  main chain, although it exists in a spatially distinct manner.

Although many different structural models have been proposed for Nafion and are similar to explain the effect of membrane morphology on its properties, such as the water absorption capacity and ion transport, the exceptionally high degree of disorder in these materials makes it difficult to deduce their morphology and, consequently, explain precisely its properties. Moreover, when Nafion is used to prepare IPMCs, the interactions between chemical, electrical, and mechanical phenomena result in nonlinear mechanical responses and time-varying behaviors [102]. For this reason, modeling, describing, and controlling Nafion-based IPMC actuators has been challenging.

Therefore, substituting perfluorinated ionic polymers with non-perfluorinated ionic copolymers with a well-defined morphology is highly desirable [72]. In this regard, block copolymers containing both rigid charged and flexible neutral blocks have garnered significant attention [103]. This is because block copolymers can spontaneously organize into precise structures, allowing for the independent control of mechanical properties and conductivity. As a result, it becomes possible to fine-tune both the mechanical and ionic conductivity characteristics [32][33]. Additionally, it has been shown that charged-neutral block copolymers exhibit the potential for achieving higher proton conductivity when compared to ionomers such as Nafion, Aciplex, and Flamion [29][104], as well as random ionic copolymers [105].

## 2.4 Block Copolymers (BCPs)

Block copolymers (BCPs) are a highly adaptable type of polymers that consist of distinct monomeric units arranged strategically in discrete blocks along the chain [106]. The study of BCPs is currently a significant focus in macromolecular chemistry, physics, and materials science, as researchers aim to enhance synthetic methods, molecular architectures, properties, and applications [107]. The unique attribute of copolymers is their ability to exhibit a wide range of molecular architectures, including linear [108], blocks [109], branched (graft and star) [110], and even cyclic structures [111]. This versatility provides various compositions and structures, allowing many applications across different industries.

In fact, since the advent of living anionic polymerization demonstrated by Michael Szwarc in 1956 [112][113] and the discovery of reversible-deactivation radical polymerizations (RDRP) in the 1990s [114], extensive research on BCPs has revolutionized industrial production. These polymerization reactions present a rapid initiation rate and negligible chain termination speed compared to propagation [115]. This allows for precise control over chain growth, resulting in a narrow molar mass distribution and copolymers with well-ordered structures [116], allowing the application of these materials in different sectors, such as food packaging [117], drug delivery [118], biomedical [109], membranes [119], electromechanical devices [103], biosensors [120], biodegradable materials [121], among others [122][123] (Figure 9).

This versatility is particularly intriguing for applications that require a well-defined morphology and a combination of antagonistic properties, such as flexibility and mechanical resistance, as seen in electromechanical devices. For instance, thermoplastic elastomers (TPEs) are a typical class of BCPs and consist of a rigid domain (A) dispersed within a matrix of soft species (B) with a low glass transition temperature ( $T_g$ ) [124]. Typically, the rigid domain is composed of polystyrene and its derivatives, while the matrix comprises rubbery domains such as dienes, (meth)acrylates, ethylene oxide, and so on [125]. Despite being immiscible and undergoing microphase separation, these phases maintain their individual properties even when mixed [126][127].



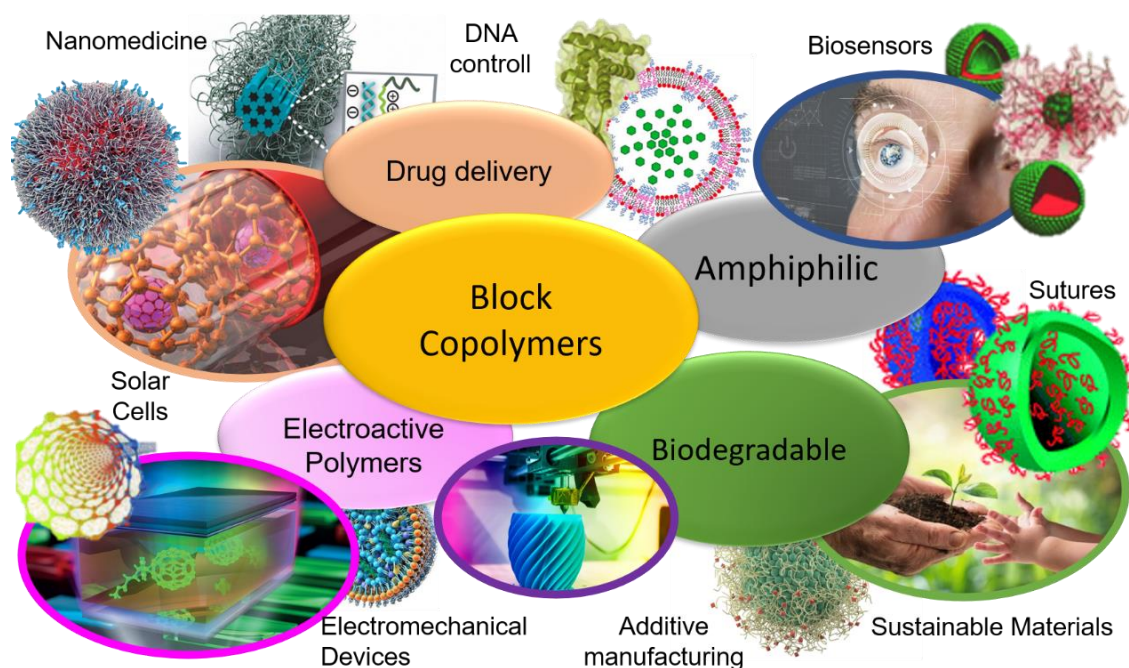


Figure 9: Block copolymer applications, including drug delivery, sutures, biosensors, solar cells, electromechanical devices, and sustainable materials.

Therefore, the development of optimized electromechanical devices requires the synthesis of amphiphilic block copolymers composed of a rigid conductive phase and flexible domain. These materials can possess several advantageous characteristics, including i) Well-defined morphology, allowing for precise control over their properties and functionality; ii) high ionic conductivity, enabling efficient ion transport ensuring superior performance; iii) flexibility, allowing mechanical deformations without compromising their functionality; iv) mechanical resistance, ensuring the longevity and durability; v) chemical, thermal, and structural stability, making the device highly reliable for a wide range of applications. By harnessing these crucial features, the synthesis of amphiphilic block copolymers plays a vital role in advancing the performance and functionality of electromechanical devices.

#### 2.4.1 Block copolymers synthesis

The groundbreaking discovery of synthesizing block copolymers was initially demonstrated by Szwarc et al. in 1956 [128]. This pioneering work shed light on the potential of organometallic initiators in inducing anionic

polymerization mechanisms. In particular, researchers uncovered an electron transfer process that enabled these complexes to initiate the polymerization of conjugated monomers. Scientists achieved precise stoichiometric control over this homogeneous anionic polymerization by meticulously controlling reaction conditions and eliminating factors such as oxygen, water, and impurities. Moreover, this study revealed the absence of termination reactions for the first time, thereby coining the term "living" anionic polymerization (LAP).

In their experiments, a sodium-naphthalene complex with a vibrant green color was utilized to initiate the polymerization reaction of styrene monomers. The transformation of the reaction medium from green to red occurred instantaneously, indicating the successful occurrence of polymerization. This color change is attributed to the specific color of the anionic end of polystyrene ( $\text{PS}^-$ ). The sustained presence of the red color for several days corroborated that the reaction was irreversible. Notably, when additional amounts of styrene and solvent were introduced in stoichiometric proportions, the viscosity of the solution increased. In other words, the addition of excess styrene prompted polymerization to restart until all the reactants were consumed, resulting in an enlargement of the polymer chains [129].

Through this experiment, Szwarc and his colleagues made significant observations that have significantly advanced our understanding of polymerization: i) the initiation reaction occurs rapidly, as evidenced by the instant color change in the reaction; ii) the absence of termination processes such as combination or disproportionation allows the polymer chains to continue growing as long as there are monomers available, enabling the synthesis of polymers with high molar mass; iii) the molar mass distribution of the polymers is narrow because all chains grow at the same average propagation speed; iv) the reaction allows for the preparation of block copolymers and the formation of polymers with functionalized chain ends, including hydroxide,  $-\text{NH}_2$ ,  $\text{COCH}_3$ ,  $-\text{OH}$ ,  $-\text{COOH}$ ,  $-\text{SH}$ ,  $-\text{CHO}$ , and epoxides. These findings have paved the way for numerous well-controlled polymerizations of cyclic and vinyl polymers, which hold significant commercial value [130].

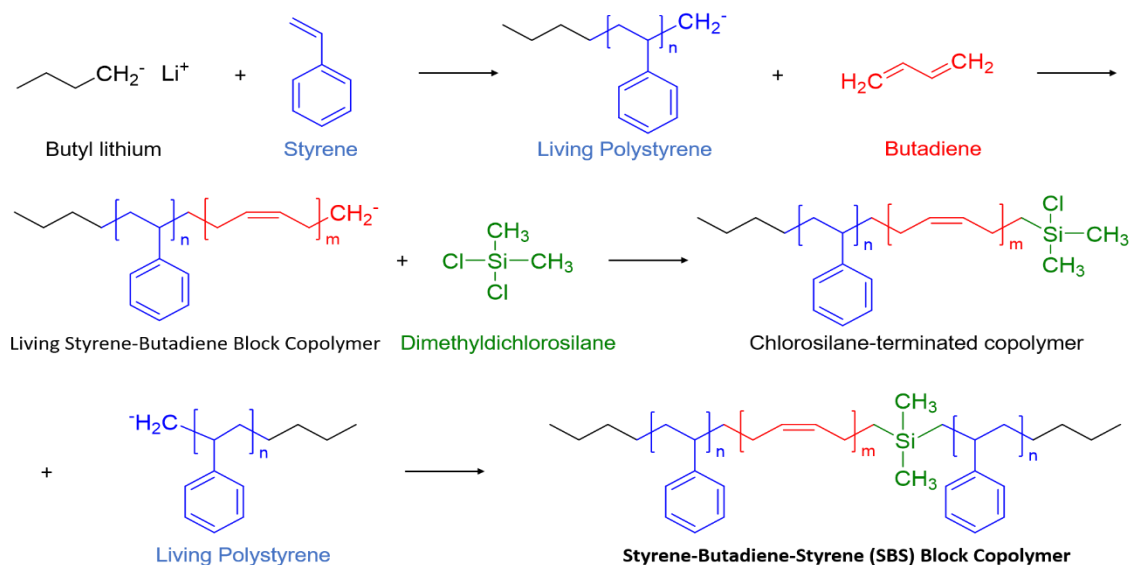


Figure 10: Commercial synthesis of styrene-butadiene-styrene (SBS) block copolymers by living anionic polymerization.

Commercially, LAP enables the production of block copolymers with well-defined structures and narrow molecular weight distributions [111][126]. The process involves three stages: initiation, propagation, and termination. Figure 10 presents the commercial synthesis of an ABA triblock copolymer. The polymerization process starts with butyl lithium ( $\text{C}_4\text{H}_9\text{Li}$ ) catalysts, which generate nucleophilic carbon anions. Subsequently, the addition of monomer A promotes the propagation of the reaction, leading to an increase in the molar mass of the polymer over time. Further incorporation of monomer B allows for the growth of a distinct block within the copolymer.

However, adding more monomer A does not form a true triblock copolymer since monomer A's reactivity is generally higher than monomer B's. In light of this necessity, adding dimethyldichlorosilane ( $\text{C}_2\text{H}_6\text{Cl}_2\text{Si}$ ) to the reaction mixture is crucial. This compound facilitates the formation of a chlorosilane-terminated copolymer, which then reacts with the live monomer A, like how  $\text{C}_2\text{H}_6\text{Cl}_2\text{Si}$  reacts with the A-B copolymer. The result is the creation of an ABA triblock copolymer, which exemplifies the synthesis of the styrene-butadiene-b-styrene (SBS) copolymer.

Despite several advantages, living anionic polymerization is only compatible with a limited range of monomers. It is highly sensitive to chemical

components, impurities, and changes in reaction conditions, necessitating specific polymerization conditions such as high vacuum and high reaction temperatures. Furthermore, it exhibits sensitivity to acidic or protic monomers [131][132]. Consequently, by employing conventional monomers, researchers have been exploring alternatives to this polymerization method to obtain polymers with complex architectures, lower costs, and amphiphilic characteristics. As a result, living/controlled free radical polymerization (CLRP) [133] or, as recommended by IUPAC [134], reversible deactivation radical polymerization (RDRP) has been developed.

#### **2.4.2 Reversible deactivation radical polymerization (RDRP)**

Reversible deactivation radical polymerization (RDRP) is an innovative approach that combines the advantages of both radical and ionic polymerization techniques to synthesize polymers with well-defined architectures under conventional reaction conditions [135]. Unlike conventional radical polymerization, RDRP reactions involve free radicals and exhibit characteristics of living polymerization, where termination and other secondary reactions that lead to the termination of propagating species are minimized [133].

This unique feature allows for high control over the polymerization process, which is difficult to achieve in traditional radical polymerization methods [136]. Conventional free radical polymerization (RP) follows a chain mechanism, which involves four types of reactions with free radicals [137]: (i) initiation, where radicals are generated from non-radical species, (ii) propagation, where radicals add to substituted alkenes, (iii) atom transfer and atom abstraction reactions (chain transfer and termination by disproportionation), and (iv) radical–radical recombination reactions (termination by combination).

This polymerization process forms very short-lived intermediates (propagating species), lasting only a few seconds, resulting in polymers with a degree of polymerization (DP) ranging from  $10^3$  to  $10^4$  and broad molecular weight distribution (usually,  $\bar{D} > 1.5$ ) [138], as presented in Figure 11a.

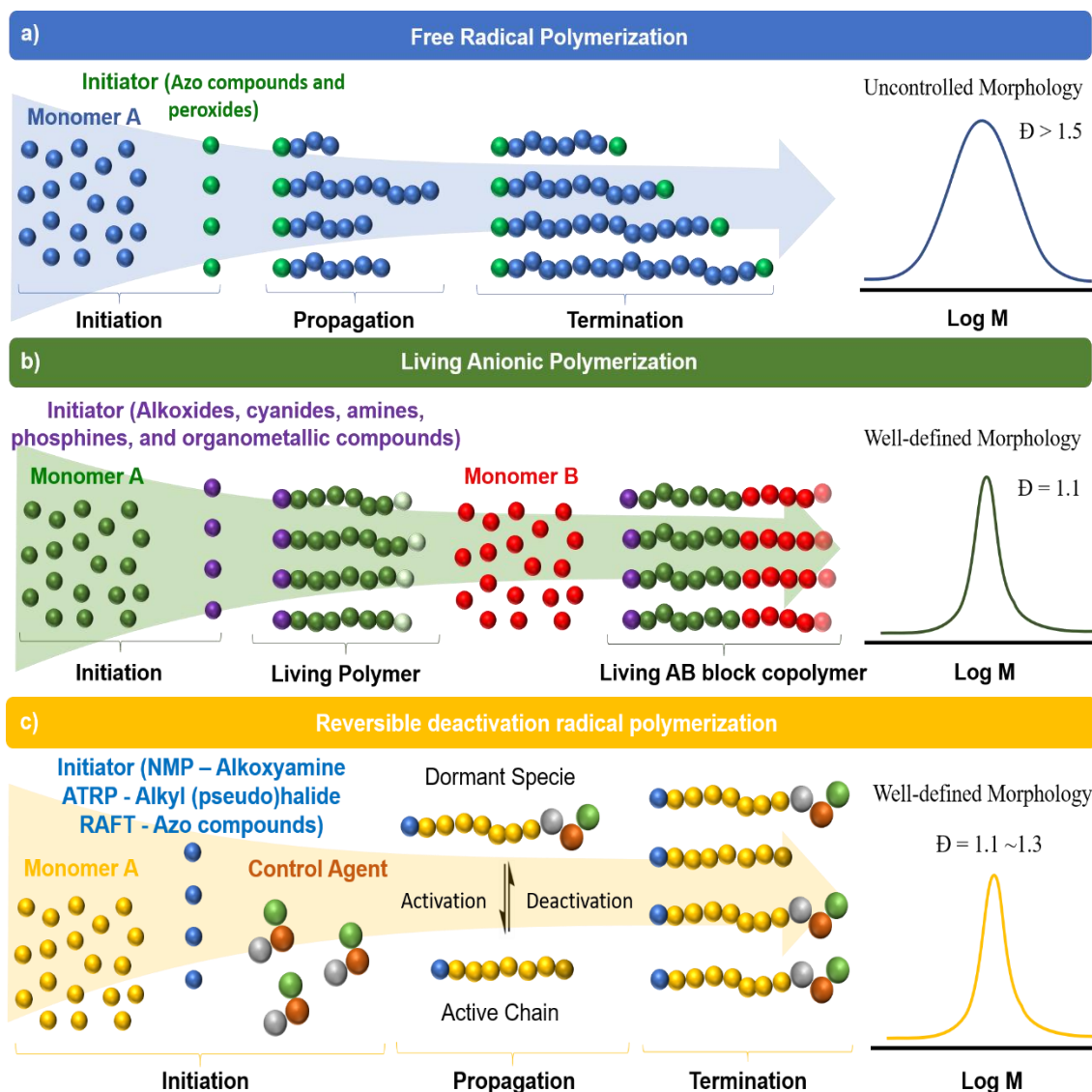


Figure 11: Simplified schematic representation of radical polymerization, living anionic polymerization, and reversible deactivation radical polymerization.

Indeed, the recombination and/or disproportionation of radicals occurs at a rate approaching the diffusion-controlled limit  $k_t = 10^8 \text{ (mol s)}^{-1}$ , which is much higher than the propagation rate,  $k_p = 10^3 \text{ (mol s)}^{-1}$  [139]. Therefore, a radical can survive only some seconds or fractions of a second before encountering another radical species. Furthermore, the initiation step is typically incomplete due to the slow decomposition of radical initiators ( $k_d = 10^{-5} \text{ s}^{-1}$ ). These kinetic factors produce polymers with undefined molar mass, broad molar mass distribution, and uncontrolled structures [140].

On the other hand, while the growing end-groups in RP are electrically neutral, they become charged in ionic polymerizations, with cationic polymerization having a positive charge and anionic polymerization bearing a negative charge [141]. In an ideal living polymerization (Figure 11b), all chains are initiated simultaneously, grow uniformly, and do not undergo irreversible termination due to electrostatic repulsion [139]. However, this type of polymerization is more complex, highly sensitive to impurities, and limited to specific monomers. Therefore, achieving such living characteristics in RP, which prevent irreversible chain termination, is particularly interesting. This can only be feasible when introducing specific reagents that either reversibly deactivate the propagating radicals or enable reversible chain transfer [140].

By employing these reagents, the polymer chains remain in a "dormant form" for most of the polymerization process, thereby avoiding premature recombination and disproportionation (Figure 11c). Consequently, researchers have focused on discovering and understanding these new mechanisms to improve control over these polymerizations, ultimately developing reversible deactivation reactions [142]. Otsu and Yoshida first introduced the concept of reversible deactivation in 1982 [143]. They discovered that a new reaction, called reversible chain-end deactivation, could be incorporated into conventional RP. A chemical compound known as initiator-transfer agent-terminator (INIFERTER) was used to do so. For RDRP to be successful, this reaction must occur frequently and within the propagation time scale, typically between 0.1 and 10 ms [138].

This discovery led to an explosion of interest in developing effective strategies to impart living characteristics to RP. The 1990s witnessed the emergence of several highly efficient techniques and strategies for RDRP, distinguished by their unique reaction mechanisms, reagents, and conditions. These systems can be broadly categorized into three distinct chemical mechanisms, as illustrated in Figure 12: stable radical-mediated polymerization [144], atom transfer radical polymerization [145], and degenerative-transfer radical polymerization [146].

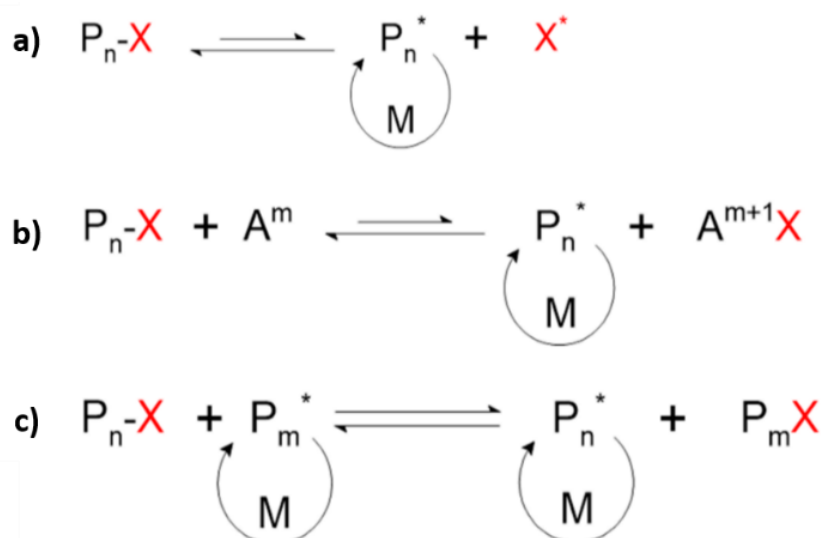


Figure 12: Simplified radical polymerization mechanisms by reversible deactivation. a) stable radical-mediated polymerization, b) atom transfer radical polymerization, and c) degenerative-transfer radical polymerization.

In these systems, the dormant-active balance is fast with respect to chain growth and is achieved with the aid of control agents (X). In the stable radical-mediated polymerization mechanism (Figure 12a), dormant polymer chains ( $P_n-X$ ) undergo thermal or photochemical dissociation to yield propagating radical species ( $P_n^*$ ) and stable free radicals ( $X^*$ ). These  $X^*$  remain inert and do not undergo any reactions apart from combining with  $P_n^*$ . Therefore, these radicals do not react with each other, do not initiate polymerization, and do not undergo disproportionation with  $P_n^*$  [147]. One of the most well-known examples of stable free radicals is nitroxides, including 2,2,6,6-tetramethylpiperidiny-1-oxyl (TEMPO) [148]. The combination rate constants ( $k_c$ ) and dissociation rate constant ( $k_d$ ) are related to the activation rates ( $k_{act}$ ) and deactivation rates ( $k_{deact}$ ) as follows:  $k_{act} = k_d$  and  $k_{deact} = k_c [X^*]$  [147], [148].

In the atom transfer radical polymerization mechanism (Figure 12b),  $P_n-X$  is activated through the catalysis of an activator ( $A^m$ ), which results in the formation of a stable species ( $A^{m+1}X$ ) [147]. Reversible deactivation radical polymerizations in this category commonly use halogens like chlorine (Cl) and bromine (Br) as the controlling agent, along with transition metal halide complexes such as copper (Cu) and ruthenium (Ru) as activators [118]. The activation rate constants and deactivation rate constants can be expressed in

terms of  $k_{\text{act}}$  and  $k_{\text{deact}}$  as follows:  $k_{\text{act}} = k_a [A^m]$  and  $k_{\text{deact}} = k_{da} [A^{m+1}X]$  [106], [111].

In degenerative-transfer radical polymerization (Figure 12c), the propagating radical ( $P_m^*$ ) attacks  $P_n-X$ , resulting in the formation of the active species  $P_n^*$  and a dormant species ( $P_m-X$ ). This process is considered an exchange reaction. The radicals  $P_n^*$  and  $P_m^*$  typically exhibit comparable kinetic properties, leading to equal degenerative chain transfer rate constants ( $k_{\text{ex}}^n = k_{\text{ex}}^m$ ). Therefore, we can express the activation rate constant as  $k_{\text{act}} = k_{\text{ex}} [P_n^*]$  and the deactivation rate constant as  $k_{\text{deact}} = k_{\text{ex}} [P_n-X]$  [147].

This mechanism is found in two types of polymerization: i) When X represents an atom or a simple group, such as iodine (I) [150]. In such cases, X is transferred directly from one radical to another without forming any kinetically significant intermediate; ii) When X is a group with a double bond accessible to adding  $P^*$  [53]. Under these circumstances, the exchange reaction proceeds by adding  $P_m^*$  to  $P_n-X$ , forming an intermediate radical  $P_n-(X^*)-P_m$ . This intermediate subsequently fragments into  $P_n^*$  and  $P_m-X$ , completing the exchange reaction [147].

In general, these mechanisms involve the ability to facilitate the simultaneous growth of all polymer chains. Also, by carefully selecting polymerization conditions, the concentration of dormant polymer chains significantly surpasses that of actively propagating species during polymerization. Typically, the ratio of dormant polymer chains to active ones ( $[P_n-X]/[P_n^*]$ ) exceeds  $10^5$  [147]. This means that a large portion of the polymerization time is spent in the dormant state, with numerous activation-deactivation cycles taking place (each lasting between 0.1 to 10 ms). Consequently, by the end of the reaction, all chains have nearly identical sizes, resulting in a polymer with a polydispersity close to 1.0.

Although numerous techniques have been developed, three of the most significant ones are Nitroxide-Mediated Polymerization (NMP), Atom Transfer Radical Polymerization (ATRP) [151], and Reversible Addition-Fragmentation Chain Transfer (RAFT) [142]. Table 2 summarizes the characteristics and challenges for each polymerization type.



Table 2: Benefits and limitations of NMP, ATRP, and RAFT.

Features	NMP	ATRP	RAFT
<b>Monomers</b>	Styrene, acrylates and acrylamides No methacrylates	All monomers, except acrylic acid and vinyl acetate	Nearly all monomers
<b>Conditions</b>	Sensitive to O <sub>2</sub> Generally elevated Temp (>120 °C)	Some tolerance to O <sub>2</sub> and Inhibitors Temp. (-30 to 150 °C)	Some tolerance to O <sub>2</sub>
<b>End groups</b>	Alkoxyamines	Alkyl halides	Thiocarbonyl thio compounds
<b>Benefits</b>	Absence of any metal Low potential for smell and staining	Versatile Capacity to tailor catalyst	Versatile Absence of any metal
<b>Limitations</b>	Least Versatile	Use of transition metals	High probability of smell and staining
<b>Mechanistic pathway</b>	Low concentration of radicals	Dormant species with a radically transferable atom	The majority of chains are dormant species
<b>Applications</b>	Pigment dispersions Memory devices	Surface modifications Nanoparticle functionalization	Block copolymers for bio-applications

As observed, RAFT stands out as one of the most versatile techniques among these techniques [152]. It offers unprecedented flexibility as it can be employed in various systems and reaction conditions, enabling the synthesis of polymers and copolymers with well-defined architecture and narrow molar weight distribution. Hence, RAFT demonstrates immense potential for advancing polymerization methods and synthesis of well-defined amphiphilic block copolymers for bio-applications, such as electromechanical devices [131].

### 2.4.3 Reversible Addition-Fragmentation Chain Transfer (RAFT)

RAFT-type polymerization is a modified version of radical polymerization that involves using a chain transfer agent (CTA), also known as a RAFT agent.

This method was first reported by the Commonwealth Scientific and Industrial Research Organization (CSIRO) [153], [154], in which methacrylates were used to create block copolymers. Initially, the technique had limited applications. However, in 1998 [131], Dr. Ezio Rizzardo demonstrated the optimization of RAFT polymerization by introducing thiocarbonyl compounds, which regulated the degenerative exchange of propagating radical species generated by conventional initiators [155].

Afterward, a breakthrough occurred in the field of polymerization with the disclosure of RAFT polymerization in a CSIRO/DuPont patent, which was published in January 1998 [156]. This landmark invention was swiftly followed by another patent, issued in December 1998, detailing the parallel development of Macromolecule Design by Xanthate Exchange (MADIX) at Rhodia [157]. The successive advancements of the RAFT technique were comprehensively elucidated in a series of reviews that graced the Australian Journal of Chemistry pages. This elucidation commenced in 2005 [140], followed by subsequent updates in 2006 [158], 2009 [159], and 2012 [160]. The intellectual pioneers behind this ground-breaking technique cemented their mastery of the subject by publishing a handbook on RAFT polymerization in 2008 [161].

Over the years, significant advancements have been made in the field, leading to the development of copolymers with various compositions, architecture, and morphologies (including block [162], star [163], branched, hyper-branched, network [164], and many others), topologies, molecular composites, and functionalities using the RAFT technique [165], as illustrated in Figure 13.

These advancements have paved the way for strategic applications, such as stimuli-responsive materials [52], surface-functionalized copolymers [166], nanoparticles and nanocomposites [167], sustainable materials [168], electromechanical devices [169], and bioapplications [135]. It is worth noting that the topic has garnered immense attention, with over 10500 publications discussing it. Notably, the article published by the CSIRO group [131] currently holds the record as the most cited article in the journal *Macromolecules*, with more than 4500 citations.

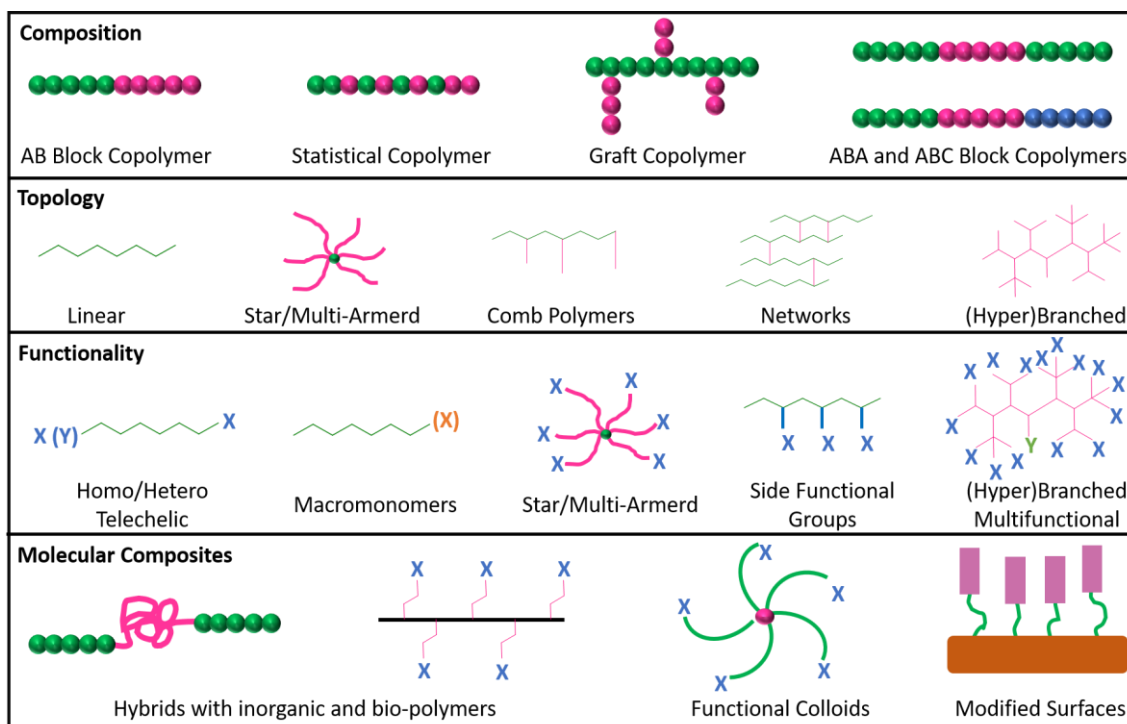


Figure 13: Schematic representation of controlled topologies, compositions, and functionalities of polymers and copolymers prepared by RAFT.

Many conventional radical polymerizations, especially solvent-based ones, have the potential to be improved by utilizing the RAFT polymerization technique. The same solvents, initiators, and reaction temperatures can be employed, and the RAFT mechanism offers a more intricate reaction pathway. Illustrated in Figure 14, the RAFT mechanism can be described in five sequential steps, namely i) initiation, ii) pre-equilibrium, iii) reinitiation, iv) main equilibrium, and v) termination. To ensure optimal control of the RAFT process, careful management of initiator concentration and the selection of the CTA are crucial. A recommended ratio for reagent quantities is as follows:  $[I]:[CTA]:[M] = [1]:[4-10]:[2000-5000]$  [51].

The reinitiation step plays a crucial role in the process, as it involves the reaction of the radical ( $R^*$ ) with another monomer, forming a new propagating radical ( $P_n^*$ ). This step marks the beginning of the main equilibrium stage, which is of utmost importance throughout the entire process [170]. During this stage, there is a rapid equilibrium between the active propagating radicals ( $P_n^*$  and  $P_m^*$ ) and the dormant polymeric thiocarbonyl compounds (3) via an intermediate component (4).

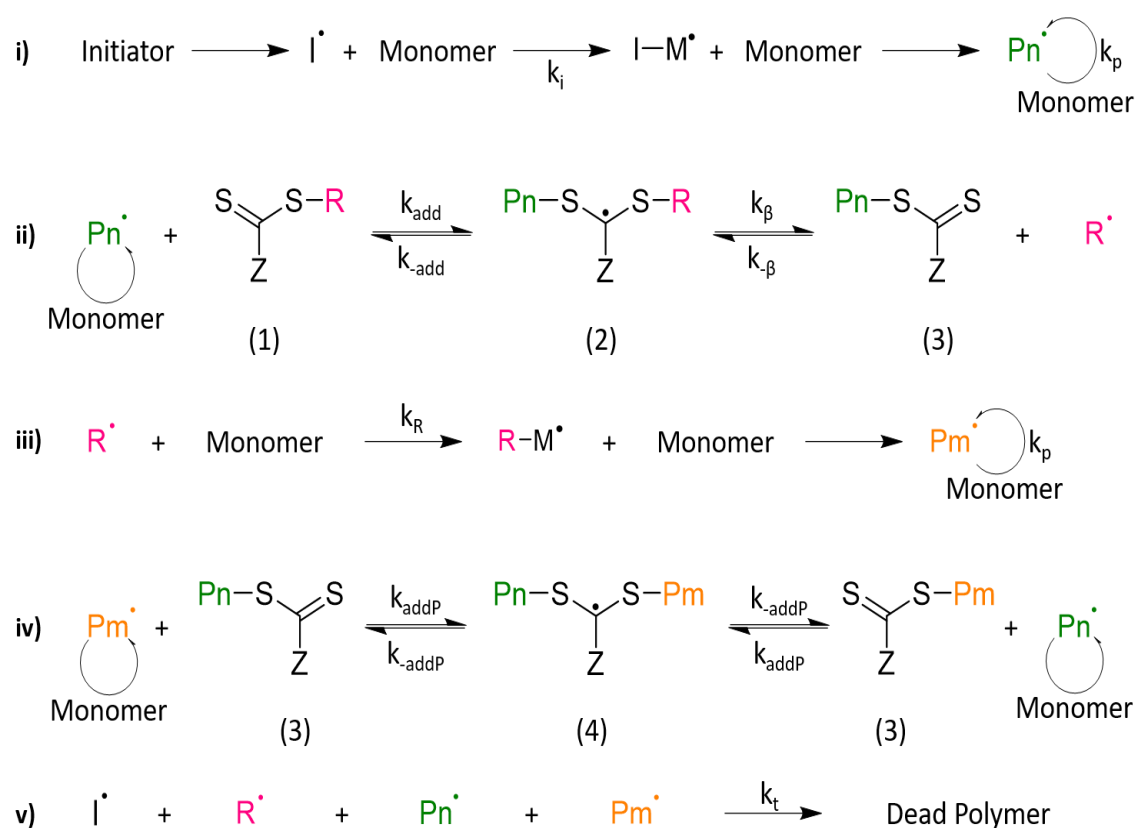


Figure 14: Proposed mechanisms for RAFT polymerization.

This equilibrium ensures an equal probability of chain growth. Once the polymerization is complete or stopped, the majority of the chains remain dormant, characterized by having a thiocarbonyl terminal group [i.e.,  $\text{P}_n\text{S}(\text{Z})\text{C}=\text{S}$ ] (3). These dormant chains can be isolated and obtained as stable materials. Finally, chains in their active form have the potential to undergo bi-radical termination, a process in which they react to form chains that cannot undergo further reactions. This leads to the formation of dead polymers. The optimal control in RAFT polymerization reactions involves selecting the appropriate CTA. Figure 15 presents a schematic representation demonstrating the general structures of these compound classes.

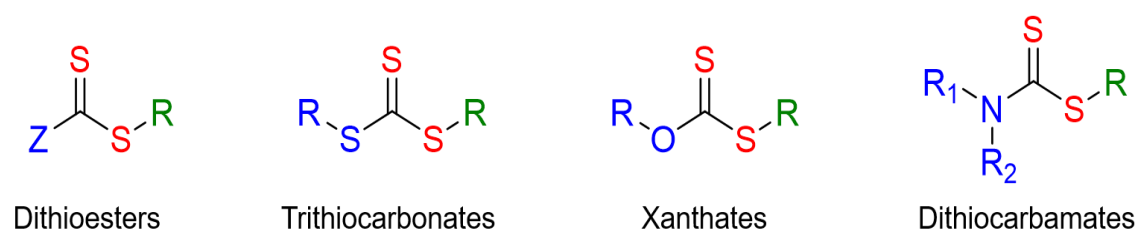


Figure 15: Chemical structure of the main RAFT agents.

The Z and R groups are crucial in determining the polymerization outcome. They govern the rate of addition and fragmentation, controlling the efficiency of chain transfer and the chances of retardation or inhibition [171]. The research literature extensively documents numerous thiocarbonyl RAFT agents, such as dithioesters ( $Z = \text{alkyl or aryl}$ ), trithiocarbonates ( $Z = \text{SR}'$ ), xanthates ( $Z = \text{OR}'$ ), and dithiocarbamates ( $Z = \text{NR}'\text{R}''$ ).

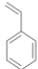
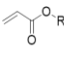
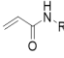
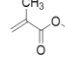
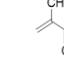


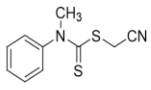
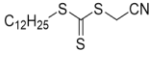
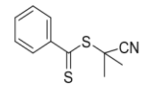
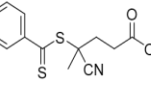
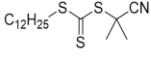
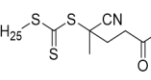
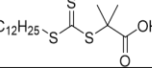
In general, the primary function of the Z group is to facilitate the activation of the double bond ( $\text{C}=\text{S}$ ) in the RAFT agent. This activation is essential for adding radicals, which helps prevent rapid and excessive radical propagation before the initial chain transfer occurs. Moreover, the Z group plays a crucial role in stabilizing radical intermediates that are formed in both the pre-equilibrium and main equilibrium of the RAFT process, thereby prolonging their lifetimes [172].

A higher activation level of the double bond between carbon and sulfur enhances the likelihood of propagating chains adding to the CTA. Consequently, this allows fewer monomer units to join the growing chains between transfer events. However, it is essential to be cautious as the excessive stabilization of intermediate radicals can result in slow fragmentation. Slow fragmentation leads to delays in the polymerization process and increases the chances of intermediate radical termination [173].

The contribution of the R group is primarily associated with the pre-equilibrium phase. Its primary function is to efficiently break down the intermediate radical and initiate the polymerization process again. For this reason, the stability of the expelled  $\text{R}^*$  radical needs to be as high as, or higher than, that of the  $\text{P}_n^*$  oligo radical to allow successful fragmentation of the intermediate radical. However, it is also crucial for the reactivity of  $\text{R}^*$  to be sufficiently high to reinitiate the monomer polymerization promptly.

The leaving group substituent R can be compared to the ability of  $\text{R}^*$  to initiate polymerization once again. So, to ensure optimal polymerization, it is crucial to select the appropriate CTA [173] carefully. Table 3 provides valuable insights into the correlation between the primary CTA and monomers, aiding decision-making.

Table 3: Correlation between the main chain transfer agents and monomers.

Monomer/CTA							
	Styrenes	Acrylates	Acrylamides	Methacrylates	Methacrylamides	Vinyl esters	Vinyl amides
1 	—	—	—	—	—	+++	+++
2 	+++	+++	+++	—	—	—	—
3 	++	+	—	+++	+++	—	—
4 	++	+	+	+++	+++	—	—
5 	+++	++	++	+++	+++	—	—
6 	+++	++	++	+++	+++	—	—
7 	+++	+++	+++	+	+	—	—

The commercial names of the CTAs present in Table 3 are 1: Cyanomethyl methyl(phenyl)carbamodithioate, 2: Cyanomethyl dodecyl trithiocarbonate, 3: 2-Cyano-2-propyl benzodithioate, 4: 4-Cyano-4-(phenylcarbonothioylthio)pentanoic acid, 5: 2-Cyano-2-propyl dodecyl trithiocarbonate, 6: 4-Cyano-4-[(dodecyl sulfanyl thiocarbonyl)sulfanyl]pentanoic acid, and 7: 2-(Dodecylthiocarbonothioylthio)-2-methyl propionic acid. The (-) symbol indicates that the CTA is incompatible with the monomer. Conversely, the symbol (+) signifies that the RAFT agent is compatible, with more symbols (+) indicating enhanced suitability. For instance, RAFT agent 4 is unsuitable for vinyl esters and vinyl amides but can be used with acrylates and acrylamides. It demonstrates good compatibility with styrenes and excellent compatibility with methacrylates and methacrylamides [174].

#### 2.4.4 Phase separation in block copolymers

The properties of block copolymers are closely linked to how the different polymer units, or mers, that make up the blocks are combined. This combination is determined by thermodynamic phase separation parameters [76,

77]. A delicate balance between enthalpy and entropy is crucial for the formation of the desired structure, and this relationship is captured by the product  $\chi_{AB}N$ . This parameter reflects the thermodynamic incompatibility between the mers. The first term,  $\chi_{AB}$ , represents the interaction parameter in the Flory-Huggins model [177].

It describes the enthalpic behavior of the system, specifically the interaction energy between two distinct polymer mers. The Gibbs energy of mixing includes both an enthalpy term and an entropy component. In the realm of regular solutions formed by molecules with comparable size, it's normally assumed that the entropy term mirrors that of an ideal solution, directing attention towards the enthalpic aspect of mixing. However, when considering solutions of molecules of different sizes, it is useful to presume a null enthalpy of mixing and place emphasis on the entropy of mixing ( $\Delta_{mix}S$ ) instead [178].

Solutions with a zero enthalpy of mixing are termed “athermal solutions” due to their characteristic of neither releasing nor absorbing heat when mixed under constant temperature and pressure conditions. While true athermal behavior is rarely observed, it is approached in mixtures of components that share similar chemical characteristics, even if their sizes differ [179].

Typically, it's advantageous to express the thermodynamic mixing properties as the aggregate of two components: i) a combinatorial contribution ( $\Delta S^C$ ), reflected in entropy (and consequently in Gibbs and Helmholtz energies), but not in enthalpy or mixing volume; and ii) a residual contribution ( $S^R$ ), influenced by variances in intermolecular forces and free volumes among the constituents. For instance, Equation 1 exemplifies the entropy of mixing.

$$\Delta_{mix}S = \Delta S^C + S^R \quad (1)$$

Where superscript *C* denotes the combinatorial contribution and superscript *R* signifies the residual contribution. In scenarios where the interactions and free volume of 2 fluid molecules (i.e., A and B) exhibit no disparity, isothermal and isobaric mixing occurs at a constant volume. Consequently, the residual mixing

properties become null, leaving only the combinatorial mixing properties to be accounted for [180]. Building upon the concept of a quasicrystalline lattice as a model for liquid, both Flory [181] in 1941 and Huggins [182] in 1942 independently derived expressions for the combinatorial entropy of mixing. Their derivations rely on statistical reasoning and several well-defined assumptions.

In the context of mixing a solvent (A) and a polymer (B), the solvent is predicted as individual spheres, while the polymer adopts a behavior similar to flexible chains, characterized by a multitude of mobile segments. Within this framework, it is postulated that each site of the quasilattice is either occupied by a solvent molecule or a polymer segment, with adjacent segments occupying adjacent sites [183]. Assuming  $M_A$  solvent molecules and  $M_B$  polymer molecules, each comprising  $r$  segments, the total number of lattice sites amounts to  $(M_A + rM_B)$ . The fractions  $\Phi_A^*$  and  $\Phi_B^*$ , denoting the proportion of sites occupied by the solvent and the polymer respectively, are determined by Equation 2.

$$\Phi_A^* = \frac{M_A}{M_A + rM_B} \quad \text{and} \quad \Phi_B^* = \frac{rM_B}{M_A + rM_B} \quad (2)$$

Flory and Huggins have shown that if the polymer and the solvent mix without any energetic effects (i.e., athermal behavior), the change in Gibbs energy ( $\Delta G^C$ ) and entropy of mixing ( $\Delta S^C$ ) are given by the remarkably simple Equation 3:

$$-\frac{\Delta G^C}{RT} = \frac{\Delta S^C}{R} = -M_A \ln \Phi_A^* + M_B \ln \Phi_B^* \quad (3)$$

Where  $R$  represents the gas constant, and  $T$  denotes the temperature. This equation is similar to that for regular solutions except that segment's fractions are used rather than mole fractions, as presented in Equation 4:



$$\frac{\Delta_{\text{mix}}S}{T} = \frac{1}{R} \left( \frac{\partial \Delta_{\text{mix}}^a}{\partial T} \right)_v = -x_A \ln x_A + x_B \ln x_B \quad (4)$$

Here,  $v$  represents volume,  $x$  denotes mole fraction, and  $a$  stand for the molar Helmholtz energy. In the specific instance where  $r = 1$ , the entropy change described by Equation 3 simplifies to that of Equation 4. However, for  $r > 1$ , Equation 3 consistently yields a combinatorial entropy greater than Equation 4 for identical values of  $M_A$  and  $M_B$ . Extensive deliberations on these equations led Hildebrand in 1947 to conclude that for nonpolar systems, Equation 4 provides a lower limit for the combinatorial entropy of mixing, while Equation 3 yields an upper limit [178]. The 'true' combinatorial entropy likely lies somewhere in between, depending on the size and configuration of the molecules involved.

Various modifications to this equation have been proposed by several researchers, including Huggins [184], Guggenheim [185], Staverman [186], Tompa [187], and Lichtenthaler [188]. The adjustments introduced by Lichtenthaler, akin to those by Tompa, offer a viable approach for calculating  $\Delta S^C$  for mixtures of molecules differing not only in size but also in shape. Lichtenthaler's model assumes that the ratio of the molecular (Van der Waals) volumes of the polymer to the solvent determines  $r$ , the number of segments in the polymer molecule.

Similarly, the ratio of the surface areas of the polymer and the solvent determines  $q$ , representing the external surface area of a polymer molecule. The ratio  $q/r$  serves as a metric for the shape of the polymer molecule, with a monomer having  $q/r = 1$ . As  $r$  grows large, approaching infinity for a linear chain,  $q$  approaches  $2/3$ , whereas for a sphere or cube,  $q/r$  tends towards 0. For globular molecules, the  $q/r$  ratio typically falls between zero and unity. Combinatorial entropies of mixing, computed using Lichtenthaler's expression, tend to fall between those derived from Equations 3 and 4, depending upon the  $q/r$  ratio [188]. When molecules A and B share identical size and shape, resulting in  $q = r = 1$ , Lichtenthaler's expression simplifies to Equation 4.

Conversely, as the coordination number (the count of nearest neighbors around a solvent molecule or segment) increases significantly, approaching a large value,  $q/r$  tends towards 1, rendering the expression identical to Equation 3, regardless of molecular shape. Although the simple Flory-Huggins expression may not always yield the presumed correct quantitative combinatorial entropy of mixing, it qualitatively captures many features of athermal polymer solutions [189].

To apply the theoretical findings of Flory and Huggins to real polymer solutions, which typically deviate from athermal behavior, it has become customary to supplement the combinatorial component of the Gibbs energy, as expressed in Equation 3, with a semiempirical term accounting for the residual contribution. Essentially, this entails incorporating a term that, in the absence of disparities in free volume, corresponds to the enthalpy of mixing. The structure of this term mirrors that employed in the van Laar-Scatchard-Hildebrand theory of solutions [190]. Specifically, the excess enthalpy is set proportionally to the solution's volume and the product of the volume fractions. Consequently, the Flory-Huggins equation for real polymer solutions can be represented by Equation 5:

$$-\frac{\Delta_{\text{mix}}G}{RT} = \frac{\Delta G^C}{RT} = \frac{G^R}{RT} - M_A \ln\Phi_A^* + M_B \ln\Phi_B^* + \chi\Phi_A^*\Phi_B^*(M_A + rM_B) \quad (5)$$

From this equation, it is observed that the Flory-Huggins interaction parameter ( $\chi$ ) is governed by intermolecular forces. Since the pioneering work of Flory and Huggins in the 1940s, a multitude of polymer-solution theories have emerged. For instance, Freed and colleagues [191] formulated a lattice-field theory for polymer solutions, offering a mathematically exact solution for the Flory-Huggins lattice. Notably, Freed's theory demonstrated good agreement between computed values and data from computer simulations. This approach has found successful application in the study of polymer blends, binary polymer solutions, and block copolymers [192].

The determination of  $\chi$  for BCPs has posed a longstanding challenge, prompting the application of numerous strategies [193]–[198]. However, these methods often yield disparate values of  $\chi$ , leading many to speculate that  $\chi$ 's value hinges on factors such as architecture, composition, molecular weight, polydispersity, or essentially all system details. Some even question whether a consistent definition for  $\chi$  exists at all. This ambiguity arises from the methodology used to determine  $\chi$ , which typically involves experimental (or simulation) measurements followed by fitting to predictions from the standard Gaussian Chain Model [199].

Accuracy in determining  $\chi$  demands precision not only in the measurement process but also in the predictive model. Typically, predictions rely on mean-field theory, where fluctuation corrections are effectively embedded within  $\chi$ . Consequently, it's unsurprising that  $\chi$  values derived from different quantities vary, as each possesses unique fluctuation corrections. Moreover, fluctuation effects are contingent upon all system parameters, leading to  $\chi$ 's dependency on these parameters as well [199]. In recent years, significant strides have been made in precisely determining the Flory-Huggins  $\chi$  parameter [200]. Researchers have leveraged data on order-disorder transitions (ODTs) in symmetric diblock polymer melts, employing mean-field theory for fitting purposes. This approach capitalizes on the accuracy of order-disorder transition temperature ( $T_{\text{ODT}}$ ) measurements and their pronounced reliance on  $\chi$ , rendering it an effective means of elucidating  $\chi$ 's value.

The second term,  $N$ , stands for the degree of polymerization and corresponds to the contribution of entropy to the Gibbs free energy. This implies that to maintain a stable structure, the blocks are organized in such a way as to minimize the amount of free energy at the interface between the different domains. This organization leads to the formation of distinct phases, which can be considered separate microdomains [201]. The  $\chi_{\text{AB}}N$  product determines whether the phase structure will exhibit order or disorder. When the  $\chi_{\text{AB}}N$  product surpasses a critical value, the system experiences phase separation, forming periodic and orderly structures.

Conversely, if the  $\chi_{AB}N$  product falls below the critical value, the system is governed by entropic factors, leading to a mixture of phases and a disordered phase structure [202]. Essentially, higher  $\chi_{AB}N$  values encourage the development of well-organized microdomains, while lower  $\chi_{AB}N$  values promote phase mixing. In other words, a strategy that can be used to obtain phase separation is to use monomers with different characteristics and synthesize copolymers with high molecular weights.

The copolymer blocks possess the remarkable ability to self-organize according to the system's energy, leading to the formation of diverse morphologies [203], as illustrated in the phase diagram in Figure 16. These morphologies can be effectively depicted in a phase diagram, wherein the  $\chi_{AB}N$  product is plotted against the volume fraction of each phase ( $f$ ). Besides, this diagram allows us to identify the stability regions for different morphological structures [204].

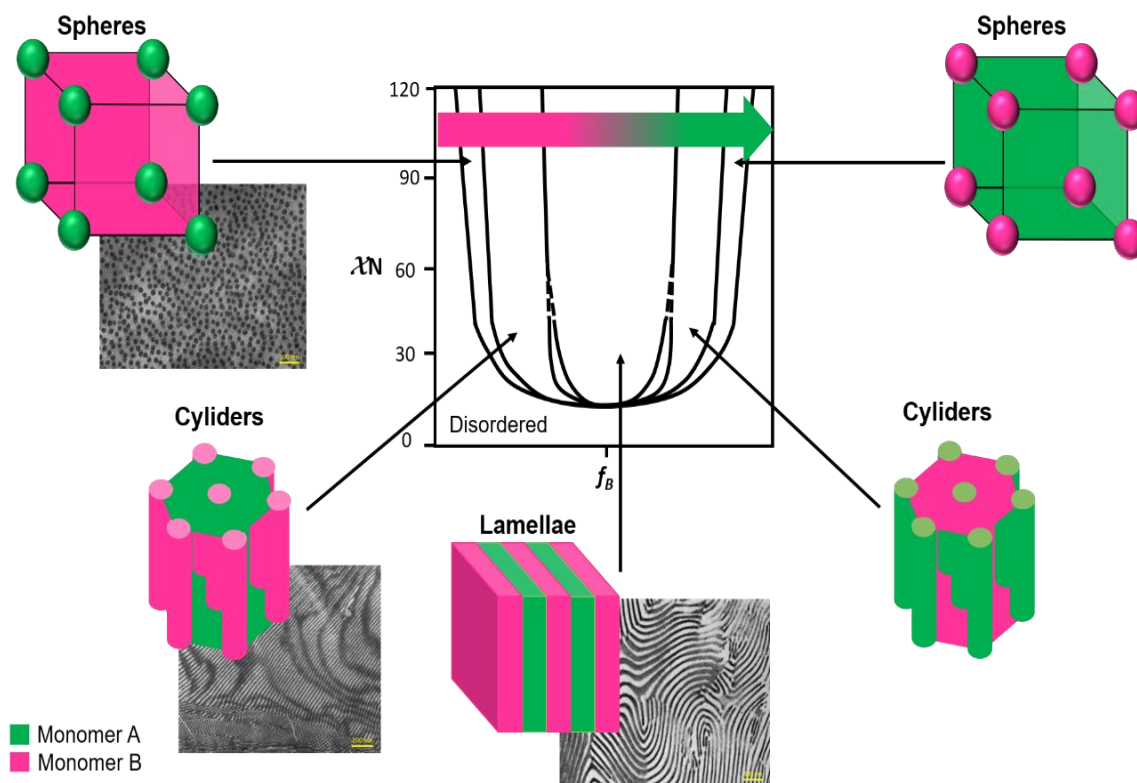


Figure 16: Phase diagram of symmetric conformational diblock copolymer [205].

The diagram illustrates the different structures that can be formed by BCPs, including spherical, cylindrical, lamellar, and cubic continuous structures with gyroid symmetry [206]. Additionally, more complex structures, such as perforated hexagonal layer arrangements [90, 91] and hexagonal ripple structures [209], can also be observed. The volume fractions of the blocks influence the formation of these structures due to curvature effects at the interface between the domains [93, 94].

Several theories have been proposed to elucidate the phase separation phenomenon in copolymers [205][212]. Based on the phase diagram, we can define two distinct regimes based on the  $\chi_{AB}N$  product [213]. The first regime is known as the Weak Segregation Limit (WSL), characterized by relatively small  $\chi_{AB}N$  values ( $\chi_{AB}N \ll 1$ ), resulting in weak interactions between microdomains. Consequently, an ordered phase is formed [86, 87]. The second regime corresponds to the Strong Segregation Limit (SSL), wherein the  $\chi_{AB}N$  product attains large values ( $\chi_{AB}N \gg 10$ ), promoting the strong segregation of domains, thereby yielding well-defined individual domains [216].

The thickness of a domain is directly proportional to its volume fraction. Therefore, when the volume fraction of block A ( $f_A$ ) is equal to that of block B ( $f_B$ ), or when  $f_A = f_B = 0.5$ , a flat interface is formed, resulting in a lamellar morphology. On the other hand, when the volume fraction of one block is between 0.3 and 0.5, the phase formed by this block exhibits a particular curvature at its interface, creating a cylindrical morphological structure in smaller quantities. If the volume fraction is less than 0.3, the curvature becomes more pronounced, resulting in a spherical morphology [217].

Correspondingly, it is important to note that the  $\chi_{AB}N$  term is inversely proportional to temperature. Consequently, as the temperature rises, the domains become less ordered, shifting towards disorder [218]. Thus, the  $T_{ODT}$  is essential for copolymers because it determines their physical properties, behavior, and applications. Moreover, this parameter holds paramount significance in delineating the Flory-Huggins parameter, underscored by the demonstrated robust correlation between  $\chi$  and  $T_{ODT}$  [219].

#### 2.4.4.1 Order to disorder transition (ODT)

In block copolymers, the incompatibility between the two phases gradually diminishes at elevated temperatures. This transition results in a spatially homogeneous state, where the polymer chains exhibit properties similar to a randomly mixed phase [220]. Figure 17 illustrates this phenomenon, where increasing the temperature disintegrates the ordered microphase-separated structure. So, an isotropic phase is formed, wherein the binary block chains interpenetrate each other.

According to Gibbs free energy equation ( $\Delta G = \Delta H - T\Delta S$ ), at higher temperatures, the value of  $\chi_{AB}$  (enthalpic contribution,  $\Delta H$ ) decreases significantly, increasing entropy ( $-T\Delta S$ ). This increase in entropy contributes to minimizing the overall change in free energy ( $\Delta G$ ). Conversely, when the temperature drops,  $\chi_{AB}$  becomes larger. Upon reaching a critical value, the entropy term begins to dominate, causing the free energy of mixing to increase. As a result, the number of contacts between the two blocks decreases, leading to phase separation at the microscale.

This transition from a structured arrangement to a mixed state signifies a significant structural transformation, resulting in notable variations in material properties. As such, the ODT in BCPs is often identified experimentally via rheological analysis [221]. When the block copolymer sample is subjected to shear, the ODT can be identified by observing a sharp reduction in the isochronal dynamic elastic moduli (or storage modulus,  $G'$ ) as the temperature increases. It has been shown that analyzing the relationship between  $\log G'$  and  $\log G''$  (loss modulus) can be applied to determine the  $T_{ODT}$  in BCPs [222].

As a burgeoning field of study, there has been considerable enthusiasm surrounding block copolymers incorporating both charged and neutral blocks. This excitement stems from the vast potential of these copolymers in numerous applications [223]. Nonetheless, to create innovative materials with precise morphology, exceptional mechanical properties, and heightened proton conductivity, a more profound comprehension of micro-phase separation in the presence of charges is indispensable and warrants further investigation.

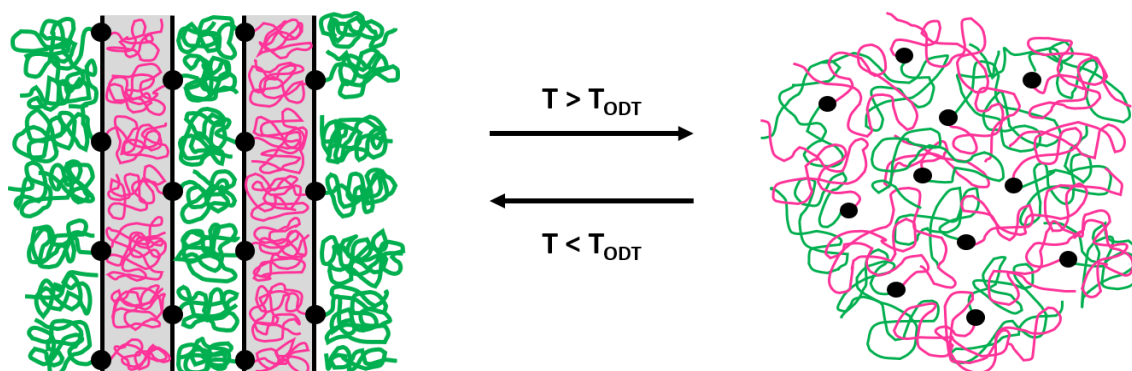


Figure 17: Order and disorder states in a symmetric diblock copolymer.

#### 2.4.5 Phase separation in amphiphilic block copolymers

Amphiphiles, derived from the Greek words "amphis," meaning both, and "philia," meaning love or friendship, are remarkable molecules that display an affinity for two different types of environments. This extraordinary dual nature is achieved by carefully linking portions of the molecule that possess distinct properties through covalent bonds. When given an opportunity, these contrasting components minimize their interaction, resulting in a preferred segregation for amphiphilic molecules [224].

Surfactants, known as surface-active agents and polar lipids, are low molecular weight amphiphiles with distinct hydrophilic and hydrophobic components. These classes of compounds have been widely studied due to their broad technical applications and biological functions throughout the 20<sup>th</sup> century, resulting in a comprehensive understanding of their properties and behavior [225]. The amphiphilic nature of surfactants and lipids allows them to interact differently with polar or nonpolar solvents and surfaces.

For this reason, these molecules can self-assemble in solution (Figure 18a) or adsorb at a surface or interface (Figure 18b) to create favorable intermolecular contacts while eliminating unfavorable ones [226]. Self-assembly is characterized by the organized formation of domains consisting of hydrophobic groups, which typically contact nonpolar solvents or surfaces, and hydrophilic groups, which are in contact with water or other polar solvents or hydrophilic surfaces.

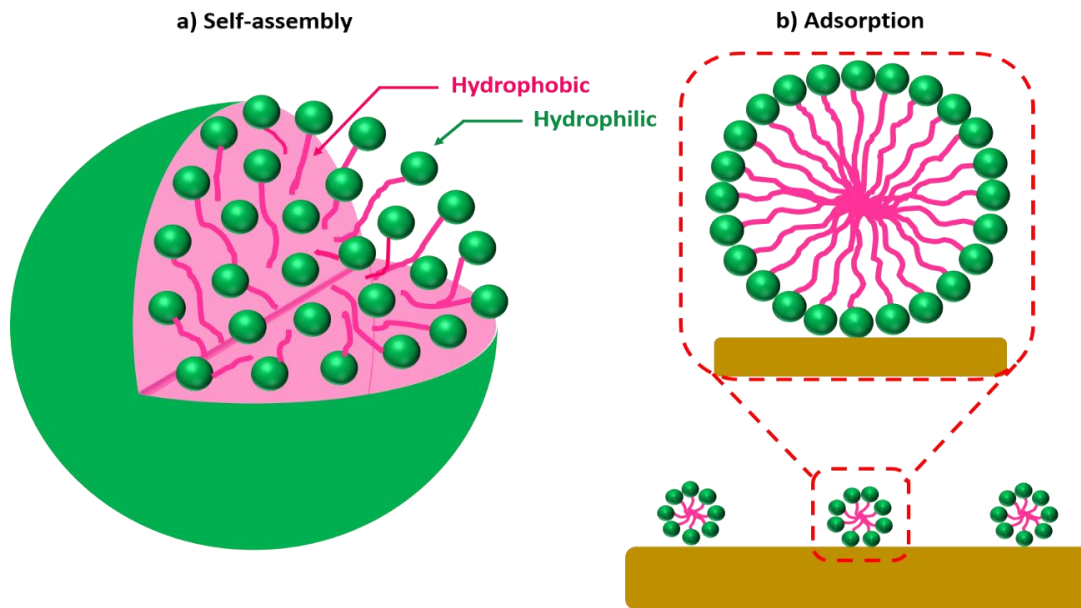


Figure 18: a) Illustration of a spherical micelle self-assembling in solution and b) adsorption at a surface.

This process exhibits a wide range of topological variations and diverse intermicellar arrangements, leading to various self-assembled microstructures, as shown in Figure 19.

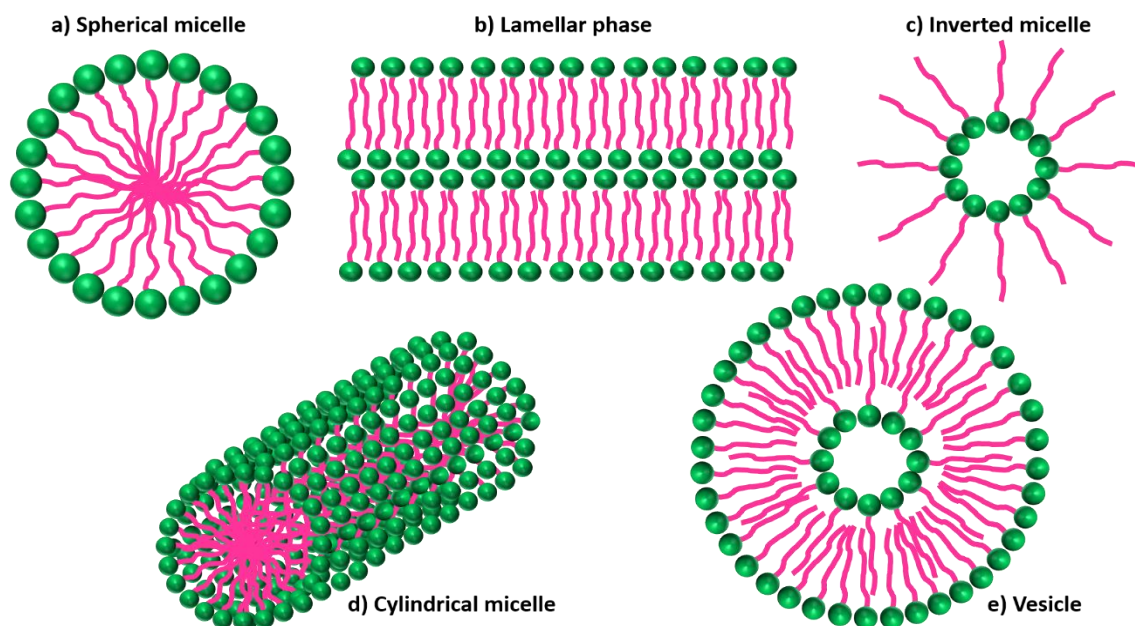


Figure 19: a) Amphiphilic structures self-assembly leads to a range of different structures: a) Spherical micelle, b) lamellar phase, c) inverted micelle, d) cylindrical micelle, and e) vesicle.



The complexity of the phase behavior is often associated with the size of the surfactant molecule [227][228]. Increasing the size of an amphiphilic molecule offers numerous benefits in both technical applications and biological functions. Firstly, a stronger amphiphile with low monomeric solubility exhibits a greater interface affinity, making it highly surface active. This enhanced surfactant ability makes it an ideal choice for applications such as detergents, dispersion stabilizers, surface modifiers, membranes, and others [229]. Secondly, larger amphiphiles provide richer self-assembly polymorphism, allowing precise control over macroscopic and microscopic properties. This versatility enables the customization of desired characteristics in various systems [230].

Another advantage lies in the dynamic nature of self-assemblies. Surfactant micelles and other aggregates are inherently dynamic, with surfactant molecules constantly exchanging positions. However, by increasing the size of the amphiphilic molecule, the residence times of the molecules within the aggregates significantly increase. This increased stability of self-assemblies is crucial in making technical systems and biological structures more resilient and less susceptible to disturbances [229]. Therefore, there is a strong incentive to enhance molecular size, as it improves the efficiency and effectiveness of surfactant properties and enhances stability, making it a desirable trait for various applications.

Most surfactants typically consist of a small polar component, usually just a few angstroms in size, accompanied by a nonpolar component that is significantly larger [230]. However, there are certain nonionic surfactants in which both components are similar in size. These particular nonionic surfactants can be compared to short AB block copolymers (where A is the charged phase) and exhibit a diverse range of phase behaviors, including various solution and liquid crystalline phases, in which the specific type of aggregation is determined by the relative proportions of the hydrophilic and hydrophobic portions present [231], similar to block copolymers. Small amphiphilic molecules are primarily restricted to the AB, ABA, and BAB chemical structures, as illustrated in Figure 20.

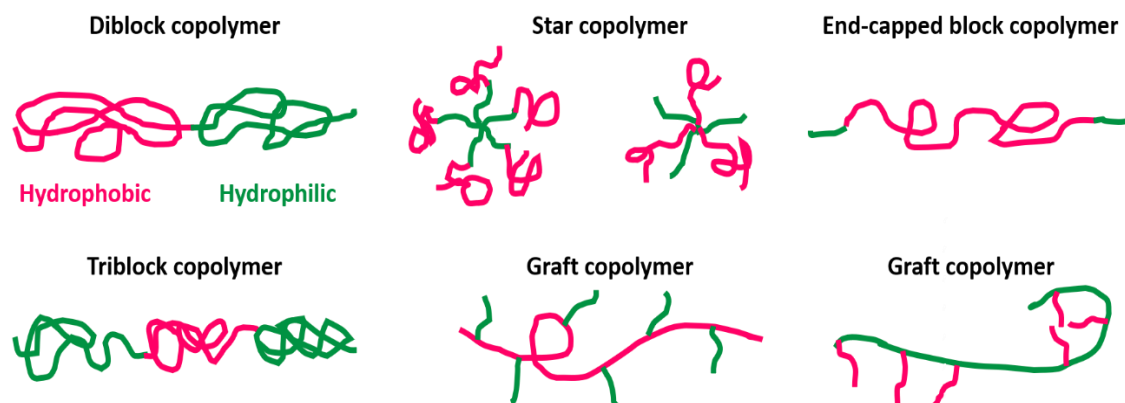


Figure 20: Schematics of block, star, and graft amphiphilic block copolymers.

However, when the  $M_n$  increases, a wide range of possibilities become available. This becomes a significant advantage when transitioning to higher molecular weight amphiphiles, as the molecular architecture can become much more diverse. It opens up the potential for block, graft, and star copolymers. Amphiphilic polymers, which have already garnered significant scientific attention and widespread industrial applications, consist of block copolymers using the AB, ABA, or BAB types and various graft copolymers [230].

Large amphiphilic molecules, such as diblock and triblock copolymers and graft copolymers with long grafts and flexible backbones, can self-assemble into micelles when dissolved in specific solvents. These molecules can also adsorb on surfaces. Initially, research focused on amphiphilic BCPs in organic solvents [232], but other studies have explored the formation of micelles in aqueous solutions [233]. BCP micelles differ from micelles formed by small amphiphiles in size and segregation, but most functional properties are common.

Hence, investigating small amphiphiles in solution is crucial for comprehending the self-assembly tendencies exhibited by amphiphilic copolymers and, then, in their solid-state counterparts [234]. In simpler systems, the morphological features of copolymer aggregates, such as spherical, rod- or worm-like micelles, and vesicles, can be predicted using the packing parameter ( $p = v/a_0L_c$ ). This parameter takes into account the volume of the hydrophobic segment ( $v$ ), the contact area of the head group ( $a_0$ ), and the length of the hydrophobic segment ( $L_c$ ) [235]. Figure 21 illustrates the relationship between the packing parameter and the micellar transition.

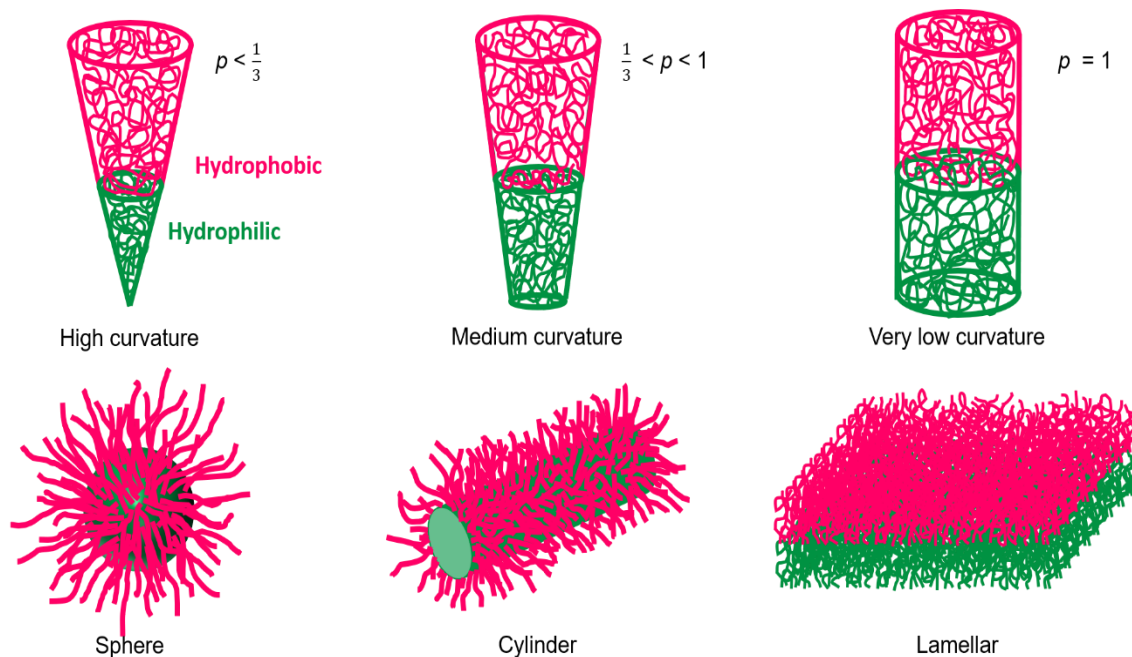


Figure 21: Different block copolymer self-assembly as a function of packing parameter  $p$ -range.

Therefore, many studies with micelles have been expanded to understand the behavior of amphiphilic polymers and copolymers, with significant progress in self-assembly. Researchers have extended these studies to comprehend a vast composition space, exploring mixtures of block copolymers with selective solvents [236]. These investigations have identified various well-defined structures in nanometer scale dimensions, mirroring those found in neutral block copolymers. Additionally, initially developed for polymer blends, scaling theories and mean field lattice models have been successfully applied to amphiphilic block copolymer solutions, yielding encouraging results [237].

The challenge and the opportunity in this field lie in the controlled manipulation and fine-tuning of morphology, specifically in selecting the appropriate components and conditions to yield the desired microstructure. Notably, large amphiphiles possess exceptional flexibility in achieving various microstructures in the absence and presence of solvents and/or other additives. Moreover, their macromolecular nature enables access to an expansive range of length and time scales. Therefore, amphiphilic block copolymers have immense potential for contributing to various applications [238].

Over the years, essential insights into the complex behavior of charged-neutral block copolymers were achieved through extensive studies of the physical properties of amphiphilic molecules and ionized multiblock thermoplastic elastomers [239]. Eisenberg et al. [240] and McGrath and Wilkes et al. [241] performed comprehensive structural investigations of block copolymer ionomers. The bulk morphologies primarily comprised spherical or rod-like ionic domains of fully charged, short ionic blocks. Other experiments have been conducted [242][243] to gain a deeper understanding of the behavior of ionic block copolymers in molten states.

Incorporating ionic or charged functional groups into one or more blocks of the copolymers expands the range of factors that can be manipulated to control the morphologies, but it also adds complexity to the phase behavior [244]–[246]. The explicit Coulomb interactions between the charged species also introduce further intricacies that have impeded progress in theoretical and simulation studies [247]. Recently, due to the versatility of controlled polymerizations, various monomers can be used to prepare amphiphilic copolymers being neutral blocks (hydrophilic or hydrophobic) or polyelectrolyte (anionic, cationic or zwitterionic) [248]–[250].

The hydrophilic block in such copolymers can be formed by polyethylene oxide (PEO) or polyethylene glycol (PEG), poly(N-isopropyl acrylamide) (PNIPAM), polyvinyl caprolactam (PVCL), Poly(N,N-dimethylacrylamide) (PDMA), poly(2-methyl-2-oxazoline) (PMeOx), polyvinyl pyrrolidone (PVP), polyvinyl alcohol (PVA), polystyrene sulfonated (PSS), poly(2-hydroxypropyl methacrylamide) (PHPMA), as well as some poly acids and polybases are also well-known [235]. The hydrophobic blocks can be of polypropylene oxide (PPO), polylactic acid (PLA), polytetrafluoroethylene (PTFE), polycaprolactone (PCL), polybutylene oxide (PBO), polystyrene oxide (PSO), polybutadiene (PB), polystyrene (PS), poly(butyl methacrylate) (PBMA), poly(butyl acrylate) (PBA), etc. Some common examples of most common the hydrophilic and hydrophobic blocks used to prepare amphiphilic block copolymers are illustrated in Figure 22.

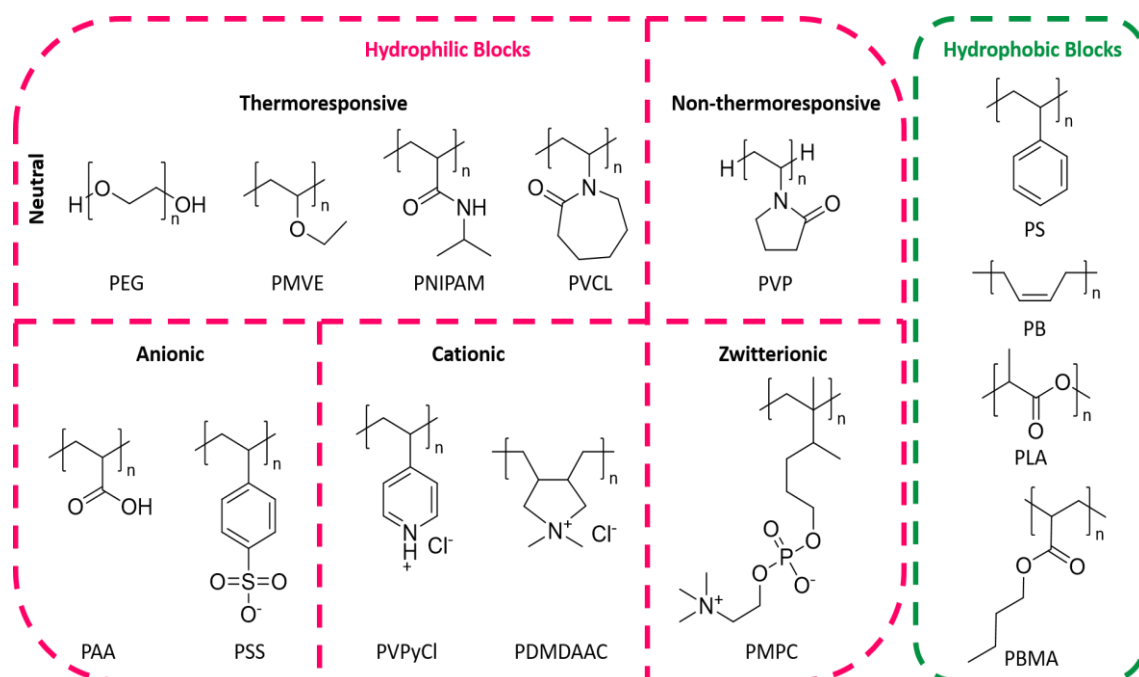


Figure 22: Examples of polymers with varied nature of hydrophilic and hydrophobic blocks.

Ion-containing block copolymers, with only one block sulfonated, are highly desirable due to their ability to combine the advantages of regular structure and ion conduction (movement of ions within the polymer matrix). One microdomain with the ionic moiety in these copolymers facilitates efficient transport, while the nonionic microdomain offers mechanical support to the membrane. These sulfonated block copolymers are particularly interesting as they allow for the creation of highly ordered morphologies with tailored transport properties, offering great potential for reliable applications.

Sulfonated block copolymers were first mentioned in patent literature in the 1960s [251]. However, it wasn't until the 1990s that academic literature began to explore this topic. During this decade, research efforts primarily focused on the sulfonation and subsequent thermal and structural characterization of styrene-based block copolymers, with a particular interest in low ion exchange capacities (IECs) of less than 0.5 meq g<sup>-1</sup> [252]–[255].

One noteworthy result from this period is the work conducted by Wiess and colleagues [256] on sulfonated poly(styrene-*b*-(ethylene-*r*-butylene)-*b*-styrene). Their research revealed the coexistence of morphological length

scales, with ionic clusters spaced approximately 3-4 nm apart within block copolymer microdomains, with a spacing of around 20-30 nm.

In the 2000s, research focused on sulfonated block copolymers with increased IECs of approximately 1-2 meq g<sup>-1</sup>, and their transport properties were examined. Notable examples of these copolymers include sulfonated poly(styrene-*b*-(ethylene-*r*-butylene)-*b*-styrene) [257][258], sulfonated poly(styrene-*b*-isobutylene-*b*-styrene) [259], sulfonated poly(vinylidene difluoride-co-hexafluoropropylene-*b*-styrene) [260], and sulfonated poly(arylene ether)s [261].

Other studies have showcased noteworthy advancements in proton conductivity when utilizing sulfonated block copolymers compared to sulfonated random copolymers. These copolymers exhibit conductivities across a wide range of temperatures and relative humidity that surpass those of Nafion (0.91 meq g<sup>-1</sup>), the industry standard for polymer membranes [262]. This advancement highlights the potential for these sulfonated block copolymers to outperform traditional materials in proton exchange applications [32].

Block copolymers containing both charged and neutral blocks have attracted considerable attention since they can combine antagonistic properties with controllable morphology. Besides, it has been shown that charged-neutral block copolymers exhibit the potential for achieving higher proton conductivity [29][104] compared to ionomers such as Nafion, Aciplex, and Flamion, as well as random ionic copolymers [105]. To accomplish this goal, further research should focus on optimizing the proton transport channels through micro-phase separation and enhancing the materials' mechanical properties [254], [263], [264].

### 3 MATERIALS AND METHODS

#### 3.1 Materials

Below, the materials used for synthesizing the block copolymer, preparing electromechanical devices, and the electromechanical system are presented in alphabetical order.

##### 3.1.1 PBMA-b-(PSS-r-PS) synthesis

2,2' - Azobis (2-methyl propionitrile) ( $[(CH_3)_2C]_2N_2$ );  
4-Cyano-4-(phenylcarbonothioylthio) pentanoic acid ( $C_{13}H_{13}NO_2S_2$ );  
4-tert-butyl catechol ( $C_{10}H_{14}O_2$ );  
4-vinylbenzenesulfonyl chloride ( $C_8H_7ClO_2S$ );  
Butyl methacrylate ( $C_8H_{14}O_2$ );  
Dichloromethane ( $CH_2Cl_2$ );  
Dimethyl formamide ( $HCON(CD_3)_2$ );  
Hexane ( $CH_3(CH_2)_4CH_3$ );  
Magnesium Sulfate ( $MgO_4S$ );  
Methanol (MeOH);  
Milli-Q water ( $H_2O$ );  
Neopentyl p-styrene sulfonate ( $C_{13}H_8NaO_3S$ );  
Neopentyl alcohol ( $C_5H_{12}O$ );  
Pyridine ( $C_5H_5N$ );  
Sodium 4-vinylbenzenesulfonate ( $C_8H_7NaO_3S$ );  
Styrene ( $C_8H_8$ );  
Tetrahydrofuran ( $C_4H_8O$ );  
Thionyl chloride ( $SOCl_2$ );  
Toluene ( $C_6H_5CH_3$ ).

##### 3.1.2 Preparation of electromechanical device

Ammonium hydroxide ( $NH_4OH$ );  
Ethyl acetate ( $CH_3COOC_2H_5$ );  
Hydrochloric acid (HCl);

Hydrogen peroxide ( $\text{H}_2\text{O}_2$ ).  
Lithium chloride ( $\text{LiCl}$ );  
Milli-Q water ( $\text{H}_2\text{O}$ );  
Potassium chloride ( $\text{KCl}$ );  
Sodium borohydride ( $\text{NaBH}_4$ );  
Sodium chloride ( $\text{NaCl}$ );  
Tetraamineplatinum (II) chloride hydrate [ $\text{Pt}(\text{NH}_3)_4\text{Cl}_2$ ].

### 3.1.3 Electromechanical System

Acrylic chamber;  
Air pumps (model NS350);  
Arduino control board (open-source hardware);  
Capacitors (100 nF)  
Computer;  
DHT22 sensor;  
Diodes (1N4001);  
Electrolytic capacitors (1000  $\mu\text{F}$ /25 V);  
Flexible vinyl tubes;  
Glass bottles;  
High-resolution camera;  
LM7812 (positive voltage regulator);  
LM7912 (negative voltage regulator);  
Load cell (MK Control, model PWZL300g);  
Mini-compressors;  
NI-9218 (data acquisition module);  
NI-9263 (voltage output module);  
OPA551 (current and voltage amplifier);  
Relay module;  
Resistor (10K ohm);  
Symmetrical source (+12V/-12V);  
Transformer (12/0/12V, 1A).



## 3.2 Experimental

### 3.2.1 Synthesis of neopentyl styrene sulfonate (NeoSS) monomer

The neopentyl *p*-styrene sulfonate (NeoSS) was successfully synthesized through a two-step process. In the first step, sodium 4-vinylbenzenesulfonate (NaSS) prepared 4-vinylbenzenesulfonyl chloride. This intermediate product was then protected with a neopentyl group (Figure 23a). The synthesis procedure closely followed previously reported methods [265] but with several modifications to improve the overall efficiency, yield, and purity of the final NeoSS product.

#### 3.2.1.1 Synthesis of 4-vinylbenzenesulfonyl chloride

Thionyl chloride (80.8g, 679 mmol, 7eq) was added dropwise to the round bottom flask containing 220 mg of 4-*tert*-butylcatechol and 60 ml of anhydrous DMF at 0 °C. The solution was mixed for 1h, sodium 4-vinyl benzenesulfonate (20g, 97 mmol, 1eq) was added in small portions (1g.min<sup>-1</sup>), stirred for 3h, and cooled in the freezer for 24h. Then, 300 ml of Milli-Q water at 0°C was added in a separating funnel, the reaction solution was slowly mixed, and the organic phase was extracted three times with toluene (150 mL portions). It was washed three times with water (150 mL portions), dried over anhydrous magnesium sulfate, concentrated on a rotary evaporator at 30 °C, and dried under a reduced vacuum (10<sup>-1</sup> mbar). A yellowish liquid (16g, 82% yield) was obtained to synthesize neopentyl styrene sulfonate monomer. <sup>1</sup>H NMR 500 (CDCl<sub>3</sub>, ppm): δ 5.43 (d, 2H, -CH=CH<sub>2</sub>), 5.87 (d, 2H, -CH=CH<sub>2</sub>), 6.70 (q, 1H, -CH=CH<sub>2</sub>), 7.53 (d, 2H, aromatic -CH-, ortho to vinyl), 7.83 (d, 2H, aromatic -CH-, meta to vinyl) (Figure 23b).

#### 3.2.1.2 Synthesis of Neopentyl *p*-Styrene Sulfonate

Neopentyl alcohol (9.13 g, 104 mmol, 1.3eq) and pyridine (27.3 g, 345.4 mmol, 4.4eq) were added in a 100 mL round-bottomed flask, it was cooled to 0 °C, and 4-vinylbenzenesulfonyl chloride (16 g, 79 mmol, 1eq) was added dropwise. The solution was stirred for 3h at 0 °C, forming a white powder. It was diluted with 200 mL of dichloromethane, washed extensively with HCl/H<sub>2</sub>O solution (2 mol.L<sup>-1</sup>), and dried over anhydrous magnesium sulfate.

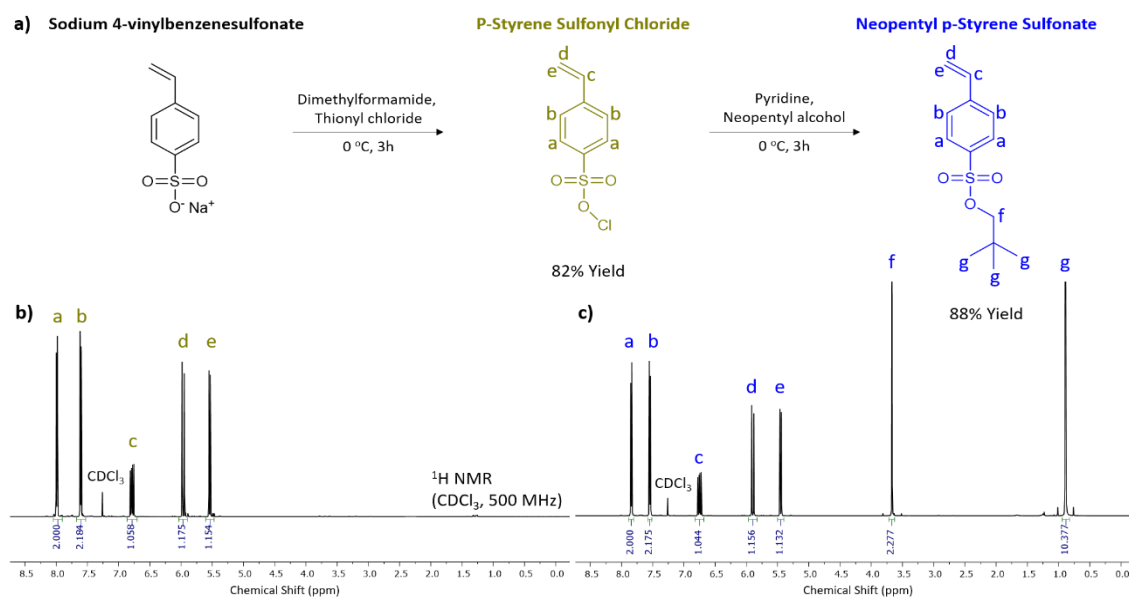


Figure 23: Synthesis of neopentyl styrene sulfonate, b) NMR spectroscopy of 4-vinylbenzenesulfonyl chloride, and c) NMR spectroscopy of neopentyl styrene sulfonate.

Dichloromethane was removed under reduced pressure at 35 °C. A white solid was obtained (17.75g, 88% yield). <sup>1</sup>H NMR 500 (CDCl<sub>3</sub>, ppm): δ 0.89 (s, 9H, -CH<sub>3</sub>), 3.66 (s, 2H, -CH<sub>2</sub>-), 5.43 (d, 2H, -CH=CH<sub>2</sub>), 5.87 (d, 2H, -CH=CH<sub>2</sub>), 6.70 (q, 1H, -CH=CH<sub>2</sub>), 7.53 (d, 2H, aromatic -CH-, ortho to vinyl), 7.83 (d, 2H, aromatic -CH-, meta to vinyl) (Figure 23c).

### 3.2.2 Synthesis of PBMA-CPADB macroinitiator

Butyl methacrylate (BMA) was polymerized using 4-Cyano-4-(phenylcarbonothioylthio)pentanoic acid (CPADB) as a chain transfer agent and initiated by 2,2'-Azobis(2-methylpropionitrile) (AIBN). In a 20 mL round-bottom Schelenk flask, BMA, CPADB, and AIBN were solubilized in dimethylformamide (DMF), mixed, degassed with argon for 1h, sealed, and polymerized at 80 °C in an oil bath. The polymerization was carried out for 12 hours, and every 30 minutes, an aliquot of the reaction was removed using a degassed syringe to determine monomer conversion and polymerization kinetics by nuclear magnetic resonance (NMR) spectroscopy and gel permeation chromatography (GPC). The reaction was terminated by precipitating the reaction in a cold

H<sub>2</sub>O:MeOH (9:1) solution. The precipitated was resolubilized in tetrahydrofuran (THF), concentrated in a rotary evaporator, and precipitated in a cold H<sub>2</sub>O:MeOH solution. This procedure was repeated 3 times, and the poly(butyl methacrylate) macroinitiator was dried under a high vacuum ( $10^{-2}$  Bar) for 12h.

### **3.2.3 Synthesis of PBMA-b-(PNeoSS-r-PS) block copolymer**

The monomers NeoSS and Sty were copolymerized using a PBMA macroinitiator and initiated by AIBN. In a 20 mL round-bottom Schelenk flask, NeoSS, Sty, PBMA, and AIBN were solubilized in DMF, mixed, degassed with argon for 1h, sealed, and polymerized at 80 °C in an oil bath. The polymerization was carried out for 8 hours, and every 30 minutes, an aliquot of the reaction was removed using a degassed syringe to determine monomer conversion and polymerization kinetics by NMR and GPC. The reaction was terminated by precipitating the reaction in cold Hexene (100 mL). The precipitated was separated, washed with MeOH (100 mL), concentrated in a rotary evaporator, and dried under a high vacuum ( $10^{-2}$  Bar) for 12h.

### **3.2.4 Preparation of PBMA-b-(PSS-r-PS) amphiphilic block copolymer**

To transform the block copolymer PBMA-b-(PNeoSS-r-PS) into an amphiphilic material, removing the neopentyl group from sulfonated neopentyl styrene is crucial. This can be accomplished through a procedure known as thermolysis. During thermolysis, the thermochemical cleavage of neopentyl groups generates sulfonic acid groups, forming a sulfonated ionic block. This procedure was determined based on the thermal characterizations and should be conducted at 160°C for 1 hour, followed by an additional 1 hour at 180°C, both under vacuum.

### **3.2.5 Preparation of PBMA-b-(PSS-r-PS) membrane**

After thermolysis, the amphiphilic copolymer, weighing 1.5 g, was dissolved in 8.5 mL of toluene, resulting in a 15% weight/volume solution. This solution was then poured into a Teflon mold with dimensions of 40mm x

100mm. The mold was left untouched for 24 hours to allow for efficient evaporation. Afterwards, the mold was placed inside an oven at 100 °C, and left for 6 hours to completely remove any remaining solvent. To further enhance the material's properties, the temperature was raised to 140 °C, initiating an annealing process. This additional step aimed to alleviate residual stress and achieve the desired equilibrium morphology. After this annealing process (24h), the sample was removed from the mold and is now prepared and available for use in creating an electromechanical device.

### 3.2.6 Bio-inspired electromechanical device preparation

IPMC sample was assembled using an optimized and reproducible method [266][267]. The reactions involved in the deposition step are presented in Table 4, and were carried out in 500 mL beakers. Initially, the copolymer was boiled for 30 min in milli-Q water. Then, an aqueous solution of  $[\text{Pt}(\text{NH}_3)_4\text{Cl}_2]$  containing 3.0 mg of  $\text{Pt}\cdot\text{cm}^{-2}$  of the membrane and 2.0 mg of  $\text{Pt}\cdot\text{mL}^{-1}$  of  $\text{H}_2\text{O}$  was prepared. A 5% ammonium hydroxide ( $\text{NH}_4\text{OH}$ ) solution were added for pH adjustment. The sample employed measures 5 cm x 5 cm, providing a total surface area of 50  $\text{cm}^2$  on both sides. Consequently, the experimental setup required 150 mg of  $[\text{Pt}(\text{NH}_3)_4\text{Cl}_2]$  dissolved in 75 mL of  $\text{H}_2\text{O}$ . Following this, 3.75 mL of a 5% ammonium hydroxide ( $\text{NH}_4\text{OH}$ ) solution were added.

Table 4: Reactions involved in the deposition process.

Reaction	Description
$[\text{Pt}(\text{NH}_3)_4(\text{Cl})_2] + 2\text{NH}_4^+ + 2\text{OH}^- + 2\text{H}^+ \rightarrow [\text{Pt}(\text{NH}_3)_6]^{+2} + 2\text{H}_2\text{O} + 2\text{Cl}^- + 2\text{H}^+$	Hydrolysis
$[\text{Pt}(\text{NH}_3)_6]^{+2} \rightarrow \text{Pt}^{2+} + 6\text{NH}_3$	Complex Activation
$\text{Pt}^{2+} + 2\text{NaBH}_4 \rightarrow \text{Pt}^0 + \text{H}_2 + \text{B}_2\text{H}_6 + 2\text{Na}^+$	Redox Reaction
$\text{B}_2\text{H}_6 + 6\text{H}_2\text{O} \rightarrow 2\text{B}(\text{OH})_3 + 6\text{H}_2$	Disproportionation
$[\text{Pt}(\text{NH}_3)_4(\text{Cl})_2] + 2\text{NH}_4^+ + 2\text{OH}^- + 2\text{H}^+ + 2\text{NaBH}_4 + 4\text{H}_2\text{O} \rightarrow \text{Pt}^0 + 7\text{H}_2 + 2\text{Na}^+ + 2\text{B}(\text{OH})_3 + 2\text{Cl}^- + 2\text{H}^+ + 6\text{NH}_3$	Global Reaction

The block copolymer was immersed in the solution for 24 h for adsorption. Then, it was removed from the previous solution, immersed in deionized water at 65 °C (6.0 ml of water per cm<sup>2</sup> of the membrane, 300 mL), and 25 mL the (NaBH<sub>4</sub>) solution was added every 30 minutes for four times. After 2 hours of the reduction process, an additional amount (75 mL) of the NaBH<sub>4</sub> solution was added to ensure that the absorbed Pt<sup>2+</sup> ions had completely reduced to Pt<sup>0</sup>. Figure 24 shows the electroless plating process and the formation of platinum electrodes on the surface of the PBMA-b-(PSS-r-PS) copolymer.

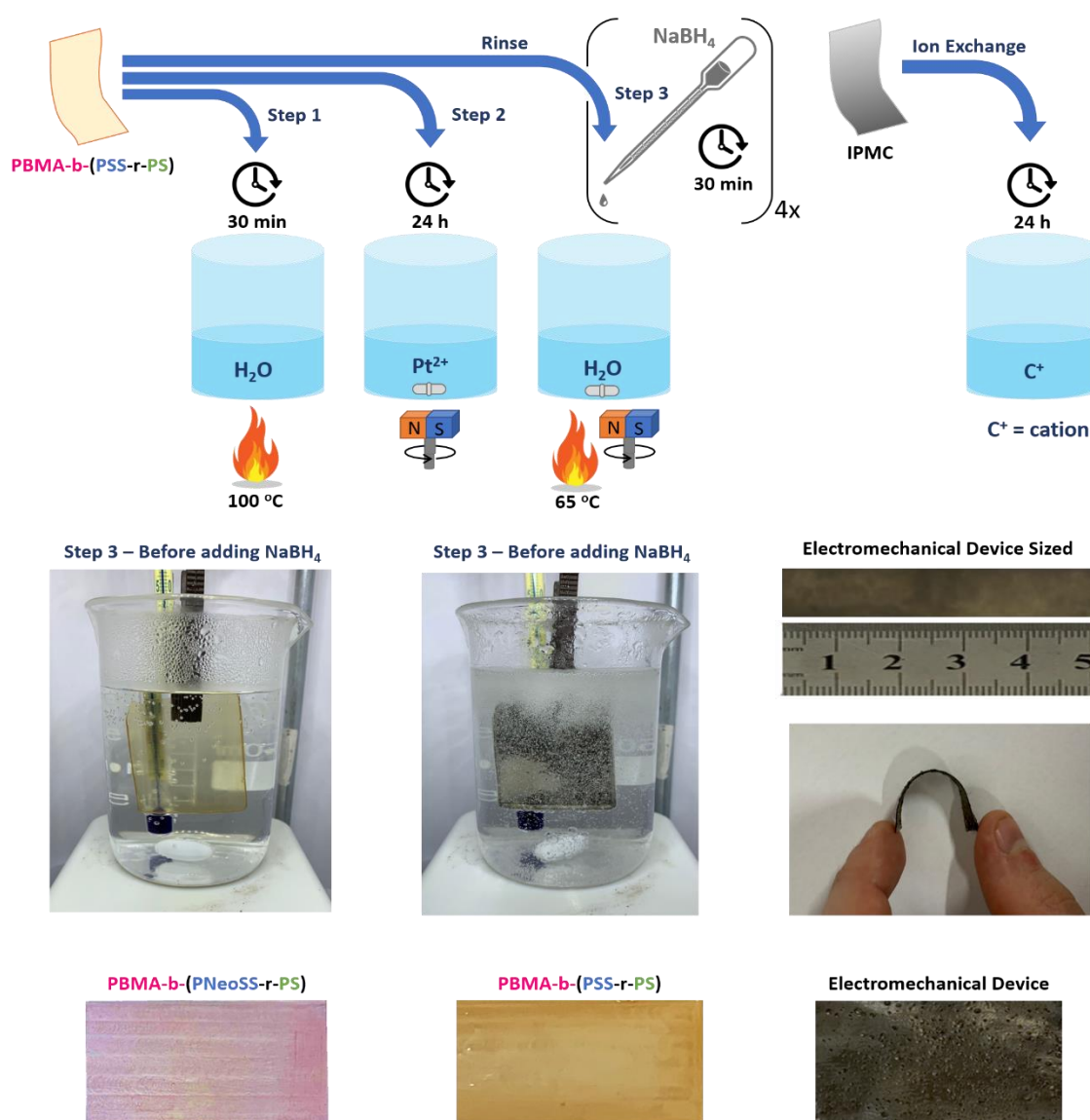


Figure 24: Step-by-step of the electroless plating process, featuring samples captured both before and after platinum reduction, resulting in the formation of metallic electrodes.

The IPMC sample was rinsed with deionized water and sized at 30.0 mm x 5.0 mm. The IPMC sample was exchanged with the desired counterion ( $H^+$ ) by soaking it in an appropriate  $0.5 \text{ mol L}^{-1}$  aqueous solution (HCl) for 24 hours at room temperature

### 3.2.7 Electromechanical system development

The electromechanical control system used to determine the electromechanical performance of the EMD is presented in Figure 25.

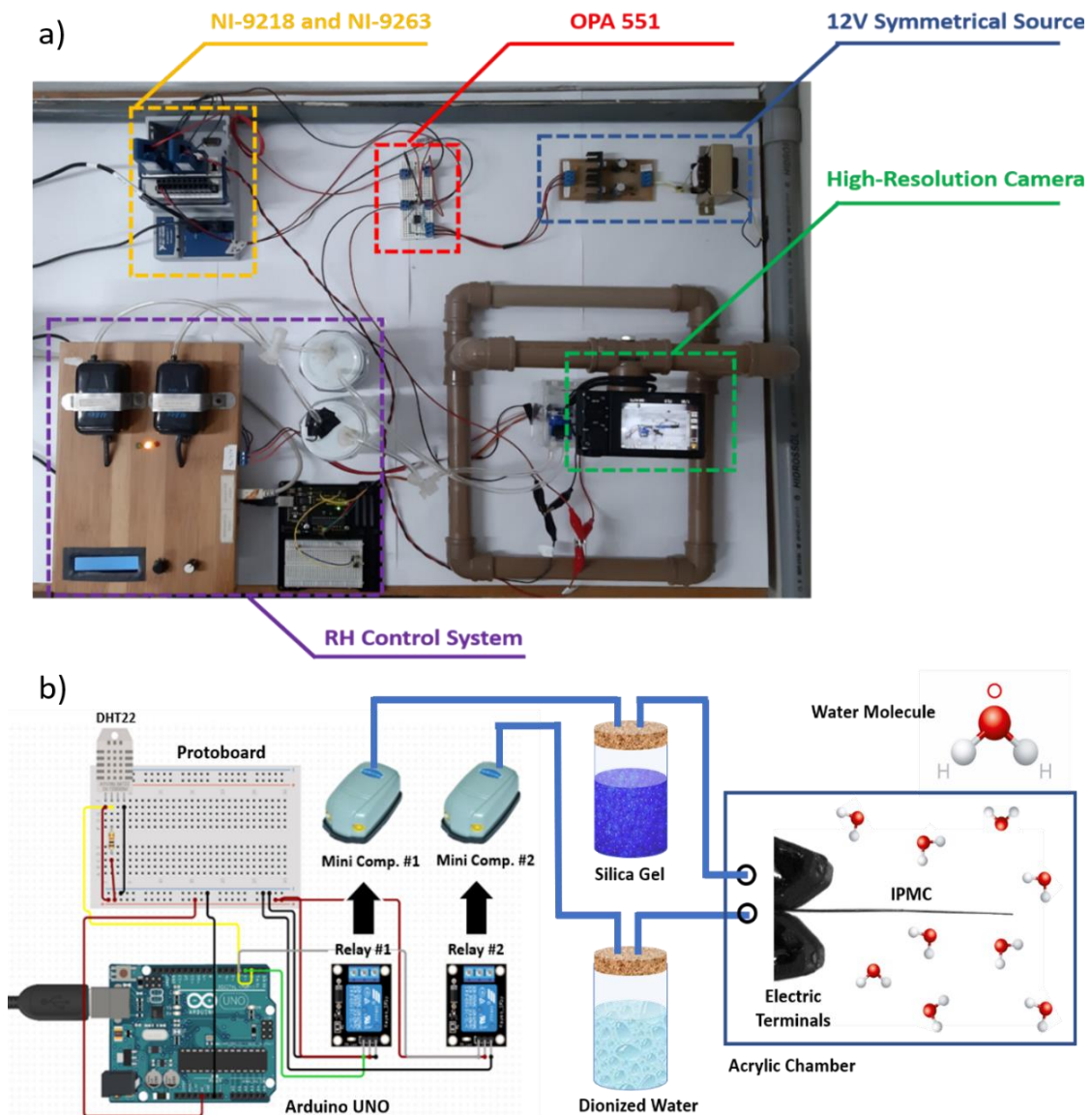


Figure 25: a) IPMC control system (top view) and b) humidity control system.

In Figure 25a, all system components are visible, whereas Figure 25b depicts a schematic of the RH control system. The entirety of the system comprises the relative humidity control system, an acrylic chamber coupled with a stepper motor (NEMA 17, 1.7 A, 4.2 kgf) (Annex A), a high-resolution camera, a computer with Laboratory Virtual Instrument Engineering Workbench (LabView), a NI-9218 data acquisition module, a NI-9263 voltage output module, a current and voltage amplifier OPA551 (Buffer), and a +12V/-12V symmetrical source (Figure 26). Each component of the system is presented in detail below.

The relative humidity control system comprises an Arduino control board, a DHT22 sensor (digital output), two air pumps (model NS350), a 2-channel relay module, a 10K ohm resistor, two glass bottles, and four flexible vinyl tubes. The vinyl tubes connect the mini-compressor, the glass bottles, and the acrylic chamber. The control board connects the relay module (operated using a 220V power source) and sensor (inside the chamber). Thus, the sensor measures the chamber RH and sends a digital signal to Arduino on the data pin.

Based on the readings taken (updated every second), the respective relay has triggered and powers up on a specific air pump that blows air through the bottle containing water or silica gel, injecting moist or dry air into the acrylic chamber respectively, keeping the RH as previously adjusted. In this manner, the samples can be characterized under varying relative humidity conditions. The software developed to control the system is presented in detail in Annex B. This system has a 1-2% humidity control accuracy, determined according to sensor limitations.

When the device is electrically tested, the samples must reach current values exceeding 200 mA, higher than the nominal value of the NI equipment. So, the implementation of a current amplifier becomes necessary. A Buffer was specifically designed to address this requirement, incorporating a voltage and current operational amplifier, namely the Texas Instruments model OPA551, in a voltage configuration. A symmetric +12V/-12V source was developed to operate the amplifier effectively, as presented in Figure 26.

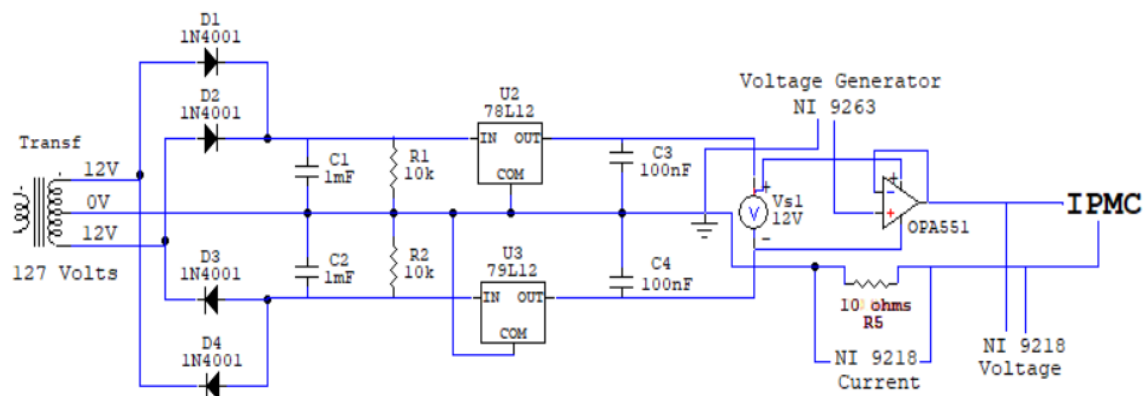


Figure 26: IPMC power source scheme.

To assemble the symmetrical source, a 12 V (12-0-12) DC transformer, four diodes (1N4001), two 1000 $\mu$ F/25V electrolytic capacitors, two 10 k $\Omega$  resistors, one positive voltage regulator (LM7812), one negative voltage regulator (LM7912), and two 100 nF capacitors were used. National Instruments modules and the electromechanical device are connected to the ground (0 V). The buffer is powered by +12V/-12V symmetrical source output. So, NI-9263 current output can be amplified, and IPMC actuation is possible. NI-9218 is responsible for acquiring current and voltage data. Likewise, under deformation, the system can capture and amplify the sensor signal.

### 3.3 Characterizations

#### 3.3.1 Gel permeation chromatography (GPC)

GPC is a separation technique in which polymer molecules are separated based on their hydrodynamic volume, allowing the relative molecular weight and the distribution of molecular weights to be determined [268]. GPC analyses were conducted using a Malvern Viscotek TriSEC Model 302 instrument. The studies were performed at an analysis temperature of 60  $^{\circ}$ C, with a 1 mL/min flow rate. All samples were analysed in DMF containing 10 mM LiBr and the concentration was kept at 0.1% by weight of DMF.



### 3.3.2 Nuclear Magnetic Resonance (NMR)

NMR is an analytical technique used to study the structure and properties of different types of molecules. It applies a magnetic field and radiofrequency pulses to a sample, causing its atomic nuclei to resonate and emit signals containing information about the molecular structure and dynamics [269]. Accordingly,  $^1\text{H}$  NMR measurements were performed using Bruker instruments at field strengths of 500, 400, or 300 MHz for NMR experiments. The Bruker TopSpin 3.2 NMR program was used for data analysis. The experiments were conducted at a probe temperature of 297 K, with a residual internal standard  $\text{CDCl}_3$  ( $\delta$  7.26). Monomer conversion calculations were performed according to the method explained in section 4.1.

### 3.3.3 Fourier transform infrared spectroscopy (FTIR)

Overall, FTIR spectroscopy is a versatile analytical tool that uses infrared light to scan test samples, providing valuable information about the chemical composition, structure, and properties of diverse samples in a non-destructive manner [270]. Therefore, a Nicolet FT-IR Nexus instrument was employed to characterize the block copolymers before and after chemical modification by thermolysis. To perform the analysis, 1 mg of the copolymer was mixed with 150 mg of Potassium Bromide (KBr). Subsequently, 7 tons was applied to the mixture for 10 minutes to form a tablet, which was later subjected to chemical composition analysis.

### 3.3.4 Thermogravimetric Analysis (TGA)

TGA is a method used to accurately quantify and track the mass and rate of change within a sample while subjecting it to controlled variations in temperature or over a specific period within a controlled environment. This versatile technique allows for analyzing materials that undergo mass reduction or increase through decomposition, oxidation, or the release of volatile components [271]. So, the thermal properties of the copolymers were assessed using a TA (Waters) Q5000IR thermal gravimetric analyzer (TGA). TGA

experiments were performed on 2.5 mg of samples with a heating rate of 10 °C/min. The temperature range for analysis was set from 25 to 800 °C, and the experiments were conducted under a controlled nitrogen atmosphere. This analysis is crucial in determining the annealing temperature necessary to relieve internal stresses and achieve morphological equilibrium within the copolymer. Furthermore, it provides valuable insight into the temperature required for the subsequent thermolysis of PNeoSS segments.

### **3.3.5 Differential Scanning Calorimetry (DSC)**

DSC measures temperatures and heat flows associated with thermal transitions in a material. It is essential in polymer science since the heat capacity, glass transition temperature, crystallization temperature, and melting temperature can be determined [272]. DSC analyses were performed in a TA Instruments equipment, model DSC Q2000, using 7 mg of sample placed in an aluminum pan. The nitrogen gas flow was set to 50 mL min<sup>-1</sup> and the method consisted of (i) heating the sample from -10 to 200 °C, at 10 °C min<sup>-1</sup>; (ii) keeping the temperature at 200 °C for 5 min; (iii) cooling the sample from 200 to -10 °C, at 10 °C min<sup>-1</sup>; (iv) isothermal step at -10 °C for 5 min; and (v) heating the sample from -10 to 200 °C, at 10 °C min<sup>-1</sup>.

### **3.3.6 Atomic force microscopy (AFM)**

AFM is a powerful technique that enables imaging of almost any surface type, including polymers, ceramics, composites, glass, and biological samples. An AFM uses a cantilever with a sharp tip to scan over a sample surface, generating images at atomic resolution [273]. Hence, the Agilent 5500 Atomic Force Microscope/Scanning Tunnelling Microscope (AFM/STM) system was used in the tapping mode to perform morphological analysis on PBMA-b-(PNeoSS-r-PS) and PBMA-b-(PSS-r-PS) thin films deposited by Spin coating on a silicon substrate.

For that, the copolymers were solubilized in toluene (30 mg/1 mL) and deposited (150 µL) by spin coating onto the substrate that had been previously

cleaned with a piranha solution (3:1)  $\text{H}_2\text{SO}_4/\text{H}_2\text{O}_2$  for 60 minutes, washed with milli-Q water and ethanol then dried under a stream of nitrogen gas. The spin coating process was carried out for 30 seconds at 4000 rpm with an acceleration of 1500 RPM/s using the SPS Spin 150 spin coater. All samples were annealed and investigated before and after thermolysis.

### 3.3.7 X-ray reflectivity (XRR)

X-ray reflectivity (XRR) is a powerful experimental technique used to characterize thin films' surface and interface structures and multi-layered structures. In the case of block copolymers, XRR can provide valuable information about the film morphology, interfacial roughness, layer thickness, and ordering within the film [274]. The XRR measurements were conducted at a laboratory X-ray source (D8 Advance diffractometer, Bruker) at the Chair, TU Munich. The instrument was operated with a copper anode, and a monochromator was used to transmit only the  $\text{Cu K}\alpha$  contribution ( $\lambda = 1.5406 \text{ \AA}$ ). The XRR curves were analyzed with the Motofit package [275].

### 3.3.8 Grazing-incident small-angle scattering (GISAXS)

Grazing-incidence small-angle scattering (GISAS) is a highly efficient scattering technique for studying nanostructured surfaces and thin films. In GISAS, the scattered probe can be either photons, using a method called grazing-incidence small-angle X-ray scattering (GISAXS), or neutrons, through grazing-incidence small-angle neutron scattering (GISANS) [276]. This technique offers a unique advantage by providing valuable insights into the structural and morphological properties of various materials at the nanoscale. Using grazing-incidence geometry, GISAS enables precise control over the penetration depth of the probing beam, allowing researchers to focus solely on the surface and near-surface regions [277].

For GISAXS experiments, it was used an in-house instrument (Ganesha, SAXSLAB, TU Munich) at  $\lambda = 1.54 \text{ \AA}$  using a sample-to-detector distance  $\text{SSD} = 466 \text{ mm}$  with a DECTRIS area detector of  $619 \text{ (horizontal)} \times 487$

(vertical) square pixels, with a pixel size of  $172 \times 172 \mu\text{m}^2$ . An incident angle  $\alpha_i \sim 0.38^\circ$  for all polymer films, larger than the critical angles of the polymer ( $\alpha_{c,pol} \sim 0.15^\circ$ ) and the substrate ( $\alpha_{c,sl} \sim 0.22^\circ$ ) was used to ensure complete penetration of the polymer film with the X-ray beam.

### 3.3.9 Rheology

Rheological analysis is crucial in characterizing the copolymer due to its high sensitivity, originating from the large viscoelastic contrast between the domains (rigid and rubbery). This technique enables the determination of (i) the transition between ordered and disordered phases, (ii) the various ordered phases present, and (iii) the kinetics of phase transformation between the disordered and ordered phases, as well as between different ordered phases [222]. Therefore, an AR G2 Rheometer from TA Instruments was used to conduct oscillatory shear experiments under nitrogen ( $\text{N}_2$ ) convection. Measurements were taken at temperatures ranging from 150 to 220 °C, while varying frequency in the dynamic mode. A parallel plate geometry with a diameter of 25 mm and a set gap of 1 mm was used. The frequency was adjusted between 0.1 and 500 rad/s. A strain amplitude of 0.5% was maintained throughout the entire frequency range to ensure linearity. It was determined by a dynamic strain amplitude sweep to obtain the linear viscoelastic regime.

### 3.3.10 Scanning electron microscopy (SEM)

SEM is a surface imaging method in which the incident electron beam scans across the sample surface and interacts with the sample to generate backscattered and secondary electrons that are used to create an image of the sample [278]. The SEM technique is used to investigate the electromechanical device electrode morphology and, at the metal-polymer interface, it is possible to verify the electrode adhesion and its thickness. The Inspect™ scanning electron microscope model FEI S50 was used.

### 3.3.11 Water uptake (WU)

To quantify the water uptake capacity, the specimen underwent a preliminary drying process at 100°C for 24 hours in a vacuum oven. The resultant dry mass ( $W_{dry}$ ) was then determined. Following this, the copolymer was wholly submerged in milli-Q water for 24 hours at room temperature, and the mass was re-measured ( $W_{wet}$ ). Consequently, the water uptake (WU) can be calculated by taking the discrepancy between the fully hydrated membrane mass and the initial dry mass, as depicted in Equation 6:

$$WU = \frac{W_{wet} - W_{dry}}{W_{dry}} \quad (6)$$

### 3.3.12 Ion exchange capacity (IEC)

The ion exchange capacity was determined through titration with an aqueous solution of sodium hydroxide (NaOH), following the procedure described in [44]. Initially, the amphiphilic block copolymer (0.5 g) was submerged in a 2 mol L<sup>-1</sup> sodium chloride (NaCl) aqueous solution for 24 hours to exchange hydrogen ions (H<sup>+</sup>) at the sulfonic acid groups in the polymer electrolyte membranes (PEMs) with sodium ions (Na<sup>+</sup>). The solution was titrated with the NaOH aqueous solution (0.1 mol L<sup>-1</sup>), while phenolphthalein was used as a pH indicator. The IEC was calculated using the Equation 7:

$$IEC = \frac{C V}{W_{dry}} \quad (7)$$

In this equation, C represents the concentration of the NaOH solution, V denotes the volume of the NaOH solution used during titration, and  $W_{dry}$  is the weight of the dry polymer. All samples were prepared in triplicate, and the error was assessed using standard deviation. The burette utilized has an absolute error of 0.05 mL.

### 3.3.13 Ionic conductivity

The ionic conductivity was studied using EIS since it can be determined through the device's resistance response and its geometry [266], [279]–[281] according to Equation 8:

$$k = \frac{d}{R A} \quad (8)$$

Where  $k$  is the ionic conductivity ( $\text{S}\cdot\text{cm}^{-1}$ ),  $R$  is the membrane resistance ( $\Omega$ ) obtained by the EIS test through data fitting to the suitable equivalent electrical circuits,  $A$  is the IPMC area ( $\text{cm}^2$ ), and  $d$  is the membrane thickness ( $\text{cm}$ ). So, a square ( $1.0 \text{ cm} \times 1.0 \text{ cm}$ ) sample was clamped with copper contacts (with the same surface area) connected to a potentiostat/galvanostat/frequency response analyzer Palmsens4 (from PalmSens BV). The impedance spectra were collected from 1 MHz down to 100 mHz with 200 mV of AC perturbation at room temperature and RH = 90%. The EIS results were analyzed using the free software EIS Spectrum Analyzer (Research Institute for Physical-Chemical Problems Belarusian, State University). Powell's algorithm and 1000 iterations were used to adjust EIS data.

### 3.3.14 Electromechanical Performance

The ability of the electromechanical device to act as a displacement sensor was evaluated using the instrumentation described in section 3.2.7. It was used an RH = 90% during conditioning (6h before the experiment started) and characterizations. The stepper motor, which Arduino controls, was used to apply the deformation, which moves the device with controlled angulation, velocity, and acceleration. The device ( $30.0 \text{ mm} \times 5.0 \text{ mm}$ ) was clamped by two electrodes connected to the electromechanical system. A real-time video was collected using the camera positioned externally at 6.0 cm, far from the device. The data was converted in displacement as a function of time using the video analysis and modeling tool. Therefore, it is possible to measure deformation

and electrical response simultaneously. The software developed to control the system is presented in detail in Annex C, making it possible to control acceleration, speed, movement amplitude, initial position, maximum angle, and minimum angle.





## 4 RESULTS AND DISCUSSIONS

### 4.1 Synthesis of PBMA-CPADB macroinitiator

Figures 27a, 27b and 27c depict the successive stages of the polymerization process, providing valuable insights into its chemical transformation. In Figure 27a, the visual representation of the polymerization reaction highlights the critical steps and the relevant protons used to estimate monomer-to-polymer conversion. Figure 27b presents the NMR spectrum of the polymerization solution at the initial time (0h), focusing on the chemical composition of BMA. Lastly, Figure 27c illustrates the NMR spectra of the aliquots taken at distinct time intervals after the polymerization begins, enabling the polymer conversion estimation.

DMF could be used as an internal standard in this study due to its consistent concentration over time. As a result, the first integral calculation was conducted on the peak at  $\delta$  8.02 (s, 1H, -CH), which is associated with DMF and can always be considered the same. Then, it was integrated the peak at  $\delta$  6.05 (s, 1H, =CH), denoted as peak (a), with its resulting value indicating either 100% monomer or 0% conversion (Figure 27c at 0h).

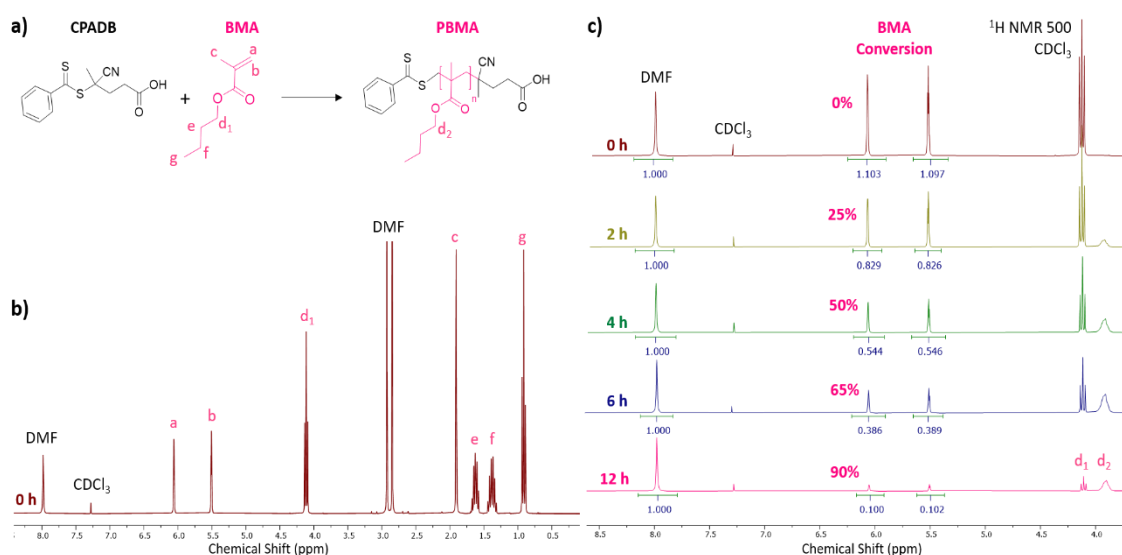


Figure 27: a) Chemical structure of the polymerization components, b) <sup>1</sup>H NMR spectrum of the polymerization solution at 0h in CDCl<sub>3</sub>, and c) <sup>1</sup>H NMR spectra of the polymerization aliquots obtained at various intervals in CDCl<sub>3</sub>.

This integral calculation was repeated after 2, 4, 6, and 12 hours. However, as the reaction progresses, it can be observed that the integral value of peak (a) decreases progressively. This decrease represents a reduction in monomer concentration during the PBMA polymerization, leading to an increase in molecular weight. By employing this method [282], the conversion can be estimated using Equation 9:

$$\text{Conversion} = \frac{a(0h) - a(Xh)}{a(0h)} \times 100\% \quad (9)$$

Where  $a(0h)$  represents the value of the integral of peak (a) before starting the reaction and  $a(Xh)$  is the value of the integral of peak (a) after  $Xh$  of polymerization. Additionally, kinetics study plays a vital role in understanding the gradual conversion of monomers into polymers over time, as depicted in Figure 28.

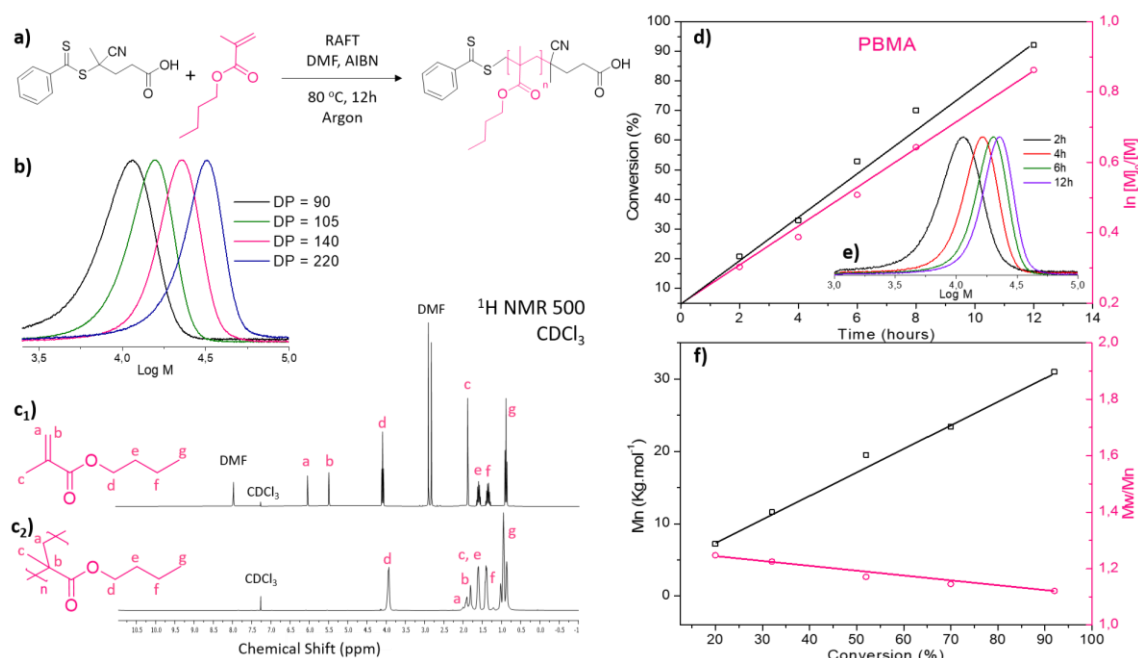


Figure 28: a) RAFT polymerization of the macroinitiator, highlighting relevant protons, b) GPC traces for PBMA-CPADB with different DP, c) NMR spectra of BMA (c<sub>1</sub>) and PBMA (c<sub>2</sub>) in CDCl<sub>3</sub>, d) Kinetic plot and conversion over time, e) GPC traces in DMF at 60 °C, and f) Mn and Đ as a function of conversion.

The overall polymerization process involves the insertion of monomers into the thiocarbonyl compound, resulting in the formation of a polymeric thiocarbonyl compound (Figure 28a) that serves as a macroinitiator for the subsequent block copolymerization [53]. Also, by controlling the reaction time and concentrations of monomer [M], chain transfer agent [CTA], and initiator [I], we successfully synthesized PBMA-CPADB macroinitiators with different molecular weights (Figure 28b).

The confirmation of macroinitiator synthesis was achieved through NMR analysis, which revealed the presence of all broad peaks associated with PBMA ( $\delta$  0.97,  $\delta$  1.45,  $\delta$  1.62,  $\delta$  1.83,  $\delta$  1.93, and  $\delta$  3.96). Furthermore, the effectiveness of the purification process was demonstrated by the disappearance of characteristic peaks related to residual monomer and solvent (Figures 28c<sub>1</sub> and 28c<sub>2</sub>). Figure 28d illustrates a well-controlled polymerization reaction characterized by the linear decrease in monomer concentration ( $\ln([M]_0/[M])$ ) over time.

This suggests the reaction follows first-order kinetics and achieves 90% conversion after 12h. By understanding this principle, one can effectively control DP by taking reaction time into account. For instance, since the conversion exhibits a linear relationship with time, if the reaction is halted after 10 hours, the expected conversion rate should be around 80%. Additionally, the predictable relationship between the average molecular weight ( $M_n$ ) and the conversion validates the controlled nature of the polymerization [140][142].

It is demonstrated by the continual increase in  $M_n$  over time, while the reduction in polydispersity from 1.30 to 1.13 (Figures 28e and 28f) provides further evidence of the absence of undesirable side reactions and improved reaction control. Notably, the absence of deviation from linearity indicates a minimal occurrence of termination events [159]. Thus, it has been observed that precise control over the [M]:[CTA]:[I] ratio allows for a well-controlled RAFT polymerization process, affecting the polymerization rate, DP, and number of active chains [161]. Table 5 presents the PBMA-CPADB macroinitiator synthesis conditions.

Table 5: PBMA-CPADB macroinitiator synthesis conditions.

Entry	DP	BMA		CPADB		AIBN		DMF	[M]:[CTA]:[I]
		(mL)	(mol.L <sup>-1</sup> )	(g)	(mmol.L <sup>-1</sup> )	(mg)	(mmol.L <sup>-1</sup> )	(mL)	
A	112	8	3.14	0.12	28.00	7.37	2.80	8	112:1:0.1
B	175	8	3.14	0.08	17.96	4.72	1.79	8	175:1:0.1
C	280	8	3.14	0.05	11.43	3.00	1.14	8	280:1:0.1

\*[M]:[CTA]:[I] = Concentrations of monomer, chain transfer agent, and initiator.

As observed, the [M] and [CTA] are crucially linked in determining the DP [53]. The concentrations of CTA and initiator also play a role in forming dead chains during polymerization since, in degenerative transfer systems, the termination of chains is related to the number of radicals present [51]. Understanding this relationship made it possible to accurately determine the necessary parameters for synthesizing a macroinitiator with the desired molecular weight, as illustrated in Table 5.

The target DP equal to 112 was intentionally set higher than the desired final DP of 90. For instance, in the case of Entry (A), the [BMA]:[CPADB]:[AIBN] = 112:1:0.1, meaning that 112 molecules of BMA react with one CPADB molecule, resulting in the formation of a PBMA with a DP of 112, assuming complete conversion. It is important to note that approximately 10% of the polymer chains are expected to be unable to continue copolymerization due to the 1.0:0.1 ratio of [CPADB] to [AIBN]. Consequently, these chains may become non-reactive and cease to grow during the polymerization process, resulting in dead chains [155][160].

However, previous experiments have demonstrated that this reaction follows first-order kinetics and can be stopped after 10 hours, achieving 80% conversion (DP = 90) with minimal termination reactions. Therefore, it was decided to target a higher DP and halt the reaction once it reached 80% conversion. Three samples of PBMA-CPADB were successfully synthesized and named according to their respective degree of polymerization. The macroinitiators with DP = 90 ( $M_n = 12800 \text{ g.mol}^{-1}$ ), 140 ( $M_n = 19900 \text{ g.mol}^{-1}$ ),

and 220 ( $M_n = 31200 \text{ g.mol}^{-1}$ ) were labeled as PBMA (90), PBMA (140), and PBMA (220), respectively.

#### 4.1.1 PBMA-CPADB RAFT proposed mechanism

The proposed RAFT mechanism for PBMA-CPADB macroinitiators is presented in Figure 29, which can be expressed in 5 steps: (i) Initiation and propagation, (ii) pre-equilibrium, (iii) reinitiation, (iv) main equilibrium, and (v) termination [51]. The reaction is thermally initiated (i) by the source of free radicals (AIBN) that breaks down to form two fragments ( $I^*$ ) that react with a single BMA molecule to produce a propagating (i.e., growing) polymeric radical, which adds more monomers, forming longer propagating radicals ( $P_n^*$ ).

At pre-equilibrium (ii), this propagating species reacts with the RAFT agent (thiocarbonyl compound  $[RSC(Z)=S]$ ), in this case CPADB, to form an intermediate RAFT radical, which can undergo a fragmentation reaction, forming a polymeric thiocarbonyl compound  $[P_nS(Z)C=S]$  and a new radical ( $R^*$ ). This is a reversible step, as the intermediate RAFT radical may lose an  $R^*$  group or the  $P_n^*$  polymer species. The reinitiation step (iii) occurs because the radical ( $R^*$ ) can react with another BMA, giving rise to a new propagation radical ( $P_m^*$ ).

The main equilibrium stage (iv) begins with this, which is the most important of the entire process. The rapid equilibrium between active propagating radicals ( $P_n^*$  and  $P_m^*$ ) and dormant polymeric thiocarbonyl compounds via the intermediate (CTA adduct radical intermediate) provides an equal chain growth probability. This occurs because the addition/fragmentation rate is higher than the propagation rate, allowing less than one monomer unit to be added per activation cycle [139].

When polymerization is complete (or stopped), most chains are dormant [i.e.,  $P_nS(Z)C=S$ ], having a terminal thiocarbonyl group, and can be isolated as stable materials. Termination processes (v) are reduced but may occur by bimolecular termination [158]. The possible termination reactions are presented below.

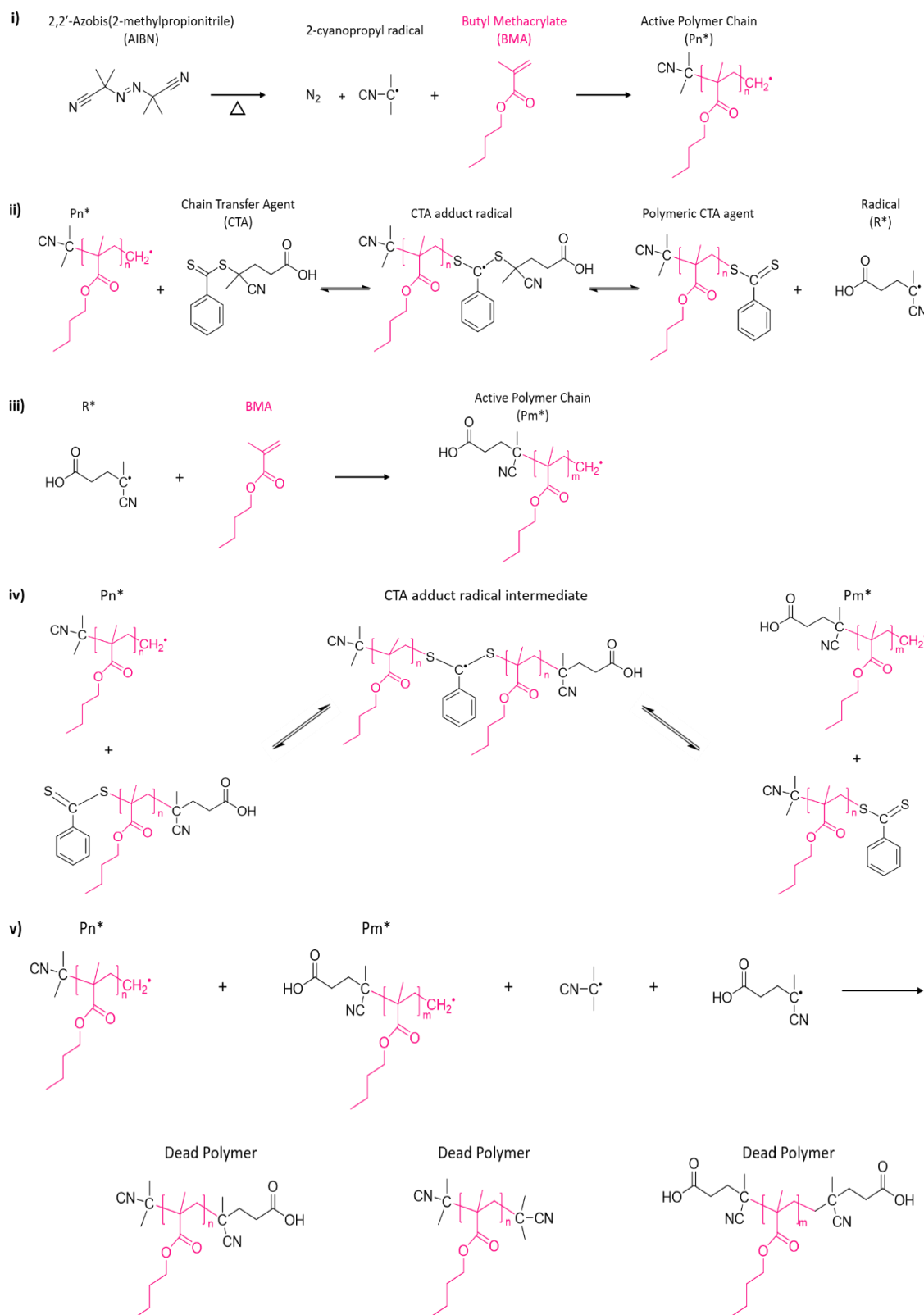


Figure 29: PBMA-CPADB macroinitiator RAFT mechanisms: (i) Initiation and propagation, (ii) pre-equilibrium, (iii) reinitiation, (iv) main equilibrium, and (v) termination.

## 4.2 Synthesis of PBMA-b-(PNeoSS-r-PS) block copolymer

Despite Sty and NeoSS having the ability to undergo simultaneous random copolymerization, their kinetics were unknown. For this reason, a test reaction was conducted to ensure the reliability of the polymerization process and verify the final product, as previously described. Figure 30a presents the overall RAFT polymerization reaction. The success of copolymerization could be reliably confirmed using NMR and GPC techniques, as demonstrated in Figures 30b and 30c, respectively.

The NMR spectrum reveals the presence of all peaks corresponding to PNeoSS, Sty, and PBMA, indicating the formation of the desired block copolymer. Precisely, the peaks at  $\delta$  0.89,  $\delta$  1.42,  $\delta$  1.83,  $\delta$  3.66,  $\delta$  6.70, and  $\delta$  7.53 correspond to PNeoSS; the peaks at  $\delta$  1.40,  $\delta$  1.83,  $\delta$  6.5, and  $\delta$  7.08 correspond to PS; and the peaks at  $\delta$  0.97,  $\delta$  1.45,  $\delta$  1.62,  $\delta$  1.83,  $\delta$  1.93, and  $\delta$  3.96 correspond to PBMA. Furthermore, the GPC traces exhibit the expected unimodal increase in molar mass for the block copolymer, indicating the absence of homopolymer impurities. This further confirms the reliability and success of the copolymerization reaction.

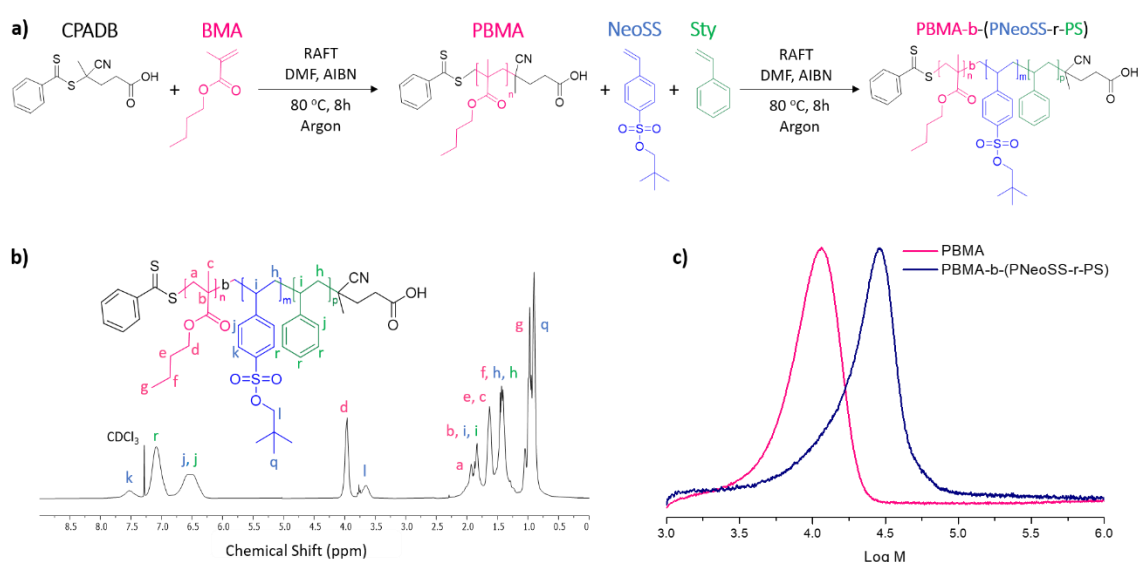


Figure 30: a) Synthesis of PBMA-b-(PNeoSS-r-PS) by RAFT polymerization, b) NMR spectroscopy of the copolymer in CDCl<sub>3</sub>, and c) GPC analysis of macroinitiator and copolymer in DMF at 60 °C.

Hence, once the viability of the reaction was confirmed, a kinetic study was performed by repeating the reaction (Figure 31). Therefore, the polymerization was carried out for 8 hours, and every 30 minutes, an aliquot of the reaction was taken to determine monomer conversion and polymerization kinetics. The polymerization kinetics were determined using the same procedure previously demonstrated for PBMA. However, in this particular case, despite the similar chemical structures, the peaks (h) corresponding to the monomers (NeoSS-  $\delta$  5.85, 5.91 and Sty -  $\delta$  5.69, 5.74) do not overlap (Figure 31b). This non-overlapping nature allows for the estimation of the conservation of each monomer independently (Figure 31c) as the reaction proceeds.

The copolymerization process involves the insertion of monomers into the polymeric thiocarbonyl compound (PBMA-CPADB) (Figure 32a), and the GPC traces exhibit the expected unimodal increase in molar mass for the copolymer (Figure 32b). This is especially significant because it guarantees the absence of substantial amounts of homopolymer in the final copolymer composition. As expected, Figures 32c and 32d illustrate a well-controlled polymerization reaction with a first-order reaction characteristic for both monomers.

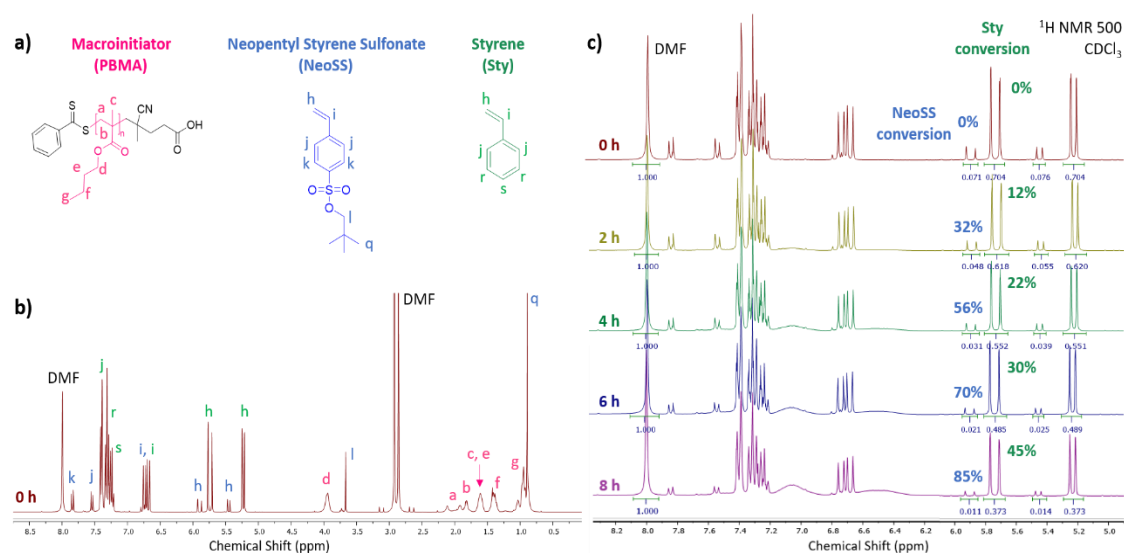


Figure 31: a) Macroinitiator, Sty, and NeoSS chemical structure, b) NMR spectrum of the polymerization solution at 0h, and c) NMR spectra of the polymerization aliquots obtained at various intervals.



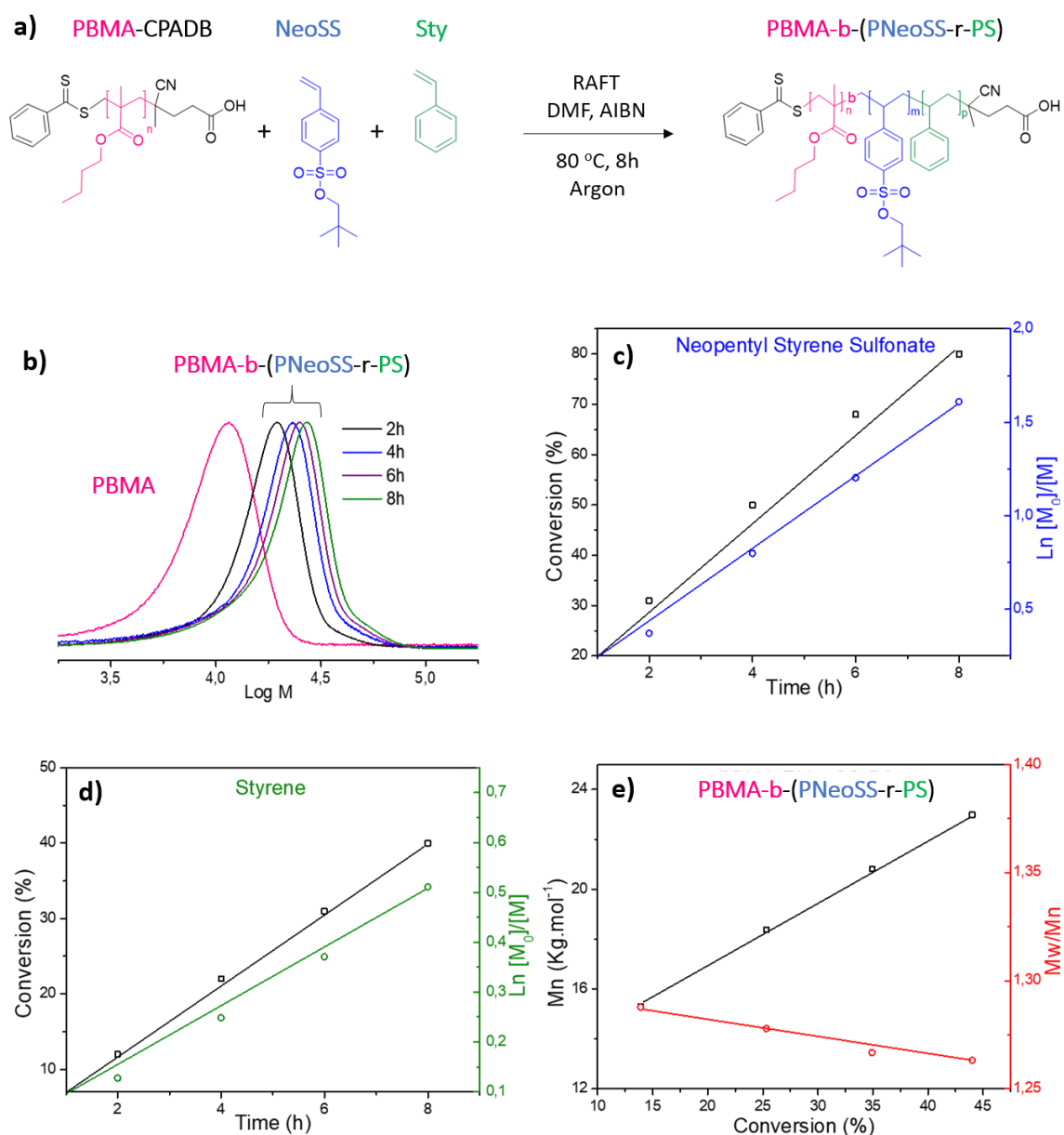


Figure 32: a) PBMA-b-(PNeoSS-r-PS) RAFT polymerization reaction, b) GPC traces in DMF at 60 °C, c) NeoSS kinetic plot and conversion over time, d) Sty kinetic plot and conversion over time, e) PBMA-b-(PNeoSS-r-PS) Mn and  $\bar{M}_w/\bar{M}_n$  as a function of conversion.

However, it has been shown that NeoSS conversion is twice greater than Sty apart from similar chemical structures, 80% and 40% after 8 hours, respectively. Moreover, the predictable relationship between the average molecular weight ( $M_n$ ) and the conversion validates the controlled nature of the

random copolymerization [139][142]. Besides, the absence of deviation from linearity indicates a minimal occurrence of termination events.

To achieve a well-controlled RAFT polymerization, it was crucial to have precise control over the [NeoSS]+[Sty]:[PBMA-CPADB]:[AIBN] ratio for the block copolymer. The same strategy used to synthesize the homopolymer was employed to ensure this, targeting a higher degree of polymerization than the desired final DP for both monomers and stopping the reaction at 80% conversion. Doing so made it possible to accurately determine the necessary parameters for synthesizing 12 distinct copolymers, each with varying molecular weights, sizes of rigid and flexible blocks, and degrees of sulfonation, as indicated in Table 6.

Table 6: PBMA-b-(PneoSS-r-PS) copolymer synthesis conditions.

Entry	NeoSS		DP	Sty		DP	AIBN		DMF	[M]:[CTA]:[I]
	(g)	(mol.L <sup>-1</sup> )		(mL)	(mol.L <sup>-1</sup> )		(mg)	(mmol.L <sup>-1</sup> )	(mL)	
1	0.44	0.46	20	1.76	4.1	178	2.10	3.45	1.50	198:1:0.15
2	0.17	0.32	14	0.69	2.82	122	1.21	3.45	1.25	136:1:0.15
3	0.56	0.61	26	1.49	3.60	156	2.04	3.45	1.50	182:1:0.15
4	0.25	0.44	18	0.66	2.57	112	1.27	3.45	1.30	130:1:0.15
5	0.62	0.49	32	2.79	4.88	326	1.80	2.25	1.50	358:1:0.15
6	0.21	0.34	22	0.95	3.40	226	1.25	2.25	1.25	248:1:0.15
7	0.68	0.62	42	2.05	4.14	276	1.60	2.25	1.50	318:1:0.15
8	0.23	0.40	27	0.68	2.66	177	0.83	2.25	1.30	204:1:0.15
9	0.54	0.46	92	2.00	3.80	760	0.57	0.75	2.00	852:1:0.15
10	0.28	0.33	33	1.32	3.46	345	0.82	0.75	1.70	380:1:0.15
11	0.53	0.49	66	1.66	3.40	452	0.78	0.75	2.00	518:1:0.15
12	0.25	0.44	44	0.77	3.00	298	0.55	0.75	1.20	342:1:0.15

\*[M] = [NeoSS]+[Sty].

As mentioned earlier, the copolymers were categorized into three distinct groups based on their molecular weights: low (Entries 1-4, approximately  $25000 \text{ g.mol}^{-1}$ ), medium (Entries 5-8, approximately  $35000 \text{ g.mol}^{-1}$ ), and high (Entries 9-12, approximately  $60000 \text{ g.mol}^{-1}$ ). Each group comprises samples with equal or variable block sizes, specifically 50/50 or 60/40 (flexible/rigid) proportions. The degree of sulfonation also varies from 8% to 12% (considering the entirety of the copolymer) or from 16 to 23% (considering only the rigid domain, PSS-PS). The control of these characteristics depends on the degree of polymerization of each monomer, and each sample has a different molecular weight, as illustrated in Table 7 and Figure 33.

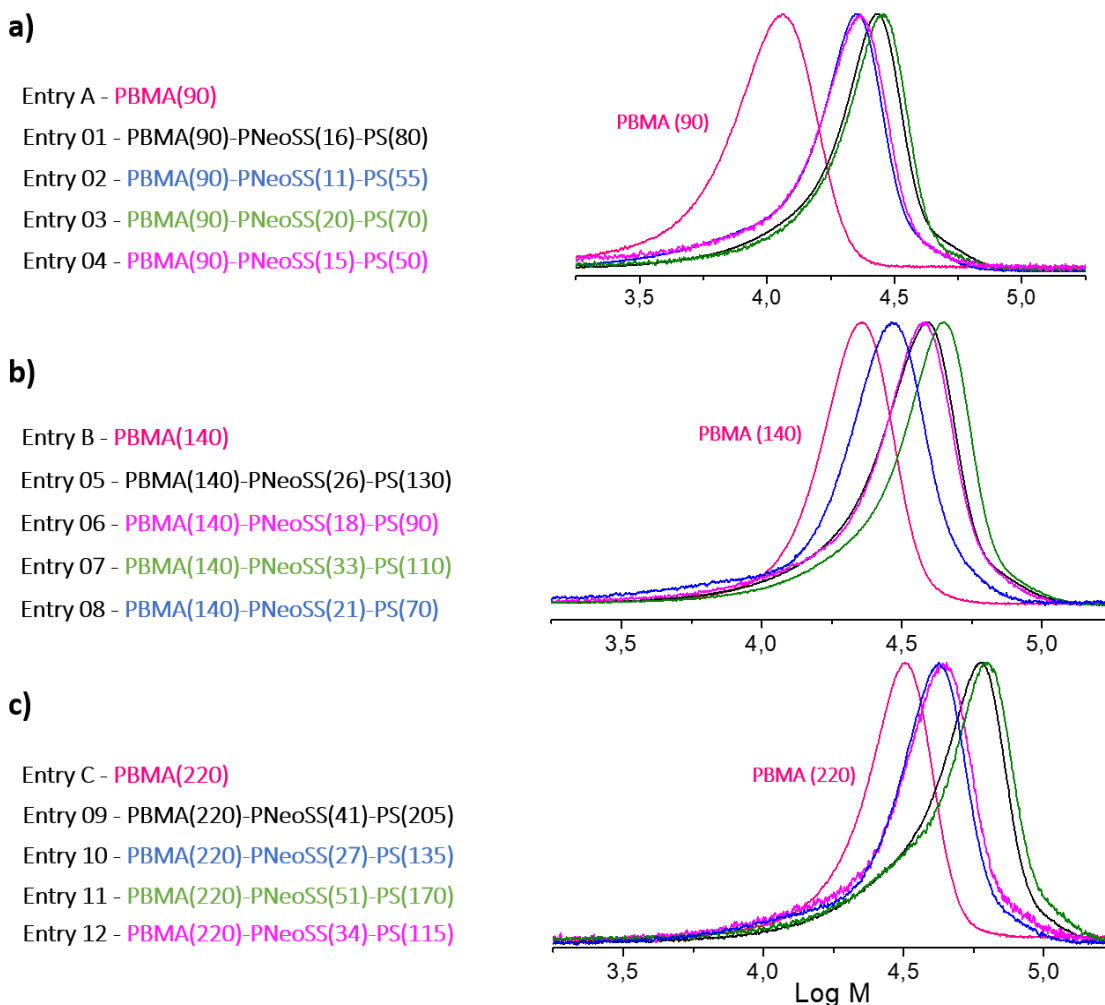


Figure 33: PBMA-b-(PNeoSS-r-PS) GPC traces in DMF at  $60 \text{ }^{\circ}\text{C}$ . a) Entries 1-4, b) Entries 5-8, and c) Entries 9-12.

Table 7: PBMA-b-(PNeoSS-r-PS) and PBMA-b-(PSS-r-PS) block copolymers library.

Entry	PBMA				PNeoSS		PS		PBMA/PNeoSS-PS		PBMA-PNeoSS-PS			PBMA-PSS-PS		PSS-PS	PBMA-PNeoSS-PS
	DP	Mn <sup>th</sup> (g.mol <sup>-1</sup> )	Mn <sup>GPC</sup> (g.mol <sup>-1</sup> )	Đ	DP	Mn <sup>th</sup> (g.mol <sup>-1</sup> )	DP	Mn <sup>th</sup> (g.mol <sup>-1</sup> )	Mn <sup>th</sup> (%)	Mn <sup>th</sup> (g.mol <sup>-1</sup> )	Mn <sup>GPC</sup> (g.mol <sup>-1</sup> )	Đ	Mn <sup>GPC</sup> (g.mol <sup>-1</sup> )	Đ	SD (%)	SD (%)	
1	90	12798	11500	1,16	16	4066	80	8332	50%	25196	19000	1,30	25000	1,25	16,67	8,60	
2	90	12798	11500	1,16	11	2795	55	5728	60%	21321	17000	1,32	19600	1,24	16,67	7,05	
3	90	12798	11500	1,16	20	5082	70	7291	50%	25171	22100	1,27	27500	1,21	22,22	11,11	
4	90	12798	11500	1,16	15	3812	50	5208	60%	21817	16500	1,26	22500	1,20	23,08	9,68	
5	140	19908	18500	1,14	26	6607	130	13540	50%	40054	33500	1,30	39000	1,25	16,67	8,78	
6	140	19908	18500	1,14	18	4574	90	9374	60%	33855	28000	1,30	32000	1,20	16,67	7,26	
7	140	19908	18500	1,14	33	8385	110	11457	50%	39750	34000	1,26	42800	1,20	23,08	11,66	
8	140	19908	18500	1,14	21	5336	70	7291	60%	32535	24000	1,30	25500	1,20	23,08	9,09	
9	220	31284	28500	1,13	41	10418	205	21351	50%	63053	58000	1,32	60000	1,24	16,67	8,80	
10	220	31284	28500	1,13	27	6861	135	14060	60%	52205	42000	1,32	46000	1,20	16,67	7,07	
11	220	31284	28500	1,13	51	12959	170	17706	50%	61949	47500	1,30	54900	1,23	23,08	11,56	
12	220	31284	28500	1,13	34	8639	115	11977	60%	51901	34700	1,30	40000	1,22	22,82	9,21	

\*DP = Degree of polymerization; Mn = Number average molecular weight; Mw = weight average molecular weight; Mn<sup>th</sup> = Theoretically estimated molecular weight; Mn<sup>GPC</sup> = Molecular weight determined by gel permeation chromatography, Đ = Polydispersity index (Mw/Mn); PBMA/PNeoSS-PS = Ratio between flexible and rigid block, SD = Sulfonation degree. The SD was calculated using the following equations:  
1 - For the overall copolymer: Number of sulfonated styrene (SSty) monomers divided by the total number of monomers (BMA + SSty + Sty).  
2 - For the rigid domain: Number of SSty monomers divided by the sum of SSty and Sty monomers.

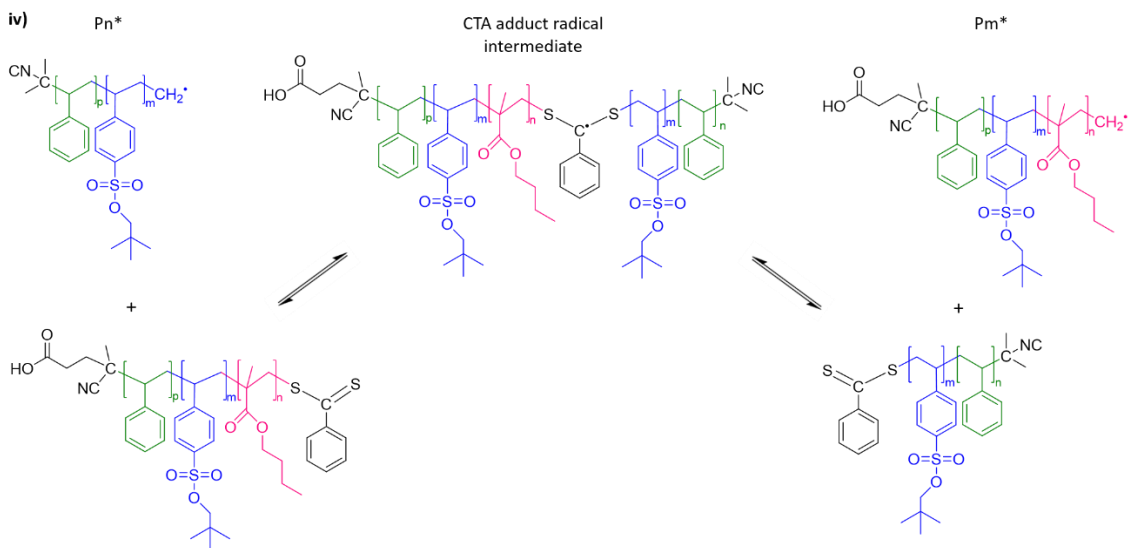
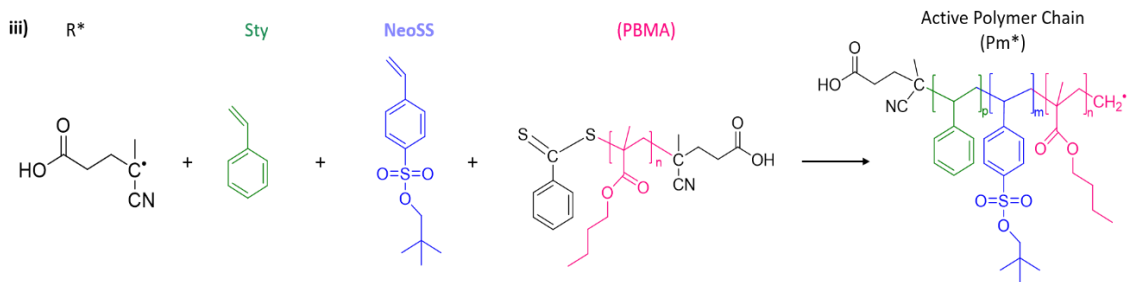
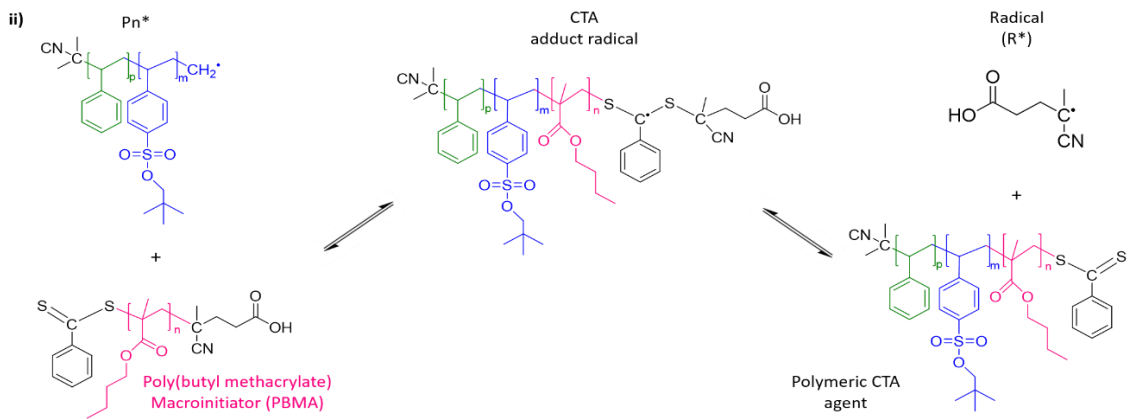
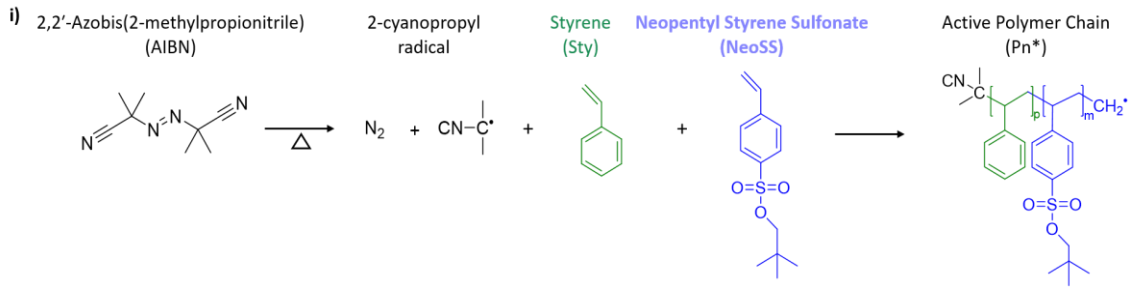
For example, Entry 01 was named PBMA(90)-PNeoSS(16)-PS(80), which means that the copolymer is composed of 90 mer of BMA, 16 mer of NeoSS, and 80 mer of Sty. In this case, the  $M_n$  of the flexible block is approximately  $12700 \text{ g.mol}^{-1}$ , and that of the rigid block is around  $12400 \text{ g.mol}^{-1}$  (PBMA/PNeoSS-PS = 50%), with a SD = 16.7% (for every five Sty units, there is one NeoSS monomer). Considering the entire copolymer, SD = 8.6% since there are 16 sulfonated monomers for a total of 186 monomers. Figure 33 shows the complete set of samples.

As expected,  $M_n$  exhibited a predictable increase following copolymerization. This trend is observed consistently across all other samples. Still, it is evident that the  $M_n$  of each group, encompassing low, medium, and high, aligns precisely with the intended specifications. Based on this, it can be confidently concluded that all samples have been successfully synthesized, exhibiting the desired characteristics, paving the way for further analyses.

#### 4.2.1 PBMA-b-(PNeoSS-r-PS) RAFT proposed mechanism

The proposed RAFT mechanism for PBMA-b-(PNeoSS-r-PS) is presented in Figure 34, which can be expressed in 5 steps [51]: (i) Initiation and propagation, (ii) pre-equilibrium, (iii) reinitiation, (iv) main equilibrium, and (v) termination [51][52]. The reaction is thermally initiated at  $80 \text{ }^\circ\text{C}$  (i) by AIBN, forming two radicals ( $I^*$ ) that react with NeoSS or Sty to produce a propagating (i.e., growing) polymeric radical, which adds more monomers (randomly NeoSS or Sty), forming longer propagating radicals ( $P_n^*$ ).

At pre-equilibrium (ii), this propagating species reacts with the PBMA-CPADB macroinitiator (polymeric thiocarbonyl compound) to form an intermediate copolymer RAFT radical, which can undergo a reversible fragmentation reaction that may create new radicals. The reinitiation step (iii) occurs because these radicals can react with another neopentyl styrene sulfonate or styrene, giving rise to a new propagation radical ( $P_m^*$ ), a propagating copolymer species. The main equilibrium stage (iv) begins with this, which is the most important of the entire process.



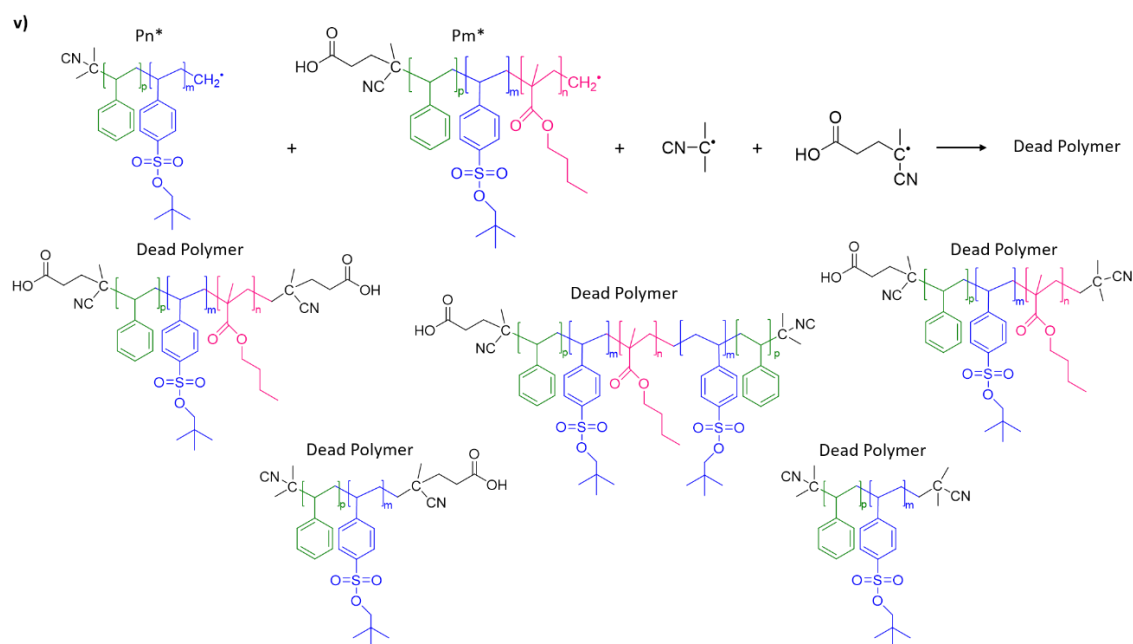


Figure 34: Copolymer RAFT mechanisms: (i) Initiation and propagation, (ii) pre-equilibrium, (iii) reinitiation, (iv) main equilibrium, and (v) termination.

In this step (iv), an equal probability of chain growth exists since equilibrium between ( $Pn^*$  and  $Pm^*$ ) and dormant polymeric thiocarbonyl compounds are very fast. Termination processes (v) are reduced but may occur by bimolecular termination. Although homopolymer formation was possible, our GPC analyses revealed no evidence of such species. This strongly suggests that their presence was effectively controlled and maintained at minimal levels.

#### 4.3 Preparation of PBMA-b-(PSS-r-PS) amphiphilic block copolymer

The thermal properties of the block copolymers were investigated to determine the most suitable method for removing the neopentyl group. This was achieved through the use of thermal gravimetric analysis (TGA) and differential scanning calorimetry (DSC), as presented in Figure 35. Thermogravimetric analysis was used to identify the temperature required for the thermolysis of the PNeoSS segment, which is a crucial step in obtaining an amphiphilic copolymer. Figure 35a illustrates the TGA results of the PBMA macroinitiator, showing the precursor samples for copolymerization.

Remarkably, the macroinitiator demonstrates exceptional thermal stability up to 200 °C. Besides, all samples tested exhibit a distinctive two-step weight loss process. The initial thermal decomposition (200–260 °C) corresponds to the scission of the C–C bond  $\beta$  to the vinyl group. Subsequently, the final step (300–350 °C) can be attributed to decomposing the remaining methoxy carbonyl side groups [283]. The copolymer was examined in Entries 1, 5, and 9 (Figure 35b). Removing neopentyl groups from PNeoSS begins at 160 °C and reaches complete removal at a higher temperature of 180 °C.

Subsequently, the PBMA-b-(PSS-r-PS) remains stable until 280 °C. Gradually, weight loss occurs between 280 °C and 480 °C due to the decomposition of the PBMA and PS backbone. The remaining weight (10%) after completion of the process is likely attributed to residue formation, resulting from the chemical reaction of the decomposed fragments in the presence of SO<sub>2</sub>, originated from the sulfonic acid group and the hydrocarbon backbone.

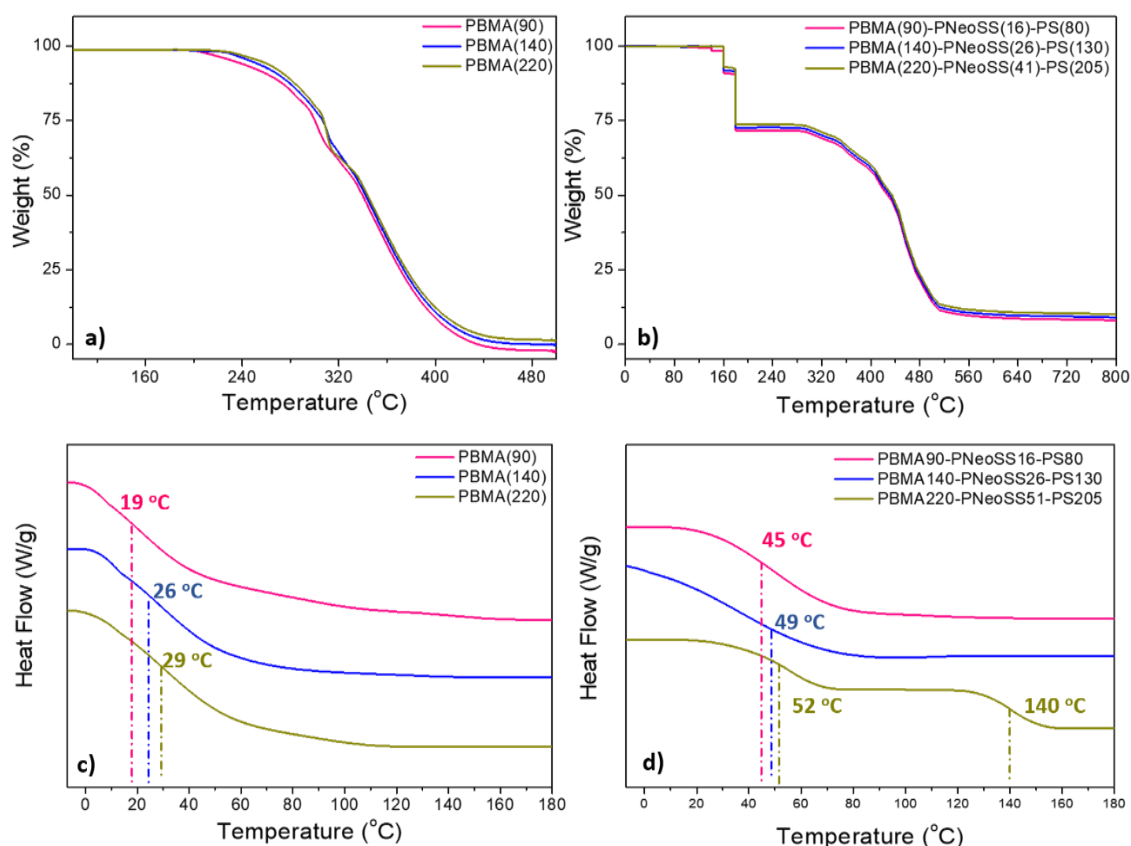


Figure 35: TGA thermograms for a) PBMA and b) PBMA-b-(PNeoSS-r-PS). DSC curves for c) PBMA and d) PBMA-b-(PNeoSS-r-PS).



The glass transition temperature ( $T_g$ ) is a crucial material property significantly influencing polymer characteristics. The primary structural factors of a polymer that affect  $T_g$  are chain stiffness and cohesive energy, leading to a complex microstructure dependence on this temperature [284]. According to DSC analysis of the homopolymers (Figure 35c), a single narrow  $T_g$  is observed for each macroinitiator, ranging from 19 to 29 °C, corresponding to the increase in molecular weight. Consistent with expectations, shorter chains exhibit increased free volume, facilitating chain mobility, leading to a lower  $T_g$  [284].

In the case of the block copolymers (Figure 35d), it was found that samples with low (PBMA90-PNeoSS16-PS80) and medium (PBMA140-PNeoSS26-PS130) molecular weights exhibited only one broad  $T_g$ . In contrast, the higher molecular weight sample (PBMA220-PNeoSS41-PS205) displayed two distinct, narrow  $T_g$ s. It is crucial to note that the  $T_g$  values are significantly lower than the thermolysis temperature. This discrepancy indicates that the glass transition temperature corresponds to the unhydrolyzed copolymer.

Morphology will be explored in greater detail in subsequent sections. However, valuable insights can be gained from DSC analyses. In the case of AB diblock copolymers, which typically form ordered structures with nearly pure A or B domains and have a very narrow interfacial width, a discrete bonded interface connecting the different phases is present [285]. For block copolymers that exhibit phase separation, a glass transition temperature for each phase is expected [286], as observed for PBMA220-PNeoSS41-PS205 copolymer. Thus, at this point, it is already possible to infer that only the high molecular weight copolymer could present phase separation. Also, an upward shift was observed in the  $T_g$  of PBMA following copolymerization. This shift arises from constrained mobility attributed to the phase structure. This shift serves as additional evidence supporting copolymerization and phase separation.

Besides, after carefully considering the thermal characterization data, it was concluded that the thermolysis procedure should be conducted at 160 °C for 1 hour, followed by an additional 1 hour at 180 °C, both under vacuum. The copolymer samples were subjected to thermolysis to validate the procedure and

subsequently analyzed using FTIR, GPC, and NMR techniques, as depicted in Figures 36a, 36b, and 36c, respectively.

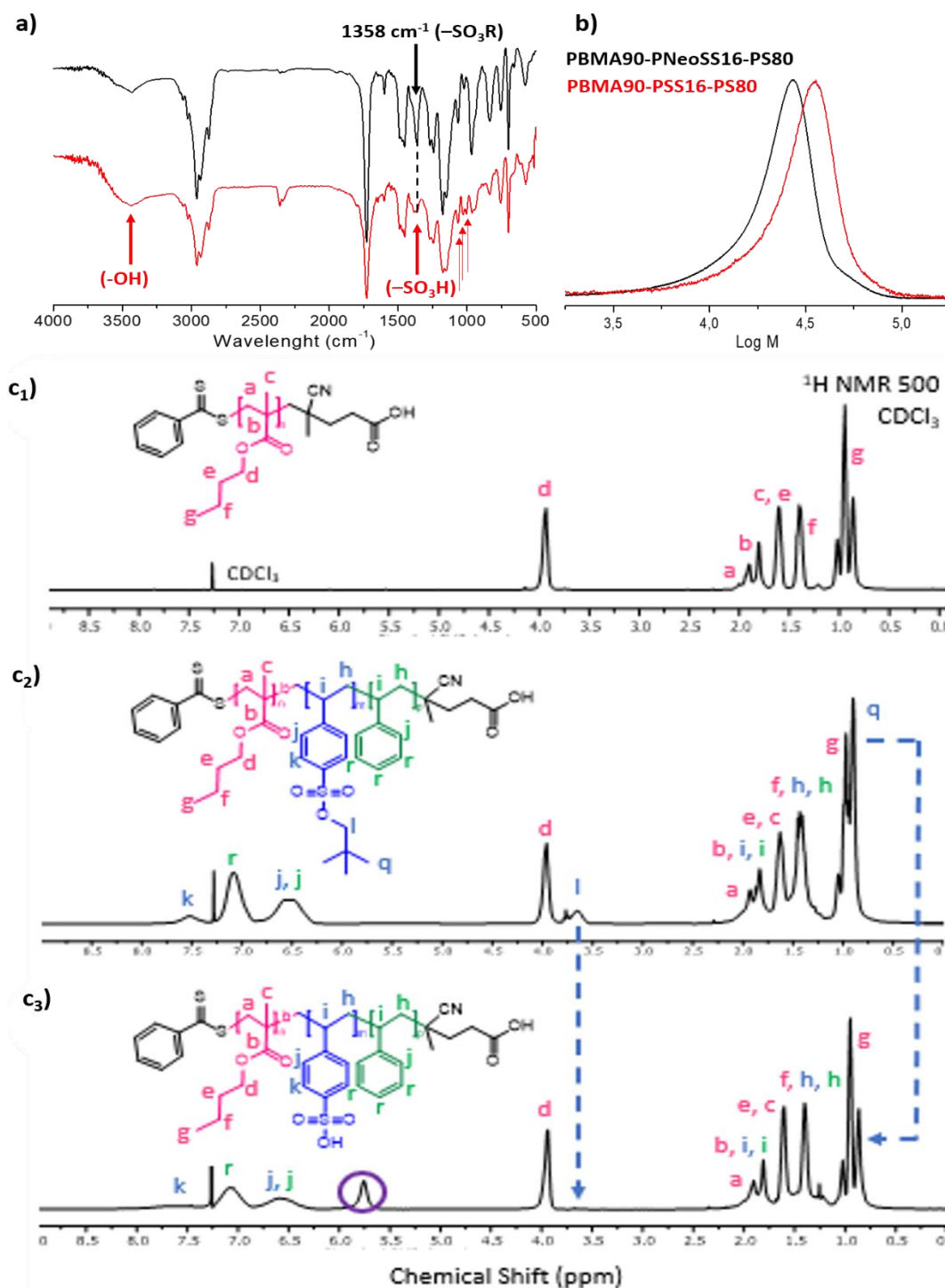


Figure 36: a) FTIR and b) GPC analysis of the copolymer before (black) and after (red) thermolysis,  $c_1$ ) PBMA,  $c_2$ ) PBMA-b-(PNeoSS-r-PS), and  $c_3$ ) PBMA-b-(PSS-r-PS) spectra in  $\text{CDCl}_3$ .

The FTIR spectra of the copolymer before (black) and after (red) thermolysis show that the sulfur ester peak ( $-\text{SO}_3\text{R}$ ) at  $1358\text{ cm}^{-1}$  in the PNeoSS is absent following thermolysis. Conversely, an elevated broad peak at  $3500\text{ cm}^{-1}$  was observed, indicating the presence of hydroxyl groups ( $-\text{OH}$ ). Furthermore, the peaks resulting from bending vibrations of the p-substituted sulfonated aromatic ring at  $1010$  and  $1128\text{ cm}^{-1}$ , as well as those resulting from symmetric and asymmetric stretching vibrations of the sulfonated groups at  $1039$  and  $1182\text{ cm}^{-1}$  [42], [43], were also noted.

Removing the neopentyl group was anticipated to lead to a decrease in  $M_n$  in the GPC-analyzed sample. However, due to the copolymer's amphiphilic nature, its hydrodynamic radius is altered, resulting in a shift towards higher  $M_n$  values, as shown in Figure 36b. Besides, GPC traces exhibit unimodal shapes, indicating the absence of chain scissions. The NMR spectra of the copolymer before and after thermolysis reveal the absence of methylene proton peaks (l) at  $\delta$  3.6 and methyl proton peaks (q) at  $\delta$  0.83 of the neopentyl group.

This last did not disappear completely; however, it is also present in the PBMA spectrum, as Figure 36c<sub>1</sub> shows. Apart from this, all other characteristic peaks of the copolymer remain unchanged. This suggests that the neopentyl group has been wholly sulfonated through deprotection, and no undesired reaction was observed. On the other hand, an artifact peak at  $\delta$  5.75 appeared in the spectra (purple circle), possibly due to interactions between the formed  $-\text{OH}$  group and  $\text{CDCl}_3$ .

Therefore, all 12 copolymers underwent a thermolysis heat treatment and subsequent characterizations to ensure complete clarity and address potential concerns. Figures 37, 38, and 39 present the FTIR spectra, GPC traces in DMF at  $60\text{ }^\circ\text{C}$ , and NMR spectra in  $\text{CDCl}_3$  and  $(\text{CD}_3)_2\text{SO}$  for all samples. As expected, in Figure 37, the FTIR spectra exhibited the disappearance of the sulfur ester peak ( $-\text{SO}_3\text{R}$ ) at  $1358\text{ cm}^{-1}$  and presented all the characteristic peaks for PBMA-b-(PSS-r-PS). Additionally, consistent with expectations, the band's intensity at  $3500\text{ cm}^{-1}$  exhibited variation across samples, owing to the differing degrees of sulfonation and quantities of PSS incorporated.

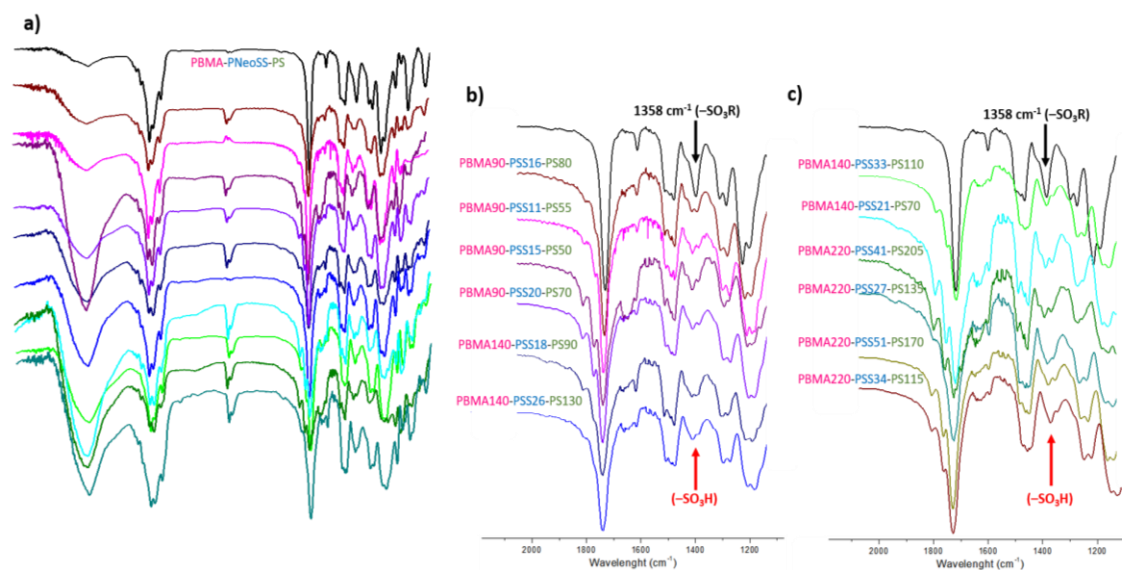


Figure 37: a) FTIR spectra for PBMA-*b*-(PNeoSS-*r*-PS) before (black) and after (colorful) thermolysis for Entries 1-12, b) image (a) amplified for Entries 1-6, and c) image (a) amplified for Entries 7-12.

Similarly, analysis conducted by GPC confirms that the presence of  $-\text{SO}_3^-$  alters the hydrodynamic radius of the copolymer when dissolved in organic solvents (Figure 38). Consequently, all the samples exhibited analogous tendencies, resulting in an upward molecular weight shift.

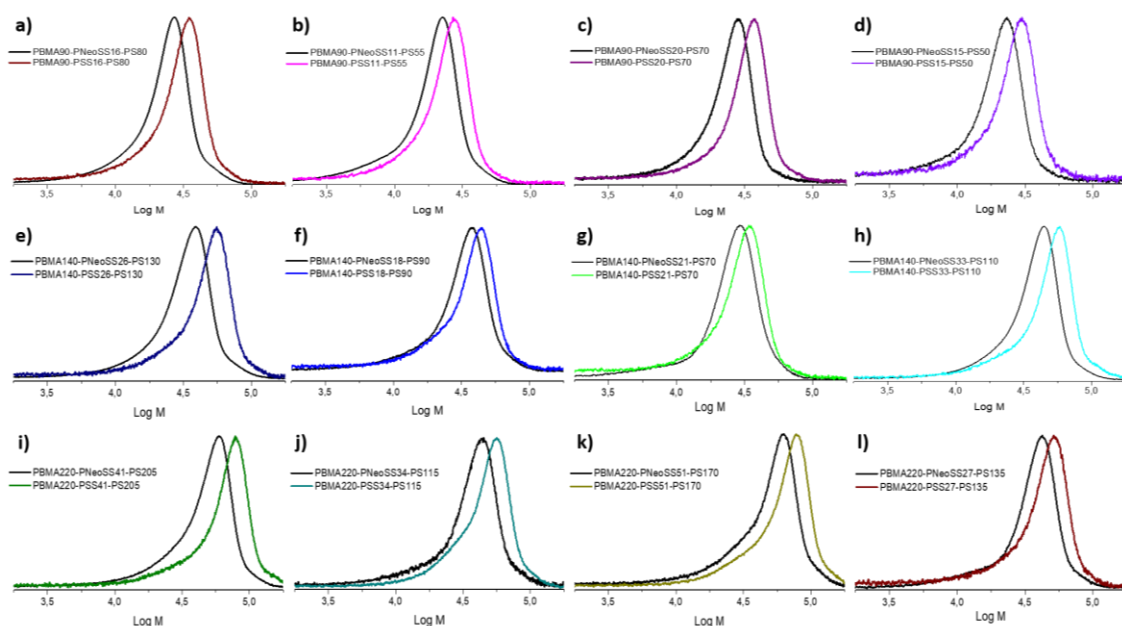


Figure 38: GPC analysis of the copolymers before (black) and after (colorful) thermolysis in DMF at 60 °C.

Besides, GPC traces exhibit the expected unimodal shape, indicating the absence of impurities or chains scission. NMR analyses used two solvents,  $\text{CDCl}_3$  and  $(\text{CD}_3)_2\text{SO}$ . The spectra obtained in  $\text{CDCl}_3$  are shown in Figure 39a, while those obtained in  $(\text{CD}_3)_2\text{SO}$  are shown in Figure 39b. It is evident that the artifact observed in Figure 36 is present in all  $\text{CDCl}_3$  samples but is not observed in  $(\text{CD}_3)_2\text{SO}$ . This observation confirms that the detected peaks stem from interactions between the hydroxyl groups and the solvent. Moreover, the chemical shift demonstrated in the interactions between the -OH groups and deuterated chloroform indicates varying levels of interaction among the samples.

This observation aligns with the findings from the FTIR analyses, providing further confirmation. Additionally, the presence of all other characteristic peaks suggests that the samples maintain their integrity without undergoing any undesirable secondary chemical reactions. These comprehensive analyses allow us to confidently conclude that the thermolysis procedure is highly successful and offers a safe means of converting the block copolymer into an amphiphilic block copolymer.

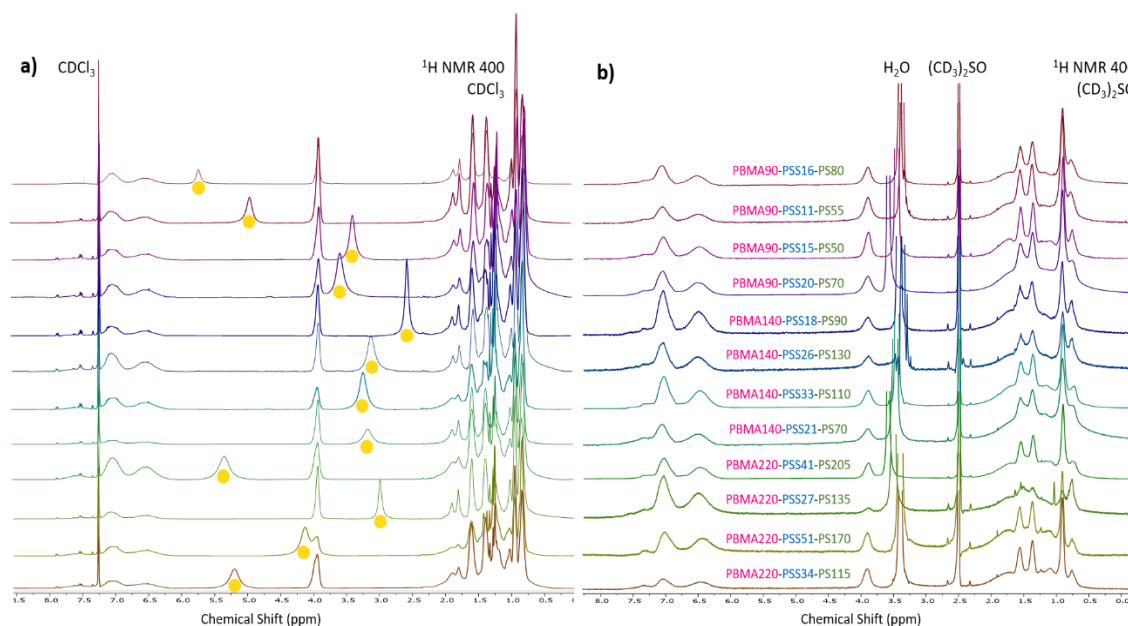


Figure 39: a) NMR spectra in  $\text{CDCl}_3$  and  $(\text{CD}_3)_2\text{SO}$  for PBMA-*b*-(PSS-*r*-PS) in DMF. The yellow circles indicate the peaks that arise due to the interactions between -OH and  $\text{CDCl}_3$ .

## 4.4 Morphological Characterization

### 4.4.1 Atomic force microscopy (AFM)

To examine the morphologies of the copolymers, AFM was employed in the tapping mode to obtain high-resolution images of the film's surface, allowing for the analysis and characterization of the copolymer morphologies. All samples were analyzed; however, since copolymers with similar molecular weights exhibited similar morphologies, only the first representative sample from each group will be presented.

Figures 40, 41, and 42 illustrate the AFM images of Entry 1 (low molecular weight), Entry 5 (medium molecular weight), and Entry 09 (high molecular weight), respectively. All figures present the copolymer's topography (2D and 3D), phase (2D and 3D), and profile images for enhanced clarity and understanding. Simple homopolymer mixtures phase-separate macroscopically; however, the covalent bonding in block copolymers restricts the size scale of the phase separation to the polymer chain dimensions, typically tens of nanometers. In this case, the relative lengths of the blocks dictate if the copolymer phase separates and its morphology [287].

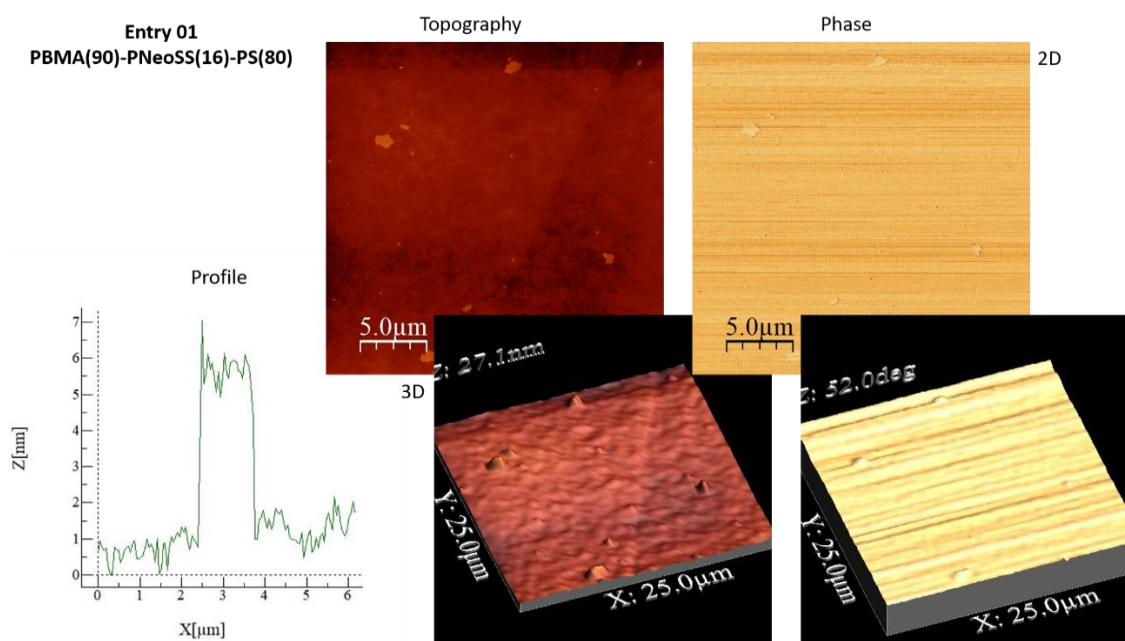


Figure 40: AFM images for Entry 01, presenting the topography in 2D and 3D, phase 2D and 3D, and profile.



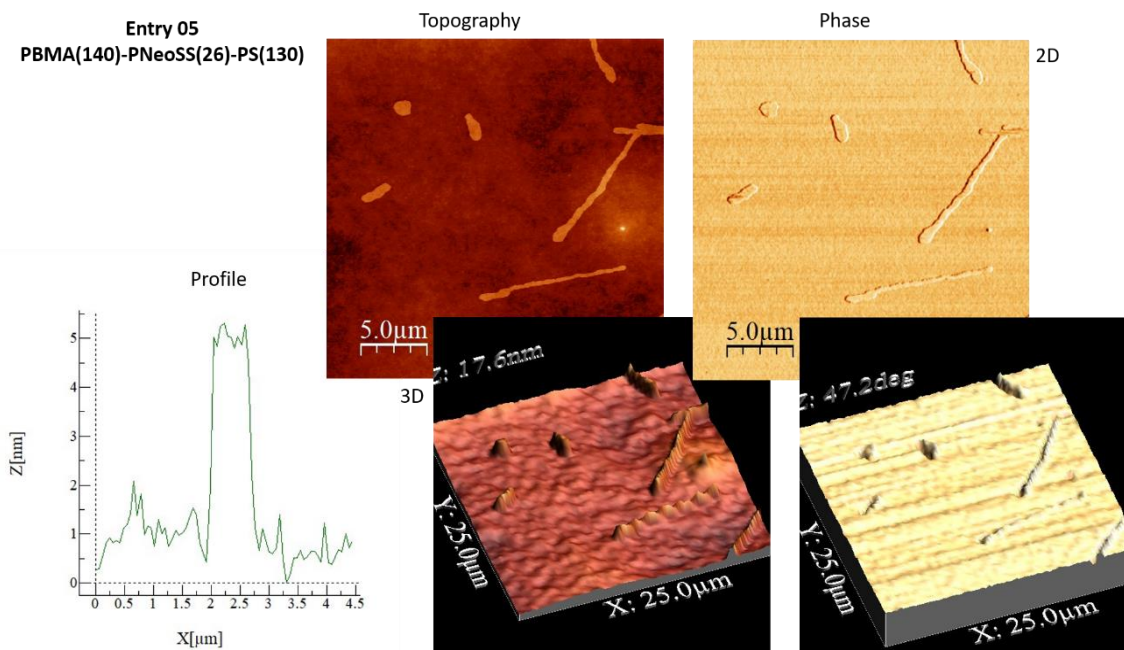


Figure 41: AFM images for Entry 05, presenting the topography in 2D and 3D, phase 2D and 3D, and profile.

The figures depict this behavior and the gradual transformation in surface structures, which correlates with the variation in molecular weight. Figures 40 and 41 present a large-scale view of the free surface of the copolymer film with low and medium molecular weight (Entry 01 and Entry 05), respectively. Notably, it displayed compact structures of a rounded shape, approximately measuring 1 micrometer in diameter and 5 nanometers in height. Conversely, Entry 05 exhibited elongated structures of around 10  $\mu\text{m}$  in length and 5 nm in height.

In these two cases, the phase images complement the standard topography images and offer distinctive contrast based on variations in material stiffness. So, these structures, which most likely indicate the rigid phase of PNeoSS-PS, tend to appear lighter in the shade. In these cases, it becomes evident that the copolymer is phase-mixed rather than exhibiting an ordered phase separation. It is crucial to note that phase separation is expected to occur below the  $T_{ODT}$  for this block copolymer. However, the absence of such phase separation can be attributed to the insufficient value of  $N$  (or DP) [202]. Thus, repulsive interactions between the blocks are not strong enough, leading to a

convergence of mixed phases. On the other hand, some degree of segregation is likely occurring in some areas of the sample.

Figure 42 presents a large-scale view of the free surface of the copolymer film with high molecular weight (Entry 09), showcasing distinct relief domains with circular shapes on their free surface, containing a diameter of 10  $\mu\text{m}$  and a height of 27 nm. These structures are in accordance with ordered symmetric copolymer films deposited on a flat solid substrate, which display relief circular domains at their free surface [288], [289]. The presence of these domains is a direct consequence of the lamellar structure, which appears spontaneously when the sample temperature is below the  $T_{\text{ODT}}$ .

Therefore, phase separation in Entry 09 can be attributed to the significant difference in chain lengths, resulting in repulsive interactions between the chains and causing phase separation. This result is in agreement with the findings from the DSC investigation. In the DSC analysis, only Entry 09 exhibited two distinct  $T_g$ s, each corresponding to a specific phase. This observation suggests that the phases are indeed present and organized in a structured manner, as confirmed by AFM.

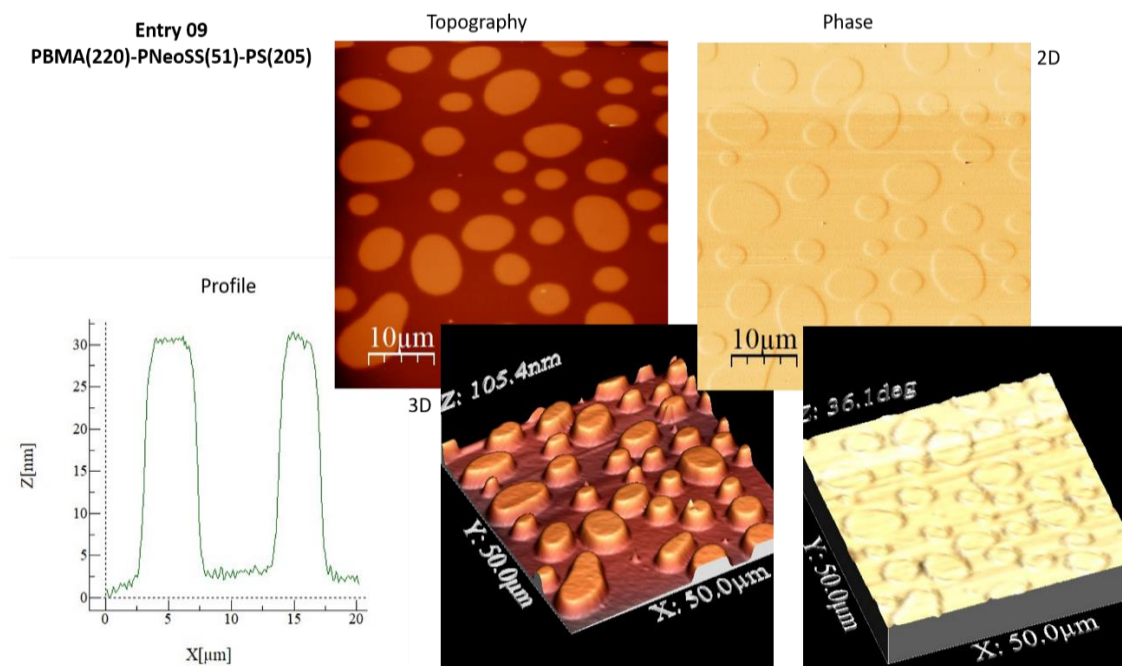


Figure 42: AFM images for Entry 09, presenting the topography in 2D and 3D, phase 2D and 3D, and profile.



Finally, Figure 43 showcases a large-scale view of the copolymer film's free surface, specifically for Entry 09, following thermolysis. Significant changes in the copolymer's morphology were observed, primarily attributed to the sulfonated groups' hydrophilic nature. Consequently, there was an evident enhancement in chemical incompatibility between the domains, facilitating phase separation and allowing for the coalescence of the PSS-PS blocks. Similarly, the spacing between the domains remained unchanged (27 nm) as the morphology continued to exhibit a lamellar structure, and there were no notable alterations in the sizes of the rigid and flexible blocks following thermolysis, as anticipated.

The findings demonstrate that a block copolymer containing a precisely defined domain containing sulfonic acid groups can readily be obtained through a straightforward heating process from neutral PBMA-*b*-(PNeoSS-*r*-PS). This direct transformation is distinct from what is achievable with polar block copolymer systems, primarily due to their disparate solubility characteristics. This distinction holds particularly true for highly sulfonated block copolymers [43]. Complementary analyses were conducted employing X-ray reflectivity and grazing-incident small-angle X-ray scattering, the results of which are presented below.

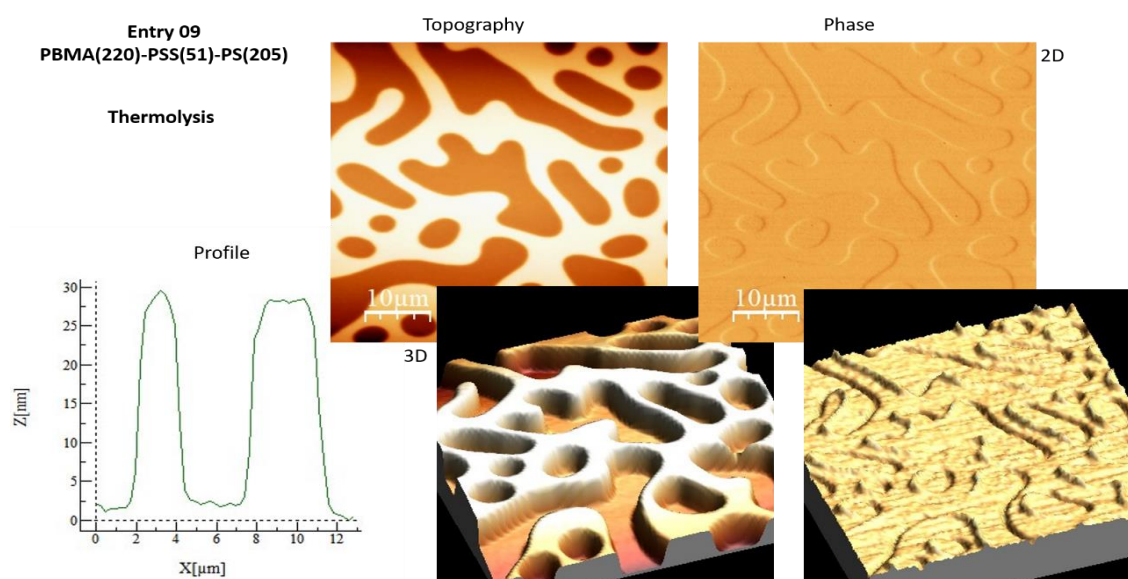


Figure 43: AFM images for Entry 09 after thermolysis, presenting the topography in 2D and 3D, phase 2D and 3D, and profile.

#### 4.4.2 X-ray reflectivity and Grazing-incident small-angle X-ray scattering

In combination, XRR and GISAXS offer a comprehensive understanding of the morphology of block copolymer thin films, including both the vertical and lateral organization of polymer domains. XRR provides information about the layering and density profile perpendicular to the film surface, while GISAXS offers insights into the nanoscale structure and ordering within the film plane. By correlating the information obtained from both techniques, it is possible to elucidate the relationship between film morphology, composition, and functionality in block copolymer systems [290], complementing the AFM data.

Figure 44 shows the XRR and GISAXS data for the PBMA-*b*-(PNeoSS-*r*-PS) block copolymer. Figure 44a plots the XRR data, reflectivity ( $R$ ), as a function of the wavevector transfer ( $q_z$ ) against  $q_z$ . The experimental data (black circles) was fitted (red line) using the MOTOFIT software [275]. Figure 44b presents the Fast Fourier Transform (FFT) analysis of the XRR data using the REFLEX software [291]. Figure 44c depicts the GISAXS scattering length density (SLD) profile vs. distance away from the Si substrate ( $z$ ), showing the different polymer layers ((a) to (f)) arranged parallel to the Si substrate. In Figure 44d, the experimental (left) and simulated (right) panels for GISAXS patterns are displayed as  $\alpha_f$  (information across the sample's plane) vs.  $2\theta_f$  (information along the sample's plane) is shown. GISAXS simulations have been performed using the BornAgain software [292]. Finally, Figure 44e presents a sketch of modelled architecture using BornAgain software.

When subjecting a block copolymer with a well-defined morphology to X-ray scattering experiments, the periodic arrangement of its domains typically results in the emergence of Bragg peaks in the scattering pattern [293]. However, in Figure 44a, these characteristic peaks are notably absent. The absence of Bragg peaks in the X-ray Reflectivity (XRR) data suggests two possible scenarios: either a single layer exists or multiple layers with varying thicknesses. Upon examining the Fast Fourier Transform (FFT) analysis presented in Figure 44b, which highlights principal components of thicknesses within the sample, a prominent peak corresponding to the total thickness is observed alongside additional peaks exhibiting intensities exceeding 10% of the

maximum peak's intensity. This observation suggests that the sample comprises a multilamellar system.

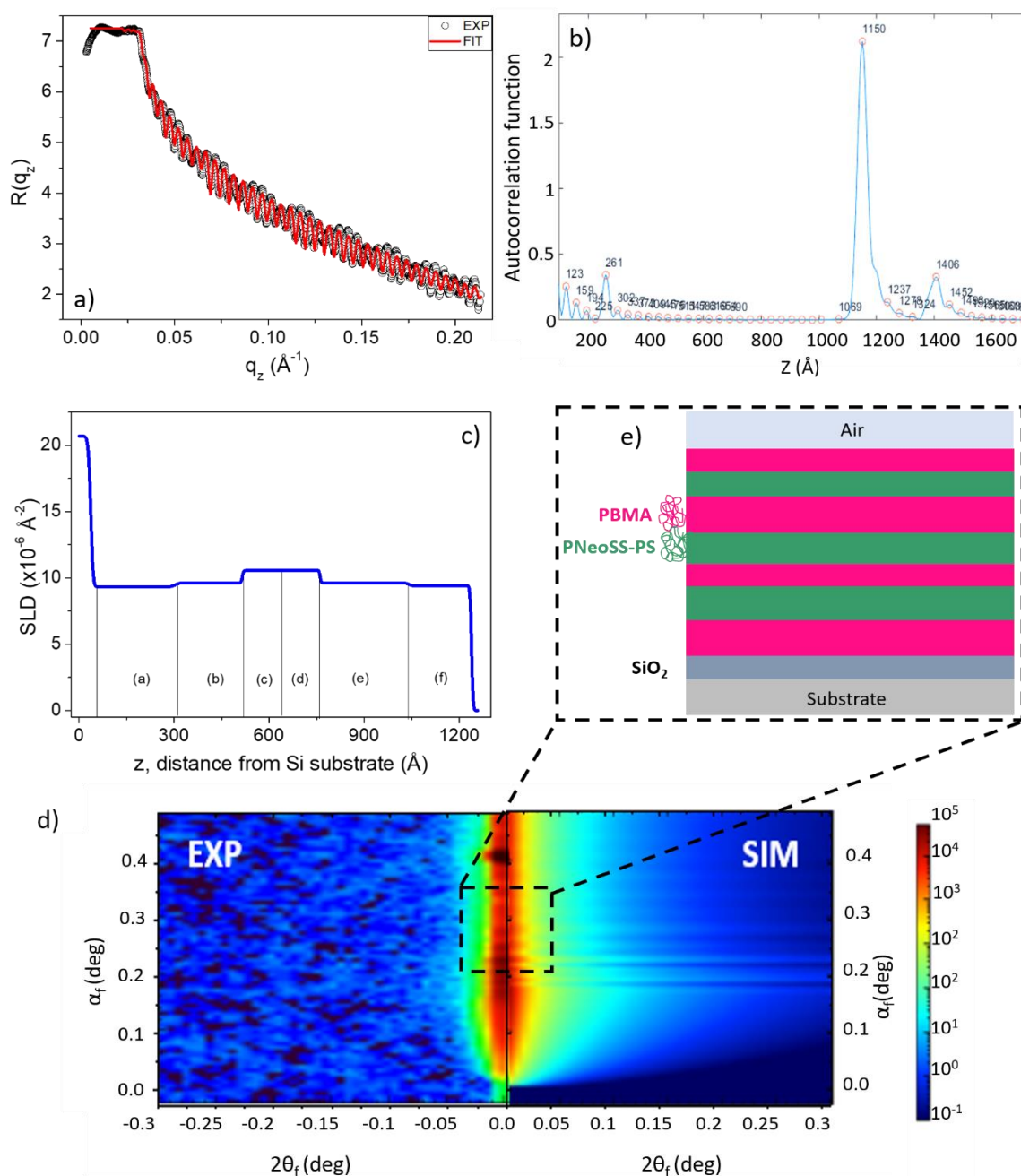


Figure 44: a) XRR data,  $R(q_z)$  vs.  $q_z$ . Experimental data (black circles) and fit (red line), b) Fast Fourier Transform (FFT) analysis, c) Scattering length density (SLD) profile vs. distance away from the Si substrate ( $z$ ), d) Experimental (left) and simulated (right) panels for GISAXS patterns. The intensity scale bar spans the range from 0.5 to  $5 \times 10^5$ , and e) Sketch of modelled architecture using BornAgain software.

This is confirmed by analyzing the SLD profile (Figure 44c), revealing the presence of different layers within the sample. Variations in SLD correspond to different polymer layers, and the regularity of these variations reflects the degree of order within the film [294]. The presence of variabilities in both lamellar thicknesses and scattering length densities (SLDs), as depicted in Figure 44c, provides conditions favorable to the absence of Bragg peaks. Such variabilities effectively mask the presence of Bragg peaks that would typically manifest in the case of perfectly uniform lamellae thicknesses and consistent scattering length densities of the polymer blocks [295]. Table 8 summarizes the extracted data from the XRR fit for PBMA-b-(PNeOSS-r-PS) block copolymer. The layer (f) corresponds to the topmost layer at the air-polymer interface (values in (\*) denote fixed parameters).

Furthermore, Figure 44d presents both experimental (left) and simulated (right) panels for GISAXS patterns. It reveals distinct intensity stripes at regular intervals along the out-of-plane axis, providing clear evidence of a lamellar morphology oriented parallel to the substrate [296]. It's important to note that the sketched pattern is obtained within the validity of the Born-Approximation. This implies that the incident angles and scattering angles are sufficiently above the critical angles of both the film and substrate as used. To complement these findings, Table 9 provides a summary of extracted data from the GISAXS simulations, providing the layer thickness, the surface roughness ( $\sigma$ ), the Hurst exponent [292], and the correlation length (or root mean square roughness).

Table 8: Summary of extracted data from the XRR fit for PBMA-b-(PNeOSS-r-PS) block copolymer.

Layer	Thickness (Å)	SLD <sub>real</sub> ( $\times 10^{-6} \text{Å}^2$ )	SLD <sub>imag</sub> ( $\times 10^{-6} \text{Å}^2$ )*	Roughness (Å)
(f)	198 (*)	9.42	$7 \times 10^{-3}$	$3.75 \pm 1.19$
(e)	280 (*)	9.613	$7 \times 10^{-3}$	6(*)
(d)	134.6(*)	10.58(*)	$7 \times 10^{-3}$	2.88(*)
(c)	110.6(*)	10.54(*)	$7 \times 10^{-3}$	4.7(*)
(b)	211(*)	9.62(*)	$7 \times 10^{-3}$	3.0(*)
(a)	267(*)	9.33(*)	$7 \times 10^{-3}$	9.4(*)

\* Fixed parameters.

Table 9: Summary of extracted data from the GISAXS simulations using the BornAgain software for PBMA-b-(PNeoSS-r-PS) block copolymer.

Layer	Thickness (Å)	$\sigma$ (Å)	Hurst	Correlation length (Å)
(f)	200 (*)	5	0.80	2000 (*)
(e)	280 (*)	6	0.85	2000 (*)
(d)	140(*)	3	1.00	2000 (*)
(c)	110(*)	5	0.30	2000 (*)
(b)	210(*)	1	0.90	2000 (*)
(a)	260(*)	1	0.90	2000 (*)

\* Fixed parameters.

Exploiting this dataset, a sketch representing the modeled architecture was prepared using BornAgain software (depicted in Figure 44e). It presents layers ordered parallel to the substrate with distinct sizes. Also, a SiO<sub>2</sub> layer with a thickness of 5 Angstrom and roughness of 5 Angstrom is observed for all samples. It may result from the cleaning step using piranha solution. Overall, we can confidently assert that the sample exhibited lamellar phase separation before heat treatment for neopentyl group removal. The variation in block sizes observed is likely attributable to the variable sizes of the blocks themselves. Likewise, analyzing the sulfonated copolymer is essential to elucidate its morphology.

Figure 45 shows the XRR and GISAXS data for the PBMA-b-(PSS-r-PS) block copolymer. All parameters and data treatment were similar to PBMA-b-(PNeoSS-r-PS). Similar to the observations in Figure 44a, the absence of Bragg peaks is notable in Figure 45a. This outcome was anticipated, given the prior confirmation of the existence of blocks with varying sizes. However, an intriguing increase in reflectivity amplitude is discernible in the  $Z = 0.5$  Å region. This likely correlates with changes in chemical composition. The substantial difference in scattering length density data (Figure 45c) supports this interpretation. As the block's chemical incompatibility intensifies post-thermolysis, the contrast between the phases becomes more pronounced,

leading to an escalation in SLD. Table 10 summarizes the extracted data from the XRR fit for PBMA-b-(PNeoS-r-PS) block copolymer.

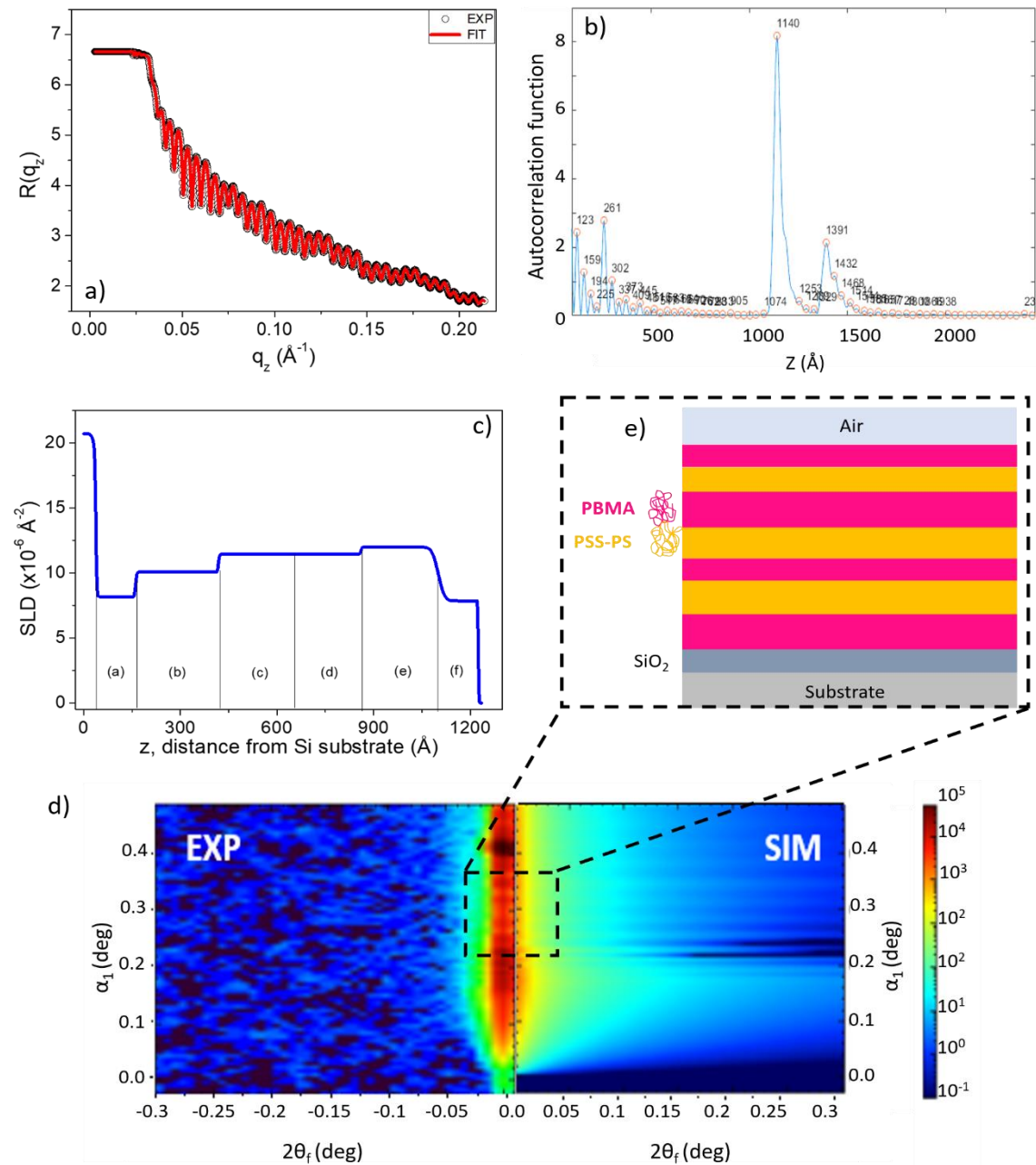


Figure 45: a) XRR data,  $R(q_z)$  vs.  $q_z$ . Experimental data (black circles) and fit (red line), b) Fast Fourier Transform (FFT) analysis, c) Scattering length density (SLD) profile vs. distance away from the Si substrate ( $z$ ), d) Experimental (left) and simulated (right) panels for GISAXS patterns. The intensity scale bar spans the range from 0.5 to  $5 \times 10^5$ , and e) Sketch of modelled architecture using BornAgain software.

Table 10: Summary of extracted data from the XRR fit for PBMA-b-(PSS-r-PS).

Layer	Thickness (Å)	SLD <sub>real</sub> (x10 <sup>-6</sup> Å <sup>2</sup> )	SLD <sub>imag</sub> (x10 <sup>-6</sup> Å <sup>2</sup> )*	Roughness (Å)
(f)	124 ± 3	7.84 ± 0.88	7x10 <sup>-3</sup>	1.4(*)
(e)	240 (*)	11.975 (*)	7x10 <sup>-3</sup>	1.5(*)
(d)	204 (*)	11.5(*)	7x10 <sup>-3</sup>	2.4(*)
(c)	238(*)	11.44(*)	7x10 <sup>-3</sup>	5.3(*)
(b)	257 ± 5	10.1(*)	7x10 <sup>-3</sup>	3.0(*)
(a)	124 ± 4	8.15 ± 0.53	7x10 <sup>-3</sup>	3.0(*)

\* Fixed parameters.

Furthermore, Figure 44d presents both experimental (left) and simulated (right) panels for GISAXS patterns. As expected, the results are similar, and the sample presents distinct intensity stripes at regular intervals along the out-of-plane axis. Table 11 provides a summary of extracted data from the GISAXS simulations. Using this information, a sketch representing the modeled architecture was prepared using BornAgain software (depicted in Figure 45e).

As anticipated, post-thermolysis, the copolymer retained its characteristic morphology, with lamellae aligned parallel to the substrate, exhibiting a range of sizes. This observation paves the way for an intriguing prospect: synthesizing block copolymers capable of self-assembling into precisely defined morphologies that persist through heat treatment-induced phase separation.

Table 11: Summary of extracted data from the GISAXS simulations using the BornAgain software for PBMA-b-(PSS-r-PS) block copolymer.

Layer	Thickness (Å)	$\sigma$ (Å)	Hurst	Correlation length (Å)
(f)	120 (*)	9	0.1	2000 (*)
(e)	250 (*)	20	0.1	2000 (*)
(d)	240(*)	1	0.1	2000 (*)
(c)	200(*)	10	0.1	2000 (*)
(b)	240(*)	10	0.1	2000 (*)
(a)	120(*)	10	1.0	20000 (*)

\* Fixed parameters.

Finally, we can conclude from AFM, XRR, and GISAXS that the similar sizes of the blocks lead to a flat interface geometry, which favors the formation of a lamellar morphology. Moreover, the parallel orientation of the block copolymer film morphology to the substrate can be explained by the selection of the species with the lowest interfacial energy (PBMA) for both the substrate and air interfaces [297], [298]. Consequently, the specific interactions of the blocks with the air and substrate interfaces result in the orientation of the lamellar microdomain morphology parallel to the external surface. Finally, the air-polymer and polymer-solid surface tensions lead to the coexistence of regions with different thicknesses, giving rise to a pattern of circular domains with minority thickness within a continuous film with majority thickness [299], as observed by AFM.

Figure 46 represents the copolymer internal structure, presenting the lamellar morphology using the AFM and GISAXS data. It is in accordance with the theoretical requirements [288][300]: (i) PBMA is at the free surface since it presents the lowest surface tension in the melt state (as proven in the AFM phase images); (ii) layers of polymer PBMA are those to be interrupted in the defect topology because PBMA is also expected to have the lowest cohesion energy; (iii) the dislocation is as close as possible to the free surface within constraints (i) and (ii), since the latter is supposed to be attractive for any defect.

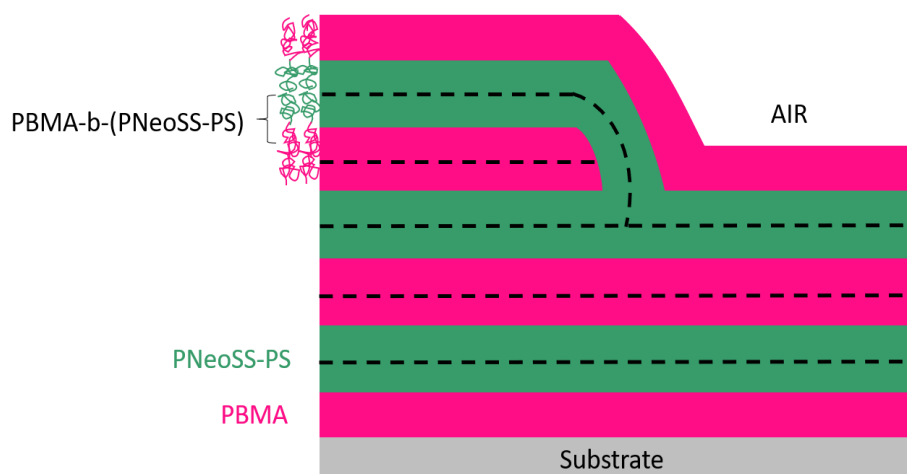


Figure 46: Assumed domain-edge structure for PBMA-b-(PNeoSS-r-PS). Dashed lines represent PNeoSS-PS-PS-PNeoSS or PBMA-PBMA separations.



Overall, it was evident that the low and medium molecular weight samples lacked any indication of phase separation, rendering them unsuitable for implementation in electromechanical devices. Furthermore, it is crucial to emphasize that among the high molecular weight samples, only Entry 09 exhibited phase separation observed by AFM. Since the attainment of a block copolymer with lamellar morphology stands as a primary objective in this study, this particular copolymer (PBMA220-b-(PSS41-r-PS205)) was selected for the fabrication of the electromechanical device. Consequently, all subsequent characterizations will solely focus on samples containing this polymer.

#### 4.4.3 Order-to-disorder transition

The low-frequency rheology proves highly effective in detecting the dissolution of ordered microstructures due to the viscoelastic contrast between the ordered and disordered states. The sample can be slowly heated to accurately determine the order-to-disorder transition temperature ( $T_{ODT}$ ) by conducting isochronous storage modulus measurements at low frequencies and utilizing low strain amplitudes. Furthermore, these measurements offer valuable insights into the material's morphology [301].

It has been shown that analyzing the relationship between  $\log G'$  and  $\log G''$  can be applied to determine the temperature of the onset of thermal degradation ( $T_{ODT}$ ) in block copolymers [222]. This method is effective because, as the temperature rises, the plot of  $\log G'$  versus  $\log G''$  exhibits a gradual variation up to a specific critical point, after which it remains relatively unchanged regardless of further temperature increase. Figure 47 provides  $\log G'$  versus  $\log G''$  for the PBMA220-b-(PSS41-r-PS205) sample at eight different temperatures: 150, 160, 170, 180, 190, 200, 210, and 220 °C. Below 150 °C, the polymer does not flow completely, and above 220 °C, degradation of the copolymer occurs.

As can be seen, for a fixed value of  $G''$ ,  $G'$  varies little with temperature in the range of 150-180 °C, then decreases suddenly as the temperature increases from 190 to 200 °C, and then remains virtually constant, regardless of temperature, at 210 °C and above. In other words, for this sample, 200 °C is the

lowest temperature at which the log  $G'$  versus log  $G''$  plots stop varying with temperature. The  $T_{ODT}$  for these symmetric copolymers corresponds to a temperature where the slope reaches a value of 2 [302], as shown below.

Based on the theoretical prediction [303] that log  $G'$  versus log  $G''$  plots for monodisperse flexible homopolymers in the melt state exhibit a negligible temperature dependence. It can be inferred from Figure 45 that the copolymer's log  $G'$  versus log  $G''$  plot displays a significant temperature dependence within a specific temperature range. This observation, supported by experimental evidence, suggests that the copolymer undergoes a thermal transition from an ordered microdomain structure to a disordered homogeneous phase.

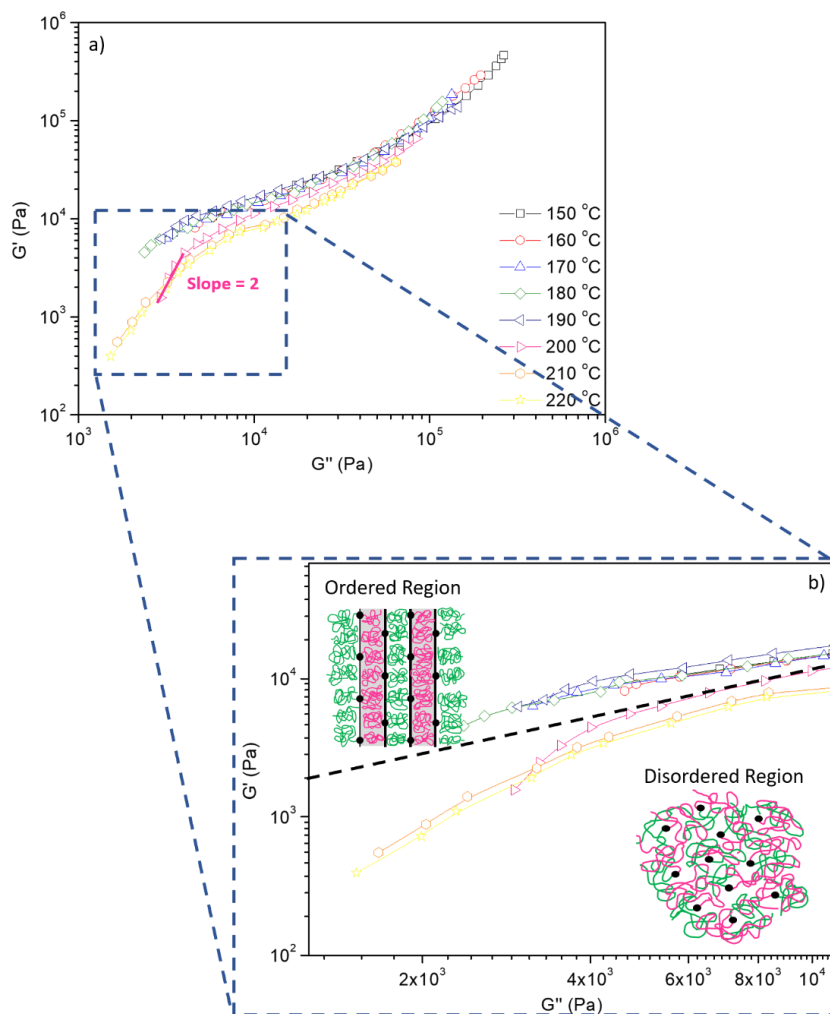


Figure 47: a) Log  $G'$  versus log  $G''$  for the PBMA-b-(PSS-r-PS) sample at various temperatures, b) low frequency region emphasizing the slope = 2 for 200 °C, showing  $T_{ODT}$ .

Hence, understanding the transition from order to disorder is essential in creating ionomers that possess specific mechanical characteristics. When the temperature is below the order-disorder transition point, the block copolymer exhibits a structured, lamellar form, as evidenced by AFM, XRR, and GISAXS, which enhances the material's mechanical strength and ionic conductivity. However, as the temperature surpasses the ODT, the BCP loses its organization, resulting in fewer defined domains.

Finally, it is essential to note that the temperature range within which the thermally induced order-disordered transition takes place in a block copolymer is highly influenced by several factors, such as the block lengths, the content of styrene and sulfonated styrene, as well as the molecular weights of the polymer chains. Consequently, the specific range of transition temperatures observed for PBMA220-b-(PSS41-r-PS205) should not be generalized to other block copolymers with different block lengths, styrene content, or molecular weights [304].

## **4.5 Ionomer Characterization**

### **4.5.1 Ion exchange capacity and water uptake**

Ion Exchange Capacity refers to the total amount of charged ions an ionomer can adsorb or exchange with its surrounding environment [305]. Similarly, water uptake quantifies the amount of water absorbed by a specific sample (expressed in grams of water per gram of sample) within a particular period. These properties are important because the electromechanical response of an IPMC is primarily influenced by its ion exchange capacity or, as commonly used, ionic migration [266], which is affected by RH [267] and counterion size [306].

Therefore, accurately estimating the ion exchange capacity and water uptake is crucial in determining the suitable application of an IPMC. Table 12 presents IEC, WU, and ionic conductivity (investigated in the subsequent section) for the block copolymer. All parameters are compared with Nafion, the commercial standard.

Table 12: IEC, WU, and ionic conductivity for PBMA-b-(PSS-r-PS) and Nafion.

<b>Ionomer</b>	<b>IEC (meq.g<sup>-1</sup>)</b>	<b>WU (wt%)</b>	<b>Ionic Conductivity (S.cm<sup>-1</sup>)</b>
PBMA-b-(PSS-r-PS)	0.61	14	0.16
Nafion 117	0.91	30	0.23

For Nafion, the IEC is determined by the equation  $IEC = 1000/EW$ , where EW represents the equivalent weight. The EW is the number of grams of dry Nafion per mole of sulfonic acid groups when the material is in the acid form. EW can be ascertained by acid-base titration, by analysis of atomic sulfur, and by FTIR spectroscopy. For Nafion 117 (used by our research group), the designation “117” refers to a film having 1100 EW and a nominal thickness of 0.007 in. (178  $\mu\text{m}$ , RH = 50%). Also, around 14  $\text{CF}_2$  units are expected to separate every side chain containing a sulfonic acid group. Consequently, the SD = 14% and the  $IEC = 1000/1100 = 0.91 \text{ meq.g}^{-1}$  [82].

In the case of PBMA220-b-(PSS41-r-PS205), the PBMA/PSS-PS ratio is 50%, with an SD = 16.7%. This means that for every 5 Sty monomers, there is 1 Sty sulfonated monomer. However, when considering the entire copolymer, the ratio of sulfonated monomers to total monomers is 1 in 11 (SD = 8.8%), giving an IEC of  $0.61 \text{ meq.g}^{-1}$  (estimated by titration as described in the experimental section). In this scenario, it's crucial to consider the SD of the entire copolymer, as the IEC was determined using 1 gram of sample. Based on a rough estimate, we can anticipate that with an SD = 14%, the copolymer would theoretically exhibit an IEC of around  $0.95 \text{ meq.g}^{-1}$ .

It must be considered that Nafion presents sulfonated groups that are laterally grafted to the main chain. This unique characteristic allows mobility to the  $-\text{SO}_3^-$  groups, causing agglomeration and percolation of sulfonated groups when the RH is increased [83], leading to the development of three-dimensional percolated channels [84]. Alternatively, the copolymer shows phase separation and the  $-\text{SO}_3^-$  groups are bonded within the main chain. In simpler terms, we can liken phase separation to percolation, as both copolymers exhibit similar ion IEC values theoretically.

However, it should be noted that the number of sulfonated groups can be readily increased in the case of PBMA-*b*-(PSS-*r*-PS). In fact, the entire domain can be synthesized with PSS, resulting in a copolymer with a higher ion exchange capacity. This would only be possible through controlled polymerization since increasing the SD may lead to degradation, undesirable cross-linking, and other unwanted side reactions with sulfonated copolymers obtained by sulfonation.

Many authors have studied the WU parameter and its relationship with IPMC electromechanical response [5], [23], [307]–[309]. As presented elsewhere [23], the water uptake capacity was used to determine an empirical relationship between the sample's hydration level as a function of the RH and counterion. Also, this data made it possible to investigate the relationship between the membrane's hydration level and the IPMC electromechanical response. Chen and co-workers [308] showed that water uptake depends on the temperature, and IPMC performance could vary with hydration. Komoroski and Mauritz [309] affirmed that water uptake depends on the cation type. Tozzi et al. [5] studied the WU and its relation with hydrolytic stability and proton conductivity.

Generally, it has been observed in these papers that increasing the RH and using smaller counterions result in higher water absorption capacities. Also, optimizing the water absorption capacity improves the electromechanical performance of the device. When comparing the water absorption capacities of Nafion and the copolymer, it is evident that the block copolymer has a lower absorption capacity. However, as discussed in the next section, this capacity is still considerable enough for the counter-ions to form complexes with water molecules, thereby enhancing ionic conductivity.

#### **4.5.2 Electrochemical Characterization**

Impedance spectroscopy stands out as a highly versatile electrochemical technique due to its ability to characterize various aspects of electrochemical systems. Semi-stationary measurements offer insights into kinetic processes occurring at the electrode surface, the structure of the double-layer, and the

transport of charged species. At its core lies the alternating current (AC) theory, which elucidates the system's response to varying frequencies. By applying a potential and measuring the resultant current response, the impedance ( $Z$ ) of the system can be obtained. This impedance reflects any factors influencing electron flow within the system [281].

Hence, the data from EIS was obtained to understand the electrochemical migration processes that occur in the device when RH = 30, 60, and 90%. The device was allowed to equilibrate for 6 hours at each relative humidity level to achieve osmotic balance with the surrounding RH. The typical resistive-capacitive response can be observed in the Nyquist plot (Figures 48a and 48b).

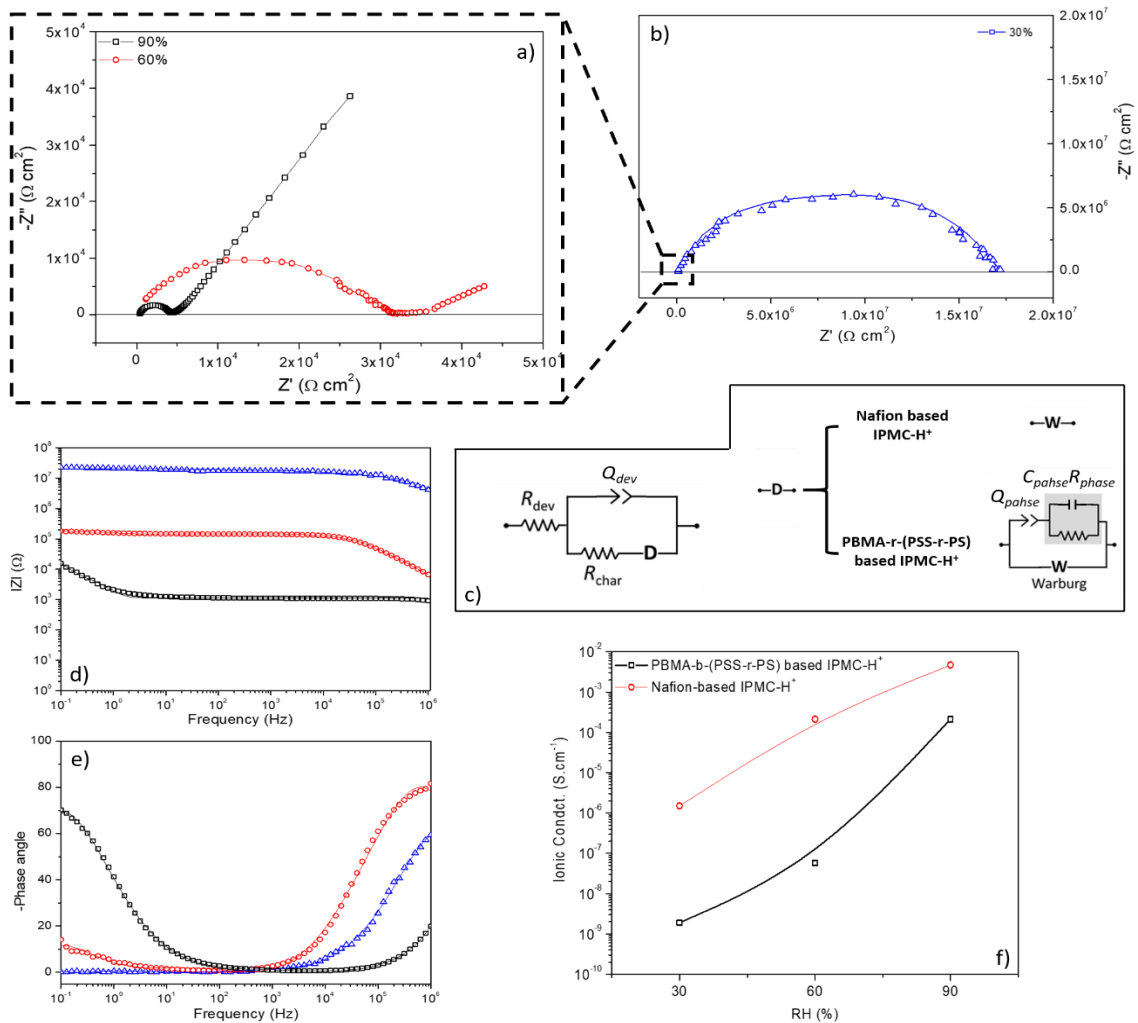


Figure 48: Nyquist plot for a) RH = 60 and 90% and b) RH = 30%, c) Modified Randles circuit, d) Bode plot of the impedance magnitude ( $|Z|$ ) e) Bode phase, and f) ionic conductivity as a function of RH.

As previously elucidated, the operational principle of an IPMC depends on the migration of ions and the accumulation of charges within its structure. Thus, the manifestation of resistive-capacitive characteristics serves as a promising indicator of the IPMC's potential utility as an electromechanical device. The electrical equivalent circuit (modified Randles circuit [310]) for ion transport can be better understood by referring to Figure 48c. It consists of various components, each with its specific function, describing the electrochemical transport in the electromechanical device. As can be observed, an R(D(RQ)) circuit, where D represents the impedance of the ion diffusion part, can satisfactorily fit the data, especially at high frequencies with  $\chi^2$  below  $10^{-5}$ .

$R_{dev}$  represents the device's resistance, which is influenced by the hydration level of the membrane and the counterion type and size.  $Q_{dev}$  characterizes the pseudo capacitance phenomenon resulting from ionic movement in the PSS-r-PS region, encompassing double-layer pseudo capacitance.  $R_{char}$  corresponds to the charge resistance of the device [311]. The impedance parameters derived from the data analysis are provided in Table 13 for reference.

Table 13: Impedance parameters obtained from data fitting.

Parameters	RH = 30%	RH = 60%	RH = 90%
$R_{dev} / \Omega \text{ cm}^2$	1057,80	636,52	333,18
$Q_{dev} / \mu\text{F s}^{1-n} \text{ cm}^{-2}$	8,23	22,29	107,22
$n_{dev}$	0,98	0,84	0,81
$R_{char} / \Omega \text{ cm}^2$	827,42	724,14	655,72
$W / \text{k}\Omega \text{ s}^{1/2} \text{ cm}^{-2}$	$23,36 \times 10^7$	$12,18 \times 10^5$	$8,03 \times 10^2$
$Q_{phase} / \mu\text{F s}^{1-n} \text{ cm}^{-2}$	0,46	0,40	0,42
$n_{phase}$	0,65	0,68	0,66
$R_{phase} / \Omega \text{ cm}^2$	1,25	1,07	3,28
$C_{phase} / \text{nF cm}^{-2}$	1,01	1,82	2,24
$\chi^2$	$2,42 \times 10^{-6}$	$6,44 \times 10^{-6}$	$1,254 \times 10^{-6}$

It is worth noting that there are two distinct mechanisms of ionic diffusion: structural and vehicular diffusion. Grotthuss or structural diffusion refers to the movement of a proton or cation through the network of H bonds, enabling it to move freely. On the other hand, vehicular diffusion takes place when a solvated proton or cation is transported through the network.  $H^+$  can diffuse through both mechanisms, while solvated cations ( $Li^+$ ,  $Na^+$ , etc.) generally tend to follow the vehicular diffusion mechanism due to the simultaneous movement of their charge and center of mass [312][313]. Consequently, vehicular diffusion occurs at a comparatively slower rate.

Therefore, for electromechanical devices using commercial membranes exchanged with  $H^+$ , the configuration of D assumes a simplified form of a pure Warburg element (W) owing to the efficient transport of protons via the Grotthuss mechanism, as depicted in Figure 48c. Hence, the copolymer-based electromechanical device in the acid form is expected to exhibit analogous behavior. On the other hand, it is important to consider the cation/domain size ratio (PSS-r-PS) and the number of sulfonated groups, as they play a crucial role in forming a favorable path for ionic migration, affecting the system's overall efficiency.

In this specific case, the system's performance is determined by the size of the rigid conducting phase, primarily composed of PS (80%, SD = 16.7%). By increasing the size of the PS backbone, a resistive component is added to the overall system impedance, resulting in a delay in the migration of ions. This delay is directly related to pseudocapacitance and  $Q_{\text{phase}}$  and impacts the overall system performance. Additionally, the migration of ionic species through this region is expected to exhibit a resistive-capacitive behavior ( $R_{\text{phase}}C_{\text{phase}}$ ). For this reason, a delay component was added to the circuit for the block copolymer, as presented in Figure 48c.

Figure 48d presents the Bode plot of the impedance magnitude ( $|Z|$ ). At low frequencies,  $|Z|$  is dominated by the ionic response (slow processes), while, at high frequencies, purely electronic processes are observed. As expected, the samples resistance is lower for higher humidity conditions since this property is directly related to the membrane hydration level. Also, when  $RH < 90\%$ , one



can observe an increase in the device resistivity at low frequencies, indicating an increase in the impediment to diffusional ion transport. The Bode phase of the device provides information about their characteristic time constants, achieved by normalizing the device resistance ( $R_{dev}$ ) to zero (as depicted in Figure 48e).

The time constants of the device exhibit variation with increasing relative humidity, as the presence of ions enables the formation of complexes with a more significant number of water molecules. Consequently, it is possible to observe that the ionic conductivity increases when the RH increases (Figure 48f), achieving its maximum at RH = 90% ( $0.16 \text{ S}\cdot\text{cm}^{-1}$ ). Moreover, through careful analysis, it becomes apparent that this electromechanical device's sensor configuration can perform optimally at high RH conditions, as it exhibits enhanced ionic transport capabilities when frequency is lower than 5 Hz. Therefore, the electromechanical characterization presented in the next section was performed in a sensor configuration at RH = 90% and frequency < 5 Hz.

#### 4.5.3 Platinum electrodes morphology

Following the preparation of the electromechanical device, an investigation into the morphological features of the platinum electrodes was conducted. The analysis encompassed both the surface characteristics and the interface region with the copolymer. Figures 49a and 49b showcase scanning electron microscopy images capturing the surface topography and the lateral region, respectively.

As previously described, the IPMC is a sandwich-type device in which Pt electrodes are formed at the surface of the copolymer by the reduction of  $\text{Pt}^{2+}$  cations incorporated by the membrane during the adsorption step. It is possible to notice clusters ranging in size from 10 to 20  $\mu\text{m}$ , spread evenly over the entire surface, forming platinum "islands". This was already expected since the deposition method involves the reduction of a metallic salt on the irregular surface and is composed of several nanometer-sized channels (PSS-PS lamellar domain).

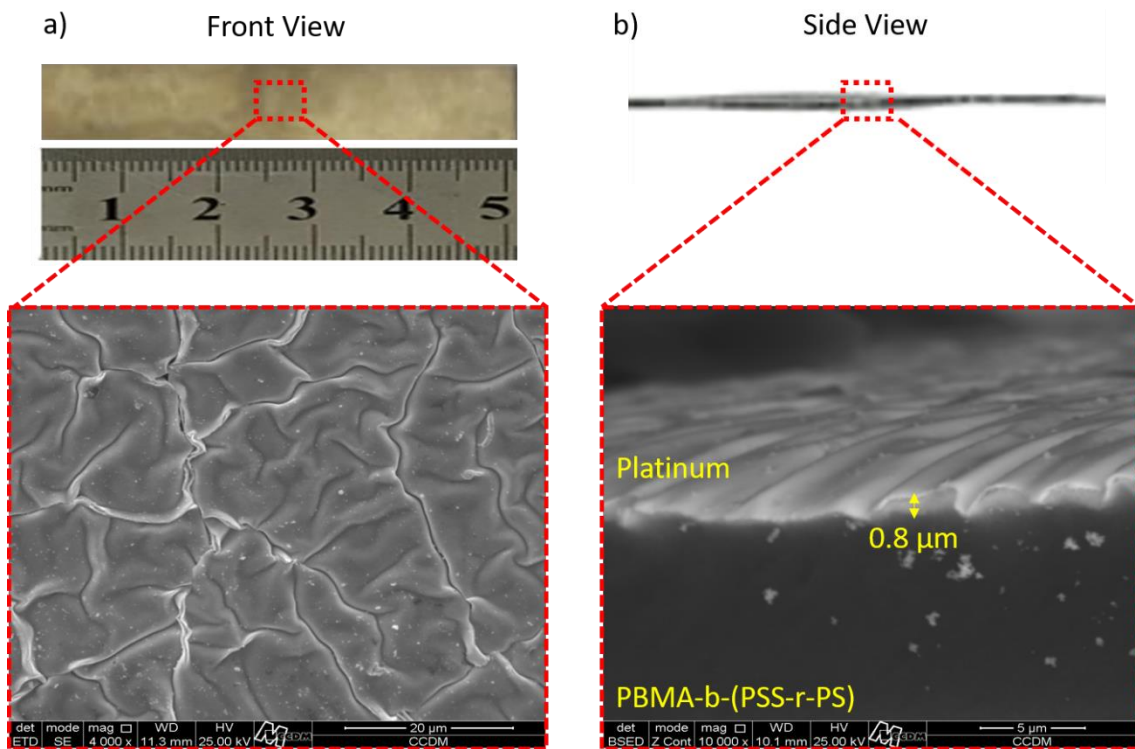


Figure 49: a) SEM micrographs of the platinum electrode surface and b) lateral cryofracture showing platinum layer thickness

Platinum ions accumulate where  $-\text{SO}_3^-$  groups are present. These groups have different positions and sizes along the rigid domain of the copolymer. Therefore, during the reduction stage, the growth of metallic platinum occurs in various regions simultaneously, that is, irregularly, resulting in a segmented structure similar to platinum islands. The structure formed is similar to that obtained in Nafion-based IPMC samples, as already demonstrated in other works by our research group [85], [314].

Additionally, in Figure 49b, the polymer morphology and the thickness of the Pt layer in a cryogenically fractured sample are observable. The total thickness of IPMC-H at 50% relative humidity measures approximately 200 μm, with 0.8 μm attributed to the Pt electrodes, constituting 0.4% of the overall thickness. It's worth noting that variations in membrane thickness may occur depending on the counterion and RH. Ripples are evident at the platinum interface with the copolymer, indicating potential surface irregularities. This

suggests that the material surface might not be entirely flat, likely due to the film preparation process involving casting.

Studying metal/polymer interfaces in electromechanical devices is crucial for advancing their functional understanding, enhancing actuation performance, improving durability and stability, optimizing sensing capabilities, and advancing fabrication techniques for various applications in robotics, biomedical devices, aerospace, and beyond [315]. Also, the metal/polymer interface in EMD devices exhibits a dynamic and multifaceted nature, encompassing a range of physical, chemical, and electrochemical phenomena.

The pioneering work in comprehending and modeling the electrode film structure was undertaken by Kim and Shahinpoor [316][317]. In their studies, they delineated metallic electrodes as the union of coagulated metallic particles. These particles are distributed both on the membrane surface and within the layer just beneath it, permeating the membrane. These layers were termed the outer electrode or metallic electrode, characterized solely by the metallic film, and the internal electrode or composite electrode or interfacial electrode, distinguished by a blend of polymer and reduced metal.

Experimental observations indicate that the noble metal (platinum, gold, palladium, and silver) particulate layer is typically buried within the surface, reaching a depth of a few microns (usually between 1 to 10  $\mu\text{m}$ ). This layer demonstrates a high degree of dispersion throughout the ionomer [316], forming either a dendritic type electrode, a granular interfacial electrode, or a layered structure [318][319]. The interaction between polymer and platinum electrodes also involves interfacial adhesion. Strong adhesion between the Nafion membrane and the platinum electrodes is essential for maintaining structural integrity and preventing delamination or detachment during actuation.

Overall, it can be inferred that the electrodeless plating deposition procedure was executed accurately and effectively. The electrode composition closely resembles that of Nafion-based electromechanical devices, showcasing exceptional adhesion to the membrane. This implies the development of a dendritic structure at the interface. Hence, it is unequivocal that the device

possesses all requisite attributes to deliver commendable electromechanical performance, whether utilized as a sensor or actuator.

#### **4.6 Electromechanical Response**

Electromechanical devices cannot only convert mechanical energy into electrical energy and vice versa but also offer the advantage of self-sensing during actuation [320]. This feature allows for acquiring deformation measurements that are much more compact, cost-effective, and lightweight than traditional transducers. Consequently, they have the potential to replace bulky vision systems [321], laser displacement sensors [322], load cells [323], and inductive sensors [324]. The proposed applications for this sensing capability encompass a wide range of fields, such as vibration sensing [325], detection of seismic waves [326], position tracking in multiple degrees of freedom [327], force measurement [328], pressure sensing [329], and flow detection [330].

Therefore, the conducted test aimed to assess the electromechanical sensors' capability to accurately convert the displacement trajectories from the stepper motor into potential curves resembling these trajectories. Consequently, diverse movements were examined, including speed, amplitude, and acceleration variations. The movement of the sensor was captured using a camera in combination with the electromechanical system, and the recorded data was used to display the displacement profile and corresponding voltage in Figure 50. The figure illustrates four distinct types of movement along with their corresponding electrical responses.

As depicted in Figure 50a, controlled mechanical deformation was applied at the IPMC-free end, capturing the damping vibration spectrum via an external camera and acquiring voltage response through the characterization system. This approach elucidates the system's proficiency in discerning electrical responses across diverse frequencies, as the initial motion diminishes with time and the electromechanical device functions across a range of frequencies. Consequently, various motions were administered at different frequencies to explore device behavior comprehensively.

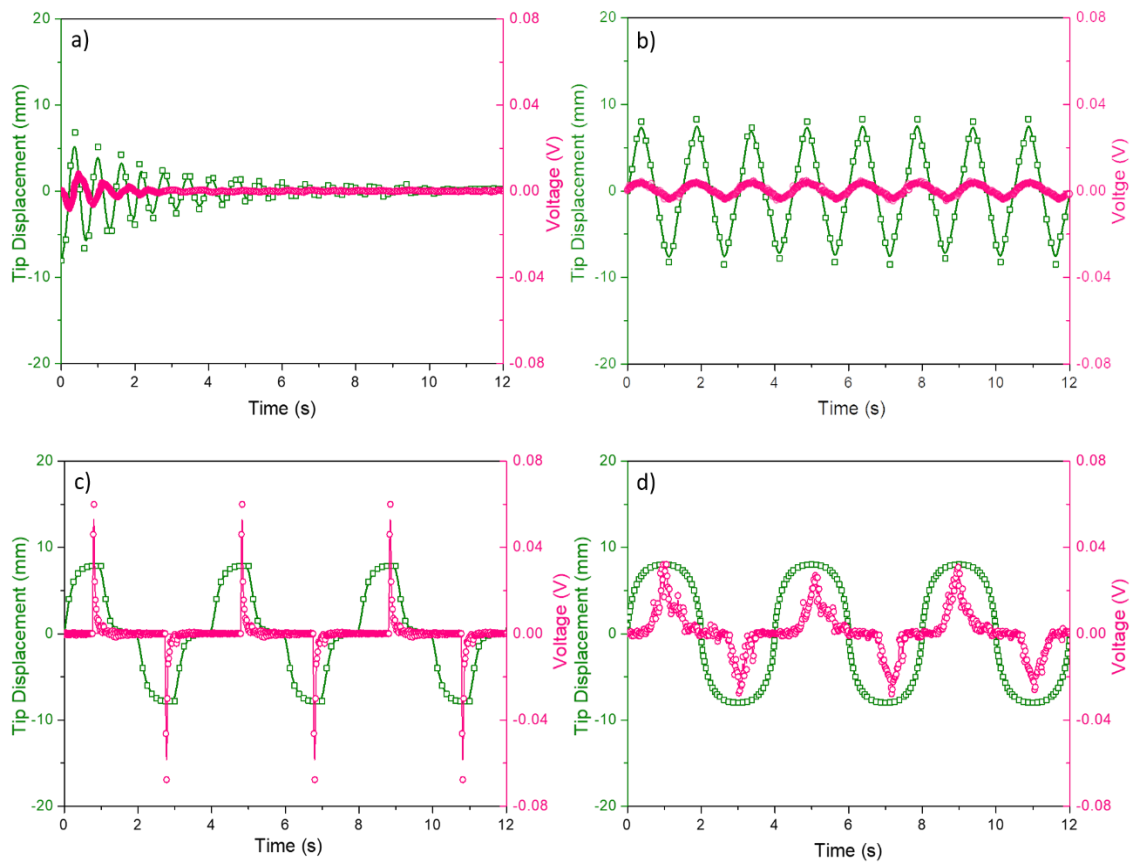


Figure 50: IPMC electromechanical response when subjected to different displacement profiles. a) Damping vibration spectrum, b) movement with constant linear speed, c) movement with non-linear speed, d) Sinusoidal movement. RH was controlled at 90%.

Figure 50b illustrates the electrical response to movement with a constant linear speed at a frequency of 0.7 Hz. Figure 50c shows movement with non-linear speed, 8 mm displacement, and 0.25 Hz, and Figure 50d depicts a sinusoidal movement with 8 mm amplitude and 0.25 Hz. It is evident that the electromechanical response exhibited excellence, as the electrical response of the IPMC synchronizes seamlessly with the external mechanical stimuli. Moreover, the absence of noise or signal inconsistencies underscores the sensor's commendable sensitivity while also attesting to the resilience and aptitude of the electromechanical characterization system in accurately measuring the electrical response.

It is noteworthy that electrical parameters play a crucial role in various applications, such as sensors and energy harvesting. In particular, voltage, current, and coulombic efficiency are significant parameters. Numerous studies have investigated the impact of cation species and water content on IPMC voltage and current generation [311], [331]–[333]. It has been observed that the amplitude of the voltage peak in response to a step-bending input shows a correlation with RH and the type of cations present. Besides, the voltage response is undesired at low relative humidity conditions.

Other researchers have suggested that for optimal IPMC current sensing, the hydration level of the membrane should be in equilibrium with the environment, without any excess water present [334]. These findings highlight the importance of carefully controlling the water content and cation species in IPMC sensing devices. For example, Bruneto et al. [335] have shown that as the membrane's hydration level varies, there will be differences in the distance between the charged species ( $-\text{SO}_3^-$  groups and counterions). Consequently, the coulombic interactions between these groups may be strong or weak, determining ion mobility, Young's modulus, and electromechanical response.

This data is fundamental for predicting and controlling an IPMC-based sensor [336]. Many efforts have been made to develop new strategies for controlling them in real-world applications; the most straightforward is the proportional–integral–derivative (PID) controller [26]. In this case, predictive (feedforward) and corrective (feedback) schemes proved to be effective methods capable of ensuring proper system functioning and reliability [337]. In this sense, the input data (displacement) and output (voltage and current) must be acquired and applied precisely.

Hence, assessing the device's capacity to convert mechanical deformation into voltage across various stimuli is crucial. Figure 51 illustrates the voltage amplitude generated when subjected to displacements of 8 mm at frequencies of 0.1, 0.2, 0.4, and 2 Hz. The voltage fluctuation across different frequencies becomes more evident when visualized in a bar graph. Additionally, the variance throughout cycles, illustrated by error bars, is more effectively highlighted.

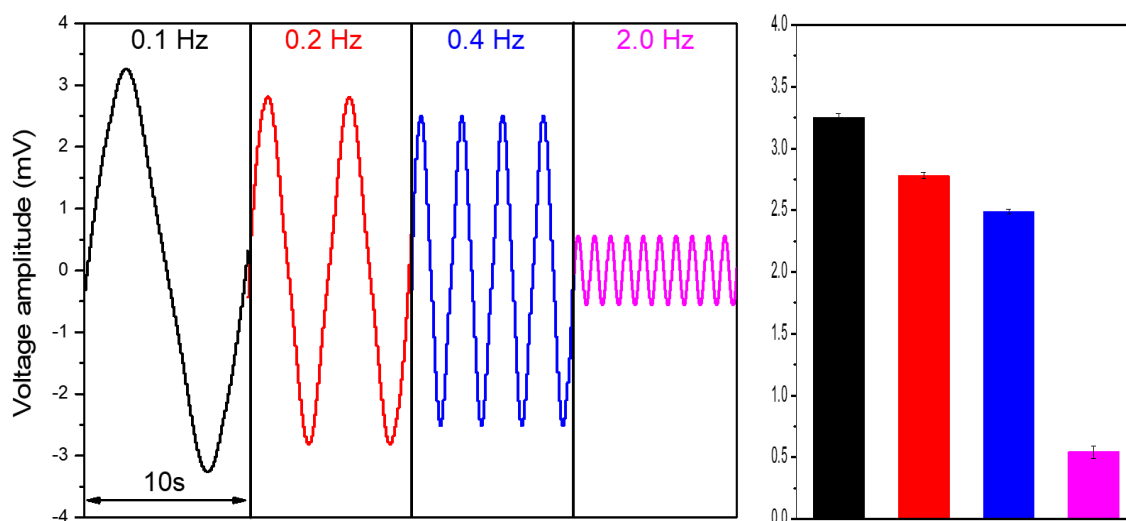


Figure 51: IPMC voltage amplitude when subjected to 0.1, 0.2, 0.4, and 2.0 Hz frequency stimuli.

When a low-frequency mechanical stimulus, such as bending or stretching, is applied to an IPMC, it causes deformation of the polymer matrix. This deformation leads to the redistribution of ions within the material as the polymer chains and metal electrodes move relative to each other. The movement of ions is facilitated by the interaction between the applied mechanical stress and the ion-containing polymer matrix [320]. In general, the device demonstrated its capability to sense applied strain by detecting changes in potential across various frequencies. As previously illustrated in Figure 48e, when operating at frequencies below 5 Hz, the device exhibited enhanced ionic conduction. This phenomenon is consistently observed in Figure 51. Decreasing the frequency leads to an amplified electrical response and improved resolution.

This phenomenon is ascribed to the duration required to establish an ionic gradient following the application of deformation. At extremely high frequencies, the limited time available for ionic motion hinders ions from migrating in adequate numbers to generate a satisfactory electrical response. Consequently, it's evident that the copolymer's ionic processes exhibit optimal performance at lower frequencies. Based on these findings, it can be inferred that the electromechanical device functions satisfactorily as a sensor, showcasing a reliable electromechanical response.

This is particularly interesting since flexible sensors have garnered extensive attention in the realm of intelligent wearable devices. Leveraging the advantageous traits of bionic structural flexibility—including excellent skin adhesion, biocompatibility, and heightened sensitivity—researchers have delved into various applications. Among these, endeavors in expression recognition and roughness detection have been pursued to showcase the distinctive capabilities of fabricated IPMC sensors [338].

By the conclusion of this section, it is anticipated that this bio-inspired electromechanical device will catalyze further strategic advancements in developing novel materials and enhance the performance of ionic sensors. Moreover, it aims to stimulate future exploration into the diverse applications of these technologies.



## 5 CONCLUSIONS

In summary, the primary objective of this study has been successfully attained. The development of bio-inspired electromechanical devices based on PBMA-b-(PSS-r-PS) amphiphilic block copolymer was successfully achieved and exhibited an outstanding sensor response. Additionally, it is important to highlight other objectives achieved individually:

- RAFT polymerization: It has been demonstrated by NMR and GPC that it is a powerful and versatile polymerization technique that combines the advantages of both radical and ionic polymerization systems to synthesize the PBMA-b-(PNeoSS-r-PS) copolymers with the desired chemical composition, molecular weight, and molecular weight distribution. Furthermore, it was possible to synthesize a copolymer with a well-defined architecture and control the degree of sulfonation using conventional reaction conditions;
- Copolymer morphology: Analysis using AFM, XRR, and GISAXS revealed that the block copolymer, with a molecular weight exceeding  $65 \text{ kg}\cdot\text{mol}^{-1}$ , exhibited a distinct lamellar morphology. Attaining such a structured morphology in lamellae holds significant importance, primarily due to the potential enhancement in proton conductivity. Additionally, order-to-disorder transitions were estimated through rheology measurements. With this achievement, it was possible to advance confidently to the subsequent stages in the development of the electromechanical device;
- Thermolysis: The successful execution of thermochemical cleavage on neopentyl groups presented in PBMA-b-(PNeoSS-r-PS) is evident from comprehensive analyses, including DSC, TGA, FTIR, NMR, and GPC. This process resulted in the generation of sulfonic acid groups, forming an amphiphilic block copolymer (PBMA-b-(PSS-r-PS)). Besides, the

procedure was straightforward and did not cause structural damage to the material;

- Electroless plating process: An electromechanical device was prepared, presenting flexibility, mechanical resistance, and elevated ionic conductivity using the electroless plating process. SEM analyses confirm the successful execution of the plating process, yielding a platinum electrode that uniformly covered the entire surface of the sample;
- Electromechanical system: This thesis details creating a low-cost system designed for controlling and characterizing these devices under varying humidity conditions. The system proved to be efficient in describing the samples, presenting a compatible, reproducible response and a noise-free signal. By integrating electromechanical and electrochemical data, we were able to gain deeper insights into certain behaviors and correlate them with specific characteristics of this bio-inspired device;
- PBMA-b-(PNeoSS-r-PS) sensor device: Impedance spectroscopy analyses clearly indicated a preference for ionic processes at lower frequencies ( $< 5$  Hz) and relative humidity levels exceeding 90%. Under these conditions, the sensor exhibited an outstanding electrical response to diverse mechanical stimuli, establishing itself as a prime candidate for intelligent wearable devices applications.

In conclusion, all primary and secondary objectives have been successfully met. Moreover, this research has identified several areas for optimization, which will be explored in greater detail in the following section.

## 6 SUGGESTIONS FOR FUTURE WORKS

Throughout the course of this study, several suggestions for future research have surfaced and are outlined below:

- Employing rubbery monomers to prepare the macroinitiator introduces an intriguing approach, as the resulting homopolymer will exhibit a low glass transition temperature. This method facilitates a notable enhancement in the degree of sulfonation of the subsequent copolymer while preserving its flexibility. Examples of such monomers include butyl acrylate (-54°C), isobutyl acrylate (-24°C), and butadiene (-90°C);
- As previously illustrated, the copolymer utilized in fabricating the electromechanical device comprises only 10% of monomers containing the sulfonic acid group. Despite this relatively low sulfonation level, its ionic conduction properties are comparable to Nafion, the leading commercial ionomer. Consequently, increasing the degree of sulfonation in a material exhibiting periodic lamellar morphology holds the potential to yield exceptional properties;
- Usually, IPMCs' water uptake is generally determined by immersing the wholly dry sample in deionized water for at least one hour and measuring the increase in weight of the swollen IPMC. However, measuring the water absorption capacity as a function of time in a controlled atmosphere is possible. Therefore, it is possible: i) Determine an empirical relationship between the hydration level as a function of the RH, ii) determine the mass variation as a function of time, and iii) connect this information with copolymer morphology, aiming to understand better the IPMCs electromechanical response;
- Modeling the Ionic Migration: Modeling ionic migration in Nafion-based IPMCs poses several challenges, notably: i) nonlinear behavior, ii) dealing with multiscale phenomena, iii) accounting for material

heterogeneity, and iv) ensuring experimental validation. Conversely, describing ionic migration in block copolymers may be comparatively more straightforward due to their well-defined morphology.

## 7 REFERENCES

- [1] J. Tani, C. G. Speziale, and J. Qiu, "Intelligent material systems: Application of functional materials," *Appl. Mech. Rev.*, vol. 51, no. 8, pp. 505–521, 1998, doi: 10.1115/1.3099019.
- [2] C. Sanchez, H. Arribart, and M. M. G. Guille, "Biomimetism and bioinspiration as tools for the design of innovative materials and systems," *Nature Materials*, vol. 4, no. 4. Nature Publishing Group, pp. 277–288, 2005. doi: 10.1038/nmat1339.
- [3] R. Bogue, "Smart materials: A review of recent developments," *Assem. Autom.*, vol. 32, no. 1, pp. 3–7, Feb. 2012, doi: 10.1108/01445151211198674.
- [4] Y. Bahramzadeh and M. Shahinpoor, "A Review of Ionic Polymeric Soft Actuators and Sensors," *Soft Robot.*, vol. 1, no. 1, pp. 38–52, 2014, doi: 10.1089/soro.2013.0006.
- [5] K. A. Tozzi *et al.*, "Improving electrochemical stability and electromechanical efficiency of ipmcs: tuning ionic liquid concentration," *J. Appl. Electrochem.*, Oct. 2022, doi: 10.1007/s10800-022-01776-w.
- [6] M. Shahinpoor, *Ionic Polymer Metal Composites (IMPCs): Smart Multi-Functional Materials and Artificial Muscles Volume 2*, vol. 2. London, United Kingdom, 2015.
- [7] J. Mu *et al.*, "Molecular-channel driven actuator with considerations for multiple configurations and color switching," *Nat. Commun.*, vol. 9, no. 1, p. 590, 2018, doi: 10.1038/s41467-018-03032-2.
- [8] T. P. Stalbaum, "Ionic Electroactive Polymer Devices: Physics- Based Modeling with Experimental Investigation and Verification," University of Nevada, Las Vegas, 2016. doi: <http://dx.doi.org/10.34917/10083216>.
- [9] B. J. Akle, C. Tawk, and E. Challita, "Design and manufacturing of an array of micro IPMC hair-like sensors," in *Proc. SPIE 9798, Electroactive Polymer Actuators and Devices (EAPAD)*, Apr. 2016, vol. 979816, no. April 2016. doi: 10.1117/12.2220776.
- [10] M. Gudarzi, P. Smolinski, and Q. M. Wang, "Bending mode ionic polymer-metal composite (IPMC) pressure sensors," *Meas. J. Int. Meas. Confed.*,

- vol. 103, pp. 250–257, 2017, doi: 10.1016/j.measurement.2017.02.029.
- [11] D. Chen and Q. Pei, “Electronic Muscles and Skins: A Review of Soft Sensors and Actuators,” *Chem. Rev.*, vol. 117, no. 17, pp. 11239–11268, 2017, doi: 10.1021/acs.chemrev.7b00019.
- [12] K. J. Kim, V. Palmre, T. Stalbaum, T. Hwang, Q. Shen, and S. Trabia, “Promising Developments in Marine Applications With Artificial Muscles: Electrodeless Artificial Cilia Microfibers,” *Marine Technology Society Journal*, vol. 50, no. 5, pp. 24–34, 2016. doi: 10.4031/MTSJ.50.5.4.
- [13] V. Palmre, D. Pugal, K. J. Kim, K. K. Leang, K. Asaka, and A. Aabloo, “Nanothorn electrodes for ionic polymer-metal composite artificial muscles,” *Sci. Rep.*, vol. 4, pp. 1–10, 2014, doi: 10.1038/srep06176.
- [14] F. Kaasik *et al.*, “Scalable fabrication of ionic and capacitive laminate actuators for soft robotics,” *Sensors Actuators, B Chem.*, vol. 246, pp. 154–163, 2017, doi: 10.1016/j.snb.2017.02.065.
- [15] A. Fallahi, Y. Bahramzadeh, S. E. Tabatabaie, and M. Shahinpoor, “A novel multifunctional soft robotic transducer made with poly (ethylene-co-methacrylic acid) ionomer metal nanocomposite,” *Int. J. Intell. Robot. Appl.*, vol. 1, no. 2, pp. 143–156, 2017, doi: 10.1007/s41315-017-0013-y.
- [16] S. Ruiz, B. Mead, V. Palmre, K. J. Kim, and W. Yim, “A cylindrical ionic polymer-metal composite-based robotic catheter platform: Modeling, design and control,” *Smart Mater. Struct.*, vol. 24, no. 1, 2015, doi: 10.1088/0964-1726/24/1/015007.
- [17] A. Monzon *et al.*, “Methods for promoting knowledge exchange and networking among young professionals in the aerospace sector - IAFs IPMC workshop 2013 insights,” *Acta Astronaut.*, vol. 118, pp. 123–129, Jan. 2016, doi: 10.1016/j.actaastro.2015.10.006.
- [18] Q. Hu, L. Xu, and X. Liu, “MOGA application feasibility research on ocean petroleum exploration platform seawater environment supervision,” in *Proceedings - 2010 6th International Conference on Natural Computation, ICNC 2010*, 2010, vol. 7, pp. 3503–3507. doi: 10.1109/ICNC.2010.5584044.
- [19] M. N. Silletto, S.-J. Yoon, and K. Arakawa, “Piezoelectric cable macro-

- fiber composites for use in energy harvesting,” *Int. J. Energy Res.*, vol. 39, no. 1, pp. 120–127, Jan. 2015, doi: 10.1002/er.3227.
- [20] K. C. Aw and A. J. McDaid, “Bio-applications of ionic polymer metal composite transducers,” *Smart Mater. Struct.*, vol. 23, no. 7, 2014, doi: 10.1088/0964-1726/23/7/074005.
- [21] A. Zolfagharian, A. Z. Kouzani, S. Y. Khoo, A. A. A. Moghadam, I. Gibson, and A. Kaynak, “Evolution of 3D printed soft actuators,” *Sensors Actuators, A Phys.*, vol. 250, pp. 258–272, 2016, doi: 10.1016/j.sna.2016.09.028.
- [22] X. Zhang, S. Yu, M. Li, M. Zhang, C. Zhang, and M. Wang, “Enhanced performance of IPMC actuator based on macroporous multilayer MCNTs/Nafion polymer,” *Sensors Actuators A Phys.*, vol. 339, p. 113489, Jun. 2022, doi: 10.1016/j.sna.2022.113489.
- [23] M. C. Saccardo *et al.*, “Electromechanical Evaluation of Ionomeric Polymer-Metal Composites Using Video Analysis,” *Mater. Res.*, vol. 24, no. suppl 2, 2021, doi: 10.1590/1980-5373-mr-2021-0317.
- [24] M. B. Karimi, F. Mohammadi, and K. Hooshyari, “Recent approaches to improve Nafion performance for fuel cell applications: A review,” *Int. J. Hydrogen Energy*, vol. 44, no. 54, pp. 28919–28938, Nov. 2019, doi: 10.1016/j.ijhydene.2019.09.096.
- [25] S. P. Fernandez Bordín, H. E. Andrada, A. C. Carreras, G. E. Castellano, R. G. Oliveira, and V. M. Galván Josa, “Nafion membrane channel structure studied by small-angle X-ray scattering and Monte Carlo simulations,” *Polymer (Guildf)*, vol. 155, pp. 58–63, 2018, doi: 10.1016/j.polymer.2018.09.014.
- [26] A. G. Zuquello *et al.*, “PI Controller for IPMC Actuators Based on Nafion®/PT Using Machine Vision for Feedback Response at Different Relative Humidities,” *Mater. Res.*, vol. 25, 2022, doi: 10.1590/1980-5373-mr-2021-0518.
- [27] S. SamPour, H. Moeinkhah, and H. Rahmani, “Electrochemical viscoelastic modeling to predict quasi-static and dynamic response of IPMC actuators,” *Mech. Mater.*, vol. 138, no. May, p. 103172, 2019, doi:

- 10.1016/j.mechmat.2019.103172.
- [28] J. Arumugam and J. N. Reddy, "Nonlinear analysis of ionic polymer–metal composite beams using the von Kármán strains," *Int. J. Non. Linear. Mech.*, vol. 98, no. September 2017, pp. 64–74, 2018, doi: 10.1016/j.ijnonlinmec.2017.10.007.
- [29] E. M. W. Tsang, Z. Zhang, Z. Shi, T. Soboleva, and S. Holdcroft, "Considerations of Macromolecular Structure in the Design of Proton Conducting Polymer Membranes: Graft versus Diblock Polyelectrolytes," *J. Am. Chem. Soc.*, vol. 129, no. 49, pp. 15106–15107, Dec. 2007, doi: 10.1021/ja074765j.
- [30] B. Bhandari, G.-Y. Lee, and S.-H. Ahn, "A review on IPMC material as actuators and sensors: Fabrications, characteristics and applications," *Int. J. Precis. Eng. Manuf.*, vol. 13, no. 1, pp. 141–163, 2012, doi: 10.1007/s12541-012-0020-8.
- [31] S. E. Smeltzer *et al.*, "Amphiphilic Block-Random Copolymers: Shedding Light on Aqueous Self-Assembly Behavior," *Macromolecules*, vol. 56, no. 4, pp. 1601–1614, Feb. 2023, doi: 10.1021/acs.macromol.2c02286.
- [32] Y. A. Elabd and M. A. Hickner, "Block Copolymers for Fuel Cells," *Macromolecules*, vol. 44, no. 1, pp. 1–11, Jan. 2011, doi: 10.1021/ma101247c.
- [33] J. Meier-Haack, A. Taeger, C. Vogel, K. Schlenstedt, W. Lenk, and D. Lehmann, "Membranes from sulfonated block copolymers for use in fuel cells," in *Separation and Purification Technology*, Feb. 2005, vol. 41, no. 3, pp. 207–220. doi: 10.1016/j.seppur.2004.07.018.
- [34] L. Francisco-Vieira, R. Benavides, L. Da Silva, E. Cuara-Diaz, and D. Morales-Acosta, "Effect of sulfonating agent in the properties of styrene copolymers for PEMFC membranes," *Int. J. Hydrogen Energy*, vol. 47, no. 70, pp. 30303–30314, Aug. 2022, doi: 10.1016/j.ijhydene.2022.07.022.
- [35] H. H. Roth, "Sulfonation of Poly (vinyl Aromatics)," *Ind. Eng. Chem.*, vol. 49, no. 11, pp. 1820–1822, Nov. 1957, doi: 10.1021/ie50575a022.
- [36] A. G. Theodoropoulos, V. T. Tsakalos, and G. N. Valkanas, "Sulfone-type crosslinks in sulfonation of macronet polystyrene backbone," *Polymer*



- (*Guldf*)., vol. 34, no. 18, pp. 3905–3910, Sep. 1993, doi: 10.1016/0032-3861(93)90518-F.
- [37] D. Baigl, T. A. P. Seery, and C. E. Williams, “Preparation and Characterization of Hydrosoluble, Partially Charged Poly(styrenesulfonate)s of Various Controlled Charge Fractions and Chain Lengths,” *Macromolecules*, vol. 35, no. 6, pp. 2318–2326, Mar. 2002, doi: 10.1021/ma011707o.
- [38] C. I. Piñón-Balderrama, C. Leyva-Porras, A. S. Conejo-Dávila, and E. A. Zaragoza-Contreras, “Sulfonated Block Copolymers: Synthesis, Chemical Modification, Self-Assembly Morphologies, and Recent Applications,” *Polymers (Basel)*., vol. 14, no. 23, p. 5081, Nov. 2022, doi: 10.3390/polym14235081.
- [39] X.-S. Wang, R. A. Jackson, and S. P. Armes, “Facile Synthesis of Acidic Copolymers via Atom Transfer Radical Polymerization in Aqueous Media at Ambient Temperature,” *Macromolecules*, vol. 33, no. 2, pp. 255–257, Jan. 2000, doi: 10.1021/ma991612a.
- [40] G. Masci *et al.*, “Atom Transfer Radical Polymerization of Potassium 3-Sulfopropyl Methacrylate: Direct Synthesis of Amphiphilic Block Copolymers with Methyl Methacrylate,” *Macromolecules*, vol. 37, no. 12, pp. 4464–4473, Jun. 2004, doi: 10.1021/ma0497254.
- [41] A. Guzik and P. Raffa, “Direct synthesis via RAFT of amphiphilic diblock polyelectrolytes facilitated by the use of a polymerizable ionic liquid as a monomer,” *Polym. Chem.*, vol. 12, no. 38, pp. 5505–5517, 2021, doi: 10.1039/D1PY00801C.
- [42] K. Baek, “Synthesis and characterization of sulfonated block copolymers by atom transfer radical polymerization,” *J. Polym. Sci. Part A Polym. Chem.*, vol. 46, no. 18, pp. 5991–5998, Sep. 2008, doi: 10.1002/pola.22568.
- [43] K. Baek, H. Kim, S. Lee, K. Cho, H. T. Kim, and S. S. Hwang, “Morphology Control of Highly Sulfonated Block Copolymers by a Simple Thermal Process,” *Macromol. Chem. Phys.*, vol. 211, no. 6, pp. 613–617, Mar. 2010, doi: 10.1002/macp.200900475.

- [44] K. Sato, T. Kajita, and A. Noro, "Synthesis of a Cross-Linked Polymer Electrolyte Membrane with an Ultra-High Density of Sulfonic Acid Groups," *ACS Appl. Polym. Mater.*, vol. 5, no. 5, pp. 3480–3488, May 2023, doi: 10.1021/acsapm.3c00150.
- [45] H. Okamura, Y. Takatori, M. Tsunooka, and M. Shirai, "Synthesis of random and block copolymers of styrene and styrenesulfonic acid with low polydispersity using nitroxide-mediated living radical polymerization technique," *Polymer (Guildf.)*, vol. 43, no. 11, pp. 3155–3162, May 2002, doi: 10.1016/S0032-3861(02)00162-3.
- [46] K. Matsumoto, S. Kage, and H. Matsuoka, "Synthesis of water-dispersible, fluorinated particles with grafting sulfonate chains by the core crosslinking of block copolymer micelles," *J. Polym. Sci. Part A Polym. Chem.*, vol. 45, no. 7, pp. 1316–1323, Apr. 2007, doi: 10.1002/pola.21903.
- [47] J. Zhang, M. R. Dubay, C. J. Houtman, and S. J. Severtson, "Sulfonated Amphiphilic Block Copolymers: Synthesis, Self-Assembly in Water, and Application as Stabilizer in Emulsion Polymerization," *Macromolecules*, vol. 42, no. 14, pp. 5080–5090, Jul. 2009, doi: 10.1021/ma900795f.
- [48] L. Chen, D. T. Hallinan, Y. A. Elabd, and M. A. Hillmyer, "Highly Selective Polymer Electrolyte Membranes from Reactive Block Polymers," *Macromolecules*, vol. 42, no. 16, pp. 6075–6085, Aug. 2009, doi: 10.1021/ma901272s.
- [49] H. Mori, E. Kudo, Y. Saito, A. Onuma, and M. Morishima, "RAFT Polymerization of Vinyl Sulfonate Esters for the Controlled Synthesis of Poly(lithium vinyl sulfonate) and Sulfonated Block Copolymers," *Macromolecules*, vol. 43, no. 17, pp. 7021–7032, Sep. 2010, doi: 10.1021/ma100905w.
- [50] J. Kolomanska *et al.*, "Design, synthesis and thermal behaviour of a series of well-defined clickable and triggerable sulfonate polymers," *RSC Adv.*, vol. 5, no. 82, pp. 66554–66562, 2015, doi: 10.1039/C5RA13867A.
- [51] A. Postma and M. Skidmore, "How to Do a RAFT Polymerization," in *RAFT Polymerization, Volume 1.*, E. R. Graeme Moad, Ed. Weinheim,

- Germany: Wiley, 2021, pp. 25–58. doi: 10.1002/9783527821358.ch3.
- [52] G. Moad, “RAFT polymerization to form stimuli-responsive polymers,” *Polym. Chem.*, vol. 8, no. 1, pp. 177–219, 2017, doi: 10.1039/C6PY01849A.
- [53] S. Perrier, “50th Anniversary Perspective : RAFT Polymerization—A User Guide,” *Macromolecules*, vol. 50, no. 19, pp. 7433–7447, Oct. 2017, doi: 10.1021/acs.macromol.7b00767.
- [54] R. Samatham *et al.*, “Active polymers: An overview,” in *Electroactive Polymers for Robotic Applications: Artificial Muscles and Sensors*, Springer London, 2007, pp. 1–36. doi: 10.1007/978-1-84628-372-7\_1.
- [55] S. K. Nayak, S. Mohanty, and L. Unnikrishnan, Eds., *Trends and Applications in Advanced Polymeric Materials*. Hoboken, NJ, USA: John Wiley & Sons, Inc., 2017. doi: 10.1002/9781119364795.
- [56] K. Gurunathan, A. V. Murugan, R. Marimuthu, U. P. Mulik, and D. P. Amalnerkar, “Electrochemically synthesized conducting polymeric materials for applications towards technology in electronics, optoelectronics and energy storage devices,” *Materials Chemistry and Physics*, vol. 61, no. 3. Elsevier Sequoia SA, pp. 173–191, Nov. 01, 1999. doi: 10.1016/S0254-0584(99)00081-4.
- [57] W. C. Roentgen, “About the changes in shape and volume of dielectrics caused by electricity,” *Annu. Phys. Chem. Ser.*, vol. 11, pp. 771–786, 1880.
- [58] M. P. Sacerdote, “On the electrical deformation of isotropic dielectric solids,” *J. Phys.*, vol. 11, no. t, pp. 282–285, 1899.
- [59] Y. Bar-Cohen, Ed., *Electroactive Polymer (EAP) Actuators as Artificial Muscles: Reality, Potential, and Challenges, Second Edition*. 1000 20th Street, Bellingham, WA 98227-0010 USA: SPIE, 2004. doi: 10.1117/3.547465.
- [60] B. Scrosati, *Applications of Electroactive Polymers*. Springer Netherlands, 1993. doi: 10.1007/978-94-011-1568-1.
- [61] Y. Bar-Cohen, S. Sherrit, and S.-S. Lih, “Characterization of the electromechanical properties of EAP materials,” in *Smart Structures and*

- Materials 2001: Electroactive Polymer Actuators and Devices*, Jul. 2001, vol. 4329, p. 319. doi: 10.1117/12.432663.
- [62] L. A. Hirano, M. T. Escote, L. S. Martins-Filho, G. L. Mantovani, and C. H. Scuracchio, "Development of Artificial Muscles Based on Electroactive Ionomeric Polymer-Metal Composites," *Artif. Organs*, vol. 35, no. 5, pp. 478–483, May 2011, doi: 10.1111/j.1525-1594.2011.01259.x.
- [63] S. Li, Y. Qin, J. Shi, Z.-X. Guo, Y. Li, and D. Zhu, "Electrical Properties of Soluble Carbon Nanotube/Polymer Composite Films," *Chem. Mater.*, vol. 17, no. 1, pp. 130–135, Jan. 2005, doi: 10.1021/cm0491025.
- [64] A. Leronni and L. Bardella, "Modeling actuation and sensing in ionic polymer metal composites by electrochemo-poromechanics," *J. Mech. Phys. Solids*, vol. 148, no. January, p. 104292, 2021, doi: 10.1016/j.jmps.2021.104292.
- [65] J. Bar-Cohen, Y.; Leary, S.; Oguro, K.; Tadokoro, S.; Harrison, J.; Smith, "Challenges to the Transition of IPMC Artificial Muscle Actuators to Practical Application," 1999. [Online]. Available: <https://dataverse.jpl.nasa.gov/dataset.xhtml?persistentId=hdl:2014/17624>
- [66] F. Carpi, A. Tralli, D. Rossi, and P. Gaudenzi, "Martian jumping rover equipped with electroactive polymer actuators: A preliminary study," *IEEE Trans. Aerosp. Electron. Syst.*, vol. 43, no. 1, pp. 79–92, Jan. 2007, doi: 10.1109/TAES.2007.357156.
- [67] N. Minaian, Z. J. Olsen, and K. J. Kim, "Ionic Polymer-Metal Composite (IPMC) Artificial Muscles in Underwater Environments: Review of Actuation, Sensing, Controls, and Applications to Soft Robotics," in *Bioinspired Sensing, Actuation, and Control in Underwater Soft Robotic Systems*, Springer International Publishing, 2021, pp. 117–139. doi: 10.1007/978-3-030-50476-2\_6.
- [68] D. Pugal, K. Jung, A. Aabloo, and K. J. Kim, "Ionic polymer-metal composite mechano-electrical transduction: review and perspectives," *Polym. Int.*, vol. 59, no. 3, pp. 279–289, Jan. 2010, doi: 10.1002/pi.2759.
- [69] I. Must *et al.*, "Ionic liquid-based actuators working in air: The effect of ambient humidity," *Sensors Actuators, B Chem.*, vol. 202, pp. 114–122,

- 2014, doi: 10.1016/j.snb.2014.05.074.
- [70] R. Tiwari and K. J. Kim, "IPMC as a mechanoelectric energy harvester: Tailored properties," *Smart Mater. Struct.*, vol. 22, no. 1, Jan. 2013, doi: 10.1088/0964-1726/22/1/015017.
- [71] J. Torop, V. Palmre, M. Arulepp, T. Sugino, K. Asaka, and A. Aabloo, "Flexible supercapacitor-like actuator with carbide-derived carbon electrodes," *Carbon N. Y.*, vol. 49, no. 9, pp. 3113–3119, Aug. 2011, doi: 10.1016/j.carbon.2011.03.034.
- [72] F. Carpi and E. Smela, *Biomedical Applications of Electroactive Polymer Actuators*. Chichester, UK: John Wiley & Sons, Ltd, 2009. doi: 10.1002/9780470744697.
- [73] R. M. Vedovatte, M. C. Saccardo, E. L. Costa, and C. E. Cava, "PEDOT:PSS post-treated by DMSO using spin coating, roll-to-roll and immersion: a comparative study," *J. Mater. Sci. Mater. Electron.*, vol. 31, no. 1, pp. 317–323, 2020, doi: 10.1007/s10854-019-02524-1.
- [74] R. H. Baughman *et al.*, "Carbon Nanotube Actuators," *Science (80-. )*, vol. 284, no. 5418, pp. 1340–1344, May 1999, doi: 10.1126/science.284.5418.1340.
- [75] A. Punning *et al.*, "Ionic electroactive polymer artificial muscles in space applications," *Sci. Rep.*, vol. 4, pp. 1–6, 2014, doi: 10.1038/srep06913.
- [76] Y. Bar-Cohen, "Electroactive polymers: current capabilities and challenges," in *Smart Structures and Materials 2002: Electroactive Polymer Actuators and Devices (EAPAD)*, Jul. 2002, vol. 4695, pp. 1–7. doi: 10.1117/12.475159.
- [77] Y. Bar-Cohen, T. Xue, M. Shahinpoor, J. S. Harrison, and J. G. Smith, "Low-mass muscle actuators using electroactive polymers (EAP)," Jul. 1998, p. 218. doi: 10.1117/12.316866.
- [78] I. Bergman, "Improvements in or relating to membrane electrodes and cells," 1,200,595, 1970, 1970
- [79] C. A. Levine and A. L. Prevost, "Process for plating permeable membrane," 1,143,883, 1967
- [80] D. B. Adolf, M. Shahinpoor, D. J. Segalman, and W. R. Witkowski,

- “Electrically controlled polymeric gel actuators,” US5250167A, 1993
- [81] K. Oguro, H. Takenaka, and Y. Kawami, “Actuator element,” US 5,268,082, 1993
- [82] K. A. Mauritz and R. B. Moore, “State of Understanding of Nafion,” *Chem. Rev.*, 2004, doi: 10.1021/cr0207123.
- [83] T. A. Zawodzinski *et al.*, “Water Uptake by and Transport Through Nafion® 117 Membranes,” *J. Electrochem. Soc.*, vol. 140, no. 4, pp. 1041–1047, Apr. 1993, doi: 10.1149/1.2056194.
- [84] G. Gebel and R. B. Moore, “Small-Angle Scattering Study of Short Pendant Chain Perfluorosulfonated Ionomer Membranes,” *Macromolecules*, vol. 33, no. 13, pp. 4850–4855, Jun. 2000, doi: 10.1021/ma9912709.
- [85] M. C. Saccardo, “Estudo do comportamento eletromecânico de músculos artificiais baseados em compósitos de polímero iomérico e metal por meio da análise de vídeo,” Universidade Federal de São Carlos, 2020. [Online]. Available: <https://repositorio.ufscar.br/handle/ufscar/12771>
- [86] R. Barbosa *et al.*, “Novel IP 2 C sensors with flexible electrodes based on plasma-treated conductive elastomeric nanocomposites,” *Smart Mater. Struct.*, vol. 33, no. 2, p. 025008, Feb. 2024, doi: 10.1088/1361-665X/ad1c50.
- [87] S. Nemat-Nasser and Y. Wu, “Comparative experimental study of ionic polymer–metal composites with different backbone ionomers and in various cation forms,” *J. Appl. Phys.*, vol. 93, no. 9, pp. 5255–5267, May 2003, doi: 10.1063/1.1563300.
- [88] W. Yanjie, C. Hualing, W. Yongquan, Z. Zicai, and L. Dichen, “Effect of Dehydration on the Mechanical and Physicochemical Properties of Gold- and Palladium -Ionomeric Polymer-Metal Composite (IPMC) Actuators,” *Electrochim. Acta*, vol. 129, pp. 450–458, 2014, doi: 10.1016/j.electacta.2014.02.114.
- [89] T. D. Gierke, G. E. Munn, and F. C. Wilson, “The morphology in nafion perfluorinated membrane products, as determined by wide- and small-angle x-ray studies,” *J. Polym. Sci. Polym. Phys. Ed.*, vol. 19, no. 11, pp.

- 1687–1704, Nov. 1981, doi: 10.1002/pol.1981.180191103.
- [90] W. Y. Hsu, T. D. Gierke, and T. D. Gierke, “Elastic Theory for Ionic Clustering in Perfluorinated Ionomers,” *Macromolecules*, vol. 15, no. 1, pp. 101–105, 1982, doi: 10.1021/ma00229a020.
- [91] W. Y. Hsu and T. D. Gierke, “Ion transport and clustering in nafion perfluorinated membranes,” *J. Memb. Sci.*, vol. 13, no. 3, pp. 307–326, Feb. 1983, doi: 10.1016/S0376-7388(00)81563-X.
- [92] M. Fujimura, T. Hashimoto, and H. Kawai, “Small-Angle X-ray Scattering Study of Perfluorinated Ionomer Membranes. 2. Models for Ionic Scattering Maximum,” *Macromolecules*, vol. 15, no. 1, pp. 136–144, 1982, doi: 10.1021/ma00229a028.
- [93] B. Dreyfus, G. Gebel, P. Aldebert, M. Pineri, M. Escoubes, and M. Thomas, “Distribution of the « micelles » in hydrated perfluorinated ionomer membranes from SANS experiments,” *J. Phys.*, vol. 51, no. 12, pp. 1341–1354, 1990, doi: 10.1051/jphys:0199000510120134100.
- [94] M. H. Litt, “Reevaluation of Nafion morphology,” *Am. Chem. Soc. Polym. Prepr. Div. Polym. Chem.*, vol. 38, no. 1, pp. 80–81, 1997.
- [95] H. G. Haubold, T. Vad, H. Jungbluth, and P. Hiller, “Nano structure of NAFION: A SAXS study,” *Electrochim. Acta*, vol. 46, no. 10–11, pp. 1559–1563, 2001, doi: 10.1016/S0013-4686(00)00753-2.
- [96] L. Rubatat, A. L. Rollet, G. Gebel, and O. Diat, “Evidence of Elongated Polymeric Aggregates in Nafion,” *Macromolecules*, vol. 35, no. 10, pp. 4050–4055, May 2002, doi: 10.1021/ma011578b.
- [97] J. A. E. and, S. Hanna\*, A. M. S. Elliott, and G. E. Cooley, “Interpretation of the Small-Angle X-ray Scattering from Swollen and Oriented Perfluorinated Ionomer Membranes,” 2000, doi: 10.1021/MA991113+.
- [98] G. Gebel, “Structural evolution of water swollen perfluorosulfonated ionomers from dry membrane to solution,” *Polymer (Guildf.)*, vol. 41, no. 15, pp. 5829–5838, 2000, doi: 10.1016/S0032-3861(99)00770-3.
- [99] K. Schmidt-Rohr, “Simulation of small-angle scattering curves by numerical Fourier transformation,” *J. Appl. Crystallogr.*, vol. 40, no. 1, pp. 16–25, Jan. 2007, doi: 10.1107/S002188980604550X.

- [100] K. Schmidt-Rohr and Q. Chen, "Parallel cylindrical water nanochannels in nafion fuel-cell membranes," *Mater. Sustain. Energy A Collect. Peer-Reviewed Res. Rev. Artic. from Nat. Publ. Gr.*, pp. 238–246, 2010, doi: 10.1142/9789814317665\_0033.
- [101] J. A. Elliott, D. Wu, S. J. Paddison, and R. B. Moore, "A unified morphological description of Nafion membranes from SAXS and mesoscale simulations," *Soft Matter*, vol. 7, no. 15, pp. 6820–6827, Aug. 2011, doi: 10.1039/c1sm00002k.
- [102] M. Abachizadeh, A. Yousefi-Koma, and M. Shariatpanahi, "Optimization of a beam-type ipmc actuator using insects swarm intelligence methods," in *ASME 2010 10th Biennial Conference on Engineering Systems Design and Analysis, ESDA2010*, 2010, vol. 1, pp. 559–566. doi: 10.1115/ESDA2010-24840.
- [103] J. Min, D. Barpuzary, H. Ham, G.-C. Kang, and M. J. Park, "Charged Block Copolymers: From Fundamentals to Electromechanical Applications," *Acc. Chem. Res.*, vol. 54, no. 21, pp. 4024–4035, Nov. 2021, doi: 10.1021/acs.accounts.1c00423.
- [104] C. Zhao, X. Li, Z. Wang, Z. Dou, S. Zhong, and H. Na, "Synthesis of the block sulfonated poly(ether ether ketone)s (S-PEEKs) materials for proton exchange membrane," *J. Memb. Sci.*, vol. 280, no. 1–2, pp. 643–650, Sep. 2006, doi: 10.1016/j.memsci.2006.02.028.
- [105] M. A. Hickner, H. Ghassemi, Y. S. Kim, B. R. Einsla, and J. E. McGrath, "Alternative Polymer Systems for Proton Exchange Membranes (PEMs)," *Chem. Rev.*, vol. 104, no. 10, pp. 4587–4612, Oct. 2004, doi: 10.1021/cr020711a.
- [106] I. W. Hamley, "Block Copolymers," in *Encyclopedia of Polymer Science and Technology*, Hoboken, NJ, USA: John Wiley & Sons, Inc., 2002. doi: 10.1002/0471440264.pst030.
- [107] T. P. Lodge, "Block Copolymers: Past Successes and Future Challenges," *Macromol. Chem. Phys.*, vol. 204, no. 2, pp. 265–273, Feb. 2003, doi: 10.1002/macp.200290073.
- [108] H. Dau *et al.*, "Linear Block Copolymer Synthesis," *Chem. Rev.*, vol. 122,



- no. 18, pp. 14471–14553, Sep. 2022, doi: 10.1021/acs.chemrev.2c00189.
- [109] P. Samaddar, A. Deep, and K.-H. Kim, “An engineering insight into block copolymer self-assembly: Contemporary application from biomedical research to nanotechnology,” *Chem. Eng. J.*, vol. 342, pp. 71–89, Jun. 2018, doi: 10.1016/j.cej.2018.01.062.
- [110] S. Zhao, L. Zhang, and J. Tan, “In Situ Synthesis of Branched Block Copolymer Assemblies via RAFT Dispersion Polymerization Using Branched Macro-RAFT Agents †,” *Chinese J. Chem.*, vol. 41, no. 12, pp. 1517–1525, Jun. 2023, doi: 10.1002/cjoc.202200761.
- [111] S. V Canevarolo, *Ciência dos Polímeros: Um texto básico para tecnólogos e engenheiros*, 3ª Edição. São Paulo - SP: Artliber, 2002. Accessed: Nov. 23, 2019. [Online]. Available: [www.artliber.com.br](http://www.artliber.com.br)
- [112] M. Szwarc, “‘Living’ polymers,” *Nature*, vol. 178, no. 4543, pp. 1168–1169, 1956, doi: 10.1038/1781168a0.
- [113] M. Szwarc, “Living polymers. Their discovery, characterization, and properties,” *J. Polym. Sci. Part A Polym. Chem.*, vol. 36, 1998, doi: doi.org/10.1002/(SICI)1099-0518(19980115)36:1<IX::AID-POLA2>3.0.CO;2-9.
- [114] A. Bagheri, S. Boniface, and C. M. Fellows, “Reversible-Deactivation Radical Polymerisation: chain polymerisation made simple,” *Chem. Teach. Int.*, vol. 3, no. 2, pp. 19–32, Jun. 2021, doi: 10.1515/cti-2020-0025.
- [115] C. L. Araújo, “Polimerização Radicalar Controlada De Estireno Com Alfa-Metil-Estireno E Metacrilato De Metila Mediada Por Nitróxido Em Reator Tubular,” Universidade Federal do Rio de Janeiro, RJ, 2010. Accessed: Nov. 23, 2019. [Online]. Available: <http://www.livrosgratis.com.br>
- [116] M. Chanda, *Introduction to Polymer Science and Chemistry*. CRC Press, 2013. doi: 10.1201/b14577.
- [117] M. A. Morris, S. C. Padmanabhan, M. C. Cruz-Romero, E. Cummins, and J. P. Kerry, “Development of active, nanoparticle, antimicrobial technologies for muscle-based packaging applications,” *Meat Sci.*, vol. 132, pp. 163–178, Oct. 2017, doi: 10.1016/j.meatsci.2017.04.234.

- [118] S. Biswas, P. Kumari, P. M. Lakhani, and B. Ghosh, "Recent advances in polymeric micelles for anti-cancer drug delivery," *Eur. J. Pharm. Sci.*, vol. 83, pp. 184–202, Feb. 2016, doi: 10.1016/j.ejps.2015.12.031.
- [119] J. R. Werber, C. O. Osuji, and M. Elimelech, "Materials for next-generation desalination and water purification membranes," *Nat. Rev. Mater.*, vol. 1, no. 5, p. 16018, Apr. 2016, doi: 10.1038/natrevmats.2016.18.
- [120] T. Guo, J. Gao, X. Qin, X. Zhang, and H. Xue, "A Novel Glucose Biosensor Based on Hierarchically Porous Block Copolymer Film," *Polymers (Basel)*, vol. 10, no. 7, p. 723, Jul. 2018, doi: 10.3390/polym10070723.
- [121] I. F. Jeeperay, T. Goto, K. Sudesh, and H. Abe, "Biodegradable block copolymer as compatibilizer and blend component of poly(3-hydroxybutyrate-co-3-hydroxyhexanoate)-based polyester blends," *Eur. Polym. J.*, vol. 196, p. 112314, Sep. 2023, doi: 10.1016/j.eurpolymj.2023.112314.
- [122] C. Cummins, R. Lundy, J. J. Walsh, V. Ponsinet, G. Fleury, and M. A. Morris, "Enabling future nanomanufacturing through block copolymer self-assembly: A review," *Nano Today*, vol. 35, p. 100936, Dec. 2020, doi: 10.1016/j.nantod.2020.100936.
- [123] N. P. S. Chauhan, *Functionalized Polymers*, 1st Editio. Boca Raton, Florida, United States: CRC Press, 2021. doi: 10.1201/9780367821913.
- [124] R. J. Spontak and N. P. Patel, "Thermoplastic elastomers: fundamentals and applications," *Curr. Opin. Colloid Interface Sci.*, vol. 5, no. 5–6, pp. 333–340, Nov. 2000, doi: 10.1016/S1359-0294(00)00070-4.
- [125] G. Holden, "Thermoplastic Elastomers," in *Applied Plastics Engineering Handbook*, Elsevier, 2011, pp. 77–91. doi: 10.1016/B978-1-4377-3514-7.10006-6.
- [126] P. Weiss, "Block copolymers – overview and critical survey, Allen Noshay and James E. Mcgrath, Academic, New York, 1977, 516 pp.," *J. Polym. Sci. Polym. Lett. Ed.*, vol. 16, no. 3, pp. 151–152, Mar. 1978, doi: 10.1002/pol.1978.130160313.

- [127] E. Dalas, C. D. Xenos, S. Sakkopoulos, and E. Vitoratos, "Epoxidized styrene-butadiene-cupric oxide polymer used as a cathode in the construction of a novel solid electrolyte dry cell," *Appl. Surf. Sci.*, vol. 119, no. 3–4, pp. 313–317, 1997, doi: 10.1016/S0169-4332(97)00199-2.
- [128] M. Szwarc, M. Levy, and R. Milkovich, "Polymerization initiated by electron transfer to monomer. A new method of formation of block polymers," *J. Am. Chem. Soc.*, vol. 78, no. 11, pp. 2656–2657, Jun. 1956, doi: 10.1021/ja01592a101.
- [129] M. Morton and L. J. Fetters, "Anionic Polymerization of Vinyl Monomers," *Rubber Chem. Technol.*, vol. 48, no. 3, pp. 359–409, Jul. 1975, doi: 10.5254/1.3547458.
- [130] K. Matyjaszewski, "Discovery of the RAFT Process and Its Impact on Radical Polymerization," *Macromolecules*, vol. 53, no. 2, pp. 495–497, Jan. 2020, doi: 10.1021/acs.macromol.9b02054.
- [131] J. Chiefari *et al.*, "Living Free-Radical Polymerization by Reversible Addition–Fragmentation Chain Transfer: The RAFT Process," *Macromolecules*, vol. 31, no. 16, pp. 5559–5562, Aug. 1998, doi: 10.1021/ma9804951.
- [132] M. A. M. Oliveira, M. Nele, and J. C. Pinto, "Polimerização RAFT em Miniemulsão," *Polímeros Ciência e Tecnol.*, vol. 23, no. 6, pp. 784–797, 2013, doi: 10.4322/polimeros.2014.013.
- [133] P. B. Zetterlund, Y. Kagawa, and M. Okubo, "Controlled/Living Radical Polymerization in Dispersed Systems," *Chem. Rev.*, vol. 108, no. 9, pp. 3747–3794, Sep. 2008, doi: 10.1021/cr800242x.
- [134] A. D. Jenkins, R. G. Jones, and G. Moad, "Terminology for reversible-deactivation radical polymerization previously called 'controlled' radical or 'living' radical polymerization (IUPAC Recommendations 2010)," *Pure Appl. Chem.*, vol. 82, no. 2, pp. 483–491, Nov. 2009, doi: 10.1351/PAC-REP-08-04-03.
- [135] C. Boyer, V. Bulmus, T. P. Davis, V. Ladmiral, J. Liu, and S. Perrier, "Bioapplications of RAFT Polymerization," *Chem. Rev.*, vol. 109, no. 11, pp. 5402–5436, Nov. 2009, doi: 10.1021/cr9001403.

- [136] G. Odian, *Principles of Polymerization*. Hoboken, NJ, USA: John Wiley & Sons, Inc., 2004. doi: 10.1002/047147875X.
- [137] J. P. A. Heuts, "Theory of Radical Reactions," in *Handbook of Radical Polymerization*, Wiley, 2002, pp. 1–76. doi: 10.1002/0471220450.ch1.
- [138] T. Fukuda, A. Goto, and Y. Tsujii, "Kinetics of Living Radical Polymerization," in *Handbook of Radical Polymerization*, Hoboken, NJ, USA: John Wiley & Sons, Inc., pp. 407–462. doi: 10.1002/0471220450.ch9.
- [139] D. Colombani, "Chain-growth control in free radical polymerization," *Prog. Polym. Sci.*, vol. 22, no. 8, pp. 1649–1720, Jan. 1997, doi: 10.1016/S0079-6700(97)00022-1.
- [140] G. Moad, E. Rizzardo, and S. H. Thang, "Living Radical Polymerization by the RAFT Process," *Aust. J. Chem.*, vol. 58, no. 6, p. 379, 2005, doi: 10.1071/CH05072.
- [141] M. Szwarc, "Living polymers and mechanisms of anionic polymerization," in *Living Polymers and Mechanisms of Anionic Polymerization*, Berlin, Heidelberg: Springer Berlin Heidelberg, pp. 1–177. doi: 10.1007/3-540-12047-5\_1.
- [142] N. Corrigan, K. Jung, G. Moad, C. J. Hawker, K. Matyjaszewski, and C. Boyer, "Reversible-deactivation radical polymerization (Controlled/living radical polymerization): From discovery to materials design and applications," *Prog. Polym. Sci.*, vol. 111, p. 101311, Dec. 2020, doi: 10.1016/j.progpolymsci.2020.101311.
- [143] T. Otsu and M. Yoshida, "Role of initiator-transfer agent-terminator (iniferter) in radical polymerizations: Polymer design by organic disulfides as iniferters," *Die Makromol. Chemie, Rapid Commun.*, vol. 3, no. 2, pp. 127–132, Feb. 1982, doi: 10.1002/MARC.1982.030030208.
- [144] R. B. Grubbs, "Nitroxide-Mediated Radical Polymerization: Limitations and Versatility," *Polym. Rev.*, vol. 51, no. 2, pp. 104–137, Apr. 2011, doi: 10.1080/15583724.2011.566405.
- [145] K. Matyjaszewski, "Advanced Materials by Atom Transfer Radical Polymerization," *Adv. Mater.*, vol. 30, no. 23, p. 1706441, Jun. 2018, doi:

10.1002/adma.201706441.

- [146] G. Moad, "Terminology in Reversible Deactivation Radical Polymerization (RDRP) and Reversible Addition–Fragmentation Chain Transfer (RAFT) Polymerization," in *RAFT Polymerization*, Wiley, 2021, pp. 15–24. doi: 10.1002/9783527821358.ch2.
- [147] A. Goto and T. Fukuda, "Kinetics of living radical polymerization," *Prog. Polym. Sci.*, vol. 29, no. 4, pp. 329–385, Apr. 2004, doi: 10.1016/j.progpolymsci.2004.01.002.
- [148] J. Nicolas, Y. Guillaneuf, C. Lefay, D. Bertin, D. Gigmes, and B. Charleux, "Nitroxide-mediated polymerization," *Prog. Polym. Sci.*, vol. 38, no. 1, pp. 63–235, Jan. 2013, doi: 10.1016/j.progpolymsci.2012.06.002.
- [149] A. K. Fung and M. L. Coote, "A mechanistic perspective on atom transfer radical polymerization," *Polym. Int.*, vol. 70, no. 7, pp. 918–926, Jul. 2021, doi: 10.1002/pi.6130.
- [150] S. M. R. Estakhrposhti and M. Abdollahi, "Reverse iodine transfer copolymerization of styrene and acrylonitrile: copolymer synthesis, characterization and kinetic study," *J. Polym. Res.*, vol. 28, no. 8, p. 283, Aug. 2021, doi: 10.1007/s10965-021-02557-3.
- [151] F. Lorandi, M. Fantin, and K. Matyjaszewski, "Atom Transfer Radical Polymerization: A Mechanistic Perspective," *J. Am. Chem. Soc.*, vol. 144, no. 34, pp. 15413–15430, Aug. 2022, doi: 10.1021/jacs.2c05364.
- [152] C. Boyer, M. H. Stenzel, and T. P. Davis, "Building nanostructures using RAFT polymerization," *J. Polym. Sci. Part A Polym. Chem.*, vol. 49, no. 3, pp. 551–595, Feb. 2011, doi: 10.1002/pola.24482.
- [153] J. Krstina, G. Moad, E. Rizzardo, C. L. Winzor, C. T. Berge, and M. Fryd, "Narrow Polydispersity Block Copolymers by Free-Radical Polymerization in the Presence of Macromonomers," *Macromolecules*, vol. 28, no. 15, pp. 5381–5385, Jul. 1995, doi: 10.1021/ma00119a034.
- [154] C. L. Moad, G. Moad, E. Rizzardo, and S. H. Thang, "Chain Transfer Activity of  $\omega$ -Unsaturated Methyl Methacrylate Oligomers," *Macromolecules*, vol. 29, no. 24, pp. 7717–7726, Jan. 1996, doi: 10.1021/ma960852c.

- [155] B. B. Wayland, G. Poszmik, S. L. Mukerjee, and M. Fryd, "Living Radical Polymerization of Acrylates by Organocobalt Porphyrin Complexes," *J. Am. Chem. Soc.*, vol. 116, no. 17, pp. 7943–7944, Aug. 1994, doi: 10.1021/ja00096a080.
- [156] E. R. Graeme Moad, "Polymerization with living characteristics," WO Patent 9801478, Jul. 03, 1998
- [157] D. M. Pascale Corpart, Dominique Charmot, Thibaud Biadatti, Samir Zard, "Procédé de synthèse de polymères à blocs par polymérisation radicalaire contrôlée," Jun. 23, 1998
- [158] G. Moad, E. Rizzardo, and S. H. Thang, "Living Radical Polymerization by the RAFT Process—A First Update," *Aust. J. Chem.*, vol. 59, no. 10, p. 669, 2006, doi: 10.1071/CH06250.
- [159] G. Moad, E. Rizzardo, and S. H. Thang, "Living Radical Polymerization by the RAFT Process - A Second Update," *Aust. J. Chem.*, vol. 62, no. 11, p. 1402, 2009, doi: 10.1071/CH09311.
- [160] G. Moad, E. Rizzardo, and S. H. Thang, "Living Radical Polymerization by the RAFT Process – A Third Update," *Aust. J. Chem.*, vol. 65, no. 8, p. 985, 2012, doi: 10.1071/CH12295.
- [161] C. Barner-Kowollik, *Handbook of RAFT Polymerization*. Wiley, 2008. doi: 10.1002/9783527622757.
- [162] D. J. Keddie, "A guide to the synthesis of block copolymers using reversible-addition fragmentation chain transfer (RAFT) polymerization," *Chem. Soc. Rev.*, vol. 43, no. 2, pp. 496–505, 2014, doi: 10.1039/C3CS60290G.
- [163] J. M. Ren *et al.*, "Star Polymers," *Chem. Rev.*, vol. 116, no. 12, pp. 6743–6836, Jun. 2016, doi: 10.1021/acs.chemrev.6b00008.
- [164] G. Moad, "RAFT (Reversible addition-fragmentation chain transfer) crosslinking (co)polymerization of multi-olefinic monomers to form polymer networks," *Polym. Int.*, vol. 64, no. 1, pp. 15–24, Jan. 2015, doi: 10.1002/pi.4767.
- [165] A. Gregory and M. H. Stenzel, "Complex polymer architectures via RAFT polymerization: From fundamental process to extending the scope using

- click chemistry and nature's building blocks," *Prog. Polym. Sci.*, vol. 37, no. 1, pp. 38–105, Jan. 2012, doi: 10.1016/j.progpolymsci.2011.08.004.
- [166] P. Vana, *Controlled Radical Polymerization at and from Solid Surfaces*, vol. 270. Cham: Springer International Publishing, 2016. doi: 10.1007/978-3-319-22138-0.
- [167] M. Beija, J.-D. Marty, and M. Destarac, "RAFT/MADIX polymers for the preparation of polymer/inorganic nanohybrids," *Prog. Polym. Sci.*, vol. 36, no. 7, pp. 845–886, Jul. 2011, doi: 10.1016/j.progpolymsci.2011.01.002.
- [168] M. Semsarilar and S. Perrier, "'Green' reversible addition-fragmentation chain-transfer (RAFT) polymerization," *Nat. Chem.*, vol. 2, no. 10, pp. 811–820, Oct. 2010, doi: 10.1038/nchem.853.
- [169] T. Wu, D. Wang, M. Zhang, J. R. Heflin, R. B. Moore, and T. E. Long, "RAFT Synthesis of ABA Triblock Copolymers as Ionic Liquid-Containing Electroactive Membranes," *ACS Appl. Mater. Interfaces*, vol. 4, no. 12, pp. 6552–6559, Dec. 2012, doi: 10.1021/am301662s.
- [170] E. M. Pearce, "Polymers: Chemistry and physics of modern materials," *J. Polym. Sci. Part A Polym. Chem.*, vol. 30, no. 8, pp. 1777–1777, Jul. 1992, doi: 10.1002/pola.1992.080300836.
- [171] D. J. Keddie, G. Moad, E. Rizzardo, and S. H. Thang, "RAFT Agent Design and Synthesis," *Macromolecules*, vol. 45, no. 13, pp. 5321–5342, Jul. 2012, doi: 10.1021/ma300410v.
- [172] M. Destarac, "On the Critical Role of RAFT Agent Design in Reversible Addition-Fragmentation Chain Transfer (RAFT) Polymerization," *Polym. Rev.*, vol. 51, no. 2, pp. 163–187, Apr. 2011, doi: 10.1080/15583724.2011.568130.
- [173] G. Moad, D. Keddie, C. Guerrero-Sanchez, E. Rizzardo, and S. H. Thang, "Advances in Switchable RAFT Polymerization," *Macromol. Symp.*, vol. 350, no. 1, pp. 34–42, Apr. 2015, doi: 10.1002/masy.201400022.
- [174] Sigma Aldrich, "RAFT: Choosing the Right Agent to Achieve Controlled Polymerization." <https://www.sigmaaldrich.com/BR/pt/technical-documents/technical-article/materials-science-and-engineering/polymer-synthesis/raft-polymerization>

- [175] M. E. Gindy, R. K. Prud'Homme, and A. Z. Panagiotopoulos, "Phase behavior and structure formation in linear multiblock copolymer solutions by Monte Carlo simulation," *J. Chem. Phys.*, vol. 128, no. 16, 2008, doi: 10.1063/1.2905231.
- [176] K. A. Davis and K. Matyjaszewski, "ABC Triblock Copolymers Prepared Using Atom Transfer Radical Polymerization Techniques," *Macromolecules*, vol. 34, no. 7, pp. 2101–2107, Mar. 2001, doi: 10.1021/ma002050u.
- [177] J. M. Prausnitz, R. N. Lichtenthaler, E. G. de Azevedo, and E. G. Prausnitz, J. M.; Lichtenthaler, R. N.; Azevedo, *Molecular Thermodynamics of Fluid-Phase Equilibria*, 3rd ed. Hoboken, New Jersey, United States: Prentice Hall, 1999.
- [178] J. H. Hildebrand, "The Entropy of Solution of Molecules of Different Size," *J. Chem. Phys.*, vol. 15, no. 5, pp. 225–228, May 1947, doi: 10.1063/1.1746484.
- [179] K. Kamide and T. Dobashi, "Ideal and Non-Athermal Solutions," in *Physical Chemistry of Polymer Solutions*, Elsevier, 2000, pp. 11–49. doi: 10.1016/B978-044489430-4/50003-X.
- [180] M. D. Donohue and J. M. Prausnitz, "Combinatorial Entropy of Mixing Molecules that Differ in Size and Shape. A Simple Approximation for Binary and Multicomponent Mixtures," *Can. J. Chem.*, vol. 53, no. 11, pp. 1586–1592, Jun. 1975, doi: 10.1139/v75-224.
- [181] P. J. Flory, "Thermodynamics of High Polymer Solutions," *J. Chem. Phys.*, vol. 9, no. 8, pp. 660–660, Aug. 1941, doi: 10.1063/1.1750971.
- [182] R. D. Ulrich, "Macromolecular Science. Contemporary Topics in Polymer Science," in *Macromolecular Science*, Boston, MA: Springer US, 1978, pp. 99–111. doi: 10.1007/978-1-4684-2853-7\_6.
- [183] F. Sabzi and A. Boushehri, "Compatibility of polymer blends. I. Copolymers with organic solvents," *J. Appl. Polym. Sci.*, vol. 101, no. 1, pp. 492–498, Jul. 2006, doi: 10.1002/app.23092.
- [184] M. L. Huggins, "The Viscosity of Dilute Solutions of Long-Chain Molecules. IV. Dependence on Concentration," *J. Am. Chem. Soc.*, vol.



- 64, no. 11, pp. 2716–2718, Nov. 1942, doi: 10.1021/ja01263a056.
- [185] E. A. Guggenheim, “Statistical thermodynamics of mixtures with non-zero energies of mixing,” *Proc. R. Soc. London. Ser. A. Math. Phys. Sci.*, vol. 183, no. 993, pp. 213–227, Nov. 1944, doi: 10.1098/rspa.1944.0033.
- [186] A. J. Staverman, “The entropy of high polymer solutions. Generalization of formulae,” *Recl. des Trav. Chim. des Pays-Bas*, vol. 69, no. 2, pp. 163–174, Jan. 1950, doi: 10.1002/recl.19500690203.
- [187] H. Tompa, “Phase relationships in polymer solutions,” *Trans. Faraday Soc.*, vol. 45, p. 1142, 1949, doi: 10.1039/tf9494501142.
- [188] R. N. Lichtenthaler, D. S. Abrams, and J. M. Prausnitz, “Combinatorial Entropy of Mixing for Molecules Differing in Size and Shape,” *Can. J. Chem.*, vol. 51, no. 18, pp. 3071–3080, Sep. 1973, doi: 10.1139/v73-458.
- [189] T. Hino, Y. Song, and J. M. Prausnitz, “Liquid-Liquid Equilibria for Copolymer Mixtures from a Perturbed Hard-Sphere-Chain Equation of State,” *Macromolecules*, vol. 27, no. 20, pp. 5681–5690, Sep. 1994, doi: 10.1021/ma00098a023.
- [190] J. H. Hildebrand, “Order from Chaos,” *Science (80-. )*, vol. 150, no. 3695, pp. 441–450, Oct. 1965, doi: 10.1126/science.150.3695.441.
- [191] A. M. Nemirovsky and K. F. Freed, “Surface transition and epsilon expansion,” *J. Phys. A. Math. Gen.*, vol. 18, no. 16, pp. 3275–3279, Nov. 1985, doi: 10.1088/0305-4470/18/16/027.
- [192] T. Hino, Y. Song, and J. M. Prausnitz, “Equation-of-State Analysis of Binary Copolymer Systems. 3. Miscibility Maps,” *Macromolecules*, vol. 28, no. 17, pp. 5725–5733, Aug. 1995, doi: 10.1021/ma00121a006.
- [193] T. P. Russell, R. P. Hjelm, and P. A. Seeger, “Temperature dependence of the interaction parameter of polystyrene and poly(methyl methacrylate),” *Macromolecules*, vol. 23, no. 3, pp. 890–893, Feb. 1990, doi: 10.1021/ma00205a033.
- [194] C. C. Lin, S. V. Jonnalagadda, P. K. Kesani, H. J. Dai, and N. P. Balsara, “Effect of Molecular Structure on the Thermodynamics of Block Copolymer Melts,” *Macromolecules*, vol. 27, no. 26, pp. 7769–7780, Dec. 1994, doi: 10.1021/ma00104a035.

- [195] G. Miquelard-Garnier and S. Roland, "Beware of the Flory parameter to characterize polymer-polymer interactions: A critical reexamination of the experimental literature," *Eur. Polym. J.*, vol. 84, pp. 111–124, Nov. 2016, doi: 10.1016/j.eurpolymj.2016.09.009.
- [196] T. Koch and G. R. Strobl, "Concentration dependence of the flory-huggins interaction parameter of a polymer blend as determined by small-angle X-ray scattering experiments," *J. Polym. Sci. Part B Polym. Phys.*, vol. 28, no. 3, pp. 343–353, Feb. 1990, doi: 10.1002/polb.1990.090280307.
- [197] D. P. Sweat *et al.*, "Rational Design of a Block Copolymer with a High Interaction Parameter," *Macromolecules*, vol. 47, no. 19, pp. 6687–6696, Oct. 2014, doi: 10.1021/ma501597g.
- [198] S. X. Zhou, D. W. Janes, C. Bin Kim, C. G. Willson, and C. J. Ellison, "Designing Intrablock Attractions To Increase the  $\chi$  Parameter of a Symmetric Diblock Copolymer," *Macromolecules*, vol. 49, no. 21, pp. 8332–8340, Nov. 2016, doi: 10.1021/acs.macromol.6b01382.
- [199] J. D. Willis, T. M. Beardsley, and M. W. Matsen, "Simple and Accurate Calibration of the Flory–Huggins Interaction Parameter," *Macromolecules*, vol. 53, no. 22, pp. 9973–9982, Nov. 2020, doi: 10.1021/acs.macromol.0c02115.
- [200] J. D. Willis, T. M. Beardsley, and M. W. Matsen, "Calibration of a lattice model for high-molecular-weight block copolymer melts," *J. Chem. Phys.*, vol. 150, no. 20, May 2019, doi: 10.1063/1.5094144.
- [201] T. Ohta and K. Kawasaki, "Comment on the free energy functional of block copolymer melts in the strong segregation limit," *Macromolecules*, vol. 23, no. 8, pp. 2413–2414, Apr. 1990, doi: 10.1021/ma00210a047.
- [202] I. Goodman, *Developments in block copolymers - 2*, 1 Ed. Berlin/Heidelberg, Germany: Elsevier Applied Science Publishers, 1985.
- [203] E. Helfand, "Block Copolymer Theory. III. Statistical Mechanics of the Microdomain Structure," *Macromolecules*, vol. 8, no. 4, pp. 552–556, Jul. 1975, doi: 10.1021/ma60046a032.
- [204] L. Leibler, "Theory of Microphase Separation in Block Copolymers," *Macromolecules*, vol. 13, no. 6, pp. 1602–1617, Nov. 1980, doi:

- 10.1021/ma60078a047.
- [205] A. Reddy, X. Feng, E. L. Thomas, and G. M. Grason, "Block Copolymers beneath the Surface: Measuring and Modeling Complex Morphology at the Subdomain Scale," *Macromolecules*, vol. 54, no. 20, pp. 9223–9257, Oct. 2021, doi: 10.1021/acs.macromol.1c00958.
- [206] I. W. Hamley, "Structure and flow behaviour of block copolymers," *Journal of Physics Condensed Matter*, vol. 13, no. 33. Aug. 20, 2001. doi: 10.1088/0953-8984/13/33/201.
- [207] Y. Mogi, H. Kotsuji, Y. Kaneko, K. Mori, Y. Matsushita, and I. Noda, "Preparation and morphology of triblock copolymers of the ABC type," *Macromolecules*, vol. 25, no. 20, pp. 5408–5411, Sep. 1992, doi: 10.1021/ma00046a043.
- [208] H. Hasegawa, H. Tanaka, K. Yamasaki, and T. Hashimoto, "Bicontinuous microdomain morphology of block copolymers. 1. Tetrapod-network structure of polystyrene-polyisoprene diblock polymers," *Macromolecules*, vol. 20, no. 7, pp. 1651–1662, Jul. 1987, doi: 10.1021/ma00173a036.
- [209] E. Helfand and Z. R. Wasserman, "Block Copolymer Theory. 5. Spherical Domains," *Macromolecules*, vol. 11, no. 5, pp. 960–966, Sep. 1978, doi: 10.1021/ma60065a023.
- [210] P. D. Olmsted and S. T. Milner, "Strong Segregation Theory of Bicontinuous Phases in Block Copolymers," *Macromolecules*, vol. 31, no. 12, pp. 4011–4022, Jun. 1998, doi: 10.1021/ma980043o.
- [211] S. Sakurai, T. Momii, K. Taie, M. Shibayama, S. Nomura, and T. Hashimoto, "Morphology transition from cylindrical to lamellar microdomains of block copolymers," *Macromolecules*, vol. 26, no. 3, pp. 485–491, May 1993, doi: 10.1021/ma00055a013.
- [212] E. Helfand and Z. Wasserman, "Block Copolymer Theory. 6. Cylindrical Domains," *Macromolecules*, vol. 13, no. 4, pp. 994–998, Jul. 1980, doi: 10.1021/ma60076a045.
- [213] F. S. Bates and G. H. Fredrickson, "Block Copolymer Thermodynamics: Theory and Experiment," *Annu. Rev. Phys. Chem.*, vol. 41, no. 1, pp. 525–557, Oct. 1990, doi: 10.1146/annurev.pc.41.100190.002521.

- [214] I. Y. Erukhimovich, "Weak segregation theory and non-conventional morphologies in the ternary ABC triblock copolymers," *Eur. Phys. J. E*, vol. 18, no. 4, pp. 383–406, Dec. 2005, doi: 10.1140/epje/e2005-00054-5.
- [215] J. F. Marko and Y. Rabin, "Microphase Separation of Charged Diblock Copolymers: Melts and Solutions," *Macromolecules*, vol. 25, no. 5, pp. 1503–1509, Sep. 1992, doi: 10.1021/ma00031a022.
- [216] E. Helfand and Z. R. Wasserman, "Block Copolymer Theory. 4. Narrow Interphase Approximation," *Macromolecules*, vol. 9, no. 6, pp. 879–888, Nov. 1976, doi: 10.1021/ma60054a001.
- [217] L. G. Amurin, "O estudo do comportamento reológico de nanocompósitos de copolímeros em bloco contendo nanocargas," Universidade de São Paulo, 2014. Accessed: Nov. 23, 2019. [Online]. Available: <https://www.teses.usp.br/teses/disponiveis/3/3133/tde-15122014-004354/pt-br.php>
- [218] A. J. Hill and M. R. Tant, "The Structure and Properties of Glassy Polymers," in *Structure and Properties of Glassy Polymers*, Washington, United States: American Chemical Society, 1999, pp. 1–20. doi: 10.1021/bk-1998-0710.ch001.
- [219] M. W. Schulze *et al.*, "Conformational Asymmetry and Quasicrystal Approximants in Linear Diblock Copolymers," *Phys. Rev. Lett.*, vol. 118, no. 20, p. 207801, May 2017, doi: 10.1103/PhysRevLett.118.207801.
- [220] L. Leibler, "Theory of Microphase Separation in Block Copolymers," *Macromolecules*, vol. 13, no. 6, pp. 1602–1617, Nov. 1980, doi: 10.1021/ma60078a047.
- [221] G. H. Fredrickson and E. Helfand, "Fluctuation effects in the theory of microphase separation in block copolymers," *J. Chem. Phys.*, vol. 87, no. 1, pp. 697–705, Jul. 1987, doi: 10.1063/1.453566.
- [222] N. Hadjichristidis, *Block Copolymers: Synthetic Strategies, Physical Properties, and Applications*, 1st Ed. New York: Wiley-Interscience, 2007.
- [223] X. Wang, M. Goswami, R. Kumar, B. G. Sumpter, and J. Mays, "Morphologies of block copolymers composed of charged and neutral blocks," *Soft Matter*, vol. 8, no. 11, p. 3036, 2012, doi:

10.1039/c2sm07223h.

- [224] A. Krishnan, S. Roy, and S. Menon, "Amphiphilic block copolymers: From synthesis including living polymerization methods to applications in drug delivery," *Eur. Polym. J.*, vol. 172, p. 111224, Jun. 2022, doi: 10.1016/j.eurpolymj.2022.111224.
- [225] R. Kurrey, M. Mahilang, M. K. Deb, and K. Shrivastava, "Analytical approach on surface active agents in the environment and challenges," *Trends Environ. Anal. Chem.*, vol. 21, p. e00061, Jan. 2019, doi: 10.1016/j.teac.2019.e00061.
- [226] R. K. Thomas and J. Penfold, "The adsorption and self-assembly of surfactant mixtures: How the detailed evaluation of adsorption properties provides access to the bulk behaviour," *Adv. Colloid Interface Sci.*, vol. 319, p. 102984, Sep. 2023, doi: 10.1016/j.cis.2023.102984.
- [227] J. J. Harris, G. A. Pantelopulos, and J. E. Straub, "Finite-Size Effects and Optimal System Sizes in Simulations of Surfactant Micelle Self-Assembly," *J. Phys. Chem. B*, vol. 125, no. 19, pp. 5068–5077, May 2021, doi: 10.1021/acs.jpcc.1c01186.
- [228] A. T. Kodama, C.-C. Kuo, T. Boatwright, and M. Dennin, "Investigating the Effect of Particle Size on Pulmonary Surfactant Phase Behavior," *Biophys. J.*, vol. 107, no. 7, pp. 1573–1581, Oct. 2014, doi: 10.1016/j.bpj.2014.08.010.
- [229] S. . Shiao *et al.*, "Chain length compatibility effects in mixed surfactant systems for technological applications," *Adv. Colloid Interface Sci.*, vol. 74, no. 1–3, pp. 1–29, Feb. 1998, doi: 10.1016/S0001-8686(97)00005-5.
- [230] B. Lindman and P. Alexandridis, "Amphiphilic molecules: small and large," in *Amphiphilic Block Copolymers*, Elsevier, 2000, pp. 1–12. doi: 10.1016/B978-044482441-7/50002-5.
- [231] M. J. Rosen, "The relationship of structure to properties in surfactants," *J. Am. Oil Chem. Soc.*, vol. 49, no. 5, pp. 293–297, May 1972, doi: 10.1007/BF02637577.
- [232] M. Pacovská, K. Procházka, Z. Tuzar, and P. Munk, "Formation of block copolymer micelles: a sedimentation study," *Polymer (Guildf.)*, vol. 34, no.

- 21, pp. 4585–4588, Nov. 1993, doi: 10.1016/0032-3861(93)90171-6.
- [233] P. Alexandridis and K. Andersson, “Effect of Solvent Quality on Reverse Micelle Formation and Water Solubilization by Poly(ethylene oxide)/Poly(propylene oxide) and Poly(ethylene oxide)/Poly(butylene oxide) Block Copolymers in Xylene,” *J. Colloid Interface Sci.*, vol. 194, no. 1, pp. 166–173, Oct. 1997, doi: 10.1006/jcis.1997.5084.
- [234] N. Jiang and D. Zhang, “Solution Self-Assembly of Coil-Crystalline Diblock Copolypeptoids Bearing Alkyl Side Chains,” *Polymers (Basel)*., vol. 13, no. 18, p. 3131, Sep. 2021, doi: 10.3390/polym13183131.
- [235] K. Kuperkar, D. Patel, L. I. Atanase, and P. Bahadur, “Amphiphilic Block Copolymers: Their Structures, and Self-Assembly to Polymeric Micelles and Polymersomes as Drug Delivery Vehicles,” *Polymers (Basel)*., vol. 14, no. 21, p. 4702, Nov. 2022, doi: 10.3390/polym14214702.
- [236] A. J. Ryan, S.-M. Mai, J. P. A. Fairclough, and I. W. Hamley, “Structures of amphiphilic block copolymers in their liquid and solid states,” in *Amphiphilic Block Copolymers*, Elsevier, 2000, pp. 151–167. doi: 10.1016/B978-044482441-7/50008-6.
- [237] P. Linse, “Modelling of the self-assembly of block copolymers in selective solvent,” in *Amphiphilic Block Copolymers*, Elsevier, 2000, pp. 13–40. doi: 10.1016/B978-044482441-7/50003-7.
- [238] P. A. Björn Lindman, *Amphiphilic block copolymers: self-assembly and applications*, 1st ed. Amsterdam: Elsevier, 2000.
- [239] X. Yu, M. R. Nagarajan, C. Li, P. E. Gibson, and S. L. Cooper, “Poly(chloropropylmethyl-dimethylsiloxane)–polyurethane elastomers: Synthesis and properties of segmented copolymers and related zwitterionomers,” *J. Polym. Sci. Part B Polym. Phys.*, vol. 24, no. 12, pp. 2681–2702, Dec. 1986, doi: 10.1002/polb.1986.090241207.
- [240] J. P. Guin, F. Bosse, D. Nguyen, C. E. Williams, and A. Eisenberg, “Microphase structure of block ionomers. 3. A SAXS study of the effects of architecture and chemical structure,” *Macromolecules*, vol. 26, no. 26, pp. 7250–7255, Dec. 1993, doi: 10.1021/ma00078a021.
- [241] D. Loveday, G. L. Wilkes, C. D. Deporter, and J. E. McGrath, “Structure

- and Properties of Butadiene-tert-Butyl Methacrylate and Butadiene/Styrene-tert-Butyl Methacrylate Triblock Copolymer Ionomers,” *Macromolecules*, vol. 28, no. 23, pp. 7822–7830, Nov. 1995, doi: 10.1021/ma00127a032.
- [242] M. J. Park and N. P. Balsara, “Phase Behavior of Symmetric Sulfonated Block Copolymers,” *Macromolecules*, vol. 41, no. 10, pp. 3678–3687, May 2008, doi: 10.1021/ma702733f.
- [243] M. Goswami *et al.*, “Tunable morphologies from charged block copolymers,” *Soft Matter*, vol. 6, no. 24, p. 6146, 2010, doi: 10.1039/c0sm00733a.
- [244] M. J. Park, S. Kim, A. M. Minor, A. Hexemer, and N. P. Balsara, “Control of Domain Orientation in Block Copolymer Electrolyte Membranes at the Interface with Humid Air,” *Adv. Mater.*, vol. 21, no. 2, pp. 203–208, Jan. 2009, doi: 10.1002/adma.200801613.
- [245] J. R. Howse, R. A. L. Jones, G. Battaglia, R. E. Ducker, G. J. Leggett, and A. J. Ryan, “Templated formation of giant polymer vesicles with controlled size distributions,” *Nat. Mater.*, vol. 8, no. 6, pp. 507–511, Jun. 2009, doi: 10.1038/nmat2446.
- [246] M. Kanapathipillai *et al.*, “Synthesis and Characterization of Ionic Block Copolymer Templated Calcium Phosphate Nanocomposites,” *Chem. Mater.*, vol. 20, no. 18, pp. 5922–5932, Sep. 2008, doi: 10.1021/cm703441n.
- [247] M. Goswami, R. Kumar, B. G. Sumpter, and J. Mays, “Breakdown of Inverse Morphologies in Charged Diblock Copolymers,” *J. Phys. Chem. B*, vol. 115, no. 13, pp. 3330–3338, Apr. 2011, doi: 10.1021/jp111001n.
- [248] Y. Mai and A. Eisenberg, “Self-assembly of block copolymers,” *Chem. Soc. Rev.*, vol. 41, no. 18, p. 5969, 2012, doi: 10.1039/c2cs35115c.
- [249] Z. Wang, C. L. C. Chan, T. H. Zhao, R. M. Parker, and S. Vignolini, “Recent Advances in Block Copolymer Self-Assembly for the Fabrication of Photonic Films and Pigments,” *Adv. Opt. Mater.*, vol. 9, no. 21, Nov. 2021, doi: 10.1002/adom.202100519.
- [250] H. Cabral, K. Miyata, K. Osada, and K. Kataoka, “Block Copolymer

- Micelles in Nanomedicine Applications,” *Chem. Rev.*, vol. 118, no. 14, pp. 6844–6892, Jul. 2018, doi: 10.1021/acs.chemrev.8b00199.
- [251] Q. R. K. E. Anthony, “Block copolyesters containing sulfonate radicals,” 1965 [Online]. Available: <https://patents.google.com/patent/US3317632A/en?q=3317632>
- [252] J. P. Gouin, C. E. Williams, and A. Eisenberg, “Microphase structure of block ionomers. 1. Study of molded styrene-4-vinylpyridinium ABA blocks by SAXS and SANS,” *Macromolecules*, vol. 22, no. 12, pp. 4573–4578, Dec. 1989, doi: 10.1021/ma00202a032.
- [253] L. N. Venkateshwaran, G. A. York, C. D. DePorter, J. E. McGrath, and G. L. Wilkes, “Morphological characterization of well defined methacrylic based di- and triblock ionomers,” *Polymer (Guildf.)*, vol. 33, no. 11, pp. 2277–2286, Jan. 1992, doi: 10.1016/0032-3861(92)90517-Z.
- [254] X. Lu, W. P. Steckle, and R. A. Weiss, “Ionic aggregation in a block copolymer ionomer,” *Macromolecules*, vol. 26, no. 22, pp. 5876–5884, Oct. 1993, doi: 10.1021/ma00074a008.
- [255] R. F. Storey, B. J. Chisholm, and Y. Lee, “Synthesis and mechanical properties of poly(styrene- b -isobutylene- b -styrene) block copolymer ionomers,” *Polym. Eng. Sci.*, vol. 37, no. 1, pp. 73–80, Jan. 1997, doi: 10.1002/pen.11646.
- [256] R. . Weiss, A. Sen, L. . Pottick, and C. . Willis, “Block copolymer ionomers: 2. Viscoelastic and mechanical properties of sulphonated poly(styrene-ethylene/butylene-styrene),” *Polymer (Guildf.)*, vol. 32, no. 15, pp. 2785–2792, Jan. 1991, doi: 10.1016/0032-3861(91)90109-V.
- [257] J. Kim, B. Kim, and B. Jung, “Proton conductivities and methanol permeabilities of membranes made from partially sulfonated polystyrene-block-poly(ethylene-ran-butylene)-block-polystyrene copolymers,” *J. Memb. Sci.*, vol. 207, no. 1, pp. 129–137, Sep. 2002, doi: 10.1016/S0376-7388(02)00138-2.
- [258] C. A. Edmondson, J. J. Fontanella, S. H. Chung, S. G. Greenbaum, and G. E. Wnek, “Complex impedance studies of S-SEBS block polymer proton-conducting membranes,” *Electrochim. Acta*, vol. 46, no. 10–11, pp.



- 1623–1628, Mar. 2001, doi: 10.1016/S0013-4686(00)00762-3.
- [259] Y. A. Elabd, E. Napadensky, J. M. Sloan, D. M. Crawford, and C. W. Walker, “Triblock copolymer ionomer membranes,” *J. Memb. Sci.*, vol. 217, no. 1–2, pp. 227–242, Jun. 2003, doi: 10.1016/S0376-7388(03)00127-3.
- [260] Z. Shi and S. Holdcroft, “Synthesis and Proton Conductivity of Partially Sulfonated Poly([vinylidene difluoride- c o -hexafluoropropylene]- b -styrene) Block Copolymers,” *Macromolecules*, vol. 38, no. 10, pp. 4193–4201, May 2005, doi: 10.1021/ma0477549.
- [261] H. Ghassemi, J. E. McGrath, and T. A. Zawodzinski, “Multiblock sulfonated–fluorinated poly(arylene ether)s for a proton exchange membrane fuel cell,” *Polymer (Guildf.)*, vol. 47, no. 11, pp. 4132–4139, May 2006, doi: 10.1016/j.polymer.2006.02.038.
- [262] M. J. Park *et al.*, “Increased Water Retention in Polymer Electrolyte Membranes at Elevated Temperatures Assisted by Capillary Condensation,” *Nano Lett.*, vol. 7, no. 11, pp. 3547–3552, Nov. 2007, doi: 10.1021/nl072617l.
- [263] F. S. Bates and G. H. Fredrickson, “Block Copolymers—Designer Soft Materials,” *Phys. Today*, vol. 52, no. 2, pp. 32–38, Feb. 1999, doi: 10.1063/1.882522.
- [264] L. Rubatat, C. Li, H. Dietsch, A. Nykänen, J. Ruokolainen, and R. Mezzenga, “Structure–Properties Relationship in Proton Conductive Sulfonated Polystyrene–Polymethyl Methacrylate Block Copolymers (sPS–PMMA),” *Macromolecules*, vol. 41, no. 21, pp. 8130–8137, Nov. 2008, doi: 10.1021/ma801543q.
- [265] P. Černoch, S. Petrova, Z. Černochová, J.-S. Kim, C. P. Simpson, and A. D. Asandei, “Mn<sub>2</sub>(CO)<sub>10</sub>-photomediated synthesis of poly(vinylidene fluoride)-b-poly(styrene sulfonate),” *Eur. Polym. J.*, vol. 68, pp. 460–470, Jul. 2015, doi: 10.1016/j.eurpolymj.2015.05.013.
- [266] R. Gonçalves, K. A. Tozzi, M. C. Saccardo, A. G. Zuquello, and C. H. Scuracchio, “Nafion-based ionomeric polymer/metal composites operating in the air: theoretical and electrochemical analysis,” *J. Solid State*

- Electrochem.*, vol. 24, no. 8, pp. 1845–1856, 2020, doi: 10.1007/s10008-020-04520-6.
- [267] M. C. Saccardo, A. G. Zuquello, K. A. Tozzi, R. Gonçalves, L. A. Hirano, and C. H. Scuracchio, “Counter-ion and humidity effects on electromechanical properties of Nafion®/Pt composites,” *Mater. Chem. Phys.*, vol. 244, Jan. 2020, doi: 10.1016/j.matchemphys.2020.122674.
- [268] L. B. Canto, G. L. Mantovani, E. R. DeAzevedo, T. J. Bonagamba, E. Hage, and L. A. Pessan, “Molecular Characterization of Styrene-Butadiene-Styrene Block Copolymers (SBS) by GPC, NMR, and FTIR,” *Polym. Bull.*, vol. 57, no. 4, pp. 513–524, Aug. 2006, doi: 10.1007/s00289-006-0577-4.
- [269] D. I. Hoult and B. Bhakar, “NMR signal reception: Virtual photons and coherent spontaneous emission,” *Concepts Magn. Reson.*, vol. 9, no. 5, pp. 277–297, 1997, doi: 10.1002/(SICI)1099-0534(1997)9:5<277::AID-CMR1>3.0.CO;2-W.
- [270] J. L. Koenig, L. D’Esposito, and M. K. Antoon, “Factor Analysis Applied to Fourier Transform Infrared Spectra,” *Appl. Spectrosc. Vol. 33, Issue 4*, pp. 351–357, vol. 33, no. 4, pp. 351–357, Jul. 1979.
- [271] H. M. Ng, N. M. Saidi, F. S. Omar, K. Ramesh, S. Ramesh, and S. Bashir, “Thermogravimetric Analysis of Polymers,” in *Encyclopedia of Polymer Science and Technology*, Wiley, 2018, pp. 1–29. doi: 10.1002/0471440264.pst667.
- [272] J. Drzeżdżon, D. Jacewicz, A. Sielicka, and L. Chmurzyński, “Characterization of polymers based on differential scanning calorimetry based techniques,” *TrAC Trends Anal. Chem.*, vol. 110, pp. 51–56, Jan. 2019, doi: 10.1016/j.trac.2018.10.037.
- [273] A. Rasmont *et al.*, “Microphase separation at the surface of block copolymers, as studied with atomic force microscopy,” *Colloids Surfaces B Biointerfaces*, vol. 19, no. 4, pp. 381–395, Dec. 2000, doi: 10.1016/S0927-7765(00)00146-6.
- [274] D. F. Sunday, J. L. Thelen, C. Zhou, J. Ren, P. F. Nealey, and R. J. Kline, “Buried Structure in Block Copolymer Films Revealed by Soft X-ray

- Reflectivity,” *ACS Nano*, vol. 15, no. 6, pp. 9577–9587, Jun. 2021, doi: 10.1021/acsnano.0c09907.
- [275] A. Nelson, “Co-refinement of multiple-contrast neutron/X-ray reflectivity data using MOTOFIT,” *J. Appl. Crystallogr.*, vol. 39, no. 2, pp. 273–276, Apr. 2006, doi: 10.1107/S0021889806005073.
- [276] J. R. Levine, J. B. Cohen, Y. W. Chung, and P. Georgopoulos, “Grazing-incidence small-angle X-ray scattering: new tool for studying thin film growth,” *J. Appl. Crystallogr.*, vol. 22, no. 6, pp. 528–532, Dec. 1989, doi: 10.1107/S002188988900717X.
- [277] D. Smilgies, P. Busch, C. M. Papadakis, and D. Posselt, “Characterization of polymer thin films with small-angle X-ray scattering under grazing incidence (GISAXS),” *Synchrotron Radiat. News*, vol. 15, no. 5, pp. 35–42, Sep. 2002, doi: 10.1080/08940880208602975.
- [278] J. I. Goldstein *et al.*, “Image Formation and Interpretation,” in *Scanning Electron Microscopy and X-Ray Microanalysis*, Boston, MA: Springer US, 1992, pp. 149–271. doi: 10.1007/978-1-4613-0491-3\_4.
- [279] S. Slade, S. A. Campbell, T. R. Ralph, and F. C. Walsh, “Ionic Conductivity of an Extruded Nafion 1100 EW Series of Membranes,” *J. Electrochem. Soc.*, vol. 149, no. 12, p. A1556, 2002, doi: 10.1149/1.1517281.
- [280] Inamuddin, A. Khan, M. Luqman, and A. Dutta, “Kraton based ionic polymer metal composite (IPMC) actuator,” *Sensors Actuators, A Phys.*, vol. 216, pp. 295–300, Sep. 2014, doi: 10.1016/j.sna.2014.04.015.
- [281] R. Gonçalves *et al.*, “Review on the use of impedance spectroscopy for IPMC-like devices: application, models, and a new approach to data treatment,” *Mater. Adv.*, 2024, doi: 10.1039/D3MA00593C.
- [282] O. Colombani, O. Langelier, E. Martwong, and P. Castignolles, “Polymerization Kinetics: Monitoring Monomer Conversion Using an Internal Standard and the Key Role of Sample  $t_0$ ,” *J. Chem. Educ.*, vol. 88, no. 1, pp. 116–121, Jan. 2011, doi: 10.1021/ed100404r.
- [283] K. Suhailath, B. K. Bahuleyan, and M. T. Ramesan, “Synthesis, Characterization, Thermal Properties and Temperature-Dependent AC

- Conductivity Studies of Poly (Butyl Methacrylate)/Neodymium Oxide Nanocomposites,” *J. Inorg. Organomet. Polym. Mater.*, vol. 31, no. 1, pp. 365–374, Jan. 2021, doi: 10.1007/s10904-020-01665-9.
- [284] C.-C. Huang, M.-X. Du, B.-Q. Zhang, and C.-Y. Liu, “Glass Transition Temperatures of Copolymers: Molecular Origins of Deviation from the Linear Relation,” *Macromolecules*, vol. 55, no. 8, pp. 3189–3200, Apr. 2022, doi: 10.1021/acs.macromol.1c02287.
- [285] A. I. Buzin, M. Pyda, P. Costanzo, K. Matyjaszewski, and B. Wunderlich, “Calorimetric study of block-copolymers of poly(n-butyl acrylate) and gradient poly(n-butyl acrylate-co-methyl methacrylate),” *Polymer (Guildf.)*, vol. 43, no. 20, pp. 5563–5569, Sep. 2002, doi: 10.1016/S0032-3861(02)00358-0.
- [286] J. Kim, M. M. Mok, R. W. Sandoval, D. J. Woo, and J. M. Torkelson, “Uniquely Broad Glass Transition Temperatures of Gradient Copolymers Relative to Random and Block Copolymers Containing Repulsive Comonomers,” *Macromolecules*, vol. 39, no. 18, pp. 6152–6160, Sep. 2006, doi: 10.1021/ma061241f.
- [287] T. P. Russell, T. E. Karis, Y. Gallot, and A. M. Mayes, “A lower critical ordering transition in a diblock copolymer melt,” *Nature*, vol. 368, no. 6473, pp. 729–731, Apr. 1994, doi: 10.1038/368729a0.
- [288] M. Maaloum, D. Ausserre, D. Chatenay, G. Coulon, and Y. Gallot, “Edge profile of relief 2D domains at the free surface of smectic copolymer thin films,” *Phys. Rev. Lett.*, vol. 68, no. 10, pp. 1575–1578, Mar. 1992, doi: 10.1103/PhysRevLett.68.1575.
- [289] S. Douadi-Masrouki *et al.*, “Neutron Reflectivity on Polymer Multilayers Doped with Magnetic Nanoparticles,” *Solid State Phenom.*, vol. 152–153, pp. 194–197, Apr. 2009, doi: 10.4028/www.scientific.net/SSP.152-153.194.
- [290] A. Di, J. Schmitt, N. Elstone, T. Arnold, and K. J. Edler, “In situ X-ray reflectivity and GISAXS study of mesoporous silica films grown from sodium silicate solution precursors,” *Microporous Mesoporous Mater.*, vol. 341, p. 112018, Aug. 2022, doi: 10.1016/j.micromeso.2022.112018.

- [291] G. Vignaud and A. Gibaud, "REFLEX: a program for the analysis of specular X-ray and neutron reflectivity data," *J. Appl. Crystallogr.*, vol. 52, no. 1, pp. 201–213, Feb. 2019, doi: 10.1107/S1600576718018186.
- [292] G. Pospelov *et al.*, "BornAgain : software for simulating and fitting grazing-incidence small-angle scattering," *J. Appl. Crystallogr.*, vol. 53, no. 1, pp. 262–276, Feb. 2020, doi: 10.1107/S1600576719016789.
- [293] C. K. Shelton and T. H. Epps, "Block copolymer thin films: Characterizing nanostructure evolution with in situ X-ray and neutron scattering," *Polymer (Guildf.)*, vol. 105, pp. 545–561, Nov. 2016, doi: 10.1016/j.polymer.2016.06.069.
- [294] P. Müller-Buschbaum, "GISAXS and GISANS as metrology technique for understanding the 3D morphology of block copolymer thin films," *Eur. Polym. J.*, vol. 81, pp. 470–493, Aug. 2016, doi: 10.1016/j.eurpolymj.2016.04.007.
- [295] P. Müller-Buschbaum, "A Basic Introduction to Grazing Incidence Small-Angle X-Ray Scattering," 2009, pp. 61–89. doi: 10.1007/978-3-540-95968-7\_3.
- [296] A. Hexemer and P. Müller-Buschbaum, "Advanced grazing-incidence techniques for modern soft-matter materials analysis," *IUCrJ*, vol. 2, no. 1, pp. 106–125, Jan. 2015, doi: 10.1107/S2052252514024178.
- [297] B. Collin, D. Chatenay, G. Coulon, D. Ausserre, and Y. Gallot, "Ordering of copolymer thin films as revealed by atomic force microscopy," *Macromolecules*, vol. 25, no. 5, pp. 1621–1622, Mar. 1992, doi: 10.1021/ma00031a042.
- [298] P. F. Green, T. M. Christensen, and T. P. Russell, "Ordering at diblock copolymer surfaces," *Macromolecules*, vol. 24, no. 1, pp. 252–255, Jan. 1991, doi: 10.1021/ma00001a038.
- [299] P. Mansky, O. K. C. Tsui, T. P. Russell, and Y. Gallot, "Phase Coherence and Microphase Separation Transitions in Diblock Copolymer Thin Films," *Macromolecules*, vol. 32, no. 15, pp. 4832–4837, Jul. 1999, doi: 10.1021/ma990140x.
- [300] P. S. Pershan, "Dislocation effects in smectic- A liquid crystals," *J. Appl.*

- Phys.*, vol. 45, no. 4, pp. 1590–1604, Apr. 1974, doi: 10.1063/1.1663462.
- [301] C. D. Han, “Rheology of Block Copolymers,” in *Rheology and Processing of Polymeric Materials: Volume 1: Polymer Rheology*, Oxford University Press, New York, 2007, pp. 296–368. doi: 10.1093/oso/9780195187823.003.0014.
- [302] N. Sakamoto, T. Hashimoto, C. D. Han, D. Kim, and N. Y. Vaidya, “Order–Order and Order–Disorder Transitions in a Polystyrene- block - Polyisoprene- block -Polystyrene Copolymer,” *Macromolecules*, vol. 30, no. 6, pp. 1621–1632, Mar. 1997, doi: 10.1021/ma960610c.
- [303] W. W. Graessley and T. C. B. McLeish, “THE DOI–EDWARDS THEORY,” in *Stealing the Gold*, Oxford University Press, 2004, pp. 318–328. doi: 10.1093/acprof:oso/9780198528531.003.0021.
- [304] J. D. Ferry, *Viscoelastic Properties of Polymers*, 3rd Ed. New York: John Wiley & Sons, Inc., 1980.
- [305] S. Dharmalingam, V. Kugarajah, and V. Elumalai, “Proton exchange membrane for microbial fuel cells,” in *PEM Fuel Cells*, Elsevier, 2022, pp. 25–53. doi: 10.1016/B978-0-12-823708-3.00011-0.
- [306] T. Okada, G. Xie, O. Gorseth, S. Kjelstrup, N. Nakamura, and T. Arimura, “Ion and water transport characteristics of Nafion membranes as electrolytes,” *Electrochim. Acta*, vol. 43, no. 24, pp. 3741–3747, Aug. 1998, doi: 10.1016/S0013-4686(98)00132-7.
- [307] M. C. Saccardo, A. G. Zuquello, K. A. Tozzi, R. Gonçalves, L. A. Hirano, and C. H. Scuracchio, “Counter-ion and humidity effects on electromechanical properties of Nafion®/Pt composites,” *Mater. Chem. Phys.*, p. 122674, Jan. 2020, doi: 10.1016/j.matchemphys.2020.122674.
- [308] Z. Chen and X. Tan, “Monolithic fabrication of ionic polymer-metal composite actuators capable of complex deformation,” *Sensors Actuators, A Phys.*, vol. 157, no. 2, pp. 246–257, 2010, doi: 10.1016/j.sna.2009.11.024.
- [309] R. A. KOMOROSKI and K. A. MAURITZ, “Nuclear Magnetic Resonance Studies and the Theory of Ion Pairing in Perfluorosulfonate Ionomers,” 1982, pp. 113–138. doi: 10.1021/bk-1982-0180.ch007.

- [310] J. Mostany and B. R. Scharifker, "Impedance spectroscopy of undoped, doped and overoxidized polypyrrole films," *Synth. Met.*, vol. 87, no. 3, pp. 179–185, Apr. 1997, doi: 10.1016/s0379-6779(97)80105-1.
- [311] Z. Zhu, T. Horiuchi, K. Kruusamäe, L. Chang, and K. Asaka, "Influence of Ambient Humidity on the Voltage Response of Ionic Polymer-Metal Composite Sensor," *J. Phys. Chem. B*, vol. 120, no. 12, pp. 3215–3225, 2016, doi: 10.1021/acs.jpcc.5b12634.
- [312] Z. Zhu, H. Chen, L. Chang, B. Li, and Y. Wang, "Influence of fabrication process steps on Pd-IPMC electrode morphologies and mechano-electrical properties," in *Electroactive Polymer Actuators and Devices (EAPAD) 2011*, Mar. 2011, vol. 7976, p. 79762T. doi: 10.1117/12.881865.
- [313] J. C. Bendert, D. D. Papadias, and D. J. Myers, "The effect of Na<sup>+</sup> impurities on the conductivity and water uptake of nafion 115 polymer electrolyte fuel cell membranes," *J. Electrochem. Soc.*, vol. 157, no. 10, 2010, doi: 10.1149/1.3479188.
- [314] A. G. Zuquello, "Método de controle de trajetória de atuadores ipmc baseados em nafion® utilizando técnica de visão de máquina em ambiente com umidade relativa controlada," Universidade Federal de São Carlos (UFSCar), 2021. [Online]. Available: [https://repositorio.ufscar.br/bitstream/handle/ufscar/14964/Ariel Gustavo Zuquello - Tese.pdf?sequence=1](https://repositorio.ufscar.br/bitstream/handle/ufscar/14964/Ariel_Gustavo_Zuquello_-_Tese.pdf?sequence=1)
- [315] X. Bai and L. Zheng, "A Facile Synthesis of Two-Dimensional Dendritic Gold Nanostructures at the Air/Water Interface," *Cryst. Growth Des.*, vol. 10, no. 11, pp. 4701–4705, Nov. 2010, doi: 10.1021/cg101220v.
- [316] K. J. Kim and M. Shahinpoor, "Ionic polymer metal composites: II. Manufacturing techniques," *Smart Mater. Struct.*, vol. 12, no. 1, pp. 65–79, Feb. 2003, doi: 10.1088/0964-1726/12/1/308.
- [317] M. Shahinpoor and K. J. Kim, "Novel ionic polymer-metal composites equipped with physically loaded particulate electrodes as biomimetic sensors, actuators and artificial muscles," *Sensors Actuators, A Phys.*, vol. 96, no. 2–3, pp. 125–132, 2002, doi: 10.1016/S0924-4247(01)00777-4.

- [318] M. Shahinpoor, Y. Bar-Cohen, J. O. Simpson, and J. Smith, "Ionic polymer-metal composites (IPMCs) as biomimetic sensors, actuators and artificial muscles - a review," *Smart Mater. Struct.*, vol. 7, no. 6, pp. R15–R30, Dec. 1998, doi: 10.1088/0964-1726/7/6/001.
- [319] Y. Wang, J. Liu, Y. Zhu, D. Zhu, and H. Chen, "Formation and Characterization of Dendritic Interfacial Electrodes inside an Ionomer," *ACS Appl. Mater. Interfaces*, vol. 9, no. 36, pp. 30258–30262, 2017, doi: 10.1021/acsami.7b08012.
- [320] W. H. Mohdlsa, A. Hunt, and S. H. HosseinNia, "Sensing and self-sensing actuation methods for ionic polymer-metal composite (IPMC): A review," *Sensors (Switzerland)*, vol. 19, no. 18, pp. 1–36, 2019, doi: 10.3390/s19183967.
- [321] A. Hunt, Z. Chen, X. Tan, and M. Kruusmaa, "Control of an inverted pendulum using an Ionic Polymer-Metal Composite actuator," in *2010 IEEE/ASME International Conference on Advanced Intelligent Mechatronics*, Jul. 2010, pp. 163–168. doi: 10.1109/AIM.2010.5695913.
- [322] T. T. Nguyen, V. K. Nguyen, Y. Yoo, and N. S. Goo, "A Novel Polymeric Micropump based on a Multilayered Ionic Polymer-Metal Composite," in *IECON 2006 - 32nd Annual Conference on IEEE Industrial Electronics*, Nov. 2006, pp. 4888–4893. doi: 10.1109/IECON.2006.347352.
- [323] K. K. Leang, Y. Shan, S. Song, and K. J. Kim, "Integrated Sensing for IPMC Actuators Using Strain Gages for Underwater Applications," *IEEE/ASME Trans. Mechatronics*, vol. 17, no. 2, pp. 345–355, Apr. 2012, doi: 10.1109/TMECH.2011.2105885.
- [324] J. Wang, A. McDaid, R. Sharma, and K. Aw, "A Compact Ionic Polymer Metal Composite (IPMC) System with Inductive Sensor for Closed Loop Feedback," *Actuators*, vol. 4, no. 2, pp. 114–126, May 2015, doi: 10.3390/act4020114.
- [325] B. Paola, L. Fortuna, P. Giannone, S. Graziani, and S. Strazzeri, "IPMCs as Vibration Sensors," in *2008 IEEE Instrumentation and Measurement Technology Conference*, May 2008, pp. 2065–2069. doi: 10.1109/IMTC.2008.4547388.



- [326] B. Ando, S. Baglio, A. Beninato, S. Graziani, F. Pagano, and E. Umana, "A seismic sensor based on IPMC combined with ferrofluids," in *2012 IEEE International Instrumentation and Measurement Technology Conference Proceedings*, May 2012, pp. 1829–1832. doi: 10.1109/I2MTC.2012.6229171.
- [327] H. Lei, M. A. Sharif, and X. Tan, "Dynamics of Omnidirectional IPMC Sensor: Experimental Characterization and Physical Modeling," *IEEE/ASME Trans. Mechatronics*, vol. 21, no. 2, pp. 601–612, Apr. 2016, doi: 10.1109/TMECH.2015.2468080.
- [328] L. Q. Liu, Y. Chen, C. Q. Xiang, Y. S. Zhao, L. N. Hao, and Z. L. Zhao, "Study on Micro-Force Sensor of Cantilever Structure Based on IPMC," *Appl. Mech. Mater.*, vol. 543–547, pp. 1262–1265, Mar. 2014, doi: 10.4028/www.scientific.net/AMM.543-547.1262.
- [329] M. Gudarzi, P. Smolinski, and Q.-M. Wang, "Compression and shear mode ionic polymer-metal composite (IPMC) pressure sensors," *Sensors Actuators A Phys.*, vol. 260, pp. 99–111, Jun. 2017, doi: 10.1016/j.sna.2017.04.010.
- [330] H. Lei, M. A. Sharif, D. A. Paley, M. J. McHenry, and X. Tan, "Performance improvement of IPMC flow sensors with a biologically-inspired cupula structure," Apr. 2016, p. 979827. doi: 10.1117/12.2219574.
- [331] C. Bonomo, L. Fortuna, P. Giannone, S. Graziani, and S. Strazzeri, "A model for ionic polymer metal composites as sensors," *Smart Mater. Struct.*, vol. 15, no. 3, pp. 749–758, Jun. 2006, doi: 10.1088/0964-1726/15/3/010.
- [332] Z. Zhu, T. Horiuchi, K. Takagi, J. Takeda, L. Chang, and K. Asaka, "Effects of cation on electrical responses of ionic polymer-metal composite sensors at various ambient humidities," *J. Appl. Phys.*, vol. 120, no. 8, p. 084906, Aug. 2016, doi: 10.1063/1.4961732.
- [333] X. J. Chew, A. Van den Hurk, and K. C. Aw, "Characterisation of ionic polymer metallic composites as sensors in robotic finger joints," *Int. J. Biomechatronics Biomed. Robot.*, vol. 1, no. 1, p. 37, 2009, doi:

- 10.1504/IJBBR.2009.030058.
- [334] C. Bonomo, L. Fortuna, P. Giannone, S. Graziani, and S. Strazzeri, "Improved Frequency Investigation of IPMC Based Sensors," in *2006 IEEE Instrumentation and Measurement Technology Conference Proceedings*, Apr. 2006, pp. 2338–2341. doi: 10.1109/IMTC.2006.328616.
- [335] P. Brunetto, L. Fortuna, P. Giannone, S. Graziani, and S. Strazzeri, "Static and dynamic characterization of the temperature and humidity influence on IPMC actuators," *IEEE Trans. Instrum. Meas.*, vol. 59, no. 4, pp. 893–908, 2010, doi: 10.1109/TIM.2009.2026613.
- [336] M. A. Rosly, H. Yussof, M. F. Shaari, Z. Samad, D. Kamaruzaman, and A. R. Omar, "Speed control mechanism for IPMC based biomimetic flapping thruster," in *Proceedings - 2017 IEEE 5th International Symposium on Robotics and Intelligent Sensors, IRIS 2017*, Jan. 2018, vol. 2018-January, pp. 218–223. doi: 10.1109/IRIS.2017.8250125.
- [337] J. D. Carrico, M. Fleming, M. A. Tsugawa, and K. K. Leang, "Precision feedback and feedforward control of ionic polymer metal composite actuators," in *RSC Smart Materials*, vol. 2016-January, no. 17, Royal Society of Chemistry, 2016, pp. 354–385. doi: 10.1039/9781782622581-00354.
- [338] L. Chang, D. Wang, J. Hu, Y. Li, Y. Wang, and Y. Hu, "Hierarchical Structure Fabrication of IPMC Strain Sensor With High Sensitivity," *Front. Mater.*, vol. 8, Aug. 2021, doi: 10.3389/fmats.2021.748687.

## ANNEX A

## Acrylic Chamber Project

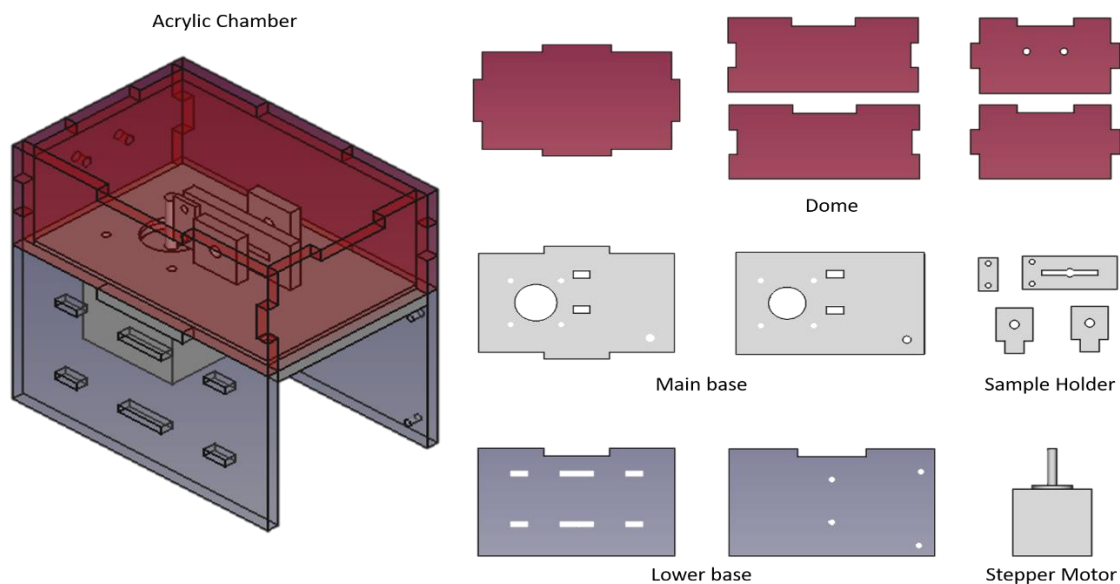


Figure A52: The acrylic chamber project, designed using FreeCAD, presents an isometric view of the assembled box alongside detailed front views of its individual components.

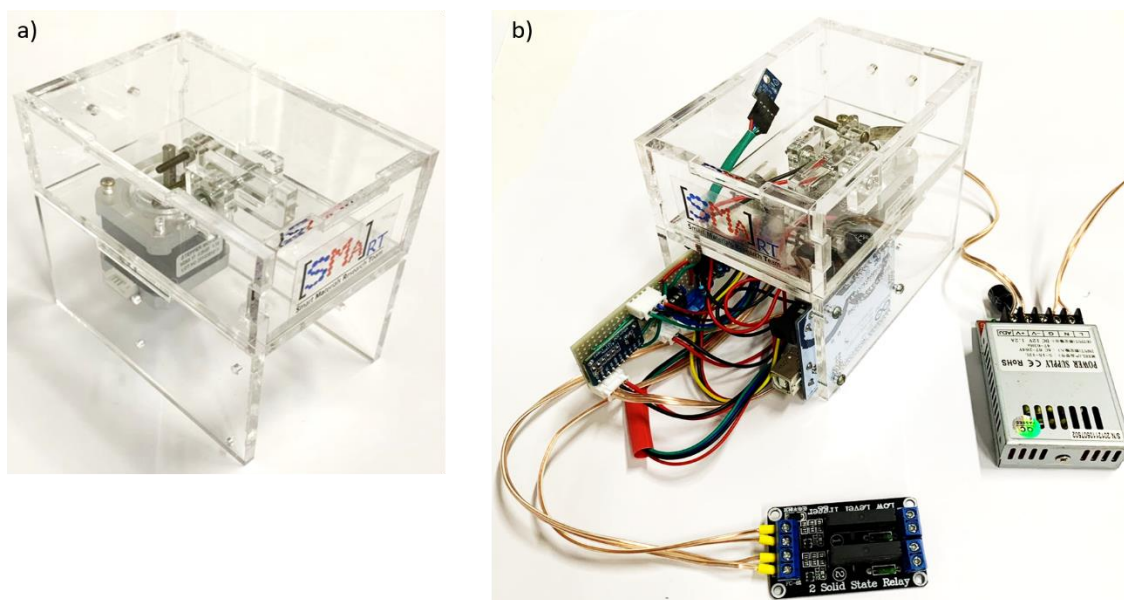
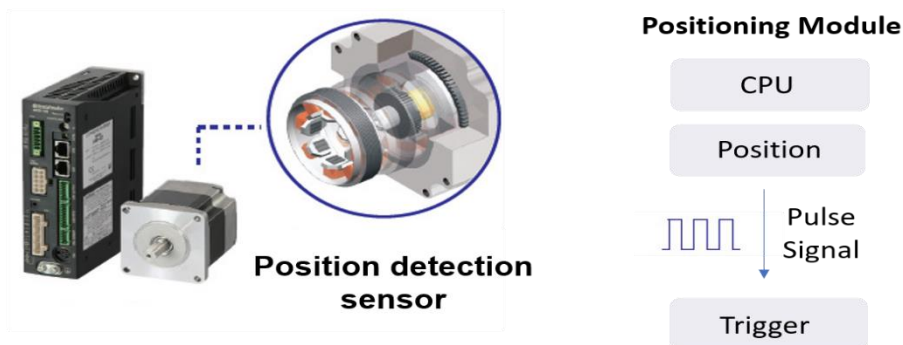
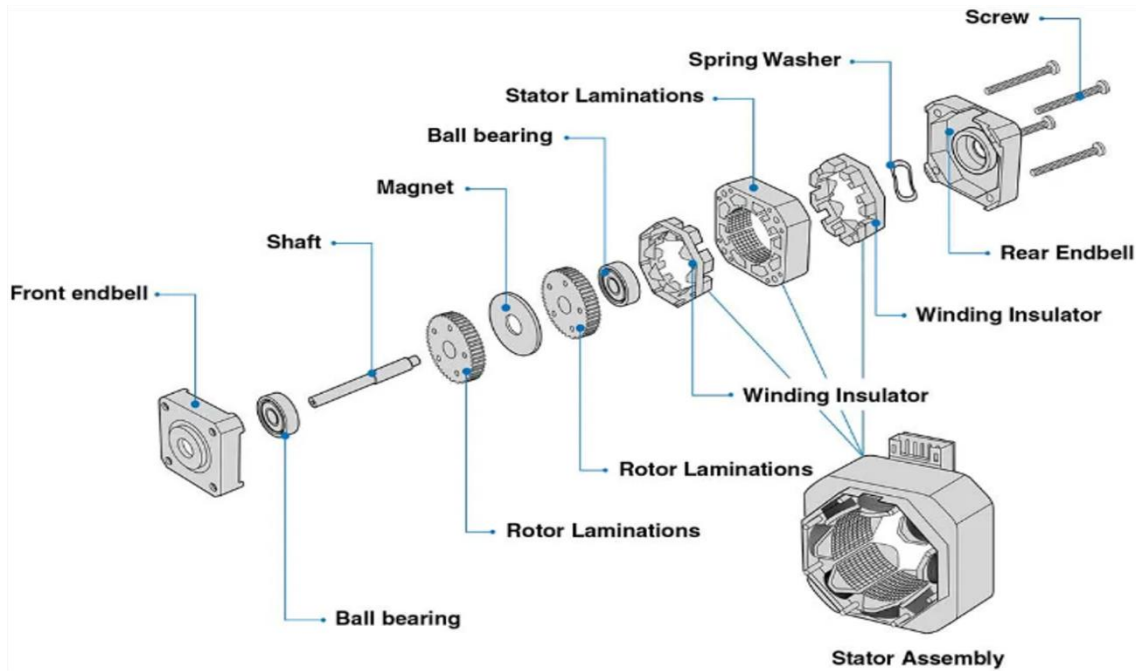


Figure A53: a) The acrylic chamber, assembled post laser-cutting of its individual components, showcases a seamless union achieved through the application of chloroform. b) Integrated within are electronic components configured to control the stepper motor and data acquisition.



The number of pulses is proportional to the amount of rotation of the stepper motor

	Phase 5	Phase 2
1 Pulse	0,72°	1,8°
10 Pulses	7,2°	18°
125 Pulses	90°	225°

Figure A54: Basic structure of a stepper motor and position control. A stepper motor rotates with a fixed step angle. The rotation angle and speed of the stepping motor can be controlled accurately using pulse signals from the controller. The length of rotation of the stepping motor is proportional to the number of pulse signal (pulse number) given to the driver.

## ANNEX B

### Software code developed to perform humidity control

The programming language used to control the relative humidity system is based on C++ and the code is written below.

```
#include <Wire.h>
#include <Adafruit_Sensor.h>
#include <Adafruit_BME280.h>

#define DHT_pin 12
#define DHT_energy 13
#define SEALEVELPRESSURE_HPA (1013.25)
#define wet_pin 8
#define dry_pin 9

Adafruit_BME280 bme;

int sensor = A0; //Analog pin to which the sensor is connected.
intSensorValue = 0; //Used to read the sensor value in real time.
int pot_val = 0;
int H_read = 0;

int adjust = 90; // Adjusted humidity

void setup() {
  Serial.begin(9600);

  pinMode(wet_pin, OUTPUT);
  pinMode(dry_pin, OUTPUT);
  pinMode(DHT_energy, OUTPUT); // DHT energy
```

```
digitalWrite(wet_pin, HIGH); // Bombs will start
digitalWrite(dry_pin, HIGH); // off

if (!bme.begin(0x76)) {
    Serial.println("Could not find a valid BME280 sensor, check wiring!");
    while (1);
}
}

void loop() {

    // Reading temperature and humidity:
    digitalWrite(DHT_energy, HIGH); // bind DHT
    delay(500);
    float H_a = (bme.readHumidity());
    float T_a = (bme.readTemperature());

    delay(250);

    float H_b = (bme.readHumidity());
    float T_b = (bme.readTemperature());
    delay(250);
    float H_c = (bme.readHumidity());
    float T_c = (bme.readTemperature());

    float H_mean = ((H_a + H_b + H_c) / 3);
    float T_mean = ((T_a + T_b + T_c) / 3);

    H_read = H_mean;

    if (isnan(H_a) || isnan(H_b) || isnan(H_c))
    {
        digitalWrite(DHT_energy, LOW); // turn off DHT
```

```
    delay(500);
    Serial.println("Sensor disconnected!");
    return;
}

// Test to trigger bombs:
if (H_read < adjust)
{
    digitalWrite(wet_pin, LOW);
    digitalWrite(dry_pin, HIGH);
}
else if (H_read > adjust)
{
    digitalWrite(wet_pin, HIGH);
    digitalWrite(dry_pin, LOW);
}
else if (H_read == adjust)
{
    digitalWrite(wet_pin, HIGH);
    digitalWrite(dry_pin, HIGH);
}

    Serial.print(T_mean);
    Serial.print(",");
    Serial.print(H_mean);
    Serial.print(",");
    Serial.print(bme.readAltitude(SEALEVELPRESSURE_HPA));
    Serial.print(",");
    Serial.print(bme.readPressure() / 100.0F);
    Serial.print(",");

    //Reading the sensor value.
```

```
int valueSensor = analogRead(sensor);
```

```
//Displaying the sensor value on the serial monitor.
```

```
Serial.print(valueSensor);
```

```
Serial.println();
```

```
delay(500);
```

```
}
```

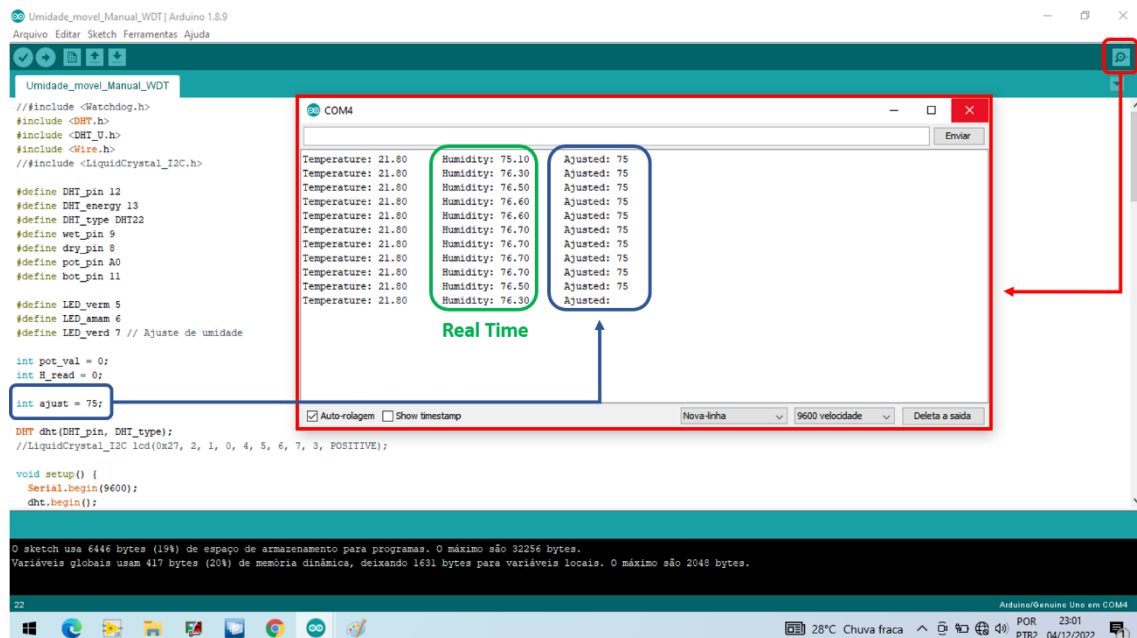


Figure B55: Relative humidity reading in real time, which can be observed both directly from the Arduino program and on the LabView front panel, as shown in Appendix C.



## ANNEX C

## Software to control the Electromechanical System - LabView

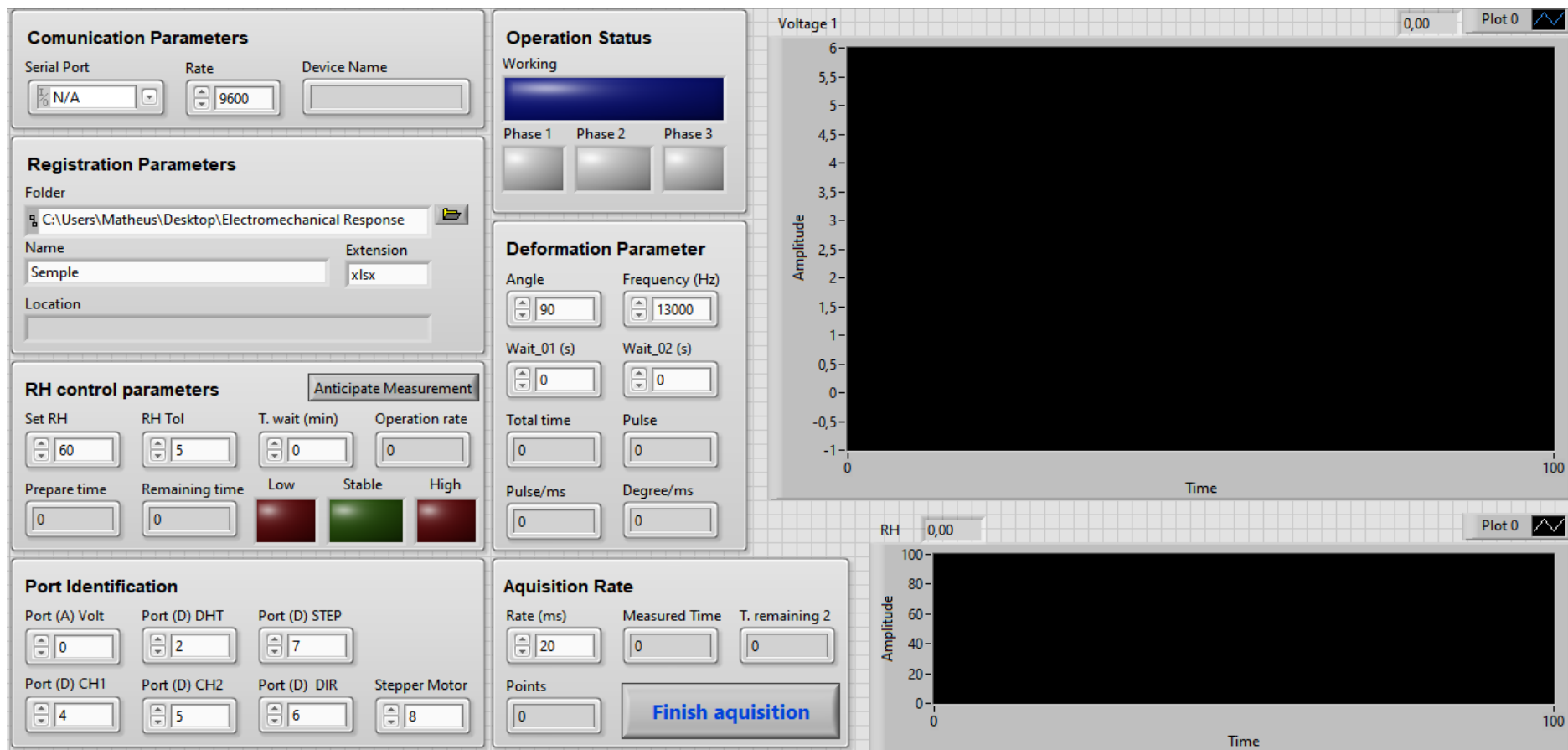


Figure C56: Front panel of the developed control system.

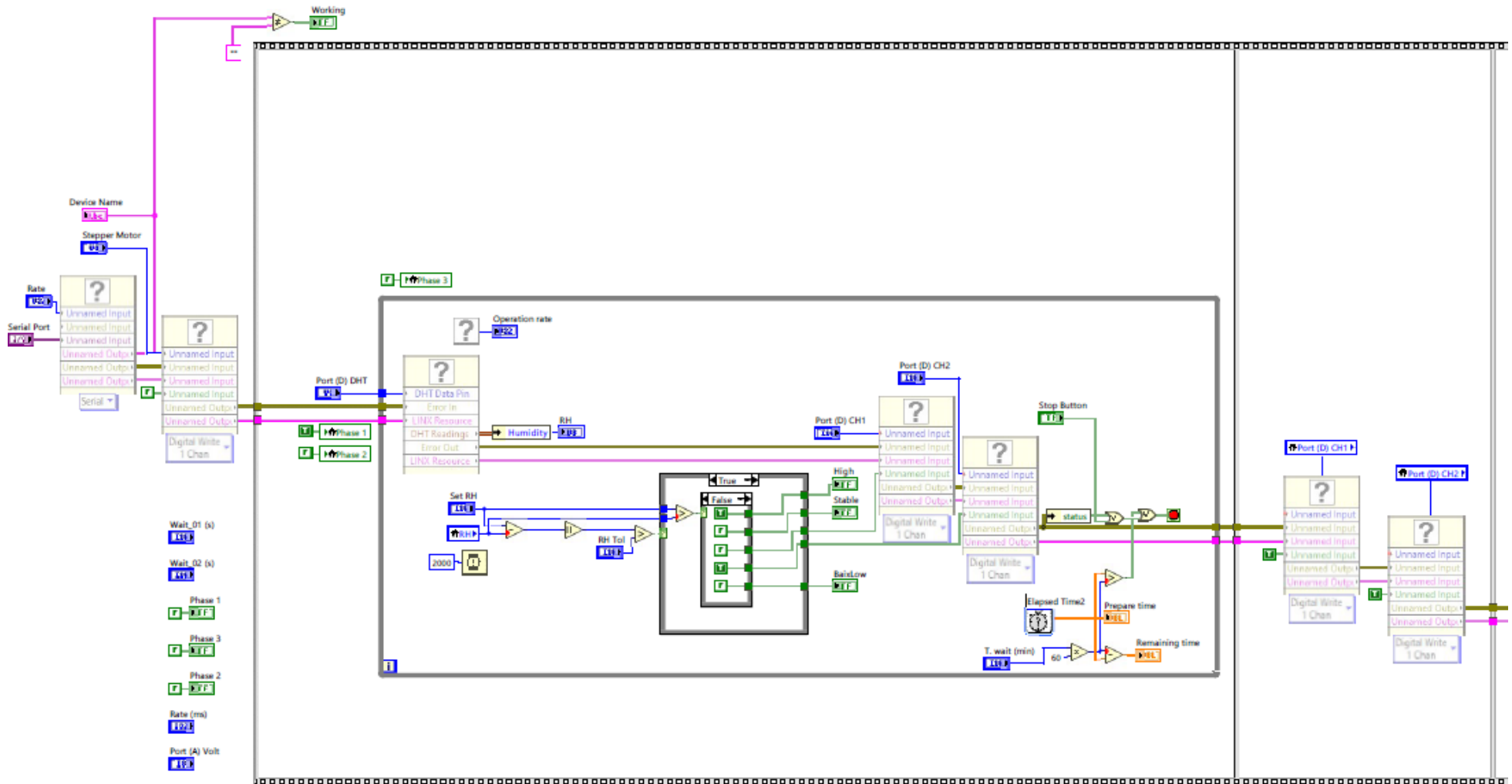


Figure C57: Pattern recognition software (part 1).

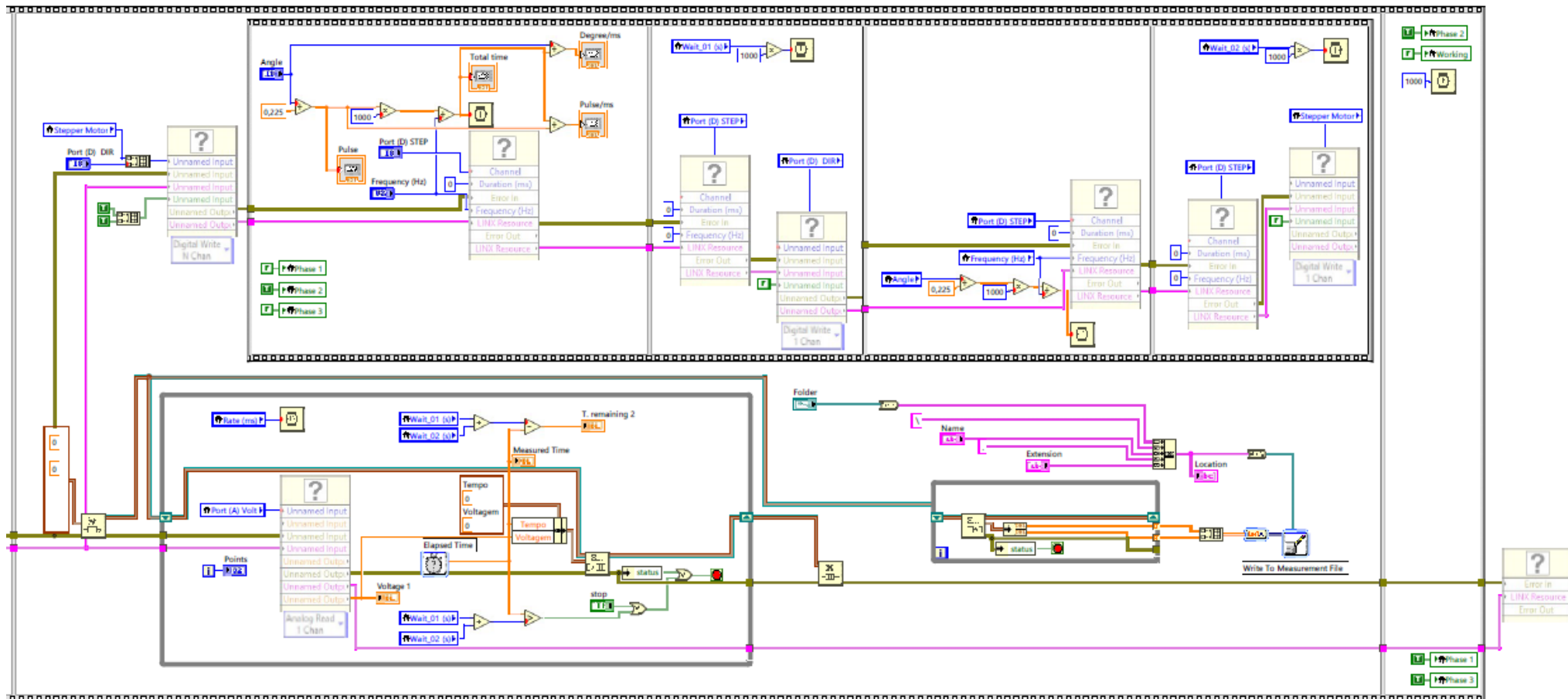


Figure C58: Pattern recognition software (part 2).